Pseudoscalar-pole contributions to Hadronic Light-by-Light scattering in the muon $g-2$ from twisted mass lattice QCD

Inaugural dissertation
at the Faculty of Science,
University of Bern

presented by

Sebastian Andreas Burri

from Burgdorf, BE and Schwarzenburg, BE

Supervisor of the doctoral thesis:

Prof. Dr. Urs Wenger

Institute for Theoretical Physics
Albert Einstein Center for Fundamental Physics
University of Bern

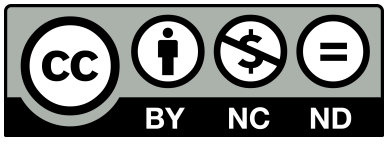

Pseudoscalar-pole contributions to Hadronic Light-by-Light scattering in the muon $g-2$ from twisted mass lattice QCD

Inaugural dissertation
at the Faculty of Science,
University of Bern

presented by

Sebastian Andreas Burri

from Burgdorf, BE and Schwarzenburg, BE

Supervisor of the doctoral thesis:

Prof. Dr. Urs Wenger

Institute for Theoretical Physics
Albert Einstein Center for Fundamental Physics
University of Bern

Accepted by the Faculty of Science.

Bern, 30.08.2023 The Dean

Prof. Dr. Marco Herwegh

Abstract

The anomalous magnetic moment of the muon provides one of the most stringent tests of the Standard Model with very precise determinations from both experiments and theory. However, there is a persistent tension between the two determinations, which has increased to 4.2 standard deviations with the latest experimental result. Currently, experimental efforts are underway to reduce the uncertainty by up to a factor of four. Testing the Standard Model on this more precise level requires that also the theory error is reduced to the same level. The Standard Model uncertainty is dominated by low-energy contributions from the strong interaction, namely the Hadronic Vacuum Polarization and the Hadronic Light-by-Light scattering. The Hadronic Light-by-Light scattering can be systematically decomposed into contributions from various intermediate states, with the dominant role played by the π^0-pole, followed by the η- and η'-poles.

In this work, the π^0- and η-pole contributions are estimated from twisted mass lattice QCD with physical light and heavy quark masses. Three ensembles generated by the Extended Twisted Mass Collaboration are used for the π^0- and one ensemble for the η-pole calculation. For the η-pole, this is the first ab-initio calculation directly at the physical point.

The main results for the pole contributions are $a_\mu^{\pi\text{-pole}} = 56.7(3.1) \times 10^{-11}$ and $a_\mu^{\eta\text{-pole}} = 13.8(5.5) \times 10^{-11}$.

Contents

Chapter 1

Introduction

The anomalous magnetic moment of the muon provides one of the most precise tests of the Standard Model (SM) and is currently measured with a precision of around 0.4 ppm [1, 2], with an uncertainty from the SM prediction at an equal level [3]. However, for about the last twenty years, there is a persistent tension between theory and experiment, which with the latest results has increased to $4.2\,\sigma$. This discrepancy has lead to a significant interest in the particle physics community, since it both constrains plausible extensions of the Standard Model and impacts our understanding of beyond-the-standard-model (BSM) physics.

The SM prediction is commonly split into quantum electrodynamic (QED), electroweak and hadronic contributions, with the hadronic contributions being split into the Hadronic Vacuum Polarization (HVP) and the Hadronic Light-by-Light scattering (HLbL). It turns out that the error in the theory prediction is dominated by the hadronic contributions. The aim of this thesis is the calculation of parts of the HLbL contribution from first principles.

The structure of this introduction is as follows. First, the magnetic moment is introduced before reviewing the current predictions of the electron and muon anomalous magnetic moments. Then, in Sec. 1.1 a brief overview on the experimental development and techniques is given before reviewing the SM contributions in Sec. 1.2. Finally, in Sec. 1.3, a few more details on the quantities calculated in this work as well as the structure of this thesis are explained.

The magnetic moment $\vec{\mu}$ is an intrinsic property of a spin-1/2 particle, defined through the interaction of the particle with an external magnetic field $\vec{B}$, with the potential energy of the magnetic moment given by $U = -\vec{\mu}\vec{B}$ [4]. It is given in natural units by

$$\vec{\mu} = g\frac{q}{2m}\vec{S}, \tag{1.1}$$

with $\vec{S}$ the particle's spin, q its charge, m its mass and g the gyromagnetic ratio which describes the overall strength of the magnetic moment in units of the classical magnetic moment [5]. The Dirac equation predicts a value of $g = 2$ for any spin-1/2 elementary particle, i.e. in particular for the three charged leptons (the electron e, muon μ and tauon τ) [6]. In the framework of relativistic quantum field theories, this "Dirac term" arises at lowest order in quantum electrodynamics (QED) from the tree-level interaction of a lepton with a real external photon.

The gyromagnetic ratio differs from 2 through contributions from radiative corrections, where the interaction of the lepton with a photon is modified by virtual loops and lines. This is a per-mille level effect for the gyromagnetic ratio of the electron and muon [5, 7]. For the charged leptons $l = e, \mu$ and τ, the anomalous magnetic moment a_l is defined by half the difference from Dirac's prediction $g_l = 2$, i.e. by

$$a_l = \frac{g_l - 2}{2}. \tag{1.2}$$

Already in 1948, the first order correction from QED was calculated by Julian Schwinger. It increases g_l universally for all three charged leptons by α/π, where α is the fine structure constant [8]. This increase was confirmed experimentally for the electron in the same year [9].

In general, quantum field theories are not analytically solvable. In the perturbative approach, quantities are expanded in powers of some coupling smaller than one in order to approximate the exact values by truncating the expansion at some power. For QED, this coupling is the fine structure constant, which is of $\mathcal{O}(10^{-2})$. Higher order corrections in the framework of perturbative QED then scale with higher powers of the fine structure constant.

Both the theoretical SM predictions and experimental measurements of a_e and a_μ are among the most precisely determined quantities in particle physics. They not only serve as a test of the SM but also as an indication of BSM physics if experiment and theory show differences, since BSM forces or virtual particles might contribute

to a_l. The SM prediction of the electron anomalous moment is dominated by QED and is in particular sensitive to the experimentally measured value of α, resulting in combined differences to the most recent experimental value of [10]

$$a_e^{\text{exp}} = 115\,965\,218.073(20) \times 10^{-11}$$

of -2.5 σ to 1.6 σ. Note that the experimental value for a_e has a precision of 0.24 ppb, while the theoretical predictions have precisions in the range of 0.1 ppb to 0.6 ppb, depending on the used determination of the fine structure constant α.
The most recent experimental value of the muon anomaly, from April 2021 [1, 2],

$$a_\mu^{\text{exp}} = 116\,592\,061(41) \times 10^{-11},$$

has a precision of 0.35 ppm, while the recommended SM value from the $g-2$ theory initiative [3],

$$a_\mu^{\text{SM}} = 116\,591\,810(43) \times 10^{-11},$$

has a precison of 0.37 ppm, resulting in the combined difference of 4.2 σ. Despite the lower precision of both the measurement and theoretical prediction of the muon anomalous moment it is of special interest since it is much more sensitive to electroweak, strong and BSM contributions compared to a_e. As pointed out in [11], any modification to the photon propagator or a new coupling to both electrons and muons would perturb a_μ by a factor $(m_\mu/m_e)^2 \approx 40\,000$ compared to a_e. In principle, the tauon anomalous moment would be even more sensitive to new physics, but its extremely short mean life time of 290.3(5) fs [12] makes a precision measurement of a_τ impossible with the currently available technologies.

1.1 Overview of the experimental development

The history of the muon $g-2$ experiments starts with the measurement published in 1957 by the Columbia Nevis group [13], with a second result published just two months later by the University of Liverpool, already reaching a precision of 1% on g_μ [14]. The Columbia Nevis group then improved their experiment, resulting in a measurement of a_μ with a precison of 6.5% which they published in 1960 [15].

Borrowing the magnet from Liverpool, the first of three experiments at CERN was started in 1959. The CERN I experiment gave a measurement with a 0.4% error on a_μ already in 1962 [16, 17]. Recognizing the need for increased observation time of the spin precession for higher precision, the CERN II experiment [18] was the first to make use of a storage ring to employ relativistic muons with a boosted mean life time in the laboratory frame compared to their mean life at rest of 2.1969811(22) μs [12]. Further improvements were made in the CERN III experiment, most notably muons at the so-called "magic momentum" of 3.1 GeV/c were stored for measuring a_μ, which cancels out the first order electric field contribution from the used focusing electric quadrupoles [19]. More details about the "magic momentum" will be given later in this section. The final report of the three CERN experiments, published in 1979, gives a precision of 7.3 ppm on a_μ when combining all CERN measurements [19]. The most recent completed experiment was conducted at the Brookhaven National Laboratory (BNL). It follows the same general technique as CERN III, with the most notable improvements being firstly direct muon injection utilizing a passive instead of a pulsed inflector magnetic and pulsed magnetic kicker, and secondly the superferric superconducting storage ring magnet with a more uniform magnetic field. After the measurements concluded in 2001, the final report was published in 2004, giving a_μ with a precision of 0.54 ppm [20].

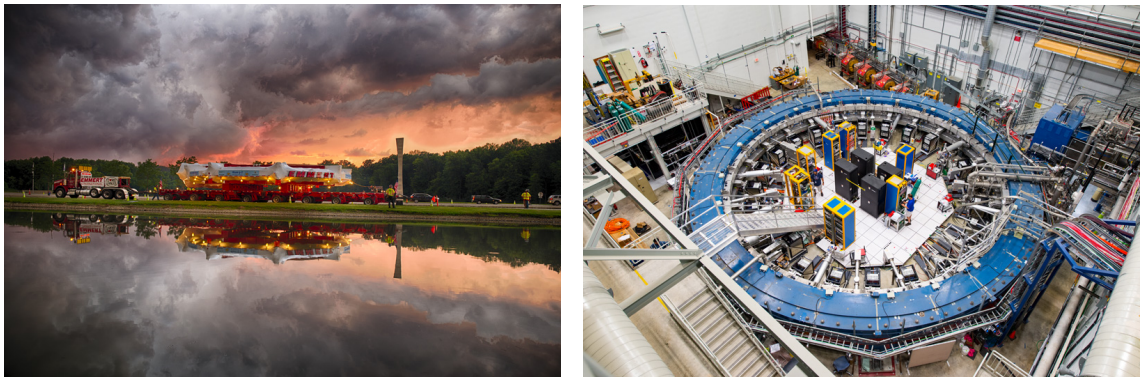

Figure 1.1: Arrival of the BNL E821 muon storage ring at Fermilab in 2013 for FNL E989 (left), installed ring in its detector hall (right). Pictures from [21].

For the Fermilab muon $g-2$ experiment, the storage ring from BNL was transported to Fermilab in 2013, see Fig. 1.1 for some photographs. The 14 m diameter ring was transported in a five-week journey of more than 5000 km over land and sea.
Notable improvements include better instrumentation for the magnetic field and the

muon spin precession frequency measurements as well as the utilization of a more intense and pure muon beam [22]. The target precision is 0.14 ppm after a total of six data taking periods, with Run-6 being completed in 2023. The Run-1 result, published in 2021, already reached the same precision as the final BNL result, the analysis from Run-2 and Run-3 is expected to be published in 2023 [1, 2].
Planned to start data taking in 2027 is the muon $g-2$/EDM experiment J-PARC (E34) in Japan. Its goal is to provide an independent measurement of a_μ with an as of yet unused approach to the muon beam line utilizing a very low-emittance muon beam, produced by re-acceleration of thermal muons, which eliminates the need for the strong focusing electric quadrupoles used at BNL or Fermilab and thus allows muon momenta different from the "magic momentum" [23–25].

The muon $g-2$ storage ring experiments inject spin-polarized muons into the magnetic storage ring and measure the relative precession frequency of the spin of the muons with respect to their momentum. This so-called anomalous precession frequency ω_a is defined as the difference between spin precession frequency ω_s and the cyclotron frequency ω_c for muons orbiting in a highly uniform magnetic field $\vec{B}$ [7]. In the absence of an electric field and for muons orbiting perpendicular to the magnetic field,

$$\vec{\omega}_a \equiv \vec{\omega}_s - \vec{\omega}_c = -a_\mu \frac{q\vec{B}}{m_\mu} \tag{1.3}$$

holds, where m_μ is the muon mass. Thus a measurement of $\vec{\omega}_a$, combined with precise knowledge of the storage ring magnetic field $\vec{B}$, allows for a precise determination of a_μ. In the presence of an electric field $\vec{E}$ and while accounting for an electric dipole moment (EDM) of the muon, the total spin precession vector with respect to its momentum is given by

$$\begin{aligned}\vec{\omega} &= \vec{\omega}_a + \vec{\omega}_\eta \\ &= -\frac{q}{m_\mu}\left[a_\mu \vec{B} - \left(a_\mu - \frac{1}{\gamma^2-1}\right)\frac{\vec{\beta}\times\vec{E}}{c} + \frac{\eta_\mu}{2}\left(\vec{\beta}\times\vec{B} + \frac{\vec{E}}{c}\right)\right],\end{aligned} \tag{1.4}$$

where $\vec{\omega}_\eta$ is the precession vector due to the EDM and $\vec{\beta}$ and γ the velocity and Lorentz factor of the muon. η_μ is the factor corresponding to g_μ for the EDM [23]. In the CERN III, BNL and Fermilab experiments, the muons are tuned to the "magic momentum" of 3.1 GeV/c, where $\gamma \approx 29.3$, such that the second term in Eq. (1.4)

goes to zero. In the Fermilab experiment, the stored muon beam has a narrow momentum spread of approximately 0.15% around the "magic momentum". This momentum spread is picked up by the detectors and taken into account for the analysis [1]. The planned experiment at J-PARC will use no electric field for focusing the muon beam, thus reducing all terms involving $\vec{E}$ in Eq. (1.4) to zero. The key requirement for storing the muon beam with only a magnetic focusing field is a muon beam with low emittance [23].

1.2 Overview of the Standard Model contributions

Turning to the theoretical calculations of a_μ, the SM prediction for the anomalous magnetic moment gets contributions from all sectors of the SM, and is commonly split into

$$a_\mu^{\mathrm{SM}} = a_\mu^{\mathrm{QED}} + a_\mu^{\mathrm{EW}} + a_\mu^{\mathrm{HVP}} + a_\mu^{\mathrm{HLbL}}, \tag{1.5}$$

with a_μ^{QED} the QED contribution, a_μ^{EW} the elektroweak (EW) contribution, a_μ^{HVP} the Hadronic Vacuum Polarization (HVP) contribution and a_μ^{HLbL} the Hadronic Light-by-Light scattering (HLbL) contribution. Both the QED and EW contributions come with negligible uncertainty, the error of the SM prediction is dominated by the hadronic contributions due to the non-perturbative strong interaction at low energies. In 2020, the Muon $g-2$ Theory Initiative published a white paper [3], with the goal to provide community-approved values for the SM contributions. An update of the white paper is expected for 2023. In Tab. 1.1, the SM values are summarized and compared to the experiment.

The most precisely determined SM contribution is a_μ^{QED}, which accounts for more than 99% of the anomalous magentic moment of the muon. a_μ^{QED} consists of all contribution only involving photons and leptons, it has been calculated both analytically and numerically up to four-loop order, the fifth-loop order contribution has been fully calculated numerically. Its uncertainty stems from four- and five-loop QED, the estimation of the six-loop QED and the fine structure constant α, with a negligible total uncertainty of 0.9 ppb, cf. [3, 26] and references therein.

Also coming with a negligible uncertainty of 8.6 ppb is a_μ^{EW}, which constitutes of all diagrams involving at least one of the EW bosons, i.e. W, Z or Higgs. They are

Contribution	Value $\times 10^{11}$
E821	116 592 089(63)
E821 + E989 Run-1	116 592 061(41)
QED	116 584 718.931(0.104)
Electroweak	153.6(1.0)
HVP (e^+e^-, LO+NLO+NNLO)	6 845(40)
HLbL (phenom. + lattice + NLO)	92(18)
SM total	116 591 810(43)
$a_\mu^{\text{E821}} - a_\mu^{\text{SM}}$	279(76)
$a_\mu^{\text{E821 + E989 Run-1}} - a_\mu^{\text{SM}}$	251(59)

Table 1.1: Experimental values and recommended SM contributions to a_μ from [3], FNL Run-1 value from [2].

strongly suppressed by the heavy masses of the EW bosons and in total contribute numerically at the same order as a_μ^{HLbL}. Their calculation has been done up to two-loop order, with dominant three-loop effects estimated from the renormalization group. The uncertainty is dominated by non-perturbative hadronic insertions entering at two-loop, cf. [3, 7] and references therein.

The most sizeable hadronic effect, contributing the most to the SM prediction error, comes from the HVP, entering at order $\mathcal{O}(\alpha^2)$ in the framework of perturbative QED. Its leading order Feynman diagram is depicted in Fig. 1.2. a_μ^{HVP} can be calculated

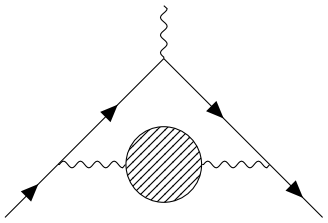

Figure 1.2: Hadronic vacuum polarization diagram in the muon $g-2$ at leading order. The striped circle indicates all possible intermediate hadronic states.

using data-driven methods, utilizing experimental input from e^+e^- annihilation into dispersion relations, or from lattice QCD. The data-driven HVP estimations have been calculated by various groups using different assumptions on the functional form of the cross section entering the dispersion relation and treating the data differently. Three such results have been merged up to NNLO to obtain the sub-percent level precision value in Tab. 1.1, see [3, 27–33]. Improvements of the data-driven estimate are expected from new $e^+e^- \to$ hadrons cross section measurements, in particular

those of the $\pi^+\pi^-$ channel. Belle-II [34], BaBar [35] and BES-III [36] are all expected to provide such data sets, while CMD-3 recently released new results [37]. On the lattice, the first result with sub-percent precision was the BMW-20 analysis published in 2020 [38]. Other recent lattice results are the LM-20 [39], ETM-22 [40] and CLS/Mainz-22 [41] analyses, of which the latter two study so-called short and intermediate distance windows. Note that these results were not yet included in [3] and that both the BMW-20 and LM-20 results would push the SM prediction for a_μ closer to the experimental value, with a combined discrepancy between theory and experiment of only $2\,\sigma$.

Entering at $\mathcal{O}(\alpha^3)$ in the framework of perturbative QED is the contribution from Hadronic Light-by-Light scattering, a_μ^{HLbL}, which also can be calculated by data-driven methods and lattice QCD. Due to its suppression by an additional power of α compared to the HVP contribution, the HLbL contribution is two orders of magnitude smaller. Since the HLbL involves four-point functions as opposed to the two-point HVP function, it is determined to a much lower relative precision than HVP, such that the second most significant contribution to the overall error of the SM prediction comes from HLbL. a_μ^{HLbL} gets contributions from single meson exchanges, axial-vector mesons, tensor mesons and charged pion and kaon loops [3]. There have been many approaches to estimate the HLbL contribution, e.g. [42–51], with the modern data-driven and dispersive methods providing model-independent evaluations of a_μ^{HLbL}. The HLbL tensor can be systematically decomposed into contributions from various intermediate states [52–55]. The bulk of a_μ^{HLbL} is expected to originate from states at energies of up to $1.5\,\mathrm{GeV/c}$, with the numerically dominant role played by the π^0-pole, followed by η- and η'-poles, while two pion and two kaon contributions are further suppressed. Its leading order Feynman diagram as well as the pseudoscalar-pole diagrams are depicted in Fig. 1.3. Lattice QCD can be utilized to both provide form factors and hadron scattering amplitudes used with the approach of systematically decomposing the HLbL tensor into contributions from intermediate states as well as for calculating the full HLbL scattering amplitude [56–62]. Recent data-driven estimates of the pseudoscalar-pole contributions include [63–65] and recent lattice QCD calculations [66–71].

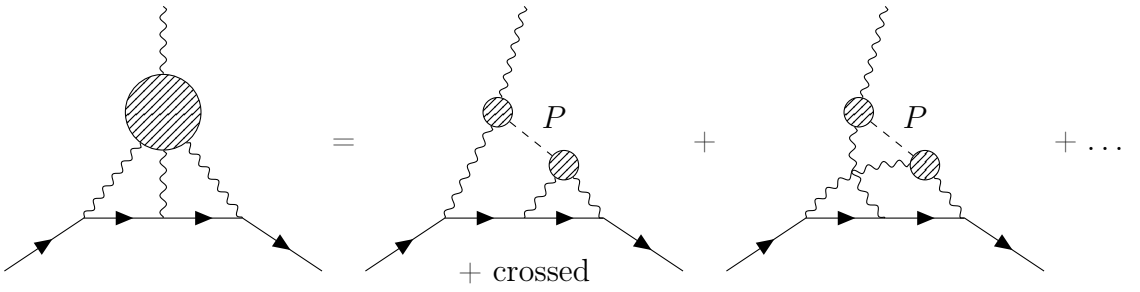

Figure 1.3: The pseudoscalar-pole diagrams contributing to the leading order HLbL scattering in the muon $g-2$. The striped circle on the left indicates all possible intermediate hadronic states, while the striped circles on the right indicate the nonperturbative $P \to \gamma^*\gamma^*$ transition form factors required to evaluate these contributions.

1.3 Hadronic Light-by-Light scattering and the aim of this thesis

The calculation of the leading pseudoscalar-pole contributions to HLbL involve the transition form factors (TFFs) $\mathcal{F}_{P\to\gamma^*\gamma^*}$ of the transition of a neutral pseudoscalar meson $P = \pi^0,\ \eta$ and η' to two (virtual) photons, $P \to \gamma^*\gamma^*$, defined by the matrix element

$$i \int d^4x\, e^{iq_1 x} \langle 0|T\{j_\mu(x) j_\nu(0)\}|P(q_1+q_2)\rangle = \varepsilon_{\mu\nu\rho\sigma} q_1^\rho q_2^\sigma \mathcal{F}_{P\to\gamma^*\gamma^*}(q_1^2, q_2^2), \tag{1.6}$$

where j_μ and j_ν are the electromagnetic currents and q_1 and q_2 the photon momenta. For the space-like single-virtual $\mathcal{F}_{P\to\gamma^*\gamma}(-Q^2, 0)$ with $Q^2 \gtrsim 1\,\mathrm{GeV}^2$, there exists experimental data from CLEO, CELLO, BaBar and Belle, cf. [72–76], while lattice QCD provides access to a broad range of (space-like) photon four-momenta complementary to the experiments. The TFFs can also be used to determine the partial decay widths

$$\Gamma(P \to \gamma\gamma) = \frac{\pi\alpha^2 m_P^3}{4} |\mathcal{F}_{P\to\gamma\gamma}(0,0)|^2, \tag{1.7}$$

where m_P is the pseudoscalar mass, and slope parameter

$$b_P = \frac{1}{\mathcal{F}_{P\to\gamma\gamma}(0,0)} \frac{\mathrm{d}\mathcal{F}_{P\to\gamma^*\gamma}(q^2,0)}{\mathrm{d}q^2}\bigg|_{q^2=0}, \tag{1.8}$$

which plays a role in the electromagnetic interaction radius of the pseudoscalar mesons.

The aim of this work is the computation of the pseudoscalar transition form factors $\mathcal{F}_{P\to\gamma^*\gamma^*}$ for the pseudoscalar states $P = \pi^0$ and η to determine the corresponding pole contributions to a_μ^{HLbL} as well as the partial decay widths $\Gamma(P \to \gamma\gamma)$ and slope parameters b_P. Twisted mass lattice QCD (tmLQCD) ensembles with $N_f = 2+1+1$ flavours tuned to the physical point, i.e. with physical light and heavy quark masses, at maximal twist [77] are used, which guarantees automatic $\mathcal{O}(a)$ improvement for the observables calculated in this work [78, 79].

The structure of this thesis is as follows. In Chapter 2, twisted mass lattice QCD is introduced and some of its properties discussed. Then, details on the lattice setup used for this thesis are given. In Chapter 3, a brief overview on the calculation of the pseudoscalar-pole contributions to HLbL is given before the computation of the amplitudes used for their calculation is discussed in detail. Finally, some properties of the employed ensembles and configurations are given. Chapter 4 reproduces the publications written as part of this work, i.e. [68, 69, 71], while Chapter 5 is a draft in preparation for publication. Finally, Chapter 6 concludes this thesis with a summary and outlook.

Appendix A gives details on the operators, symmetries and conventions used in the pion-pole calculation and is part of the draft in Ch. 5, appendix B deals with theoretical aspects relevant for Ch. 2 and 3 and in particular with the symmetries and operators relevant for the η-pole calculation. Next, appendix C gives details on model averaging and error calculation, while the final appendix D contains a selection of plots complementary to the ones shown in Ch. 3 to 5.

Chapter 2

Twisted mass lattice QCD and lattice setup

In this chapter, twisted mass lattice QCD is introduced in Sec. 2.1. It starts with a short discussion on lattice QCD and Wilson lattice QCD in Secs. 2.1.1 to 2.1.3 before turning to Wilson twisted mass lattice QCD in Secs. 2.1.4 to 2.1.8. Finally, the used lattice setup is discussed in Sec. 2.2.

2.1 Twisted mass lattice QCD

In this section, the basics of twisted mass lattice QCD (tmLQCD) are reviewed, closely following [80–82], with other references explicitly pointed out where relevant. It is organized as follows. After some introductory remarks, the Wilson lattice regularization scheme is introduced and a few of its properties as well as the problem of unphysical zero modes are discussed, leading to its modification by the twisted mass term to alleviate the problem of the unphysical fermion zero modes. Then, the equivalence of twisted mass QCD (tmQCD) and QCD in the continuum are sketched and cutoff effects in tmLQCD are discussed. After that, non-degenerate quarks and additional flavours are introduced. Finally, the section ends with some concluding remarks. For general introductions to lattice QCD the interested reader is referred

to [83–86], while more details on twisted mass lattice QCD can be found in [77–79].

2.1.1 Introduction to lattice QCD

In order to discuss quantum chromodynamics (QCD), the fundamental quantum field theory of quarks and gluons, in a mathematically well-defined way it has to be regularized. QCD has the property of asymptotic freedom, meaning that the renormalized dimensional coupling of QCD, g_0, which depends on the energy scale of the considered physical process and measures the strength of the interaction at said energy scale, is decreasing with increasing energy. Thus pertubation theory can be used to make phenomenological predictions in the high energy region, but not in the low energy region where g_0 is of order $\mathcal{O}(1)$. An effective approach which has become a standard method in elementary particle physics is the replacement of space-time by an Euclidean lattice. There are multiple sensible discretizations of the continuum QCD action, with the simple one proposed by Wilson [87, 88] getting rid of the so-called fermion doubling problem, see e.g. [83], at the cost of explicitly breaking chiral symmetry in the discretized theory. Lattice QCD, being non-perturbative, makes it possible to compute physical quantities in the low energy region, such as the mass spectrum or hadronic matrix elements. In lattice QCD, the path integral is regularized by replacing the continuous space-time by a four dimensional finite lattice with lattice constant a, given for a hypercubic lattice by

$$\Lambda = \{n | n_i \in \{0, 1, ..., N_x - 1\} \text{ for } i \in \{1, 2, 3\}, n_4 \in \{0, 1, ..., N_t - 1\}\}, \qquad (2.1)$$

with $n = (n_1, n_2, n_3, n_4)$, where N_x is the spatial and N_t the temporal extent of the lattice. The lattice constant a has the physical dimension of length and is thus called "lattice spacing". Physical space-time points are then given by $x = an$, but to keep the notation compact, only n is used here. The fermionic degrees of freedom are $\psi(n), \bar{\psi}(n)$, while the gauge degrees of freedom are the link variables $U_\mu(n) = \exp(ig_0 a G_\mu(n))$, $n \in \Lambda$, where G_μ is the gluon field and g_0 the bare gauge coupling. Note that there is a relation between the coupling constant g_0 and the lattice spacing a in physical units through the renormalization group equations, see

e.g. [89]. Then, n-point correlation functions are given by

$$\langle \mathcal{O}(n_1, ..., n_m) \rangle = \mathcal{Z}^{-1} \int D[U, \psi, \bar{\psi}]\, e^{-S} \mathcal{O}(n_1, ..., n_m), \tag{2.2}$$

with $\mathcal{O}(n_1, ..., n_m)$ a product of local gauge invariant composite fields localized at $n_1, ..., n_m$, $n_i \in \Lambda$. The partition function is given by

$$\mathcal{Z} = \langle 1 \rangle = \int D[U, \psi, \bar{\psi}]\, e^{-S}, \tag{2.3}$$

where S is the Euclidean action of the system discretized on the lattice such that the Euclidean continuum action is recovered for $a \to 0$. The path integral measures on the lattice are products of measures of all quark field components and link variables, i.e.

$$D[\psi, \bar{\psi}] = \prod_{n \in \Lambda} \prod_{f,\alpha,c} d\psi^f_{\alpha,c}(n) d\bar{\psi}^f_{\alpha,c}(n), \qquad D[U] = \prod_{n \in \Lambda} \prod_{\mu=1}^{4} dU_\mu(n), \tag{2.4}$$

with explicit flavour index $f \in \{1, 2, 3, 4, 5, 6\}$, Dirac index $\alpha \in \{1, 2, 3, 4\}$ and color index $c \in \{1, 2, 3\}$. Using Monte Carlo methods, it is possible to simulate QCD in a finite volume lattice and calculate such correlation functions at finite lattice spacing. To obtain results for the correlation functions in the continuum, the limit $a \to 0$ needs to be taken. For more details see [84].

Using the Wilson fermion action, errors of order $\mathcal{O}(a)$ are introduced in the results of the simulations. $\mathcal{O}(a)$ cutoff effects in on-shell quantities can be cancelled using Symanzik's improvement program [90–93] by the addition of local $\mathcal{O}(a)$ counterterms to the lattice action. Applied to Wilson quarks, it turns out that particle masses and energies can be $\mathcal{O}(a)$ improved by adding just a single counterterm to the action, the Sheikholeslami-Wohlert (SW) or clover term [94], but matrix elements of composite operators come with sets of counterterms for each operator, and [95] shows that $\mathcal{O}(a)$ improvement becomes impractical for quarks with non-degenerate masses. Further, the Wilson fermion action suffers from unphysical fermionic zero modes in quenched and partially quenched simulations, as discussed in Sec. 2.1.3.

While twisted mass QCD was introduced to solve the problem of these unphysical fermionic zero modes in lattice QCD with Wilson quarks, it turns out that it can also be used to circumvent some lattice renormalization problems [77, 96] and that

scaling violations can be reduced to $\mathcal{O}(a^2)$ by "automatic $\mathcal{O}(a)$ improvement", not needing all the counterterms from the standard Wilson formulation [78].

2.1.2 The Wilson lattice action

The QCD action can be decomposed in a pure gauge and a fermionic part, i.e. $S = S_g + S_f$. Focussing on the fermionic part S_f of the QCD action, the Wilson lattice regularization scheme is characterized by the fermionic lattice action [88]

$$S_f = a^4 \sum_x \bar{\psi}(x) \left[D_W + m_0 \right] \psi(x), \tag{2.5}$$

$$D_W = \sum_{\mu=0}^{3} \left\{ \frac{1}{2} \left(\nabla_\mu + \nabla_\mu^* \right) \gamma_\mu - ar \nabla_\mu^* \nabla_\mu \right\}, \tag{2.6}$$

where ψ, $\bar{\psi}$ are the quark and antiquark fields, m_0 is the bare mass parameter matrix and the covariant lattice derivatives ∇_μ, ∇_μ^* in the Wilson-Dirac D_W operator are defined in App. B.1. The so-called Wilson parameter r is always set to 1 unless otherwise specified. The quark field is a vector in flavour space with N_f components labelled by ψ_f while m_0 is diagonal with components m_{0f}, $f \in \{1, ..., N_f\}$. In the case of degenerate quark masses, i.e. $m_{01} = ... = m_{0N_f}$, the fermionic Wilson lattice action (2.5) is invariant under $SU(N_f)_V$ global vector transformations of the fermion field, given by

$$\begin{aligned} \psi(x) \to \psi'(x) &= \exp\left[i\alpha_V^a \frac{\lambda^a}{2} \right] \psi(x), \\ \bar{\psi}(x) \to \bar{\psi}'(x) &= \bar{\psi}(x) \exp\left[-i\alpha_V^a \frac{\lambda^a}{2} \right], \end{aligned} \tag{2.7}$$

with transformation parameter α_V^a where the group generators in the fundamental representation are the flavour matrices $\lambda^a/2$, $a \in \{1, ..., N_f^2 - 1\}$, given for $N_f = 2$ by the three Pauli matrices and for $N_f = 3$ by the eight Gell-Mann matrices. Note that the standard continuum action of QCD, cf. App. B.2, with degenerate quark masses is also invariant under this vector (or isospin) symmetry. On the other hand,

global axial transformations of the fermion field, given by

$$\begin{aligned}\psi(x) \to \psi'(x) &= \exp\left[i\alpha_A^a \frac{\lambda^a}{2}\gamma_5\right]\psi(x),\\ \bar{\psi}(x) \to \bar{\psi}'(x) &= \bar{\psi}(x)\exp\left[i\alpha_A^a \frac{\lambda^a}{2}\gamma_5\right],\end{aligned} \tag{2.8}$$

do not leave (2.5) invariant even for $m_0 = 0$ due to the Wilson term $ar\nabla_\mu^*\nabla_\mu$, while they would leave the standard continuum action of QCD with $m_0 = 0$ invariant. Thus the chiral group $SU_L(N_f) \times SU_R(N_f)$ is not a symmetry of Wilson fermions. Inter alia, consequences of the explicit breaking of all axial symmetries are a linear mass divergence of the renormalized quark mass since the quark mass term is not protected against additive renormalization, a non-trivial multiplicative renormalization required to restore the current algebra up to $\mathcal{O}(a)$ effects for the non-singlet axial current since axial transformations are not an exact symmetry and it also leads to the leading cutoff effects having $\mathcal{O}(a)$.

2.1.3 Unphysical fermionic zero modes with Wilson quarks

Due to the aforementioned additive renormalization of the quark mass, the value of m_0 corresponding to the physical light quark masses is typically negative in simulations with Wilson quarks, which leaves the massive Wilson-Dirac operator $D_W + m_0$ unprotected against zero modes. These are considered unphysical since one expects from the continuum theory that zero modes of the Wilson-Dirac operator are prohibited by any non-zero value of the renormalized quark mass. To illustrate this phenomenon, consider the eigenvalues of $D_W + m_0$. They are given by

$$m_0 + c_i, \tag{2.9}$$

where c_i are the eigenvalues of the massless Wilson-Dirac operator D_W. These eigenvalues are in general complex numbers, but it is also possible that they are real, i.e. $c_i = r_i$. If $m_0 + r_i \ll 1$, i.e. if the massive Wilson-Dirac operator has a very small eigenvalue, the numerical inversion of $D_W + m_0$ breaks down [84].

The textbook example from [80,81], illustrating a case where this could be problematic

due to not including the quark determinant in the generation of an ensemble of gauge configurations dictated by the limited available computing power in the past, goes as follows. Consider for $N_f = 2$ quarks the pion two-point function given by

$$\begin{aligned} G^{ab}(x) &= -\left\langle \bar{\psi}(x)\gamma_5\frac{\tau^a}{2}\psi(x)\bar{\psi}(0)\gamma_5\frac{\tau^b}{2}\psi(0)\right\rangle \\ &= -\mathcal{Z}^{-1}\int D[U,\psi,\bar{\psi}]\, e^{-S}\bar{\psi}(x)\gamma_5\frac{\tau^a}{2}\psi(x)\bar{\psi}(0)\gamma_5\frac{\tau^b}{2}\psi(0), \end{aligned} \tag{2.10}$$

with τ^a the three Pauli matrices acting in flavour space and $\mathcal{Z}$ given in Eq. (2.3). Introducing the Hermitian Wilson operator,

$$Q_W \equiv \gamma_5(D_W + m_0), \qquad Q_W = Q_W^\dagger, \tag{2.11}$$

by noting the γ_5-hermiticity of D_W, i.e. $\gamma_5 D_W \gamma_5 = D_W^\dagger$, and performing the functional integrals over the fermion fields leads to

$$G^{ab}(x) = \frac{1}{2}\delta^{ab}\mathcal{Z}^{-1}\int D[U]\, e^{-S_g}\det\left(Q_W^2\right)\mathrm{Tr}\left[Q_W^{-1}(0,x)Q_W^{-1}(x,0)\right], \tag{2.12}$$

with the trace running over colour and spin indices. This expression is never singular as shown in the following, which is an example of the fact that a functional integral over Grassmann variables cannot diverge. Using the eigenfunctions $\phi_i(x)$ and eigenvalues λ_i of Q_W yields

$$G^{ab}(x) = \frac{1}{2}\delta^{ab}\mathcal{Z}^{-1}\int D[U]\, e^{-S_g}\left[\prod_i \lambda_i^2\right]\sum_{j,k}\phi_j(0)\frac{1}{\lambda_j}\phi_j^*(x)\phi_k(x)\frac{1}{\lambda_k}\phi_k^*(0), \tag{2.13}$$

so eigenvalues in the quark propagators, i.e. those in the denominator, are cancelled by corresponding factors coming from the fermionic determinant.

Historically, in the so-called quenched model the quark determinant $\det(Q_W^2)$ was not included in the generation of an ensemble of gauge configurations to significantly reduce the computational cost. Thus contributions from vanishing eigenvalues to a fermionic correlator are not compensated by the determinant in this case, which leads to large fluctuations in some observables. Such gauge field configurations are called "exceptional". The inclusion of such exceptional configurations in the ensemble average would lead to much larger errors on the affected observables, i.e. in principle

any observable depending on quark propagators, but they cannot just be omitted since that would invalidate the Markov chains in the Monte Carlo procedure.
With the increase in available computing power in recent years, modern lattice QCD simulations are in general unquenched, i.e. including the quark determinant in the generation of an ensemble of gauge configurations. As a consequence, gauge configurations leading to vanishing eigenvalues of the massive Wilson-Dirac operator are never accepted when generating an ensemble since they get a weight of zero in the Metropolis accept-reject step due to the vanishing quark determinant in that case, cf. e.g. [83, 84].

2.1.4 Twisted mass lattice QCD

The main motivation for the introduction of the twisted mass term were the zero modes discussed in Sec. 2.1.3. The Wilson twisted mass lattice regularization scheme for a doublet of two mass degenerate quarks is characterized by the fermionic lattice action

$$S_f = a^4 \sum_x \bar{\chi}(x) \left[D_W + m_0 + i\mu_q \gamma_5 \tau^3 \right] \chi(x), \tag{2.14}$$

where μ_q is the bare twisted mass parameter and χ, $\bar{\chi}$ are used to denote the quark and antiquark fields in the twisted basis. Extensions to non-degenerate quarks and additional flavours will be discussed later in this section. It is indeed straightforward to see that the presence of the twisted mass parameter eliminates the unphysical fermionic zero modes, since for the Wilson twisted mass operator

$$Q = \gamma_5 (D_W + m_0 + i\mu_q \gamma_5 \tau^3) = Q_W + i\mu_q \tau^3 \tag{2.15}$$

holds, using $\det(\gamma_5) = 1$ thus yields

$$\begin{aligned} \det\left(D_W + m_0 + i\mu_q \gamma_5 \tau^3\right) &= \det \begin{pmatrix} Q_W + i\mu_q & 0 \\ 0 & Q_W - i\mu_q \end{pmatrix} \\ &= \det\left(Q_W^2 + \mu_q^2\right) > 0 \end{aligned} \tag{2.16}$$

for $\mu_q \neq 0$, such that exceptional configurations only appear in the massless $\mu_q = 0$ theory. Note that the Wilson term breaking the axial symmetries (2.8) even when

$m_0 = 0$ implies that the twisted mass term cannot be eliminated by an axial rotation, thus there is no exact equivalence between the fermionic Wilson lattice action with vanishing and non-vanishing twisted mass parameter. However, as discussed in the next subsection, both regularizations are equivalent in the continuum limit.

2.1.5 Equivalence of tmQCD and QCD

For the moment still only considering a doublet of two mass degenerate quarks, the fermionic continuum action of twisted mass QCD takes the form

$$\begin{aligned} S_f &= \int d^4x\, \bar{\chi}(x) \left[\not{D} + m_0 + i\mu_q \gamma_5 \tau^3 \right] \chi(x) \\ &= \int d^4x\, \bar{\chi}(x) \left[\not{D} + M_{\text{inv}} \exp\left[i\omega\gamma_5\tau^3 \right] \right] \chi(x), \end{aligned} \tag{2.17}$$

with $\not{D} = \gamma_\mu D_\mu$, the covariant derivative $D_\mu = \partial_\mu + G_\mu$ and G_μ the gluon field. Further, $M_{\text{inv}} = \sqrt{m_0^2 + \mu_q^2}$ and the twist angle ω is defined by $\tan(\omega) = \mu_q / m_0$. Under a global chiral field rotation

$$\begin{aligned} \chi \to \chi' &= \exp\left[i\frac{\alpha}{2}\gamma_5\tau^3 \right] \chi, \\ \bar{\chi} \to \bar{\chi}' &= \bar{\chi} \exp\left[i\frac{\alpha}{2}\gamma_5\tau^3 \right], \end{aligned} \tag{2.18}$$

the fermionic continuum tmQCD action (2.17) transforms to

$$S_f = \int d^4x\, \bar{\chi}'(x) \left[\not{D} + M_{\text{inv}} \exp\left[i(\omega - \alpha)\gamma_5\tau^3 \right] \right] \chi'(x). \tag{2.19}$$

Thus for $\tan(\alpha) = \tan(\omega) = \mu_q / m_0$ the standard fermionic continuum QCD action,

$$S_f = \int d^4x\, \bar{\psi}(x) \left[\not{D} + M_{\text{inv}} \right] \psi(x), \tag{2.20}$$

is recovered. See App. B.2 for more details. The basis $\{\bar{\psi}, \psi\}$, where the continuum QCD action takes the standard form is called the physical basis, while $\{\bar{\chi}, \chi\}$ is used to distinguish quark fields for which the continuum QCD action takes the from (2.17). Note that tmQCD may thus be regarded as a family of equivalent theories, parametrized by M_{inv} and the twist parameter ω. Since standard QCD is part of this

family, tmQCD and QCD share all symmetries, with the symmetry transformations in the twisted basis being the standard symmetries transformed using Eq. (2.18). These transformations will be called twisted symmetries, the ones used in this thesis at $\omega = \pi/2$ are collected in App. A.1.2 to A.1.4 and B.3. Further, the n-point correlation functions given in Eq. (2.2) can be expressed in both the physical and twisted basis using (2.17), giving the relation

$$\langle \mathcal{O}[\psi, \bar{\psi}] \rangle_{(M_{\text{inv}},0)} = \langle \mathcal{O}[\psi, \bar{\psi}] \rangle_{(M_{\text{inv}},\omega)} \equiv \langle \mathcal{O}[\chi, \bar{\chi}] \rangle_{(m_0,\mu_q)}, \tag{2.21}$$

where the index $(M_{\text{inv}}, 0)$ indicates that the correlation function has been computed in standard QCD with quark mass M_{inv}, while the indices (M_{inv}, ω) or (m_0, μ_q) indicate that it has been computed in tmQCD with masses m_0 and μ_q at twist angle $\tan(\omega) = \mu_q/m_0$. Chiral multiplets relevant for this work can be constructed from the axial and vector (Noether) currents V_μ^a and A_μ^a as well as the non-singlet pseudo-scalar (axial) density P^a and the singlet scalar density S^0, given in the twisted basis for $N_f = 2$ as

$$\begin{aligned} V_\mu^a &= \bar{\chi}\gamma_\mu \frac{\tau^a}{2}\chi, \quad A_\mu^a = \bar{\chi}\gamma_\mu\gamma_5 \frac{\tau^a}{2}\chi, \\ P^a &= \bar{\chi}\gamma_5 \frac{\tau^a}{2}\chi, \quad S^0 = \bar{\chi}\chi, \end{aligned} \tag{2.22}$$

and in the physical basis as $V_\mu'^a = \bar{\psi}\gamma_\mu \frac{\tau^a}{2}\psi$, analogous for the other three. Again using Eq. (2.18) yields

$$\begin{aligned} V_\mu'^1 &= \cos(\omega)V_\mu^1 + \sin(\omega)A_\mu^2, & A_\mu'^1 &= \cos(\omega)A_\mu^1 + \sin(\omega)V_\mu^2, \\ V_\mu'^2 &= \cos(\omega)V_\mu^2 - \sin(\omega)A_\mu^1, & A_\mu'^2 &= \cos(\omega)A_\mu^2 - \sin(\omega)V_\mu^1, \\ V_\mu'^3 &= V_\mu^3, & A_\mu'^3 &= A_\mu^3, \\ P'^a &= P^a \text{ for } a \in \{1,2\}, & S'^0 &= \cos(\omega)S^0 + 2i\sin(\omega)P^3, \\ P'^3 &= \cos(\omega)P^3 + \frac{1}{2}i\sin(\omega)S^0. \end{aligned} \tag{2.23}$$

The standard example for a correlator is then

$$\langle A_\mu'^1(x)P'^1(y)\rangle_{(M_{\text{inv}},0)} = \cos(\omega)\langle A_\mu^1(x)P^1(y)\rangle_{(M_{\text{inv}},\omega)} + \sin(\omega)\langle V_\mu^2(x)P^1(y)\rangle_{(M_{\text{inv}},\omega)} \tag{2.24}$$

and more general correlation functions in standard QCD will be linear combinations of tmQCD correlation functions at the same twist angle ω. Further, the classical

partially conserved axial current (PCAC) and partially conserved vector current (PCVC) relations, given by

$$\partial_\mu A'^a_\mu = 2M_{\text{inv}} P'^a, \tag{2.25}$$

$$\partial_\mu V'^a_\mu = 0, \tag{2.26}$$

in the physical basis are equivalent to

$$\partial_\mu A^a_\mu = 2M_{\text{inv}} \cos(\omega) P^a + iM_{\text{inv}} \sin(\omega) \delta^{3a} S^0, \tag{2.27}$$

$$\partial_\mu V^a_\mu = -2M_{\text{inv}} \sin(\omega) \varepsilon^{3ab} P^b, \tag{2.28}$$

in the twisted basis. In summary, the relation between classical QCD and tmQCD in the continuum is given by a change of the quark fields and mass variable, thus continuum tmQCD is just a particular way of writing down QCD. For these considerations to carry over to the lattice, the theory needs to be regularized with a regulator which preserves the chiral symmetry of the massless theory, i.e. the transformation (2.8) and thus in particular also (2.18).

Such a regularization is given by Ginsparg-Wilson (GW) quarks on the lattice. Using GW fermions, the same steps as performed formally in the continuum can be repeated at finite lattice spacing, in particular, Eq. (2.21) is a valid expression in the bare theory. For the renormalized theories to be equivalent, all members of a chiral multiplet need to be renormalized in the same way and all multiplicative renormalization constants have to be independent of the twist angle ω exactly [77]. An example for such a renormalization scheme is a mass-independent scheme constructed by imposing renormalization conditions in the chiral limit. In this case, Eqs. (2.23) holds for renormalized correlators. Note that this means that with GW fermions there is, as was the case for the considerations in the continuum, no reason to even introduce a twisted mass term, it can be rotated away since both massless theories are invariant under chiral rotations.

From universality, one expects that tmQCD and standard QCD lead to the same renormalized correlation functions up to cutoff effects also in other regularizations, even if they are not chirally symmetric [77]. Note that this has been established in particular for lattice regularizations with Wilson quarks [97]. Twisted mass QCD with Wilson quarks leads to differing regularizations at finite lattice spacings, parametrized by the twist angle ω, since even in the massless limit, the twisted mass

term cannot be rotated away due to the Wilson term, but they all have the same continuum limit.

2.1.6 Automatic order $\mathcal{O}(a)$ improvement

As mentioned in Sec. 2.1.1, at maximal twist $\omega = \pi/2$, tmQCD has the property of "automatic $\mathcal{O}(a)$ improvement" [78, 79], while standard Wilson quarks in principle require the introduction of (a set of) counterterms for each operator of interest to achieve $\mathcal{O}(a)$ improvement. To go to maximal twist, the bare untwisted quark mass m_0 has to be tuned to the so-called "critical mass" $m_{\rm cr}$, which maximally disaligns the Wilson term and the mass term. The critical mass is the value of m_0 for which the physical quark mass vanishes. Some more general remarks on this tuning can be found in [82, 98, 99], while the tuning used for this work is discussed in detail in [100]. For tmQCD at maximal twist it can be shown that $\mathcal{O}(a)$ counterterms at most contribute at $\mathcal{O}(a^2)$. There are different arguments for automatic $\mathcal{O}(a)$ improvement, the one recapitulated here follows [82].
Using Symanzik's improvement program, Symanzik's effectve fermionic action close to the continuum limit is given by

$$S_{\rm eff} = S_0 + aS_1 + a^2 S_2 + \mathcal{O}(a^3), \tag{2.29}$$

where

$$S_0 = \int d_x^4 \, \bar{\chi}(x) \left[\not{D} + m_R + i\mu_R \gamma_5 \tau^3 \right] \chi(x), \tag{2.30}$$

with m_R and μ_R being renormalized mass parameters. Further,

$$S_k = \int d^4 y \, \mathcal{L}_k, \tag{2.31}$$

with the Lagrangians $\mathcal{L}_k$ being linear combinations of local composite fields with dimension $4 + k$. Note that the gauge action has leading $\mathcal{O}(a^2)$ discretization errors, thus its form is not relevant for the discussion here. Composite lattice fields $\Phi_{\rm latt}$ are of the form

$$\Phi_{\rm latt} = \Phi_0 + a\Phi_1 + a^2 \Phi_2 + \mathcal{O}(a^3), \tag{2.32}$$

Term	$\mathcal{R}_5^1$	$\mathcal{D}$	$\mu_q \to -\mu_q$
$\sum_x \sum_\mu \bar{\chi} \left(\nabla_\mu + \nabla_\mu^*\right) \gamma_\mu \chi$	$+$	$+$	$+$
$\sum_x \sum_\mu \bar{\chi} \nabla_\mu^* \nabla_\mu \chi$	$-$	$-$	$+$
$m_{\mathrm{cr}} \sum_x \bar{\chi} \chi$	$-$	$-$	$+$
$i\mu_q \sum_x \bar{\chi} \gamma_5 \tau^3 \chi$	$+$	$-$	$-$

Table 2.1: Parity of the terms of the tmLQCD action Eq. (2.14) with Wilson fermions under the transformations Eqs. (2.34) to (2.36).

where Φ_0 is d-dimensional for a d-dimensional lattice field, and Φ_k is $d+k$ dimensional. This gives for the lowest-order Symanzik expansion

$$\langle \Phi_{\mathrm{latt}} \rangle = \langle \Phi_0 \rangle_0 + a \langle \Phi_1 \rangle_0 - a \int d^4y \, \langle \Phi_0 \mathcal{L}_1 \rangle_0 + \mathcal{O}(a^2), \tag{2.33}$$

where $\langle . \rangle_0$ stands for the continuum expectation value taken with S_0. Automatic improvement means that the terms $a\langle \Phi_1 \rangle_0$ and $a \int d^4y \, \langle \Phi_0 \mathcal{L}_1 \rangle_0$ vanish exactly due to symmetries of the continuum theory at maximal twist. Defining the discrete chiral transformations in the first isospin direction $\mathcal{R}_5^1$

$$\mathcal{R}_5^1 : \; \chi \to i\gamma_5 \tau^1 \chi, \qquad \bar{\chi} \to i\bar{\chi}\gamma_5 \tau^1, \tag{2.34}$$

the operator dimensionality transformations $\mathcal{D}$

$$\begin{aligned} \chi(x) &\to \exp\left[\frac{3\pi i}{2}\right] \chi(-x) \\ \bar{\chi}(x) &\to \bar{\chi}(-x) \exp\left[\frac{3\pi i}{2}\right] \\ U_\mu(x) &\to U_\mu^\dagger(-x - a\hat{\mu}) \end{aligned} \tag{2.35}$$

and the twisted mass sign flip transformations

$$\mu_q \to -\mu_q, \tag{2.36}$$

the tmQCD fermion action Eq. (2.14) is invariant under $\mathcal{R}_5^1 \times \mathcal{D} \times [\mu_q \to -\mu_q]$, see Tab. 2.1. Note that operators of even dimension d are even under $\mathcal{D}$, while operators of odd dimension d are odd under $\mathcal{D}$. Further, $\mathcal{R}_5^1$ is a symmetry of the theory since the continuum action Eq. (2.30) is even under $\mathcal{R}_5^1$. The terms in Eq. (2.33) transform as follows.

Φ_{latt} can be assumed to be even under $\mathcal{R}_5^1$ and to have even dimension d such that $\langle\Phi_{\text{latt}}\rangle$ is invariant under $\mathcal{R}_5^1 \times \mathcal{D} \times [\mu_q \to -\mu_q]$, which is a symmetry of the lattice theory as shown above. This implies that the other terms in (2.33) are also invariant under $\mathcal{R}_5^1 \times \mathcal{D} \times [\mu_q \to -\mu_q]$. Φ_0, being the continuum counterpart of Φ_{latt}, is then also even under $\mathcal{R}_5^1$ and has even dimension d. Φ_1 has dimension $d+1$ and is thus odd under $\mathcal{D}$. Since $\langle\Phi_1\rangle_0$ is even under $\mathcal{R}_5^1 \times \mathcal{D} \times [\mu_q \to -\mu_q]$, Φ_1 must be odd under $\mathcal{R}_5^1$. Since $\langle\Phi_1\rangle_0$ is the expectation value of an $\mathcal{R}_5^1$-odd observable weighted with an $\mathcal{R}_5^1$-even action S_0, it vanishes. $\langle\Phi_0\mathcal{L}_1\rangle_0$ also vanishes, since $\mathcal{L}_1$ is odd under $\mathcal{D}$ and odd under $\mathcal{R}_5^1$, such that $\Phi_0\mathcal{L}_1$ is odd under $\mathcal{R}_5^1$. Thus at maximal twist the terms proportional to a vanish, i.e.

$$\langle\Phi_{\text{latt}}\rangle = \langle\Phi_0\rangle_0 + \mathcal{O}(a^2). \tag{2.37}$$

More details and arguments using other transformations can be found in [78, 79] and [80–82].

2.1.7 Introducing non-degenerate quarks and additional flavours

There are two proposals for both intoducing non-degenerate light quarks as well as adding further doublets of heavier quarks [101, 102]. In the first proposal [101], a flavour off-diagonal splitting is introduced in the fermionic action,

$$S_f = \int d^4x\, \bar{\chi}(x) \left[\not{D} + m_0 + i\mu_q\gamma_5\tau^3 + \delta_m\tau^1\right] \chi(x), \tag{2.38}$$

with mass splitting parameter δ_m. Going to the physical basis is done by first performing an isovector rotation of $\alpha_2 = \pi/2$,

$$\begin{aligned} \chi \to \chi' &= \exp\left[i\alpha_2\frac{\tau^2}{2}\right]\chi\Big|_{\alpha_2=\pi/2} = \frac{1}{\sqrt{2}}(1+i\tau^2)\chi, \\ \bar{\chi} \to \bar{\chi}' &= \bar{\chi}\exp\left[-i\alpha_2\frac{\tau^2}{2}\right]\Big|_{\alpha_2=\pi/2} = \bar{\chi}\frac{1}{\sqrt{2}}(1-i\tau^2), \end{aligned} \tag{2.39}$$

which transforms the Lagrangean density as

$$\not{D} + m_0 + i\mu_q\gamma_5\tau^3 + \delta_m\tau^1 \to \not{D} + m_0 - i\mu_q\gamma_5\tau^1 + \delta_m\tau^3. \tag{2.40}$$

The axial rotation in the direction of the twisted mass term now takes the form

$$\begin{aligned} \chi' \to \psi &= \exp\left[-i\alpha_1\frac{\tau^1}{2}\gamma_5\right]\chi', \\ \bar{\chi}' \to \bar{\psi} &= \bar{\chi}'\exp\left[-i\alpha_1\frac{\tau^1}{2}\gamma_5\right], \end{aligned} \tag{2.41}$$

yielding the fermionic action in the physical basis for $\tan(\alpha_1) = \mu_q/m_0$ as

$$S_f = \int d^4x\,\bar{\psi}(x)\left[\not{D} + M_{\text{inv}} + \delta_m\tau^3\right]\psi(x), \tag{2.42}$$

such that the mass spectrum is obtained as $M_\pm = M_{\text{inv}} \pm \delta_m$. The fermion determinant will then be positive if $M_{\text{inv}} > \delta_m$. This trivially extends to additional doublets of heavier quarks by adding additional sets of the three mass parameters. The fermionic Wilson twisted mass action with two non-degenerate quarks on the lattice then takes the form

$$S_f = a^4\sum_x \bar{\chi}(x)\left[D_W + m_0 + i\mu_q\gamma_5\tau^3 + \delta_m\tau^1\right]\chi(x). \tag{2.43}$$

The second proposal [102] to introduce non-degenerate quarks and additional flavour doublets, illustrated here for four quark fields, i.e. $\bar{\chi} = (\bar{u}, \bar{d}, \bar{s}, \bar{c})$, uses the continuum action

$$S_f = \int d^4x\,\bar{\chi}(x)\left[\not{D} + m + i\mu\gamma_5\tau^3\right]\chi(x), \tag{2.44}$$

where

$$\begin{aligned} m &= \begin{pmatrix} m_u & 0 & 0 & 0 \\ 0 & m_d & 0 & 0 \\ 0 & 0 & m_s & 0 \\ 0 & 0 & 0 & m_c \end{pmatrix} \\ &= \begin{pmatrix} M_u\cos(\omega_l) & 0 & 0 & 0 \\ 0 & M_d\cos(\omega_l) & 0 & 0 \\ 0 & 0 & M_s\cos(\omega_h) & 0 \\ 0 & 0 & 0 & M_c\cos(\omega_h) \end{pmatrix}, \end{aligned} \tag{2.45}$$

and

$$\mu = \begin{pmatrix} \mu_u & 0 & 0 & 0 \\ 0 & \mu_d & 0 & 0 \\ 0 & 0 & \mu_s & 0 \\ 0 & 0 & 0 & \mu_c \end{pmatrix} = \begin{pmatrix} M_u \sin(\omega_l) & 0 & 0 & 0 \\ 0 & -M_d \sin(\omega_l) & 0 & 0 \\ 0 & 0 & M_s \sin(\omega_h) & 0 \\ 0 & 0 & 0 & -M_c \sin(\omega_h) \end{pmatrix}, \tag{2.46}$$

with $M_i = \sqrt{m_i^2 + \mu_i^2}$, $i \in \{u, d, s, c\}$ and two twist angles ω_l and ω_h, satisfying

$$\tan(\omega_l) = \frac{\mu_u}{m_u} = -\frac{\mu_d}{m_d}, \qquad \tan(\omega_h) = \frac{\mu_s}{m_s} = -\frac{\mu_c}{m_c}. \tag{2.47}$$

Thus the non-degeneracy and additional flavours are introduced in such a way that the mass term remains diagonal. Standard QCD is recovered for $\omega_l = \omega_h = 0$. The relation to the physical basis takes the form

$$\begin{aligned} \chi \to \psi &= \exp\left[i\omega_l \frac{\tau_l^3}{2}\gamma_5 + i\omega_h \frac{\tau_l^3}{2}\gamma_5 \right] \chi, \\ \bar{\chi} \to \bar{\psi} &= \bar{\chi} \exp\left[i\omega_l \frac{\tau_l^3}{2}\gamma_5 + i\omega_h \frac{\tau_l^3}{2}\gamma_5 \right], \end{aligned} \tag{2.48}$$

where

$$\tau_l^3 = \begin{pmatrix} 1 & 0 & 0 & 0 \\ 0 & -1 & 0 & 0 \\ 0 & 0 & 0 & 0 \\ 0 & 0 & 0 & 0 \end{pmatrix}, \qquad \tau_h^3 = \begin{pmatrix} 0 & 0 & 0 & 0 \\ 0 & 0 & 0 & 0 \\ 0 & 0 & 1 & 0 \\ 0 & 0 & 0 & -1 \end{pmatrix}, \tag{2.49}$$

with the standard four flavour QCD action taking the form

$$S_f = \int d^4x \, \bar{\psi}(x) \left[\not{D} + m \right] \psi(x). \tag{2.50}$$

On the lattice, it however turns out that the fermionic determinant in this case is only positive if both the up and down quarks and the strange and charm quarks are mass degenerate. For simulations, usually degenerate light quarks are used, either

together with twisted non-degenerate quenched heavy quarks, or with untwisted non-degenerate heavy quarks.

2.1.8 Closing remarks

In conclusion, twisted mass lattice QCD with Wilson quarks provides interesting advantages over the standard Wilson lattice regularization at the cost of parity and flavour symmetry breaking, which are only recovered in the continuum, and the restriction to an even number of quarks. In particular important for this work is the isospin breaking at finite lattice spacing, which allows a splitting between neutral and charged pions. This splitting is not physical, for $N_f = 2$ degenerate quarks in the continuum limit a degenerate triplet of pions is obtained. The isospin splitting is an $\mathcal{O}(a^2)$ effect, independent of the twist angle ω, cf. [81]. The discussed advantages are the positivity of the tmQCD fermion determinant at non-vanishing twisted mass μ_q and the automatic $\mathcal{O}(a)$ improvement at maximal twist. Another important advantage not discussed here lies in bypassing some lattice renormalization problems of standard Wilson quarks, see [80, 81] for an introduction.

2.2 Lattice setup

For this thesis, gauge ensembles produced by the Extended Twisted Mass Collaboration (ETMC) in isospin-symmetric QCD (isoQCD) with $N_f = 2 + 1 + 1$ flavours of Wilson Clover twisted mass quarks are used, with quark masses tuned very close to their physical values [40, 100, 103–105]. The renormalizable lattice action

$$S = S_{\mathrm{g}}[U] + S_{\mathrm{q,sea}}[\psi_l, \psi_h, U] + S_{\mathrm{q,val}}[\{q_f, q'_f\}, U] + S_{\mathrm{ghost}}[\{\phi_f, \phi'_f\}, U] \tag{2.51}$$

is used, which corresponds to a mixed lattice setup, i.e. with separate actions for sea and valence quarks, with twisted mass [77, 78] and Osterwalder-Seiler fermions [106]. In this way, any undesired strange-charm quark mixing through cutoff effects in the valence quarks is avoided and automatic $\mathcal{O}(a)$ improvement of physical observables is preserved [79].
For the gluon action $S_{\mathrm{g}}[U]$ the Iwasaki improved gluon action [107] is chosen, given e.g in [100] by

$$S_{\mathrm{g}} = \frac{\beta}{3} \sum_x \left(b_0 \sum_{\substack{\mu,\nu=1 \\ 1 \le \mu < \nu}}^{4} \left\{ 1 - \mathrm{Re}\,\mathrm{Tr}\big(U^{1\times 1}_{x,\mu,\nu}\big) \right\} + b_1 \sum_{\substack{\mu,\nu=1 \\ \mu \neq \nu}}^{4} \left\{ 1 - \mathrm{Re}\,\mathrm{Tr}\big(U^{1\times 2}_{x,\mu,\nu}\big) \right\} \right), \tag{2.52}$$

with bare inverse gauge coupling $\beta = 6/g_0^2$, $b_1 = -0.331$ and $b_0 = 1 - 8b_1$. $U^{1\times 1}_{x,\mu,\nu}$ is a simple plaquette loop and $U^{1\times 2}_{x,\mu,\nu}$ a rectangle loop [108], i.e.

$$\begin{aligned} U^{1\times 1}_{x,\mu,\nu} &= U_\mu(x) U_\nu(x + a\hat{\mu}) U_\mu^{-1}(x + a\hat{\nu}) U_\nu^{-1}(x), \\ U^{1\times 2}_{x,\mu,\nu} &= U_\mu(x) U_\nu(x + a\hat{\mu}) U_\nu(x + a\hat{\mu} + a\hat{\nu}) U_\mu^{-1}(x + 2a\hat{\nu}) U_\nu^{-1}(x + a\hat{\nu}) U_\nu^{-1}(x), \end{aligned} \tag{2.53}$$

where $U_\mu(x) = \exp(i g_0 a G_\mu(x))$ with $G_\mu(x)$ the gluon field, cf. Fig. 2.1. The fermionic part of the action is split into a sea quark and a valence quark action. The sea quark action $S_{\mathrm{q,sea}}$ takes the form [40, 101]

$$\begin{aligned} S_{\mathrm{q,sea}} = a^4 \sum_x \Big\{ &\overline{\psi}_l(x) \left[\gamma_\mu \tilde{\nabla}_\mu + \mu_l - i\gamma_5 \tau^3 W^{\mathrm{cl}}_{\mathrm{cr}} \right] \psi_l(x) \\ &+ \bar{\psi}_h \left[\gamma_\mu \tilde{\nabla}_\mu + \mu_\sigma + \tau^3 \mu_\delta - i\gamma_5 \tau^1 W^{\mathrm{cl}}_{\mathrm{cr}} \right] \psi_h \Big\} \end{aligned} \tag{2.54}$$

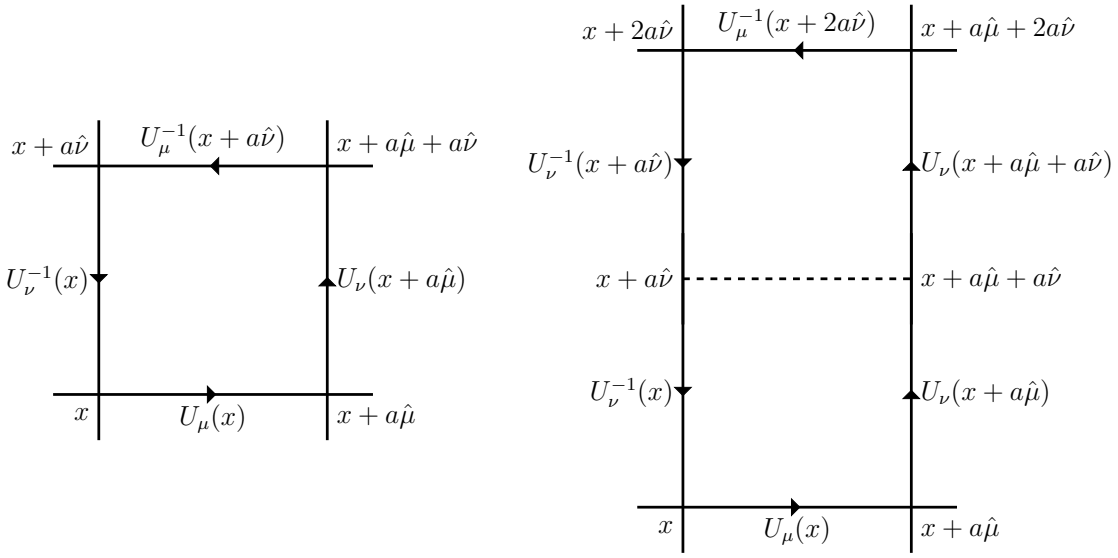

Figure 2.1: The simple plaquette loop $U^{1\times1}_{x,\mu,\nu}$ (left) and rectangle loop $U^{1\times2}_{x,\mu,\nu}$ (right) with base at x lying in the $\mu\nu$-plane [108].

written in terms of a light $\bar{\psi}_l = (\bar{u}_{\text{q,sea}}, \bar{d}_{\text{q,sea}})$ and heavy $\bar{\psi}_h = (\bar{c}_{\text{q,sea}}, \bar{s}_{\text{q,sea}})$ quark doublet. $W^{\text{cl}}_{\text{cr}}$ is the critical Wilson Clover operator, which inter alia contains the critical mass m_{cr}, and it is defined later in this section. $\tilde{\nabla}_\mu = \frac{1}{2}(\nabla_\mu + \nabla^*_\mu)$ with the covariant lattice derivatives ∇_μ, ∇^*_μ defined in App. B.1.
In [40], the valence quark action $S_{\text{q,val}}$ is given for several replica of each quark flavour, labelled by $\eta \in \{1, 2, ...\}$, with different values of the Wilson parameter $r_{f,\eta}$. In practise, it is restricted to $r_{f,\eta} = (-1)^{\eta-1} \in \{-1, 1\}$. The valence quark action is then given by

$$S_{\text{q,val}} = a^4 \sum_x \sum_{f,\eta} \left\{ \bar{q}_{f,\eta}(x) \left[\gamma_\mu \tilde{\nabla}_\mu + m_f - \text{sign}(r_{f,\eta}) i\gamma_5 W^{\text{cl}}_{\text{cr}}|_{r=1} \right] q_{f,\eta} \right\}, \tag{2.55}$$

where $q_{f,\eta}$ is a single flavour field with $f \in \{u, d, s, c\}$. The critical Wilson Clover operator is defined as

$$W^{\text{cl}}_{\text{cr}}|_r = -\frac{1}{2} a r \nabla^*_\mu \nabla_\mu + m_{\text{cr}}(r) + \frac{1}{32} a c_{SW}(r) \gamma_\mu \gamma_\nu a^{-1} \left[Q_{\mu\nu} - Q_{\nu\mu} \right], \tag{2.56}$$

containing the Wilson term, a critical mass m_{cr} term as well as a Clover term $\frac{1}{32} a c_{SW}(r) \gamma_\mu \gamma_\nu a^{-1} [Q_{\mu\nu} - Q_{\nu\mu}]$. The Clover term is a lattice discretization of the Pauli term $\frac{i}{4} c_{SW} \sigma_{\mu\nu} F_{\mu\nu}$, see [94, 109, 110] for more details. The Sheikholeslami-Wohlert coefficient c_{SW} is identical for all sea and valence flavours, it is fixed by

using an estimate from 1-loop tadpole boosted perturbation theory [111] by

$$c_{SW} \simeq 1 + 0.113(3)\frac{g_0^2}{P}, \tag{2.57}$$

with P the plaquette expectation value. Isospin breaking lattice artefacts, entering at $\mathcal{O}(a^2)$, can be significant in the case of the neutral pion mass, but they can be suppressed by introducing a Clover term as in Eq. (2.56), see [81, 100, 103]. This allows simulations close to physical light quark masses with the lattice spacings used in this work. In Eq. (2.54), $W_{\rm cr}^{\rm cl} = W_{\rm cr}^{\rm cl}|_{r=1}$ and the flavour structure is given by the Pauli matrices τ^1 and τ^3. In both the sea and valence quark action, the critical Wilson Clover term is taken at maximal twist with respect to the light and heavy Wilson bare quark masses to profit from automatic $\mathcal{O}(a)$ improvement [78, 112]. For this, the critical mass $m_{\rm cr}$ is set to the same value for all flavours [79].
The valence ghost action takes the form

$$S_{\rm ghost} = a^4 \sum_x \sum_{f,\eta} \left\{ \bar{\phi}_{f,\eta}(x) \left[\gamma_\mu \tilde{\nabla}_\mu + m_f - \mathrm{sign}(r_{f,\eta}) i\gamma_5 W_{\rm cr}^{\rm cl}|_{r=1} \right] \phi_{f,\eta} \right\}, \tag{2.58}$$

with the ghost field $\phi_{f,\eta}$ being a complex spin-1/2 boson field. It is included to exactly cancel the valence fermion contributions to the effective gluonic action [40]. Note that no ghost fields ever occur in the actual computations. The ghosts are needed to cancel surplus degrees of freedom of the local gauge fields compared to the physical degrees of freedom [86, 113, 114].
For the light quark doublet, both in the sea and valence action, the bare quark mass takes a single value $\mu_l = \mu_u = \mu_d$ such that the pion mass is close to $M_\pi^{phys} = M_\pi^{isoQCD} = 135.0(2)\,\mathrm{MeV}$ [104].
The masses of the strange and charm sea quarks are set within approximately 5% to their physical values by tuning μ_σ and μ_δ, using the phenomenological determinations of the ratios $M_{D_s}/f_{D_s} = 7.9(0.1)$, i.e.the ratio of the D_s meson mass and decay constant, and $m_c/m_s = 11.8(0.2)$ [40, 100, 103, 104].
The strange and charm valence quark masses can be fixed accurately by two physical inputs, e.g. by the kaon and D-meson masses [100, 103–105, 115] or equivalently by reproducing the energies of the ϕ and J/ψ resonances [40]. Up to lattice artefacts in the charm sector, both methods lead to agreeing values for the strange and charm valence quark masses. In this work, the strange and charm valence quark masses

have been fixed by the Ω-baryon mass for the $\pi \to \gamma^*\gamma^*$ calculation and the η-meson mass for the $\eta \to \gamma^*\gamma^*$ calculation as well as the Λ_c^+-baryon mass.

Chapter 3

Lattice calculation of $a_\mu^{P-\text{pole}}$

In this chapter, details of the lattice calculation of $a_\mu^{P-\text{pole}}$ not covered in Chapters 4 and 5, i.e. the publications written as part of this thesis, are discussed. First, in Sec. 3.1, some general remarks on the construction of the pseudoscalar-pole contributions in Minkowski space are made in Secs. 3.1.1 and 3.1.2 before turning to the calculation from lattice QCD in Secs. 3.1.3 to 3.1.7. Then, an overview of the needed amplitudes is given in Sec. 3.2 before detailed expressions for the amplitudes connecting to the data available for this thesis are given in Secs. 3.3 and 3.4 for the pion-pole calculation and in Secs. 3.5 and 3.6 for the η-meson pole calculation. Finally, Secs. 3.7 and 3.8 contain details relevant for the extraction of the transition form factors and the employed ensembles and correlators. Further technical details regarding model averaging and error calculation can be found in App. C.

3.1 Pseudoscalar-pole contributions to HLbL

Here, the theoretical background for the determination of the Hadronic Light-by-Light (HLbL) contribution to the muon anomaly is reviewed, with a focus on the pseudoscalar-pole contributions to HLbL and the transition form factors (TFFs) appearing in these contributions. First, some relevant definitions for HLbL are introduced, before the pole contributions themselves are discussed. The section ends

with the introduction of the TFFs in Euclidean space and their construction on the lattice.

3.1.1 Basic definitions

Following [50, 116], the quantity of interest for obtaining the muon gyromagnetic ratio is the muon proper vertex function $\Gamma_\rho(p', p)$, defined as

$$\begin{aligned}(-ie)\bar{u}(p')\Gamma_\rho(p', p)u(p) \\ = \langle \mu^-(p')|(-ie)\sum_l(\bar{\psi}_l\gamma_\rho\psi_l)(0) + (ie)\sum_q e_q(\bar{q}\gamma_\rho q)(0)|\mu^-(p)\rangle,\end{aligned} \tag{3.1}$$

at vanishing momentum transfer, with $p^2 = p'^2 = m_\mu^2$, with m_μ the muon mass. The spinor wave functions are denoted by $\bar{u}$ and u, e denotes the electric charge of the electron. The first sum runs over the charged lepton flavours $l = e^-, \mu^-, \tau^-$ and the second sum over the quark flavours with e_q the corresponding quark electric charge in units of $|e|$. The vertex function restricted to only the light and strange quark pieces of the electromagnetic current insertion, (u, d, s), is denoted by $\hat{\Gamma}_\rho(p', p)$. Denoting the light and strange quark electromagnetic current as

$$j_\rho(x) = \frac{2}{3}(\bar{u}\gamma_\rho u)(x) - \frac{1}{3}(\bar{d}\gamma_\rho d)(x) - \frac{1}{3}(\bar{s}\gamma_\rho s)(x), \tag{3.2}$$

the lowest order electroweak diagram for the HLbL contribution to the vertex function is

$$\begin{aligned}(-ie)\bar{u}(p')\hat{\Gamma}_\rho(p', p)u(p) &= \langle \mu^-(p')|(ie)j_\rho(0)|\mu^-(p)\rangle \\ &= \int \frac{d^4q_1}{(2\pi)^4}\frac{d^4q_2}{(2\pi)^4}\frac{-i}{q_1^2}\frac{-i}{q_2^2}\frac{-i}{(k-q_1-q_2)^2} \\ &\times \frac{i}{(p'-q_1)^2 - m_\mu^2}\frac{i}{(p'-q_1-q_2)^2 - m_\mu^2} \\ &\times (-ie)^3\bar{u}(p')\gamma^\mu(\not{p}' - \not{q}_1 + m_\mu)\gamma^\nu(\not{p}' - \not{q}_1 - \not{q}_2 + m_\mu)\gamma^\lambda u(p) \\ &\times (ie)^4\Pi_{\mu\nu\lambda\rho}(q_1, q_2, k - q_1 - q_2),\end{aligned} \tag{3.3}$$

where $k = p' - p = q_1 + q_2 + q_3$ with p the incoming and p' the outgoing muon momentum, k the external photon momentum and the q_i the internal photon momenta. See Fig. 3.1 for an illustration. The second line, i.e. the first line under the integral sign, denotes the internal photon propagators, the third and fourth lines are the internal muon propagators with three electromagnetic vertex factors, and the final line contains the fourth-rank light quark hadronic vacuum polarization tensor. It corresponds to the hadronic "blob" in the diagram in Fig. 3.1. The tensor is defined

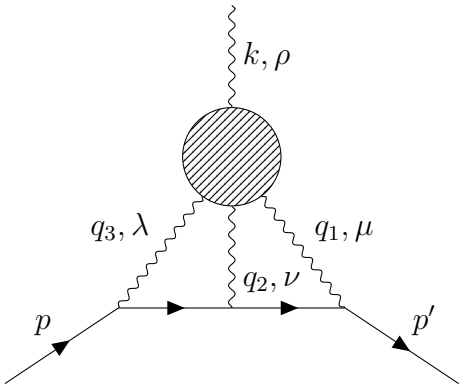

Figure 3.1: Hadronic Light-by-Light scattering diagram, showing the momentum assignment for the calculation of the muon electromagnetic vertex, cf. Eq. (3.3). The striped blob represents the fourth-rank light quark hadronic vacuum polarization tensor, defined in Eq. (3.4). Omitted for brevity are the additional five possible permutations of the q_i.

as

$$\Pi_{\mu\nu\lambda\rho}(q_1, q_2, q_3) = \int d^4x_1 d^4x_2 d^4x_3 e^{i(q_1x_1+q_2x_2+q_3x_3)} \langle 0|T\{j_\mu(x_1)j_\nu(x_2)j_\lambda(x_3)j_\rho(0)\}|0\rangle, \quad (3.4)$$

where $|0\rangle$ denotes the QCD vacuum. The external photon momentum k is incoming, the momenta of the internal photons outgoing from the hadronic "blob". Since $j_\mu(x)$ is conserved, the hadronic tensor obeys the Ward identities

$$\left\{q_1^\mu, q_2^\nu, q_3^\lambda, (q_1 + q_2 + q_3)^\rho\right\} \Pi_{\mu\nu\lambda\rho}(q_1, q_2, q_3) = 0, \quad (3.5)$$

from which it follows that

$$\Pi_{\mu\nu\lambda\rho}(q_1, q_2, k - q_1 - q_2) = -k^\sigma \frac{\partial}{\partial k^\rho} \Pi_{\mu\nu\lambda\sigma}(q_1, q_2, k - q_1 - q_2), \quad (3.6)$$

such that the tensor is linear in k when going to the static limit $k^\mu \to 0$ in which the anomalous magnetic moment is defined. Further, one obtains the decomposition

$$\bar{u}(p')\hat{\Gamma}_\rho(p',p)u(p) = \bar{u}(p')\left[\gamma_\rho \hat{F}_1(k^2) + \frac{i}{2m}\sigma_{\rho,\tau}k^\tau \hat{F}_2(k^2)\right]u(p), \tag{3.7}$$

with the Pauli form factors $\hat{F}_1(k^2)$ and $\hat{F}_1(k^2)$, cf. [50] and references therein for more details. Further it follows that $\hat{\Gamma}_\rho(p',p) = k^\sigma \hat{\Gamma}_{\rho\sigma}(p',p)$, where the two index vertex function is given by

$$\begin{aligned}\bar{u}(p')\hat{\Gamma}_{\rho\sigma}(p',p)u(p) = -ie^6 \int \frac{d^4q_1}{(2\pi)^4}\frac{d^4q_2}{(2\pi)^4}\frac{1}{q_1^2}\frac{1}{q_2^2}\frac{1}{(k-q_1-q_2)^2} \\ \times \frac{1}{(p'-q_1)^2-m_\mu^2}\frac{1}{(p'-q_1-q_2)^2-m_\mu^2} \\ \times \bar{u}(p')\gamma^\mu(\not{p}'-\not{q}_1+m_\mu)\gamma^\nu(\not{p}'-\not{q}_1-\not{q}_2+m_\mu)\gamma^\lambda u(p) \\ \times \frac{\partial}{\partial k^\rho}\Pi_{\mu\nu\lambda\rho}(q_1,q_2,k-q_1-q_2).\end{aligned} \tag{3.8}$$

Using $k^\rho k^\sigma \bar{u}(p')\hat{\Gamma}_{\rho\sigma}(p',p)u(p) = 0$ and following [117], it is found that $\hat{F}_1(0) = 0$, such that the HLbL contribution to the muon magnetic moment can be extracted in a simple way from the two index vertex function as

$$\hat{F}_2(0) = \frac{1}{48m}\mathrm{Tr}\left[(\not{p}+m)\left[\gamma^\rho,\gamma^\sigma\right](\not{p}+m)\hat{\Gamma}_{\rho\sigma}(p,p)\right]. \tag{3.9}$$

Note that the HLbL contribution to the muon magnetic moment can also be extracted from the one index vertex function $\hat{\Gamma}_\rho(p',p)$, see [50].

3.1.2 Pseudoscalar-pole contributions

As mentioned in Sec. 1.2, the pseudoscalar-pole contributions, for on-shell intermediate pseudoscalar states $P \in \{\pi^0, \eta, \eta'\}$, play the numerically dominant role amongst all contributions to HLbL in a systematic decomposition into various intermediate states [52–55]. They are depicted in the two diagrams to the right in Fig. 1.3, where the striped blobs represent the transition form factors $\mathcal{F}_{P\to\gamma^*\gamma^*}$.
Further following [50], the contributions to $\Pi_{\mu\nu\lambda\rho}(q_1,q_2,q_3)$ arising from the exchange

of a single pseudoscalar are given by

$$\begin{aligned}
&\Pi^{(P)}_{\mu\nu\lambda\rho}(q_1,q_2,q_3) = \\
&\quad i\frac{\mathcal{F}_{P\to\gamma^*\gamma^*}(q_1^2,q_2^2)\mathcal{F}_{P\to\gamma^*\gamma^*}(q_3^2,(q_1+q_2+q_3)^2)}{(q_1+q_2)^2-m_P^2}\epsilon_{\mu\nu\alpha\beta}q_1^\alpha q_2^\beta\epsilon_{\lambda\rho\sigma\tau}q_3^\sigma(q_1+q_2)^\tau \\
&\quad + i\frac{\mathcal{F}_{P\to\gamma^*\gamma^*}(q_1^2,(q_1+q_2+q_3)^2)\mathcal{F}_{P\to\gamma^*\gamma^*}(q_2^2,q_3^2)}{(q_2+q_3)^2-m_P^2}\epsilon_{\mu\rho\alpha\beta}q_1^\alpha(q_2+q_3)^\beta\epsilon_{\nu\lambda\sigma\tau}q_2^\sigma q_3^\tau \\
&\quad + i\frac{\mathcal{F}_{P\to\gamma^*\gamma^*}(q_1^2,q_3^2)\mathcal{F}_{P\to\gamma^*\gamma^*}(q_2^2,(q_1+q_2+q_3)^2)}{(q_1+q_3)^2-m_P^2}\epsilon_{\mu\lambda\alpha\beta}q_1^\alpha q_3^\beta\epsilon_{\nu\rho\sigma\tau}q_2^\sigma(q_1+q_3)^\tau, \quad (3.10)
\end{aligned}$$

with m_P the on-shell pseudoscalar mass. The transition form factors are defined by

$$\begin{aligned}
M_{\mu\nu}(p,q_1) &= i\int d^4x\, e^{iq_1x}\,\langle 0|T\{j_\mu(x)j_\nu(0)\}|P(p)\rangle \\
&= \varepsilon_{\mu\nu\alpha\beta}q_1^\alpha q_2^\beta\mathcal{F}_{P\to\gamma^*\gamma^*}(q_1^2,q_2^2), \quad (3.11)
\end{aligned}$$

or equivalently by

$$-2\left[q_1^2\cdot q_2^2-(q_1\cdot q_2)^2\right]\mathcal{F}_{P\to\gamma^*\gamma^*}(q_1^2,q_2^2) = \varepsilon_{\mu\nu\alpha\beta}q_1^\alpha q_2^\beta M_{\mu\nu}(p,q_1), \quad (3.12)$$

where $p = (E_P,\vec{p})^T$ is the pseudoscalar momentum and $q_1 = (\omega_1,\vec{q}_1)^T$ and $q_2 = (\omega_2,\vec{q}_2)^T$ the photon virtualities. Note that $p = q_1 + q_2$, and $p^2 = E_P^2 - \vec{p}^2 = m_P^2$, i.e. we fix the mostly negative metric sign convention, and $\mathcal{F}_{P\to\gamma^*\gamma^*}(q_1^2,q_2^2) = \mathcal{F}_{P\to\gamma^*\gamma^*}(q_2^2,q_1^2)$. Further, the pseudoscalar state is normalized relativistically as $\langle P(p)|P(q)\rangle = (2\pi)^3(2E_P)\delta(\vec{p}-\vec{q})$ and uses the Fourier convention $|P(\vec{p})\rangle = \sum_x e^{i\vec{p}\vec{x}}|P(\vec{x})\rangle$ for going from momentum to position space.
To obtain corresponding contributions to a_μ, the derivative

$$\begin{aligned}
&\frac{\partial}{\partial k^\rho}\,\Pi^{(P)}_{\mu\nu\lambda\sigma}(q_1,q_2,k-q_1-q_2)\Big|_{k=0} = \\
&\quad i\frac{\mathcal{F}_{P\to\gamma^*\gamma^*}(q_1^2,q_2^2)\mathcal{F}_{P\to\gamma^*\gamma^*}((q_1+q_2)^2,0)}{(q_1+q_2)^2-m_P^2}\epsilon_{\mu\nu\alpha\beta}q_1^\alpha q_2^\beta\epsilon_{\lambda\sigma\rho\tau}(q_1+q_2)^\tau \\
&\quad + i\frac{\mathcal{F}_{P\to\gamma^*\gamma^*}(q_1^2,0)\mathcal{F}_{P\to\gamma^*\gamma^*}(q_2^2,(q_1+q_2)^2)}{q_1^2-m_P^2}\epsilon_{\mu\sigma\tau\rho}q_1^\tau\epsilon_{\nu\lambda\alpha\beta}q_1^\alpha q_2^\beta \\
&\quad + i\frac{\mathcal{F}_{P\to\gamma^*\gamma^*}(q_1^2,(q_1+q_2)^2)\mathcal{F}_{P\to\gamma^*\gamma^*}(q_2^2,0)}{q_2^2-m_P^2}\epsilon_{\mu\lambda\alpha\beta}q_1^\alpha q_2^\beta\epsilon_{\nu\sigma\rho\tau}q_2^\tau \quad (3.13)
\end{aligned}$$

is inserted into Eq. (3.8), which after taking the corresponding Dirac traces yields

$$
\begin{aligned}
a_\mu^{P-\text{pole}} &= \hat{F}_2(0)\Big|_{P-\text{pole}} = \\
&- e^6 \int \frac{d^4q_1}{(2\pi)^4}\frac{d^4q_2}{(2\pi)^4}\frac{1}{q_1^2 q_2^2 (q_1+q_2)^2[(p+q_1)^2-m_\mu^2][(p-q_2)^2-m_\mu^2]} \\
&\quad \times \left[\frac{\mathcal{F}_{P\to\gamma^*\gamma^*}(q_1^2,(q_1+q_2)^2)\mathcal{F}_{P\to\gamma^*\gamma^*}(q_2^2,0)}{q_2^2-m_P^2} T_1(q_1,q_2;p)\right. \\
&\quad \left. + \frac{\mathcal{F}_{P\to\gamma^*\gamma^*}(q_1^2,q_2^2)\mathcal{F}_{P\to\gamma^*\gamma^*}((q_1+q_2)^2,0)}{(q_1+q_2)^2-m_P^2} T_2(q_1,q_2;p)\right],
\end{aligned}
\tag{3.14}
$$

where $T_1(q_1,q_2;p)$ and $T_2(q_1,q_2;p)$ are given in [50].
After a Wick rotation of the momenta, with the rotated Euclidean momenta denoted here by capital letters, i.e. $Q_i^2 = -q_i^2$, $P^2 = -p^2 = -m_\mu^2$ and using the method of Gegenbauer polynomials to average over the direction of the muon momentum p, it is possible to perform all angular integrations in Eq. (3.14) except for the one over the angle θ between the four-momenta Q_1 and Q_2 for arbitrary TTFs, see [50, 118]. This leads to the three-dimensional integral representation

$$
a_\mu^{P-\text{pole}} = \left(\frac{\alpha}{\pi}\right)^3 \left[a_\mu^{P-\text{pole}(1)} + a_\mu^{P-\text{pole}(2)}\right], \tag{3.15}
$$

with

$$
\begin{aligned}
a_\mu^{P-\text{pole}(1)} &= \int_0^\infty dQ_1 \int_0^\infty dQ_2 \int_{-1}^1 d\tau \\
&\quad w_1(Q_1,Q_2,\tau)\mathcal{F}_{P\to\gamma^*\gamma^*}(-Q_1^2,-Q_3^2)\mathcal{F}_{P\to\gamma^*\gamma^*}(-Q_2^2,0),
\end{aligned}
\tag{3.16}
$$

and

$$
\begin{aligned}
a_\mu^{P-\text{pole}(2)} &= \int_0^\infty dQ_1 \int_0^\infty dQ_2 \int_{-1}^1 d\tau \\
&\quad w_2(Q_1,Q_2,\tau)\mathcal{F}_{P\to\gamma^*\gamma^*}(-Q_1^2,-Q_2^2)\mathcal{F}_{P\to\gamma^*\gamma^*}(-Q_3^2,0),
\end{aligned}
\tag{3.17}
$$

where α is the fine structure constant. The integrations run over the lengths of the two Euclidean four-momenta Q_1, Q_2 and the angle θ between them, with $\tau = \cos\theta$ and $Q_3^2 = Q_1^2 + Q_2^2 + 2Q_1Q_2\tau$. The dimensionless weight functions $w_1(Q_1,Q_2,\tau)$ and $w_2(Q_1,Q_2,\tau)$ are given in App. A.2. w_2 is symmetric under the exchange $Q_1 \leftrightarrow Q_2$ and both $w_{1,2}$ go to zero for $Q_{1,2} \to 0$ and $\tau \to \pm 1$. This separates the generic

kinematics of the pole contribution, described by the weight functions, from the dependence on the TFFs [118]. Illustrations of the kinematical reach in the lattice setup used in this thesis can be found in App. D.3.

3.1.3 Obtaining the transition form factors in Euclidean spacetime

Below the threshold for hadron production, i.e. if $q_{1,2}^2 < M_V^2 = \min(M_\rho^2, 4m_\pi^2)$, such that the integration contour does not encounter a singularity, where one of the photons can mix with a heavier on-shell state, the matrix element in Eq. (3.11) can be written in Euclidean spacetime [66, 119–122]. For this, the Wick rotation $x_0 \to -i\tau$ is performed, yielding

$$\int dx_0 \to -i \int d\tau, \quad \text{and} \quad e^{i\omega_1 x_0} \to e^{\omega_1 \tau}. \tag{3.18}$$

The current operators in Euclidean space $j_\mu^E(x)$ are related to the Minkowski space current operators via

$$j_\mu(x) = -i^{\delta_{\mu,0}-1} j_\mu^E(x), \tag{3.19}$$

using $\gamma_0^E = \gamma_0$ and $\gamma_i^E = -i\gamma_i$ in the mostly negative sign metric convention. Note that on the r.h.s of Eq. (3.19) there is no sum over μ, $\delta_{\mu,0}$ simply counts the number of temporal indices of $j_\mu(x)$. For the matrix element, this Wick rotation yields

$$\begin{aligned} M_{\mu\nu} &= i^{n_0} M_{\mu\nu}^E = \varepsilon_{\mu\nu\alpha\beta} q_1^\alpha q_2^\beta \mathcal{F}_{P\to\gamma^*\gamma^*}(q_1^2, q_2^2), \\ M_{\mu\nu}^E(p, q_1) &= -\int d\tau e^{\omega_1 \tau} \tilde{A}_{\mu\nu}(\tau), \end{aligned} \tag{3.20}$$

where $n_0 = \delta_{\mu,0} + \delta_{\nu,0}$ counts the number of temporal Lorentz indices. The amplitude under the τ integration is given by

$$\tilde{A}_{\mu\nu}(\tau) = \int d^3\vec{x} e^{-i\vec{q}_1\vec{x}} \langle 0|T\{j_\mu^E(\vec{x}, \tau) j_\nu^E(0)\}|P(\vec{p})\rangle. \tag{3.21}$$

Note that by fixing all spatial momenta, $M_{\mu\nu}^E(p, q_1) = M_{\mu\nu}^E(\omega_1)$, i.e. ω_1 is the remaining free parameter, cf. Eq. (3.24). Inverting the relation between $M_{\mu\nu}^E(\omega_1)$ and $\tilde{A}_{\mu\nu}(\tau)$

yields

$$\tilde{A}_{\mu\nu}(\tau) = -\frac{1}{2\pi i}\int_{\gamma-i\infty}^{\gamma+i\infty} d\omega_1\, e^{-\omega_1\tau} M^E_{\mu\nu}(\omega_1), \tag{3.22}$$

where the integration contour is valid for any $E_P - |\vec{q}_2| \leq \gamma \leq |\vec{q}_1|$, avoiding the aforementioned threshold for hadron production. More details are given in [66, 67]. To extract the transition form factors $\mathcal{F}_{P\to\gamma^*\gamma^*}(q_1^2, q_2^2)$ from Eq. (3.20), the kinematic factor $\varepsilon_{\mu\nu\alpha\beta}q_1^\alpha q_2^\beta$ needs to be removed. In this thesis, the pseudoscalars are taken at rest, i.e. with $p = (E_P, \vec{p})^T = (m_P, \vec{0})^T$, such that the relation between the pseudoscalar momentum and photon momenta takes the form

$$\begin{pmatrix} E_P \\ \vec{p} \end{pmatrix} = \begin{pmatrix} m_P \\ \vec{0} \end{pmatrix} = \begin{pmatrix} \omega_1 \\ \vec{q}_1 \end{pmatrix} + \begin{pmatrix} \omega_2 \\ \vec{q}_2 \end{pmatrix}, \tag{3.23}$$

implying $q_2 = (m_P - \omega_1, -\vec{q}_1)^T$ and giving

$$q_1^2 = \omega_1^2 - \vec{q}_1^{\,2}, \qquad q_2^2 = (E_P - \omega_1)^2 - (\vec{p} - \vec{q}_1)^2 = (m_P - \omega_1^2) - \vec{q}_1^{\,2}, \tag{3.24}$$

for the photon virtualities. The kinematic factor with one or more temporal indices vanishes, since

$$M^E_{00} \propto \varepsilon_{00\alpha\beta}q_1^\alpha q_2^\beta = 0, \tag{3.25}$$

$$M^E_{0k} \propto \varepsilon_{0k\alpha\beta}q_1^\alpha q_2^\beta = -\varepsilon_{0kij}q_1^i q_1^j = 0, \tag{3.26}$$

and the kinematic factor with two spatial indices takes the form

$$M^E_{ij} \propto \varepsilon_{ij\alpha\beta}q_1^\alpha q_2^\beta = \varepsilon_{ijk}m_P q_1^k. \tag{3.27}$$

Using the behaviour of the kinematic factor for a pseudoscalar at rest leads to the introduction of the scalar amplitude $\tilde{A}(\tau)$,

$$\tilde{A}_{ij}(\tau) = -\varepsilon_{ijk}m_P q_1^k \tilde{A}(\tau) \Leftrightarrow \tilde{A}(\tau) = -\frac{\varepsilon_{ijk}q_1^k}{m_P|\vec{q}_1^{\,2}|}\tilde{A}_{ij}(\tau), \tag{3.28}$$

where

$$\tilde{A}(\tau) = -\frac{1}{2\pi i}\int_{\gamma-i\infty}^{\gamma+i\infty} d\omega_1\, e^{-\omega_1\tau}\mathcal{F}_{P\to\gamma^*\gamma^*}(q_1^2, q_2^2), \tag{3.29}$$

with

$$\mathcal{F}_{P\to\gamma^*\gamma^*}(q_1^2, q_2^2) = -\int_{-\infty}^{\infty} d\tau\, e^{\omega_1 \tau} \tilde{A}(\tau). \tag{3.30}$$

Note that $\tilde{A}_{\mu\nu}(\tau)$ with one or two temporal indices vanishes, and that, since $\tilde{A}(\tau)$ is a function of $|\vec{q}_1^{\,2}| = |\vec{q}_2^{\,2}|$, multiple choices of $\vec{q}_1$ with a fixed value of $|\vec{q}_1^{\,2}|$ can be averaged, cf. App. B.7.
The superscript E is now dropped and it is assumed that the expressions are stated in Euclidean spacetime unless otherwise specified.

3.1.4 Construction of $\tilde{A}(\tau)$ on the lattice

The construction of $\tilde{A}(\tau)$ used in this thesis follows [66,67], with the main important difference being the placement of the pseudoscalar annihilation operator to the far Euclidean future instead of the far Euclidean past as in the references. The connection between the two conventions is given in Sec. 3.1.5.
Consider the three-point (3pt) correlation function $C_{\mu\nu}(\tau, t_f)$ on the lattice given by

$$C_{\mu\nu}(\tau, t_f) = a^6 \sum_{\vec{x},\vec{y}} e^{-i\vec{p}\vec{y}} e^{i\vec{q}_1\vec{x}} \langle T\{P(\vec{y}, t_f) j_\mu^\dagger(\vec{x}, -\tau) j_\nu^\dagger(\vec{0}, 0)\}\rangle, \tag{3.31}$$

with $P = i\bar{\psi}\gamma_5\tau^P\psi$ a pseudoscalar annihilation operator to the far Euclidean future, and $j_\mu^\dagger$ vector current creation operators, cf. App. A.1 and B.8. Note that by fixing the pseudoscalar momentum and the momentum of one of the vector currents, the momentum of the other vector current is given by conservation of momentum or translation invariance. Introducing the propagation time t_P as

$$t_P = \begin{cases} t_f - |\tau|, & \tau < 0, \\ t_f, & \tau > 0, \end{cases} \tag{3.32}$$

the asymptotic behaviour of $C_{\mu\nu}(\tau, t_f)$ can be studied by inserting complete sets of eigenstates, cf. App. B.4. For $t_P \to \infty$ this results in

$$C_{\mu\nu}(\tau, t_f) \approx \frac{Z_P\, a^3}{2E_P} \sum_{\vec{x}} e^{i\vec{q}_1\vec{x}} e^{-E_P t_f} \langle P(p)|T\{j_\mu^\dagger(\vec{x}, -\tau) j_\nu^\dagger(\vec{0}, 0)\}|0\rangle, \tag{3.33}$$

or

$$\begin{aligned}
\tau < 0: \quad C_{\mu\nu}(\tau, t_f) &\approx \frac{Z_P\, a^3}{2E_P} \sum_{\vec{x}} e^{i\vec{q}_1\vec{x}} e^{-E_P t_P} \langle P(p)|j_\mu^\dagger(\vec{x}, 0) j_\nu^\dagger(\vec{0}, \tau)|0\rangle, \\
\tau > 0: \quad C_{\mu\nu}(\tau, t_f) &\approx \frac{Z_P\, a^3}{2E_P} \sum_{\vec{x}} e^{i\vec{q}_1\vec{x}} e^{-E_P t_P} \langle P(p)|j_\nu^\dagger(\vec{0}, 0) j_\mu^\dagger(\vec{x}, -\tau)|0\rangle,
\end{aligned} \tag{3.34}$$

where the factor $2E_P$ appears as a consequence of the relativistic normalization of $|P\rangle$ and where the overlap factor Z_P is defined by

$$Z_P = \langle 0|P(\vec{0}, 0)|P(\vec{p})\rangle = e^{-i\vec{p}\vec{x}} \langle 0|P(\vec{x}, 0)|P(\vec{p})\rangle. \tag{3.35}$$

Note that for the pion, Z_P is set to be $Z_\pi = Z_\pi^* = F_\pi m_\pi^2 / m_{\mathrm{PCAC}} > 0$ by the PCAC relation for the choice of the pseudoscalar operator used here, cf. [66, 67, 123].
Both the overlap factor Z_P and energy E_P for the pseudoscalar operator can be obtained from fitting the corresponding pseudoscalar two-point (2pt) function

$$C^{(2)}(t) = a^3 \sum_x e^{-i\vec{x}\vec{p}} \langle 0|P(\vec{x}, t) P^\dagger(\vec{0}, 0)|0\rangle \xrightarrow{t\to\infty} \frac{|Z_P|^2}{2E_P} e^{-E_P t}. \tag{3.36}$$

Following Eq. (3.21), $\tilde{A}(\tau)$ can then be defined as

$$\tilde{A}_{\mu\nu}(\tau) = \lim_{t_P \to \infty} \frac{2E_P}{Z_P} e^{E_P t_P} C_{\mu\nu}(\tau, t_f). \tag{3.37}$$

For a pseudoscalar at rest, the definition of the scalar amplitude $\tilde{A}(\tau)$ follows from Eq. (3.28), with an analogous construction to define a scalar amplitude $C(\tau)$ from $C_{\mu\nu}(\tau, t_f)$. A discussion and diagrams of the Wick contractions contributing to $C^{(2)}(t)$ and $C_{\mu\nu}(\tau, t_f)$ can be found in Sec. 3.2.

3.1.5 Connection to the standard definition

The standard definition of $C_{\mu\nu}(\tau, t_f)$, found e.g. in [66, 67], places a pseudoscalar creation operator in the far Euclidean past. The 3pt correlation function with the pseudoscalar to the far future defined in Eq. (3.31) and calculated in Wilson tmLQCD can be connected to this standard definition using symmetries. As pointed out in [81],

standard $\mathcal{CPT}$ is a symmetry of Wilson tmLQCD, with $\mathcal{C}$ and $\mathcal{PT}$ being symmetries individually. Note that standard $\mathcal{P}$ and $\mathcal{T}$ are not symmetries of Wilson tmLQCD, instead one has twisted parity and twisted timereversal symmetries, cf. App. A.1.3 and App. A.1.4.
Under $\mathcal{PT}$, Eq. (3.31) transforms as

$$C_{\mu\nu}(\tau, t_f) = a^6 \sum_{\vec{x},\vec{y}} e^{-i\vec{p}\vec{y}} e^{i\vec{q}_1\vec{x}} \langle T\{j_\nu^\dagger(\vec{0},0) j_\mu^\dagger(-\vec{x},\tau) P(-\vec{y},-t_f)\}\rangle. \tag{3.38}$$

Noting that $P^\dagger = -P$ leads to the form

$$\begin{aligned} C_{\mu\nu}(\tau, t_f) &= a^6 \sum_{\vec{x},\vec{y}} e^{i\vec{p}\vec{y}} e^{-i\vec{q}_1\vec{x}} \langle T\{j_\mu^\dagger(\vec{x},\tau) j_\nu^\dagger(\vec{0},0) P(\vec{y},-t_f)\}\rangle \\ &= -a^6 \sum_{\vec{x},\vec{y}} e^{i\vec{p}\vec{y}} e^{-i\vec{q}_1\vec{x}} \langle T\{j_\mu(\vec{x},\tau) j_\nu(\vec{0},0) P^\dagger(\vec{y},-t_f)\}\rangle. \end{aligned} \tag{3.39}$$

The asymptotic behaviour is given by

$$C_{\mu\nu}(\tau, t_f) \approx -\frac{Z_P^* a^3}{2E_P} \sum_{\vec{x}} e^{-i\vec{q}_1\vec{x}} e^{-E_P t_f} \langle 0|T\{j_\mu^\dagger(\vec{x},\tau) j_\nu^\dagger(\vec{0},0)\}|P(p)\rangle, \tag{3.40}$$

thus the PCAC relation implies that $\tilde{A}_{\mu\nu}(\tau)$ is the same in both definitions up to a sign. This sign is always included later unless stated otherwise, such that $\tilde{A}(\tau)$ can be used to obtain the TFFs as detailed in Sec. 3.1.3.

3.1.6 Backward propagation

Due to the finite-time extent of the lattice, backward propagating pions may contribute to correlation functions. By the "method of images", where an operator at time t has images at $t + nL_t$, with $n \in \mathbb{Z}$ and L_t the temporal extent of the lattice, correlation functions on a time-torus can be linked to corresponding amplitudes in infinite Euclidean space. As demonstrated in detail in App. B.5 for generic 2pt correlators, one finds

$$C_{ft}^{(2)}(t) \xrightarrow{t\to\infty} \frac{|Z_P|^2}{2E_P} \left(e^{-E_P t} + e^{-E_P(L_t - t)}\right) \tag{3.41}$$

for the pseudoscalar 2pt function when considering the most dominant contribution from backward propagation, where the subscript "ft" stands for the finite-time corrected amplitude.
For the 3pt amplitude $C_{\mu\nu}(\tau, t_f)$ the calculation of the finite-time correction is slightly more involved, cf. App. B.6. One finds

$$\begin{aligned} C_{\mu\nu,ft}(\tau, t_f) = &\frac{Z_P\, a^3}{2E_P} \sum_{\vec{x}} e^{i\vec{q}_1\vec{x}} e^{-E_P t_f} \langle P(p)|T\{j_\mu^\dagger(\vec{x}, -\tau) j_\nu^\dagger(\vec{0}, 0)\}|0\rangle \\ &+ \frac{Z_P\, a^3}{2E_P} \sum_{\vec{x}} e^{i\vec{q}_1\vec{x}} e^{-E_P(L_t - t_f - \tau)} \langle P(p)|T\{j_\nu^\dagger(\vec{0}, -\tau) j_\mu^\dagger(\vec{x}, 0)\}|0\rangle, \end{aligned} \tag{3.42}$$

including only the most dominant correction. For the scalar amplitude $\tilde{A}(\tau)$ one finds

$$\begin{aligned} \tau < 0: &\quad \tilde{A}_{ft}(\tau) = \tilde{A}(\tau)\left(1 - e^{-E_P(L_t - 2t_P + \tau)}\right), \\ \tau > 0: &\quad \tilde{A}_{ft}(\tau) = \tilde{A}(\tau)\left(1 - e^{-E_P(L_t - 2t_P - \tau)}\right). \end{aligned} \tag{3.43}$$

Note that the lattice calculation yields $C_{ft}^{(2)}(t)$ and $\tilde{A}_{ft}(\tau)$. For $C^{(2)}(t)$ this is taken into account by an appropriate fit function when extracting E_P and Z_P, namely by using a cosh, see Sec. 3.4.1. For the extraction of $\tilde{A}(\tau)$ the factors from Eq. (3.43) are used. In principle, images which have wrapped more than one time are also included in the finite-time amplitudes, but due to their exponential suppression with additional factors of L_t they are not considered here.

3.1.7 Isospin rotation

As mentioned in Sec. 2.1, at finite lattice spacing a, isospin symmetry is broken in Wilson tmLQCD, which is an $\mathcal{O}(a^2)$ effect. For the 3pt amplitudes, these artefacts can be avoided by only keeping the isospin preserving parts. The light electromagnetic current operator is decomposed into definite isospin contributions as

$$j_\mu = \sum_f Q_f \bar{\psi}_f \gamma_\mu \psi_f = \frac{2}{3}\bar{u}\gamma_\mu u - \frac{1}{3}\bar{d}\gamma_\mu d = \frac{1}{6} j_\mu^{0,0} + \frac{1}{2} j_\mu^{1,0}, \tag{3.44}$$

where u and d stand for the up and down quark fields, and

$$j_\mu^{0,0} = \bar{u}\gamma_\mu u + \bar{d}\gamma_\mu d, \tag{3.45}$$

$$j_\mu^{1,0} = \bar{u}\gamma_\mu u - \bar{d}\gamma_\mu d. \tag{3.46}$$

Note that the first index in the superscript stands for the total isospin I and the second index for its third component I_z. If one also considers heavy quark contributions, they would be included in $j_\mu^{0,0}$ with appropriate charge factors, since only the u and d contributions rotate under isospin. Introducing the short-hand notation $C_{\mu\nu} = \langle P j_\mu j_\nu \rangle$ for Eq. (3.31), i.e. showing only the operators relevant for this discussion, yields in terms of the isospin decomposed currents

$$\begin{aligned} C_{\mu\nu} =& \frac{1}{12}\langle P j_\mu^{0,0} j_\nu^{1,0}\rangle + \frac{1}{12}\langle P j_\mu^{1,0} j_\nu^{0,0}\rangle \\ &+ \frac{1}{36}\langle P j_\mu^{0,0} j_\nu^{0,0}\rangle + \frac{1}{4}\langle P j_\mu^{1,0} j_\nu^{1,0}\rangle. \end{aligned} \tag{3.47}$$

For the π^0, which has isospin $I = 1$, only the first line in Eq. (3.47) contributes to the full $C_{\mu\nu}$ in the isospin symmetric limit. In the same limit for the η- and η'-meson, both having isospin $I = 0$, only the second line contributes.
In the isospin symmetric limit, the neutral pion form factor can be transformed into the charged form factor by an isospin rotation. In the physical basis, consider the vector isospin rotation

$$\begin{aligned} \psi &\to e^{i\theta_a \tau^a/2}\psi, \\ \overline{\psi} &\to \overline{\psi} e^{-i\theta_a \tau^a/2}, \end{aligned} \tag{3.48}$$

for $\theta_2 = \pi/2$, $\theta_1 = \theta_3 = 0$. This defines the isospin transformation I_y. Using the identity

$$e^{-i\theta\tau^a/2}\tau^b e^{i\theta\tau^a/2} = \tau^b \cos\theta + \frac{1}{2i}[\tau^a, \tau^b]\sin\theta + \delta_{ab}\tau^a[1 - \cos\theta], \tag{3.49}$$

the neutral pion operator transforms as

$$\pi^0 = i\bar{\psi}\gamma_5\tau^3\psi \xrightarrow{I_y} i\bar{\psi}\gamma_5\tau^1\psi = \pi^+ + \pi^-, \tag{3.50}$$

and the vector currents as

$$\begin{aligned} j_\mu^{0,0} &\xrightarrow{I_y} j_\mu^{0,0}, \\ j_\mu^{1,0} &\xrightarrow{I_y} j_\mu^{1,+} + j_\mu^{1,-}, \end{aligned} \tag{3.51}$$

where all operators are defined in App. A.1. For the isospin preserving parts of the amplitude, this yields

$$\begin{aligned} \langle \pi^0 j_\mu^{0,0} j_\nu^{1,0} \rangle &\xrightarrow{I_y} \langle \pi^+ j_\mu^{0,0} j_\nu^{1,-} \rangle + \langle \pi^- j_\mu^{0,0} j_\nu^{1,+} \rangle, \\ \langle \pi^0 j_\mu^{1,0} j_\nu^{0,0} \rangle &\xrightarrow{I_y} \langle \pi^+ j_\mu^{1,-} j_\nu^{0,0} \rangle + \langle \pi^- j_\mu^{1,+} j_\nu^{0,0} \rangle. \end{aligned} \tag{3.52}$$

In the twisted basis, the vectorial isospin rotation takes the form

$$\chi \to e^{-i\omega\gamma_5\tau^3/2} e^{i\theta_a\tau^a/2} e^{i\omega\gamma_5\tau^3/2} \chi, \tag{3.53}$$

$$\overline{\chi} \to \overline{\chi} e^{i\omega\gamma_5\tau^3/2} e^{-i\theta_a\tau^a/2} e^{-i\omega\gamma_5\tau^3/2}, \tag{3.54}$$

where $\omega = \pi/2$ at maximal twist. Acting with I_y on the neutral pion operator yields

$$\pi^0 = \overline{\chi}\chi \xrightarrow{I_y} -i\overline{\chi}\gamma_5(\tau^+ + \tau^-)\chi = -i(\pi^+ + \pi^-), \tag{3.55}$$

where the factor of $-i$ arises due to the normalization chosen for the operators in this thesis. The vector current operators in the twisted basis transform as

$$V_\mu^{0,0} \xrightarrow{I_y} V_\mu^{0,0}, \tag{3.56}$$

$$V_\mu^{1,0} \xrightarrow{I_y} iA_\mu^{1,+} - iA_\mu^{1,-}, \tag{3.57}$$

where $V_\mu^{0,0}$ and $V_\mu^{1,0}$ are the twisted versions of $j_\mu^{0,0}$ and $j_\mu^{1,0}$. All operators are again given in more detail in App. A.1. For the isospin preserving parts of $C_{\mu\nu}$ one finds

$$\begin{aligned} \langle \pi^0 V_\mu^{0,0} V_\nu^{1,0} \rangle &\xrightarrow{I_y} \langle \pi^- V_\mu^{0,0} A_\nu^{1,+} \rangle - \langle \pi^+ V_\mu^{0,0} A_\nu^{1,-} \rangle, \\ \langle \pi^0 V_\mu^{1,0} V_\nu^{0,0} \rangle &\xrightarrow{I_y} \langle \pi^- A_\mu^{1,+} V_\nu^{0,0} \rangle - \langle \pi^+ A_\mu^{1,-} V_\nu^{0,0} \rangle. \end{aligned} \tag{3.58}$$

Note that each charged 3pt function is (twisted) charge odd, thus the difference between the two charged 3pt functions on each line of Eq. (3.58) is charge even, cf. App. A.1.2 and App. B.3. Thus the even charge parity of the neutral 3pt amplitude is preserved under I_y. Further note that the replacement of the amplitudes with their isospin rotated counterparts is valid since it just modifies the coefficients of the

extrapolation to the continuum limit without changing the value of the amplitude itself in the continuum limit.

3.2 Contributions to $C^{(2)}$ and $C_{\mu\nu}$

The Wick contractions contributing in the case of the 2pt function $C^{(2)}(t)$ and 3pt function $C_{\mu\nu}(\tau, t_P)$ are depicted in Figs. 3.2 and 3.3. Lines in these diagrams correspond to quark propagators, which in the case of twisted mass fermions satisfy a more complicated γ_5-hermiticity, namely

$$D(x,y) = \gamma_5\tau^1 D^\dagger(y,x)\gamma_5\tau^1, \quad \text{and} \quad S(x,y) = \gamma_5\tau^1 S^\dagger(y,x)\gamma_5\tau^1, \tag{3.59}$$

where D is the twisted mass Dirac operator and S the corresponding propagator (the inverse of D, cf. [84]). This modification is needed since the twisted mass term flips sign under the usual γ_5 Hermitian conjugation, the conjugation by τ^1 flips the sign of the twisted mass term again while not affecting the remaining isospin-invariant pieces of the twisted mass Dirac operator. Note that for a flavour doublet, this modified γ_5-hermiticity implies a flavour change. Using the short-hand notation $S(x,y) = S_{xy}$ and introducing flavour indices, one has

$$S_{xy}^{f_1,f_2} = \gamma_5 (S_{yx}^{f_2,f_1})^\dagger \gamma_5, \tag{3.60}$$

where f_1, f_2 denotes the two flavours.

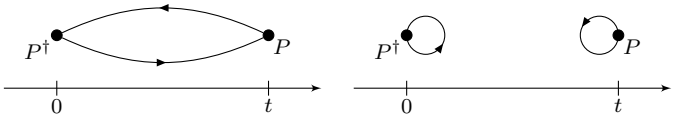

Figure 3.2: Wick contractions contributing to $C^{(2)}(t)$. There are connected (left) and (fully) disconnected diagrams (right).

Writing the pseudoscalar and current operators in the form

$$\mathcal{O}(t) = (\bar{\chi}\Gamma_{\mathcal{O}}\chi)(t), \tag{3.61}$$

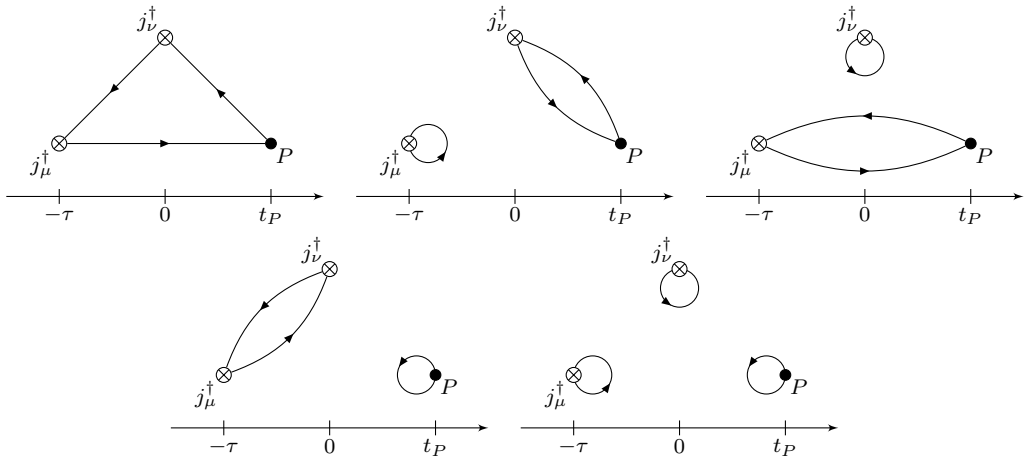

Figure 3.3: Wick contractions contributing to $C_{\mu\nu}(\tau, t_P)$. These are the connected (top left), vector-current disconnected ("V-disconnected", top middle and right), pseudoscalar disconnected ("P-disconnected", bottom left) and fully disconnected (bottom right) diagrams. Note that there would be a second connected diagram where the quark propagators run in the opposite direction which is omitted here.

where $\Gamma_{\mathcal{O}}$ contains the appropriate normalization, Dirac and flavour structure for the operator of interest, the Wick contractions for the 2pt function depicted in Fig. 3.2 schematically correspond to

$$\text{connected: } \langle(\overbrace{\bar{\chi}\Gamma_P\chi}(t)\overbrace{(\bar{\chi}\Gamma_{P^\dagger}\chi)}(0)\rangle, \tag{3.62}$$

$$\text{disconnected: } \langle(\overbrace{\bar{\chi}\Gamma_P\chi}(t)(\overbrace{\bar{\chi}\Gamma_{P^\dagger}\chi})(0)\rangle. \tag{3.63}$$

Using the same notation, the Wick contractions for the 3pt function depicted in Fig. 3.3 in the same order as in the figure schematically correspond to

$$\text{connected: } \langle(\overbrace{\bar{\chi}\Gamma_P\chi}(t_P)\overbrace{(\bar{\chi}\Gamma_{j_\nu^\dagger}\chi)}(0)\overbrace{(\bar{\chi}\Gamma_{j_\mu^\dagger}\chi)}(-\tau)\rangle, \tag{3.64}$$

$$\text{V-disconnected: } \langle(\overbrace{\bar{\chi}\Gamma_P\chi}(t_P)\overbrace{(\bar{\chi}\Gamma_{j_\nu^\dagger}\chi)}(0)(\overbrace{\bar{\chi}\Gamma_{j_\mu^\dagger}\chi})(-\tau)\rangle, \tag{3.65}$$

$$\text{V-disconnected: } \langle(\overbrace{\bar{\chi}\Gamma_P\chi}(t_P)(\overbrace{\bar{\chi}\Gamma_{j_\nu^\dagger}\chi})(0)\overbrace{(\bar{\chi}\Gamma_{j_\mu^\dagger}\chi)}(-\tau)\rangle, \tag{3.66}$$

$$\text{P-disconnected: } \langle(\overbrace{\bar{\chi}\Gamma_P\chi})(t_P)\overbrace{(\bar{\chi}\Gamma_{j_\nu^\dagger}\chi)}(0)\overbrace{(\bar{\chi}\Gamma_{j_\mu^\dagger}\chi)}(-\tau)\rangle, \tag{3.67}$$

$$\text{fully disconnected: } \langle(\overbrace{\bar{\chi}\Gamma_P\chi})(t_P)(\overbrace{\bar{\chi}\Gamma_{j_\nu^\dagger}\chi})(0)(\overbrace{\bar{\chi}\Gamma_{j_\mu^\dagger}\chi})(-\tau)\rangle. \tag{3.68}$$

Explicit expressions for the relevant Wick contractions for both the π^0 and η/η' correlators using propagators will be given in the following sections.

3.3 Pion Wick contractions contributing in $C_{\mu\nu}$

As detailed in Sec. 3.1.7, the neutral pion 3pt amplitude can be related to the charged pion amplitude. Since there is no charged pion loop, i.e. no possible Wick contraction of the charged pion operator with itself due to its quark content, the P-disconnected and fully disconnected Wick contractions vanish, cf. Fig 3.3. Note that for the neutral pion 3pt amplitude in twisted mass, they would need to be included since the neutral pion loop does not vanish due to isospin breaking. This leaves the connected and V-disconnected Wick contractions, where for the connected contractions only light currents contribute, while in the disconnected contractions also currents involving s and c quarks need to be considered, since they are present in the sea quarks. The operators, conventions and symmetries relevant for this section can be found in App. A.1.

3.3.1 Connected contraction

To make the discussion of the Wick contractions both more legible as well as a bit more general, a change of notation is made. The pion operator insertion time in the far future is now labelled by t_f, the current operator j_μ sits at source time t_i, the current operator j_ν at insertion time t_c, with analogous temporal labels for twisted and isospin rotated currents V_μ and A_μ. Define $\tau = t_c - t_i$ as the temporal separation between the two current operators and t_P as the temporal separation between the pseudoscalar and the closest current operator in the temporal direction. The indices on the temporal labels are then also used for the propagators, see Eq. (3.60).

The connected contractions in $C_{\mu\nu}$ are given by Eqs. (3.47) and (3.58) as

$$\begin{aligned} C_{\mu\nu}^{\text{conn.}} =& \frac{1}{12}\left(\langle \pi^- V_\mu^{0,0} A_\nu^{1,+}\rangle_{\text{conn.}} - \langle \pi^+ V_\mu^{0,0} A_\nu^{1,-}\rangle_{\text{conn.}}\right) \\ &+ \frac{1}{12}\left(\langle \pi^- A_\mu^{1,+} V_\nu^{0,0}\rangle_{\text{conn.}} - \langle \pi^+ A_\mu^{1,-} V_\nu^{0,0}\rangle_{\text{conn.}}\right). \end{aligned} \tag{3.69}$$

These connected amplitudes can now be expressed using the quark propagators, e.g.

$$\langle \pi^+ A_\mu^{1,-} V_\nu^{0,0}\rangle_{\text{conn.}} = \operatorname{Tr}\left[S_{ic}^u \gamma_\nu S_{cf}^u \gamma_5 S_{fi}^d \gamma_\mu \gamma_5\right] + \operatorname{Tr}\left[S_{if}^u \gamma_5 S_{fc}^d \gamma_\nu S_{ci}^d \gamma_\mu \gamma_5\right], \tag{3.70}$$

while suppressing the Fourier factors. The connected 3pt data sets available for this thesis contain data for arbitrary counter-clockwise contractions, defined explicitly by

$$\langle F_3 F_2 F_1(\vec{p},\vec{q},\Gamma_f,\Gamma_c,\Gamma_i)\rangle \equiv \sum_{\vec{x},\vec{y}} e^{i\vec{p}\vec{y}} e^{-i\vec{q}\vec{x}} \operatorname{Tr}\left[S_{if}^{F_3}\Gamma_f S_{fc}^{F_2}\Gamma_c S_{ci}^{F_1}\Gamma_i\right], \tag{3.71}$$

where $x_f = (\vec{y}, t_f), x_c = (\vec{x}, t_c), x_i = (\vec{0}, t_i = 0)$, $S_{ab}^F = S^F(x_a, x_b)$ and Γ_a gives the appropriate Dirac structure. Note that $\vec{p}$ is the pion momentum and $\vec{q}$ the momentum of the current at insertion, with the momentum of the current at source given by momentum conservation. The clockwise contractions can be transformed into counter-clockwise contractions using γ_5-hermiticity. One finds

$$\operatorname{Tr}\left[S_{ic}^{F_1}\Gamma_c S_{cf}^{F_2}\Gamma_f S_{fi}^{F_3}\Gamma_i\right] = \operatorname{Tr}\left[(S_{ci}^{\bar{F}_1})^\dagger \Gamma_c^c (S_{fc}^{\bar{F}_2})^\dagger \Gamma_f^c (S_{if}^{\bar{F}_3})^\dagger \Gamma_i^c\right], \tag{3.72}$$

where $\bar{F}$ stands for the opposite flavour of F within the doublet and where the superscript c denotes a conjugation of the Dirac structure with γ_5, i.e. $\Gamma^c = \gamma_5\Gamma\gamma_5 = \pm\Gamma^\dagger = \pm\Gamma$ for the gamma matrices used in this thesis, cf. App. A.1.5. Going back to the example in Eq. (3.70) one finds for the clockwise contraction

$$\begin{aligned} \operatorname{Tr}\left[S_{ic}^u \gamma_\nu S_{cf}^u \gamma_5 S_{fi}^d \gamma_\mu \gamma_5\right] &= \operatorname{Tr}\left[(S_{ci}^d)^\dagger(-\gamma_\nu)(S_{fc}^d)^\dagger \gamma_5 (S_{if}^u)^\dagger(-\gamma_\mu\gamma_5)\right] \\ &= \operatorname{Tr}\left[\gamma_5\gamma_\mu S_{if}^u \gamma_5 S_{fc}^d \gamma_\nu S_{ci}^d\right]^* \\ &= -\operatorname{Tr}\left[S_{if}^u \gamma_5 S_{fc}^d \gamma_\nu S_{ci}^d \gamma_\mu \gamma_5\right]^*, \end{aligned} \tag{3.73}$$

where in the last step cyclicity of the trace and $\{\gamma_5, \gamma_\mu\} = 0$ was used. Using the explicit definition in Eq. (3.71), the clockwise contraction takes the form

$$-\langle udd(-\vec{p}, -\vec{q}, \gamma_5, \gamma_\nu, \gamma_\mu\gamma_5)\rangle^*. \tag{3.74}$$

Converting the clockwise contractions to counter-clockwise contractions thus corresponds for the charged connected contractions to taking the complex conjugated counter-clockwise contractions with flipped flavours and momenta while keeping the Dirac structure. Thus suppressing the Dirac structure, the connected amplitude in Eq. (3.69) is given by

$$\begin{aligned} C_{\mu\nu}^{\text{conn.}} =& \frac{1}{12}\left(\langle dud(\vec{p}, \vec{q})\rangle - \langle dud(-\vec{p}, -\vec{q})\rangle^*\right) \\ &- \frac{1}{12}\left(\langle udu(\vec{p}, \vec{q})\rangle - \langle udu(-\vec{p}, -\vec{q})\rangle^*\right) \\ &+ \frac{1}{12}\left(\langle duu(\vec{p}, \vec{q})\rangle - \langle duu(-\vec{p}, -\vec{q})\rangle^*\right) \\ &- \frac{1}{12}\left(\langle udd(\vec{p}, \vec{q})\rangle - \langle udd(-\vec{p}, -\vec{q})\rangle^*\right). \end{aligned} \tag{3.75}$$

Next, the average with the twisted parity ($P\tau^1$) flipped state is taken, see App. A.1.3. Each of the amplitudes flips sign and transforms into its charge conjugated partner with flipped momenta. Additionally, a sign σ is picked up if both indices are either temporal or spatial, i.e. $\sigma = -(-1)^{n_0}$, with n_0 the number of temporal indices. The twisted parity averaged amplitude takes the form

$$\begin{aligned} &\frac{1}{2}(\mathbb{1} + P\tau^1)C_{\mu\nu}^{\text{conn.}} = \\ &\quad \frac{1}{2}\frac{1}{12}\left(\langle dud(\vec{p}, \vec{q})\rangle - \langle dud(-\vec{p}, -\vec{q})\rangle^* - \sigma\langle udu(-\vec{p}, -\vec{q})\rangle + \sigma\langle udu(\vec{p}, \vec{q})\rangle^*\right) \\ &- \frac{1}{2}\frac{1}{12}\left(\langle udu(\vec{p}, \vec{q})\rangle - \langle udu(-\vec{p}, -\vec{q})\rangle^* - \sigma\langle dud(-\vec{p}, -\vec{q})\rangle + \sigma\langle dud(\vec{p}, \vec{q})\rangle^*\right) \\ &+ \frac{1}{2}\frac{1}{12}\left(\langle duu(\vec{p}, \vec{q})\rangle - \langle duu(-\vec{p}, -\vec{q})\rangle^* - \sigma\langle udd(-\vec{p}, -\vec{q})\rangle + \sigma\langle udd(\vec{p}, \vec{q})\rangle^*\right) \\ &- \frac{1}{2}\frac{1}{12}\left(\langle udd(\vec{p}, \vec{q})\rangle - \langle udd(-\vec{p}, -\vec{q})\rangle^* - \sigma\langle duu(-\vec{p}, -\vec{q})\rangle + \sigma\langle duu(\vec{p}, \vec{q})\rangle^*\right). \end{aligned} \tag{3.76}$$

As shown in Sec. 3.1.3, for the case of a pion in the rest frame, i.e. $\vec{p} = 0$, only the spatial components of $C_{\mu\nu}$ contribute to the TFFs, thus $\sigma = -1$ and $\frac{1}{2}(\mathbb{1} + P\tau^1)C_{\mu\nu}^{\text{conn.}}$

takes the simple form

$$\begin{aligned}\frac{1}{2}(\mathbb{1}+P\tau^1)C^{\text{conn.}}_{\mu\nu} = \\ \frac{1}{12}\text{Re}\left(\langle dud(\vec{q})\rangle - \langle dud(-\vec{q})\rangle - \langle udu(\vec{q})\rangle + \langle udu(-\vec{q})\rangle\right) \\ +\frac{1}{12}\text{Re}\left(\langle duu(\vec{q})\rangle - \langle duu(-\vec{q})\rangle - \langle udd(\vec{q})\rangle + \langle udd(-\vec{q})\rangle\right).\end{aligned} \tag{3.77}$$

Two examples for the $\vec{p}=0$ charged connected 3pt amplitude after contracting the Lorentz structure and averaging over the momentum orbit as described in Sec. 3.1.3 can be found in Fig. 3.4.

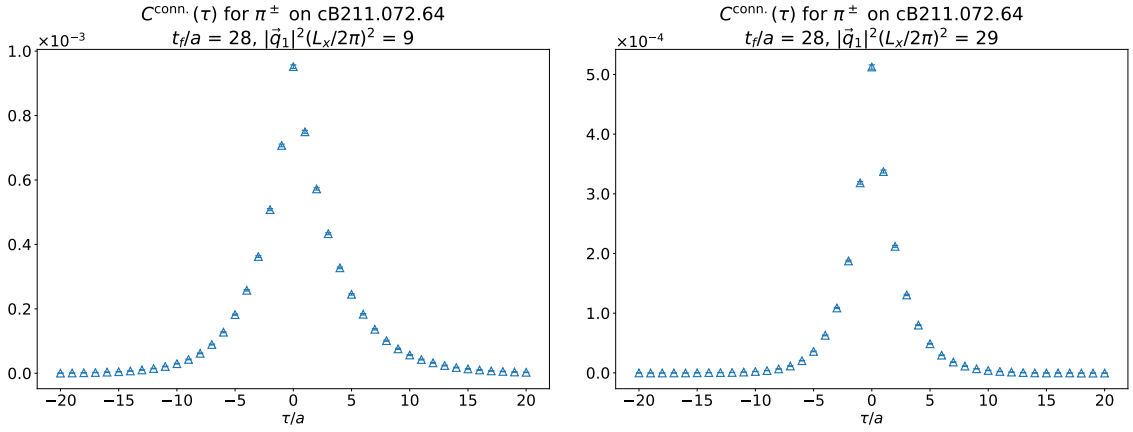

Figure 3.4: Momentum orbit averaged $C^{\text{conn.}}(\tau, t_f = 2.23\,\text{fm})$ for $\tau/a \in [-20, 20]$ on cB211.072.64 for two orbits. Note the small errors on the connected amplitude. A more comprehensive overview, also showing amplitudes for the other ensembles, can be found in App. D.1.

3.3.2 V-disconnected contraction

The V-disconnected contractions in $C_{\mu\nu}$ are given by Eqs. (3.47) and (3.58) as

$$\begin{aligned}C^{\text{V}-\text{disc.}}_{\mu\nu} =& \frac{1}{12}\left(\langle\pi^- V^{0,0}_\mu A^{1,+}_\nu\rangle_{\text{V}-\text{disc.}} - \langle\pi^+ V^{0,0}_\mu A^{1,-}_\nu\rangle_{\text{V}-\text{disc.}}\right) \\ &+\frac{1}{12}\left(\langle\pi^- A^{1,+}_\mu V^{0,0}_\nu\rangle_{\text{V}-\text{disc.}} - \langle\pi^+ A^{1,-}_\mu V^{0,0}_\nu\rangle_{\text{V}-\text{disc.}}\right) \\ &-\frac{1}{6}(V \leftrightarrow V^s) + \frac{2}{6}(V \leftrightarrow V^c),\end{aligned} \tag{3.78}$$

where ($V \leftrightarrow V^s$) and ($V \leftrightarrow V^c$) stands for the same expressions as in the brackets in the two lines above them while exchanging the vector currents by

$$V_\mu^{0,0;s} = \bar{s}\gamma_\mu s, \quad \text{or} \quad V_\mu^{0,0;c} = \bar{c}\gamma_\mu c. \tag{3.79}$$

These are the s and c vector currents, they can contribute here through disconnected loops. It is convenient to split the V-disconnected contribution as

$$C_{\mu\nu}^{\mathrm{V-disc.}} = C_{\mu\nu}^{\mathrm{V-disc.},l} + C_{\mu\nu}^{\mathrm{V-disc.},s} + C_{\mu\nu}^{\mathrm{V-disc.},c}. \tag{3.80}$$

Quark propagators can again be used to express these amplitudes, with the vector current loop and pion-axial current correlator given by

$$L_\mu^F(\vec{q}, \Gamma_x) = \sum_{\vec{x}} e^{-i\vec{q}\vec{x}} \,\mathrm{Tr}\big[S_{xx}^F \Gamma_x\big], \tag{3.81}$$

$$AP_\mu^{F\bar{F}}(\vec{p}, \vec{q}, \Gamma_f, \Gamma_x) = \sum_{\vec{x},\vec{y}} e^{i\vec{p}\vec{y}} e^{-i\vec{q}\vec{x}} \,\mathrm{Tr}\Big[S_{fx}^F \Gamma_x S_{xf}^{\bar{F}} \Gamma_f\Big], \tag{3.82}$$

where $x_f = (\vec{y}, t_f), x_c = (\vec{x}, t_c), x_i = (\vec{0}, t_i = 0)$, $S_{ab}^F = S^F(x_a, x_b)$ and Γ_a gives the appropriate Dirac structure. The pion has momentum $\vec{p}$ and the current at insertion momentum $\vec{q}$. Note that the light vector current loop $L^l(\vec{q}, \Gamma_x)$ is simply given by the sum of the u and d loops, i.e. $L^l(\vec{q}, \Gamma_x) = L^u(\vec{q}, \Gamma_x) + L^d(\vec{q}, \Gamma_x)$. Introducing a generic loop $L(\vec{q}, \Gamma_x)$ and defining a generic V-disconnected contribution,

$$\begin{aligned} C_{\mu\nu}^{\mathrm{V-disc.},gen} =& \langle \pi^- V_\mu^{0,0} A_\nu^{1,+} \rangle_{\mathrm{V-disc.}} - \langle \pi^+ V_\mu^{0,0} A_\nu^{1,-} \rangle_{\mathrm{V-disc.}} \\ &+ \langle \pi^- A_\mu^{1,+} V_\nu^{0,0} \rangle_{\mathrm{V-disc.}} - \langle \pi^+ A_\mu^{1,-} V_\nu^{0,0} \rangle_{\mathrm{V-disc.}}, \end{aligned} \tag{3.83}$$

and rewriting it in terms of loops and correlators yields

$$\begin{aligned} C_{\mu\nu}^{\mathrm{V-disc.},gen} =& \\ & L_\mu(-\vec{q}, \Gamma_i) \times AP_\nu^{ud}(\vec{p}, \vec{q}, \Gamma_f, \Gamma_c) - L_\mu(-\vec{q}, \Gamma_i) \times AP_\nu^{du}(\vec{p}, \vec{q}, \Gamma_f, \Gamma_c) \\ & + L_\nu(\vec{q}, \Gamma_c) \times AP_\mu^{ud}(\vec{p}, -\vec{q}, \Gamma_f, \Gamma_i) - L_\nu(\vec{q}, \Gamma_c) \times AP_\mu^{du}(\vec{p}, -\vec{q}, \Gamma_f, \Gamma_i). \end{aligned} \tag{3.84}$$

Since the s and c vector currents transform in the same way as their light counterpart under (twisted) parity one has the same properties as in Sec. 3.3.1 when taking the average with the parity flipped state. Again using $\sigma = -(-1)^{n_0}$, the twisted parity

averaged amplitude takes the form

$$\begin{aligned}
&\frac{1}{2}(\mathbb{1}+P\tau^1)C_{\mu\nu}^{\mathrm{V-disc.},gen} = \frac{1}{2}\Big[\\
&\quad L_\mu(-\vec{q},\Gamma_i)\times AP_\nu^{ud}(\vec{p},\vec{q},\Gamma_f,\Gamma_c) - L_\mu(-\vec{q},\Gamma_i)\times AP_\nu^{du}(\vec{p},\vec{q},\Gamma_f,\Gamma_c) \\
&-\sigma L_\mu(\vec{q},\Gamma_i)\times AP_\nu^{du}(-\vec{p},-\vec{q},\Gamma_f,\Gamma_c) + \sigma L_\mu(\vec{q},\Gamma_i)\times AP_\nu^{ud}(-\vec{p},-\vec{q},\Gamma_f,\Gamma_c) \\
&+L_\nu(\vec{q},\Gamma_c)\times AP_\mu^{ud}(\vec{p},-\vec{q},\Gamma_f,\Gamma_i) - L_\nu(\vec{q},\Gamma_c)\times AP_\mu^{du}(\vec{p},-\vec{q},\Gamma_f,\Gamma_i) \\
&-\sigma L_\nu(-\vec{q},\Gamma_c)\times AP_\mu^{du}(-\vec{p},\vec{q},\Gamma_f,\Gamma_i) + \sigma L_\nu(-\vec{q},\Gamma_c)\times AP_\mu^{ud}(-\vec{p},\vec{q},\Gamma_f,\Gamma_i)\Big]. \quad (3.85)
\end{aligned}$$

For the case of a resting pseudoscalar, $\sigma = -1$ since only the spatial components contribute, cf. Eq. 3.28, and thus

$$\begin{aligned}
&\frac{1}{2}(\mathbb{1}+P\tau^1)C_{\mu\nu}^{\mathrm{V-disc.},gen} = \frac{1}{2}\Big[\\
&\quad L_\mu(-\vec{q},\Gamma_i)\times AP_\nu^{ud}(\vec{q},\Gamma_f,\Gamma_c) - L_\mu(-\vec{q},\Gamma_i)\times AP_\nu^{du}(\vec{q},\Gamma_f,\Gamma_c) \\
&+L_\mu(\vec{q},\Gamma_i)\times AP_\nu^{du}(-\vec{q},\Gamma_f,\Gamma_c) - L_\mu(\vec{q},\Gamma_i)\times AP_\nu^{ud}(-\vec{q},\Gamma_f,\Gamma_c) \\
&+L_\nu(\vec{q},\Gamma_c)\times AP_\mu^{ud}(-\vec{q},\Gamma_f,\Gamma_i) - L_\nu(\vec{q},\Gamma_c)\times AP_\mu^{du}(-\vec{q},\Gamma_f,\Gamma_i) \\
&+L_\nu(-\vec{q},\Gamma_c)\times AP_\mu^{du}(\vec{q},\Gamma_f,\Gamma_i) - L_\nu(-\vec{q},\Gamma_c)\times AP_\mu^{ud}(\vec{q},\Gamma_f,\Gamma_i)\Big]. \quad (3.86)
\end{aligned}$$

The corresponding l, s and c V-disconnected contributions are then given by inserting the appropriate vector current loop and normalization, i.e.

$$\frac{1}{2}(\mathbb{1}+P\tau^1)C_{\mu\nu}^{\mathrm{V-disc.},l} = \frac{1}{12}\frac{1}{2}(\mathbb{1}+P\tau^1)C_{\mu\nu}^{\mathrm{V-disc.},gen}\Big|_{L_\mu=L_\mu^l}, \quad (3.87)$$

$$\frac{1}{2}(\mathbb{1}+P\tau^1)C_{\mu\nu}^{\mathrm{V-disc.},s} = -\frac{1}{6}\frac{1}{2}(\mathbb{1}+P\tau^1)C_{\mu\nu}^{\mathrm{V-disc.},gen}\Big|_{L_\mu=L_\mu^s}, \quad (3.88)$$

$$\frac{1}{2}(\mathbb{1}+P\tau^1)C_{\mu\nu}^{\mathrm{V-disc.},c} = \frac{2}{6}\frac{1}{2}(\mathbb{1}+P\tau^1)C_{\mu\nu}^{\mathrm{V-disc.},gen}\Big|_{L_\mu=L_\mu^c}. \quad (3.89)$$

Note that as mentioned in Sec. 2.2, Osterwalder-Seiler fermions are used for the s and c quarks, which needs to be taken into account in the actual construction. More details on this can be found in Sec. 3.5.2. Some examples for the $\vec{p}=0$ charged V-disconnected 3pt amplitudes after contracting the Lorentz structure and averaging over the momentum orbit as described in Sec. 3.1.3 can be found in Fig. 3.5. Note that the momentum at insertion t_c is used for the orbit averaging.

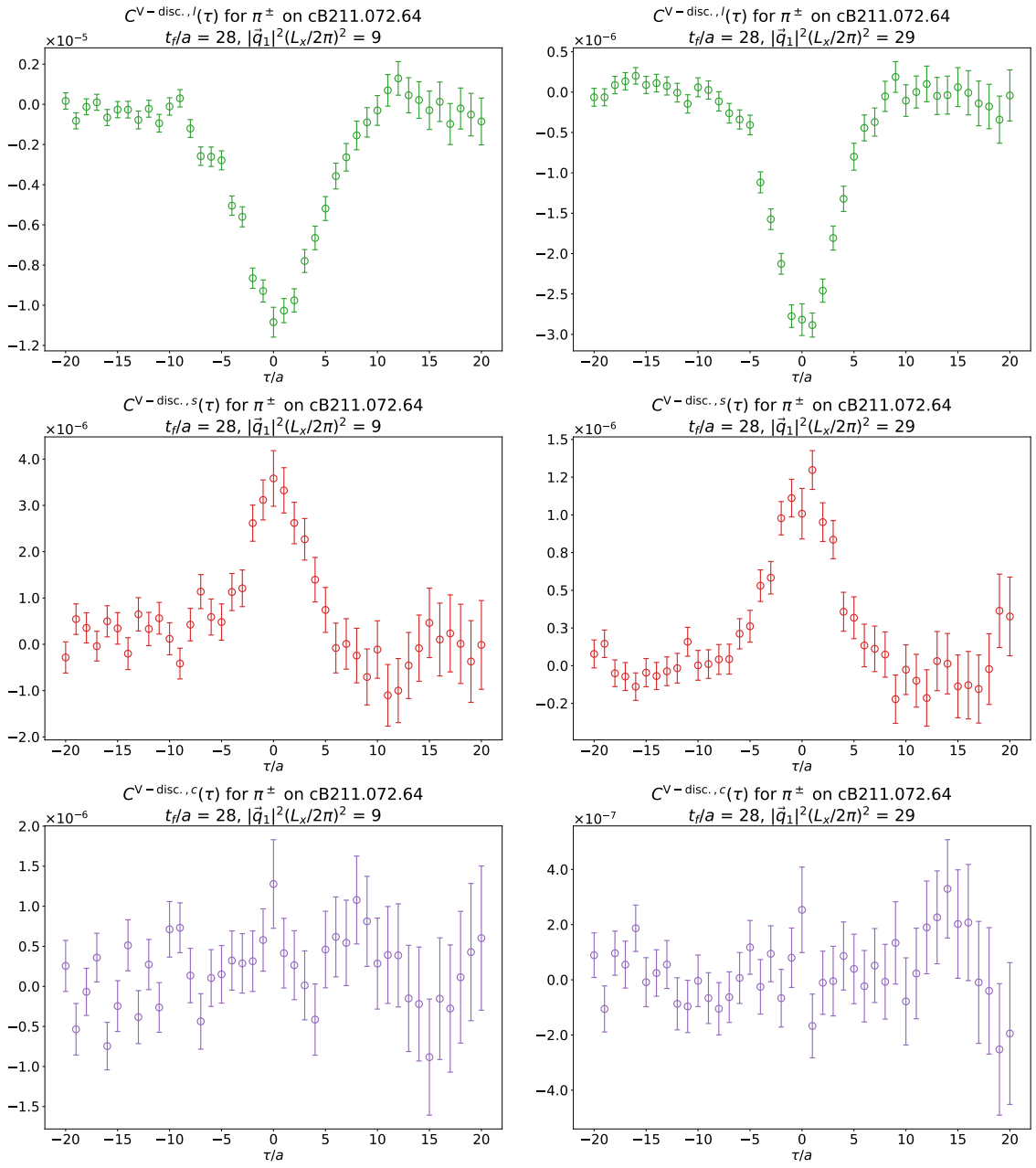

Figure 3.5: Momentum orbit averaged $C^{\mathrm{V-disc.}}(\tau, t_f = 2.23\,\mathrm{fm})$ for $\tau/a \in [-20, 20]$ on cB211.072.64 for two orbits. The top row shows V-disconnected contributions with a disconnected light current loop, the middle row with a disconnected strange current loop and the bottom row with a disconnected charm current loop. The V-disconnected contributions typically are 2-3 orders of magnitude smaller than the connected contribution with errors which are well under control. For some momentum orbits signals for $C^{\mathrm{V-disc.},l}$ and $C^{\mathrm{V-disc.},s}$ can be extracted, while $C^{\mathrm{V-disc.},c}$ just adds noise. See App. D.1 for more examples.

3.4 Pion Wick contractions contributing in $C^{(2)}$

The neutral pion 2pt amplitude can also be related to the charged pion 2pt amplitude, again simplifying the calculation since there is no disconnected charged pion contribution. Under the isospin rotation given in Sec. 3.1.7, the neutral 2pt amplitude for a pion with momentum $\vec{p}$ at $x_f = (\vec{y}, t_f)$ and a pion with opposite momentum at $x_i = (\vec{x}, t_i)$ transforms as

$$\langle \pi^0(t_f)\pi^0(t_i)\rangle \xrightarrow{I_y} -\langle \pi^+(t_f)\pi^-(t_i)\rangle - \langle \pi^-(t_f)\pi^+(t_i)\rangle. \tag{3.90}$$

Using quark propagators, the 2pt functions are written as

$$PP^{F_1F_2}(\vec{p}, \Gamma_f, \Gamma_i) = \sum_{\vec{x},\vec{y}} e^{i\vec{p}\vec{y}} e^{-i\vec{p}\vec{x}} \operatorname{Tr}\left[S_{fi}^{F_1}\Gamma_i S_{if}^{F_2}\Gamma_f\right], \tag{3.91}$$

with Γ_a giving the appropriate Dirac structure. Suppressing this structure, since here $\Gamma_f = \Gamma_i = \gamma_5$, the charged pion 2pt amplitude is written as

$$C^{(2)}(t_i, t_f) = -PP^{du}(\vec{p}) - PP^{ud}(\vec{p}). \tag{3.92}$$

Using γ_5-hermiticity, one finds

$$\operatorname{Tr}\left[S_{fi}^{F_1}\gamma_5 S_{if}^{F_2}\gamma_5\right] = \operatorname{Tr}\left[S_{fi}^{F_1}\gamma_5 S_{if}^{F_2}\gamma_5\right]^*, \tag{3.93}$$

implying

$$PP^{F_1F_2}(\vec{p}) = PP^{F_1F_2}(-\vec{p})^*. \tag{3.94}$$

Twisted parity transforms each amplitude into its charge conjugated partner and flips each momentum, such that

$$\begin{aligned}
\frac{1}{2}(\mathbb{1} + P\tau^1)C^{(2)}(t_i, t_f) &= -\frac{1}{2}\left[PP^{du}(\vec{p}) + PP^{ud}(-\vec{p}) + PP^{ud}(\vec{p}) + PP^{du}(-\vec{p})\right] \\
&= -\frac{1}{2}\left[PP^{du}(\vec{p}) + PP^{ud}(\vec{p})^* + PP^{ud}(\vec{p}) + PP^{du}(\vec{p})^*\right] \\
&= -\mathrm{Re}\left[PP^{du}(\vec{p}) + PP^{ud}(\vec{p})\right].
\end{aligned} \tag{3.95}$$

Note that one arrives at the same result in the case of $\vec{p} = 0$ by just using Eq. (3.94). An illustration for the $\vec{p} = 0$ charged 2pt amplitude can be found in Fig. 3.6.

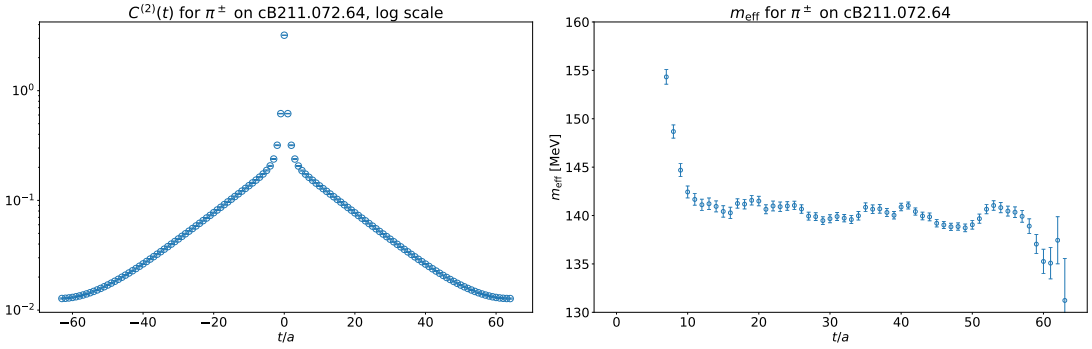

Figure 3.6: $C^{(2)}(t)$ (left) and the effective mass m_{eff} in MeV (right) on cB211.072.64. Note the clean exponential decay, which is determined by the ground state energy. The effective mass is introduced in Sec. 3.6.3. For the calculation of m_{eff}, backwards propagation is taken into account. The 2pt functions on the other two ensembles can be found in App. D.1.

3.4.1 Fitting the charged pion 2pt function

To extract the overlap factor $|Z_{\pi_\pm}|^2$ and pion energy $E_{\pi_\pm} = m_{\pi_\pm}$ for the resting pion while taking the finite-time correction from Eq. (3.41) into account, the charged pion 2pt function is fitted with the fit function

$$C^{(2)}(t = t_f - t_i) = A \cdot 2e^{-B \cdot L_t/2} \cosh\left(B \cdot (t - L_t/2)\right). \tag{3.96}$$

The fit parameters A, B then correspond to

$$A = \frac{|Z_{\pi_\pm}|^2}{2m_{\pi_\pm}}, \tag{3.97}$$

$$B = m_{\pi_\pm}. \tag{3.98}$$

Since the signals for the charged 2pt amplitudes are very precise, i.e. they have a large signal-to-noise ratio, the actual fits are done including one excited state, resulting in the charged pion mass values shown in Tab. 3.1 for the three ensembles used in this thesis.

3.4.2 Pion $\tilde{A}$

The construction of $\tilde{A}(\tau)$ in principle requires the placement of the pseudoscalar operator at asymptotically large Euclidean time, cf. Eq. (3.37). This limit is approximated here by studying multiple fixed temporal separations between the pseudoscalar operator and the current operator at source. These temporal separations are called source-sink separations. If there is no difference in $\tilde{A}(\tau)$ with increasing temporal separation, i.e. no excited state contamination, the limit is well approximated. With

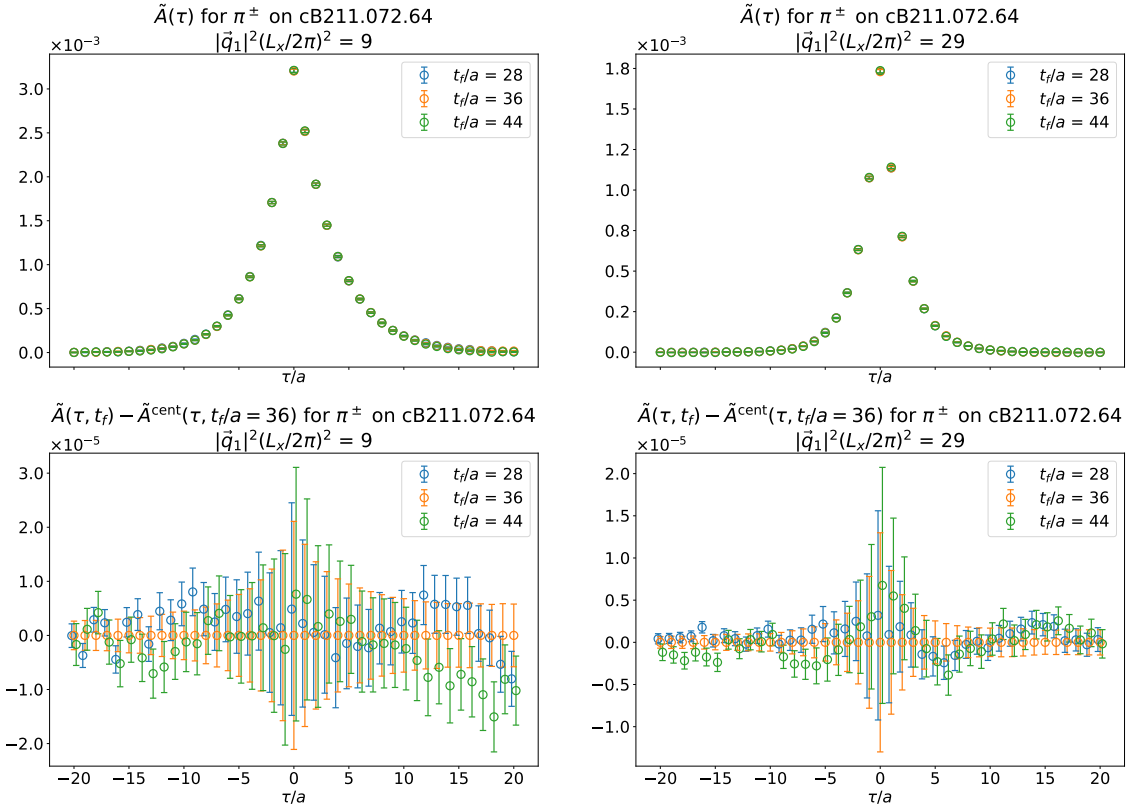

Figure 3.7: Momentum orbit averaged $\tilde{A}(\tau)$ (top row) and difference between $\tilde{A}(\tau)$ and the central value of $\tilde{A}(\tau, t_f/a = 36)$ (bottom row) using $t_f \in \{2.23, 2.87, 3.50\}$ fm for $\tau/a \in [-20, 20]$ on cB211.072.64 for two orbits. In the bottom row, the points are shifted slightly along the τ/a-axis for better legibility. Note the excellent convergence for the different t_f, indicating that there is no excited state contamination. Plots of the variance for these two orbits can be found in Fig. 3.8. Other examples can be found in App. D.1.

the exception of one momentum orbit on cD211.054.96, there is no excited state contamination for any of the used source-sink separations, thus the smallest on each

ensemble was used since this minimizes the statistical errors on $\tilde{A}(\tau)$. Two examples for the $\vec{p} = 0$ charged $\tilde{A}(\tau)$ and its variance after contracting the Lorentz structure and averaging over the momentum orbit as described in Sec. 3.1.3 can be found in Figs. 3.7 and 3.8.

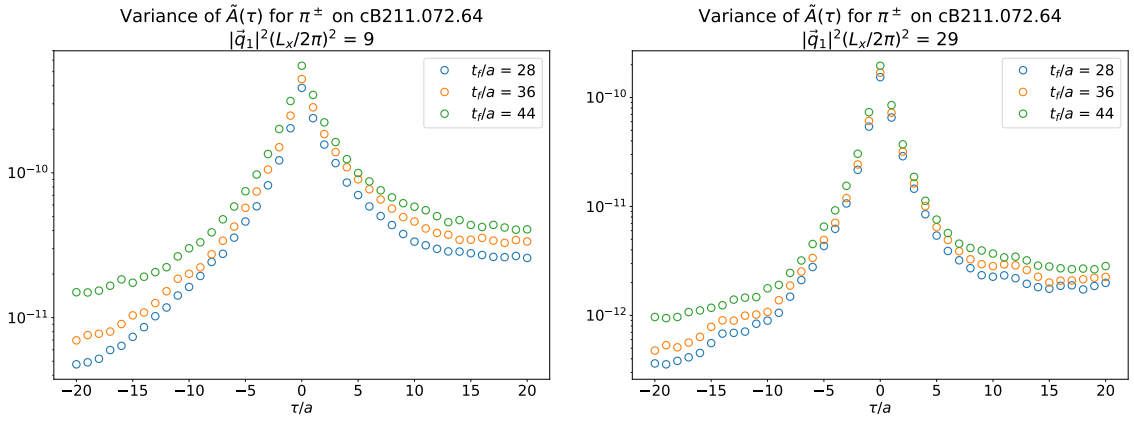

Figure 3.8: Variance on the momentum orbit averaged $\tilde{A}(\tau)$ using $t_f \in \{2.23, 2.87, 3.50\}$ fm for $\tau/a \in [-20, 20]$ on cB211.072.64 for the same two orbits as in Fig. 3.7. Note that the variance increases with increasing t_f for each value of τ/a.

3.5 η- and η'-meson Wick contractions contributing in $C_{\mu\nu}$

For the η- and η'-meson 3pt amplitude, all Wick contractions depicted in Fig 3.3 need to be included in principle. However, at the presently achievable accuracy, all V-disconnected diagrams as well as the P-disconnected diagram with c quark vector currents are not relevant and thus not included here, see also [71]. Further, at the time this thesis was written, only data on the cB211.072.64 ensemble was available, cf. Sec. 3.8, and the quality of the data only allowed the extraction of the η_8 2pt and 3pt amplitudes. The operators, conventions and symmetries relevant for this section can be found in App. A.1 and App. B.8, details on the projection on the η-meson state in Sec. 4.3.7.3.

3.5.1 Mixing of singlet and octet state

Only considering the strong interaction, the quark model of the three lightest quarks predicts nine eigenstates, two of which are

$$\eta_1 = \frac{1}{\sqrt{3}}(\bar{u}u + \bar{d}d + \bar{s}s), \tag{3.99}$$

$$\eta_8 = \frac{1}{\sqrt{6}}(\bar{u}u + \bar{d}d - 2\bar{s}s), \tag{3.100}$$

with the same quantum numbers, which together with the π^0 form the centre of the pseudoscalar meson nonet with $J^P = 0^-$, i.e. with total spin 0 and odd parity built from pairs of u, d and s quarks and the corresponding anti-quarks. The indices 1 and 8 indicate that η_1 belongs to a singlet and η_8 to an octet in the $SU(3)$ symmetry theory of quarks for the three lightest quarks, with the pseudoscalar nonet formed by the singlet and octet. Due to electroweak interaction, bound states with the same overall quantum numbers can mix, such that the physical η and η' states are given by a linear combination of the singlet and octet states, i.e.

$$\begin{pmatrix} \eta \\ \eta' \end{pmatrix} = \begin{pmatrix} \cos\theta_P & -\sin\theta_P \\ \sin\theta_P & \cos\theta_P \end{pmatrix} \begin{pmatrix} \eta_8 \\ \eta_1 \end{pmatrix}, \tag{3.101}$$

with mixing angle $\theta_P = -11.3^\circ \approx -0.2$ [12]. As detailed in Sec. 4.3.7.3, the η-meson state can be extracted from the η_8 operator without explicitly taking the mixing into account due to its overlap with the η-meson state.

3.5.2 Osterwalder-Seiler strange quarks

In twisted mass Osterwalder-Seiler calculations, two strange quark flavours $s_\pm$ (up- and down-type strange quark) are considered, they form a flavour degenerate doublet and are analogous to the up and down quark for the light contribution, the difference being that they both carry the same charge factor of $-1/3$ [106]. This gives the extended isospin symmetry group $SU(2)_{u,d} \times SU(2)_{s_+,s_-}$, up to lattice artefacts. Discrete symmetries act on the strange doublet like on the light doublet.
In the continuum limit, where explicit flavour symmetry breaking terms are absent,

it would not matter if one uses s_+ or s_-. Since they are treated here like the up and down quark, there will be additional factors of 1/2 such that the normalization is consistent with respect to the light contribution.
Replacing s by $(s_+, s_-)^T$ in the corresponding operators, cf. App. B.8, yields

$$\eta_s = i\bar{\psi}\gamma_5\epsilon\psi, \tag{3.102}$$

and

$$J_\mu^{Q,s} = \bar{\psi}\gamma_\mu Q\psi, \tag{3.103}$$

with

$$Q = \begin{pmatrix} -1/3 & 0 \\ 0 & -1/3 \end{pmatrix}, \tag{3.104}$$

where $\psi = (s_+, s_-)^T$. The corresponding current operator takes the form

$$J_\mu^{Q,s} = -\frac{1}{3}\bar{s}_+\gamma_\mu s_+ - \frac{1}{3}\bar{s}_-\gamma_\mu s_-, \tag{3.105}$$

and will be treated like the strange current in Sec. 3.3.2.

3.5.3 Classification of the relevant Wick contractions

As discussed in Sec. 3.1.7, only the second line in Eq. (3.47) contributes to $C_{\mu\nu}$ for η- and η'-meson. Using the short-hand notation $C_{\mu\nu} = \left\langle P J_\mu^Q J_\nu^Q \right\rangle$, the Wick contractions considered here are

$$\begin{aligned}
\left\langle P J_\mu^Q J_\nu^Q \right\rangle = & \quad \left\langle \eta_l J_\mu^{Q,l} J_\nu^{Q,l} \right\rangle_{\text{conn.}} && \text{light connected} && (3.106)\\
& + \left\langle \eta_l J_\mu^{Q,l} J_\nu^{Q,l} \right\rangle_{\text{P-disc.}} && \text{light disconnected} && (3.107)\\
& + \left\langle \eta_s J_\mu^{Q,s} J_\nu^{Q,s} \right\rangle_{\text{conn.}} && \text{strange connected} && (3.108)\\
& + \left\langle \eta_s J_\mu^{Q,s} J_\nu^{Q,s} \right\rangle_{\text{P-disc.}} && \text{strange disconnected} && (3.109)\\
& + \left\langle \eta_s J_\mu^{Q,l} J_\nu^{Q,l} \right\rangle_{\text{P-disc.}} && \text{mixed disconnected I} && (3.110)\\
& + \left\langle \eta_l J_\mu^{Q,s} J_\nu^{Q,s} \right\rangle_{\text{P-disc.}} && \text{mixed disconnected II,} && (3.111)
\end{aligned}$$

with the operators given in the twisted basis in App. B.8. In the following, the construction of these contractions is discussed. Note that both η_l and η_s pick up a normalization factor of $1/\sqrt{6}$ when constructing the η_8 3pt amplitude and a normalization factor of $1/\sqrt{3}$ when constructing the η_1 3pt amplitude. These factors are not explicitly included in the following.

3.5.4 Light connected contraction

Here, the light connected contribution to the amplitude, given in Eq. (3.106), is considered. To lighten the notation, the superscript l is dropped for the rest of this subsection. In terms of quark propagators, the data available for this thesis is of the form Eq. (3.71), i.e. given in terms of arbitrary counter-clockwise contractions. Inserting $F = F_1 = F_2 = F_3$ yields

$$\langle F(\vec{p},\vec{q})\rangle^{ccw} = \langle F(\vec{p},\vec{q},\Gamma_f,\Gamma_c,\Gamma_i)\rangle \equiv \sum_{\vec{x},\vec{y}} e^{i\vec{p}\vec{y}} e^{-i\vec{q}\vec{x}} \operatorname{Tr}\left[S^F_{if}\Gamma_f S^F_{fc}\Gamma_c S^F_{ci}\Gamma_i\right] \tag{3.112}$$

for these contractions. Directly going to $\vec{p}=0$ and suppressing the Dirac structure, one finds

$$\begin{aligned}\left\langle \eta J^Q_\mu J^Q_\nu \right\rangle_{\text{conn.}} &= \frac{1}{36}\left\langle \eta V^{0,0}_\mu V^{0,0}_\nu \right\rangle_{\text{conn.}} + \frac{1}{4}\left\langle \eta V^{1,0}_\mu V^{1,0}_\nu \right\rangle_{\text{conn.}} \\ &= \frac{5}{18}\left(\langle u(\vec{q})\rangle^{ccw}_{\text{conn.}} + \langle u(\vec{q})\rangle^{cw}_{\text{conn.}} - \langle d(\vec{q})\rangle^{ccw}_{\text{conn.}} - \langle d(\vec{q})\rangle^{cw}_{\text{conn.}}\right),\end{aligned} \tag{3.113}$$

where the clockwise contractions are defined analogous to Eq. (3.112). Under twisted parity, the spatial components of the amplitude are odd, cf. App. B.8.1, such that for μ,ν both spatial

$$\begin{aligned}&\frac{1}{2}\left(\mathbb{1} + P\tau^1\right)\left\langle \eta V^{0,0/1,0}_\mu(\vec{q}) V^{0,0/1,0}_\nu \right\rangle_{\text{conn.}} = \\ &\quad \frac{1}{2}\left(\left\langle \eta V^{0,0/1,0}_\mu(\vec{q}) V^{0,0/1,0}_\nu \right\rangle_{\text{conn.}} - \left\langle \eta V^{0,0/1,0}_\mu(-\vec{q}) V^{0,0/1,0}_\nu \right\rangle_{\text{conn.}}\right),\end{aligned} \tag{3.114}$$

holds, and thus

$$\frac{1}{2}\left(\mathbb{1}+P\tau^1\right)\left\langle \eta J_\mu^Q J_\nu^Q\right\rangle_{\text{conn.}} = \\ \frac{1}{2}\cdot\frac{5}{18}\left[\langle u(\vec{q})\rangle_{\text{conn.}}^{ccw} - \langle u(-\vec{q})\rangle_{\text{conn.}}^{ccw} + \langle u(\vec{q})\rangle_{\text{conn.}}^{cw} - \langle u(-\vec{q})\rangle_{\text{conn.}}^{cw}\right. \\ \left. - \langle d(\vec{q})\rangle_{\text{conn.}}^{ccw} + \langle d(-\vec{q})\rangle_{\text{conn.}}^{ccw} - \langle d(\vec{q})\rangle_{\text{conn.}}^{cw} + \langle d(-\vec{q})\rangle_{\text{conn.}}^{cw}\right] \tag{3.115}$$

Counterclockwise and clockwise amplitudes are related to one another through γ_5-hermiticity

$$\langle u(\vec{q})\rangle_{\text{conn.}}^{ccw} = \langle d(-\vec{q})\rangle_{\text{conn.}}^{cw,*}\,, \tag{3.116}$$

with the given Dirac structures, yielding in terms of flavour components

$$\frac{1}{2}\left(\mathbb{1}+P\tau^1\right)\left\langle \eta J_\mu^Q J_\nu^Q\right\rangle_{\text{conn.}} = \\ \frac{5}{18}\text{Re}\left[\langle u(\vec{q})\rangle_{\text{conn.}}^{ccw} - \langle d(\vec{q})\rangle_{\text{conn.}}^{ccw} - \langle u(-\vec{q})\rangle_{\text{conn.}}^{ccw} + \langle d(-\vec{q})\rangle_{\text{conn.}}^{ccw}\right]. \tag{3.117}$$

Two examples for the $\vec{p}=0$ connected 3pt amplitude for η_8 after contracting the Lorentz structure and averaging over the momentum orbit are shown in Fig. 3.9.

3.5.5 Light disconnected contraction

Next, the light disconnected contribution to the amplitude, given in Eq. (3.107), is considered. Again, the index l is dropped for the rest of this subsection. The relevant objects in terms of quark propagators are the loops and vector current correlators given by

$$L^F(\vec{p},\Gamma_f) = \sum_{\vec{y}} e^{i\vec{p}\vec{y}}\,\text{Tr}\left[S_{ff}^F\Gamma_x\right], \tag{3.118}$$

$$VV_{\mu\nu}^F(\vec{q},\Gamma_c,\Gamma_i) = \sum_{\vec{x}} e^{-i\vec{q}\vec{x}}\,\text{Tr}\left[S_{ic}^F\Gamma_c S_{ci}^F\Gamma_i\right], \tag{3.119}$$

where again $x_f=(\vec{y},t_f), x_c=(\vec{x},t_c), x_i=(\vec{0},t_i=0)$, $S_{ab}^F=S^F(x_a,x_b)$ and Γ_a gives the appropriate Dirac structure. The pseudoscalar has momentum $\vec{p}$ and the current at insertion momentum $\vec{q}$. Suppressing the Dirac structure, the light P-disconnected

contraction is then written as

$$\left\langle \eta J_\mu^Q J_\nu^Q \right\rangle_{\mathrm{P-disc.}} = \frac{5}{18}\left(L^u(\vec{p}) - L^d(\vec{p})\right)\left(VV_{\mu\nu}^u(\vec{q}) + VV_{\mu\nu}^d(\vec{q})\right). \tag{3.120}$$

Under twisted parity the amplitude transforms as

$$\begin{aligned}
&\frac{1}{2}\left(\mathbb{1} + P\tau^1\right)\left\langle \eta J_\mu^Q J_\nu^Q \right\rangle_{\mathrm{P-disc.}} \\
&\quad = \frac{1}{2}\cdot\frac{5}{18}\left\{\left(L^u(\vec{p}) - L^d(\vec{p})\right)\left(VV_{\mu\nu}^u(\vec{q}) + VV_{\mu\nu}^d(\vec{q})\right)\right. \\
&\qquad\qquad \left. - \left(L^u(-\vec{p}) - L^d(-\vec{p})\right)\left(VV_{\mu\nu}^u(-\vec{q}) + VV_{\mu\nu}^d(-\vec{q})\right)\right\}.
\end{aligned} \tag{3.121}$$

By using γ_5-hermiticity, i.e.

$$L^{d,u}(\vec{p}) = L^{u,d}(-\vec{p})^*, \tag{3.122}$$

$$VV_{\mu\nu}^{d,u}(\vec{q}) = VV_{\mu\nu}^{u,d}(-\vec{q})^*, \tag{3.123}$$

all d-quark contributions can be transformed into u-quark contributions,

$$\begin{aligned}
&\frac{1}{2}\left(\mathbb{1} + P\tau^1\right)\left\langle \eta J_\mu^Q J_\nu^Q \right\rangle_{\mathrm{P-disc.}} \\
&\quad = \frac{1}{2}\cdot\frac{5}{18}\left\{\left(L^u(\vec{p}) - L^u(-\vec{p})^*\right)\left(VV_{\mu\nu}^u(\vec{q}) + VV_{\mu\nu}^u(-\vec{q})^*\right)\right. \\
&\qquad\qquad \left. - \left(L^u(-\vec{p}) - L^u(\vec{p})^*\right)\left(VV_{\mu\nu}^u(-\vec{q}) + VV_{\mu\nu}^u(\vec{q})^*\right)\right\} \\
&\quad = \frac{5}{18}\mathrm{Re}\left[\left(L^u(\vec{p}) - L^u(-\vec{p})^*\right)\left(VV_{\mu\nu}^u(\vec{q}) + VV_{\mu\nu}^u(-\vec{q})^*\right)\right].
\end{aligned} \tag{3.124}$$

Finally, for $\vec{p} = 0$, one gets

$$\begin{aligned}
&\frac{1}{2}\left(\mathbb{1} + P\tau^1\right)\left\langle \eta(\vec{p}=0) J_\mu^Q J_\nu^Q \right\rangle_{\mathrm{P-disc.}} \\
&\quad = \frac{5}{18}\mathrm{Re}\left[2i\mathrm{Im}[L^u(0)]\left(VV_{\mu\nu}^u(\vec{q}) + VV_{\mu\nu}^u(-\vec{q})^*\right)\right] \\
&\quad = \frac{5}{18}\mathrm{Re}\left[2i\mathrm{Im}[L^u(0)] i\mathrm{Im}[VV_{\mu\nu}^u(\vec{q}) + VV_{\mu\nu}^u(-\vec{q})^*]\right] \\
&\quad = -\frac{5}{9}\mathrm{Im}[L^u(0)]\mathrm{Im}[VV_{\mu\nu}^u(\vec{q}) - VV_{\mu\nu}^u(-\vec{q})].
\end{aligned} \tag{3.125}$$

Two examples for the $\vec{p} = 0$ P-disconnected 3pt amplitude for η_8 after contracting the Lorentz structure and averaging over the momentum orbit are shown in Fig. 3.10.

3.5.6 Strange connected contraction

Following the same procedure as for the light connected contribution, the the strange connected contribution to the amplitude, given in Eq. (3.108), takes the form

$$\begin{aligned}\left\langle \eta_s J_\mu^{Q,s}\ J_\nu^{Q,s} \right\rangle_{\text{conn.}} \\ = \epsilon \frac{1}{2} \cdot \frac{1}{9} \left(\langle s_+(\vec{q}) \rangle_{\text{conn.}}^{ccw} + \langle s_+(\vec{q}) \rangle_{\text{conn.}}^{cw} - \langle s_-(\vec{q}) \rangle_{\text{conn.}}^{ccw} - \langle s_-(\vec{q}) \rangle_{\text{conn.}}^{cw} \right), \end{aligned} \tag{3.126}$$

where a factor of $1/2$ is included to account for double counting of diagrams due to the use of Osterwalder-Seiler fermions. After converting all clockwise to counter-clockwise contributions using γ_5-hermiticity, the twisted parity averaged amplitude is then given by

$$\frac{1}{2} \left(\mathbb{1} + P\tau^1 \right) \left\langle \eta_s J_\mu^{Q,s} J_\nu^{Q,s} \right\rangle_{\text{conn.}} = \tag{3.127}$$

$$\epsilon \frac{1}{18} \text{Re} \left[\langle s_+(\vec{q}) \rangle_{\text{conn.}}^{ccw} - \langle s_-(\vec{q}) \rangle_{\text{conn.}}^{ccw} - \langle s_+(-\vec{q}) \rangle_{\text{conn.}}^{ccw} + \langle s_-(-\vec{q}) \rangle_{\text{conn.}}^{ccw} \right], \tag{3.128}$$

in terms of flavour components, where $\epsilon = -2$ for η_8 and $\epsilon = 1$ for η_1. Two examples for the $\vec{p} = 0$ connected 3pt amplitude for η_8 after contracting the Lorentz structure and averaging over the momentum orbit are shown in Fig. 3.9.

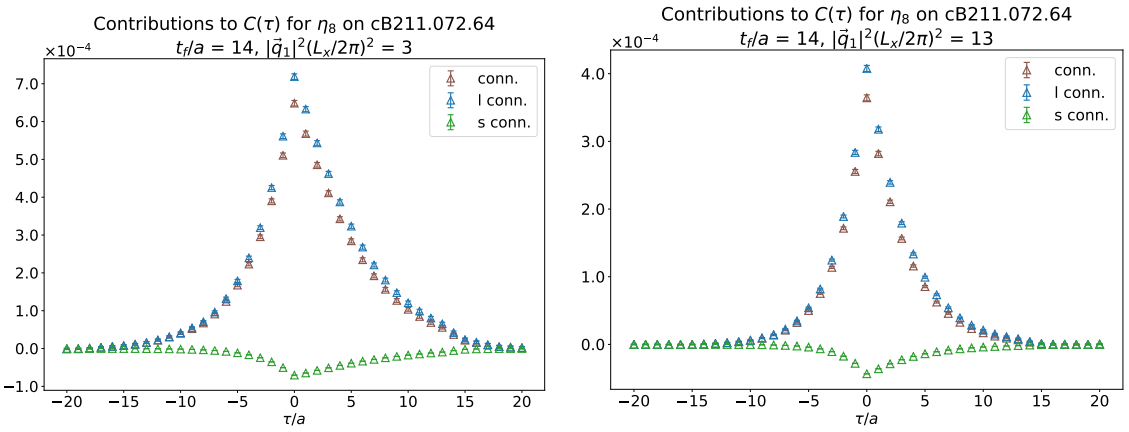

Figure 3.9: Momentum orbit averaged connected $C(\tau, t_f = 1.11\,\text{fm})$ for η_8 for $\tau/a \in [-20, 20]$ on cB211.072.64 for two orbits. Shown in brown is the full connected contribution, in blue the connected contribution involving only light quarks ("l conn.") and in green the one involving only strange quarks ("s conn."). Note the suppression of the strange contribution with respect to the light one. A more comprehensive overview can be found in App. D.2.

3.5.7 Strange disconnected contraction

For the strange disconnected contribution to the amplitude, given in Eq. (3.109), the derivation for the light disconnected contribution can be followed, with a factor of 1/2 both for the loop and for the current contribution. The 3pt amplitude reads

$$\left\langle \eta_s J_\mu^{Q,s} J_\nu^{Q,s} \right\rangle_{\text{P}-\text{disc.}} = \epsilon \left(\frac{1}{2}\right)^2 \cdot \frac{1}{9} \left(L^{s_+}(\vec{p}) - L^{s_-}(\vec{p})\right) \left(VV_{\mu\nu}^{s_+}(\vec{q}) + VV_{\mu\nu}^{s_-}(\vec{q})\right), \quad (3.129)$$

which after converting all s_-- to s_+-quark contributions and taking the twisted parity average leads to

$$\begin{aligned} &\frac{1}{2}\left(\mathbb{1} + P\tau^1\right) \left\langle \eta_s J_\mu^{Q,s} J_\nu^{Q,s} \right\rangle_{\text{P}-\text{disc.}} \\ &\quad = \epsilon \frac{1}{36} \text{Re}\left[\left(L^{s_+}(\vec{p}) - L^{s_+}(-\vec{p})^*\right) \left(VV_{\mu\nu}^{s_+}(\vec{q}) + VV_{\mu\nu}^{s_+}(-\vec{q})^*\right)\right]. \end{aligned} \quad (3.130)$$

For $\vec{p}=0$ one then finds

$$\begin{aligned}&\frac{1}{2}\left(\mathbb{1}+P\tau^1\right)\left\langle\eta_s(\vec{p}=0)J_\mu^{Q,s}J_\nu^{Q,s}\right\rangle_{\mathrm{P-disc.}}\\&\quad=-\epsilon\frac{1}{18}\mathrm{Im}[L^{s+}(0)]\mathrm{Im}[VV_{\mu\nu}^{s+}(\vec{q})-VV_{\mu\nu}^{s+}(-\vec{q})],\end{aligned}\tag{3.131}$$

with $\epsilon=-2$ for η_8 and $\epsilon=1$ for η_1. Two examples for the $\vec{p}=0$ P-disconnected 3pt amplitude for η_8 after contracting the Lorentz structure and averaging over the momentum orbit are shown in Fig. 3.11.

3.5.8 Mixed disconnected I contraction

Here, the mixed disconnected contribution with a strange loop and light current correlator to the amplitude, given in Eq. (3.110), is considered. One factor of 1/2 needs to be included to account for double counting due to the strange loop, resulting in

$$\left\langle\eta_s J_\mu^{Q,l}J_\nu^{Q,l}\right\rangle_{\mathrm{P-disc.}}=\epsilon\frac{1}{2}\cdot\frac{5}{18}\left(L^{s+}(\vec{p})-L^{s-}(\vec{p})\right)\left(VV_{\mu\nu}^{u}(\vec{q})+VV_{\mu\nu}^{d}(\vec{q})\right).\tag{3.132}$$

For $\vec{p}=0$, this leads to

$$\begin{aligned}&\frac{1}{2}\left(\mathbb{1}+P\tau^1\right)\left\langle\eta_s(\vec{p}=0)J_\mu^{Q,l}J_\nu^{Q,l}\right\rangle_{\mathrm{P-disc.}}\\&\quad=-\epsilon\frac{5}{18}\mathrm{Im}[L^{s+}(0)]\mathrm{Im}[VV_{\mu\nu}^{u}(\vec{q})-VV_{\mu\nu}^{u}(-\vec{q})].\end{aligned}\tag{3.133}$$

Two examples for the $\vec{p}=0$ P-disconnected 3pt amplitude for η_8 after contracting the Lorentz structure and averaging over the momentum orbit are shown in Fig. 3.10.

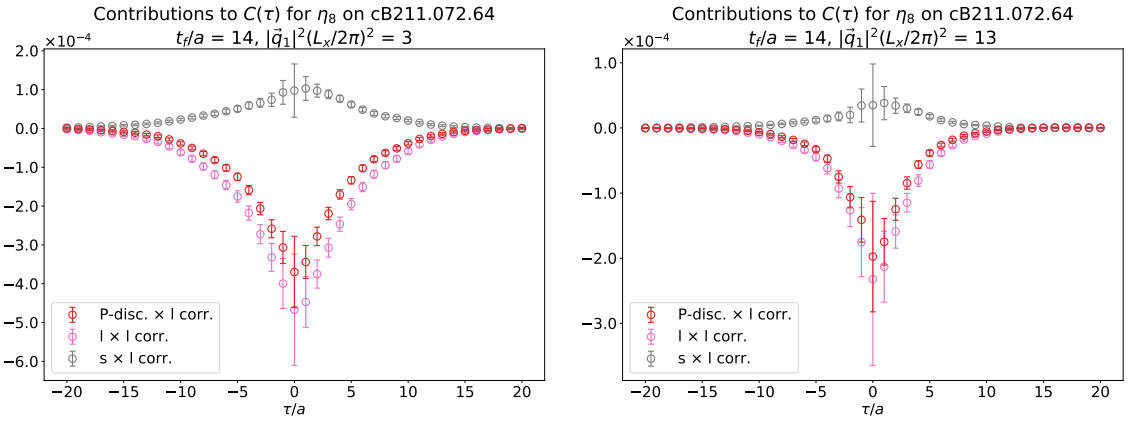

Figure 3.10: Momentum orbit averaged P-disconnected $C(\tau, t_f = 1.11\,\text{fm})$ for η_8 for $\tau/a \in [-20, 20]$ on cB211.072.64 for two orbits. Shown in red is the full P-disconnected contribution with the light current correlator, in pink the disconnected contribution involving only light quarks ("l × l corr.", corresponds to light disconnected) and in grey the one involving a disconnected strange quark and the light current correlator ("s × l corr.", corresponds to mixed disconnected I). The cancellation between the P-disconnected contribution with light current correlators and the light connected contribution shown in Fig. 3.9 is crucial when building the amplitude for η_8. More momentum orbits are shown in App. D.2.

3.5.9 Mixed disconnected II contraction

Finally, the mixed disconnected contribution with a light loop and strange current correlator to the amplitude, given in Eq. (3.111), is considered. One factor of 1/2 needs to be included to account for double counting due to the strange current, giving

$$\left\langle \eta_l J_\mu^{Q,s} J_\nu^{Q,s} \right\rangle_{\text{P-disc.}} = \frac{1}{2} \cdot \frac{1}{9} \left(L^u(\vec{p}) - L^d(\vec{p}) \right) \left(VV_{\mu\nu}^{s+}(\vec{q}) + VV_{\mu\nu}^{s-}(\vec{q}) \right). \tag{3.134}$$

For $\vec{p} = 0$, this leads to

$$\begin{aligned} &\frac{1}{2} \left(\mathbb{1} + P\tau^1 \right) \left\langle \eta_l(\vec{p}=0) J_\mu^{Q,s} J_\nu^{Q,s} \right\rangle_{\text{P-disc.}} \\ &\quad = -\frac{1}{9} \text{Im}[L^u(0)] \text{Im}[VV_{\mu\nu}^{s+}(\vec{q}) - VV_{\mu\nu}^{s+}(-\vec{q})]. \end{aligned} \tag{3.135}$$

Two examples for the $\vec{p} = 0$ P-disconnected 3pt amplitude for η_8 after contracting the Lorentz structure and averaging over the momentum orbit are shown in Fig. 3.11.

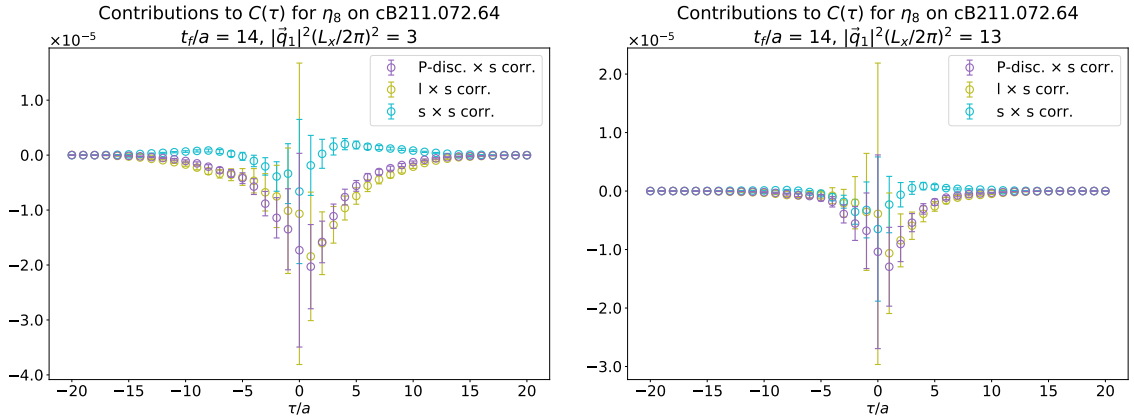

Figure 3.11: Momentum orbit averaged P-disconnected $C(\tau, t_f = 1.11\,\text{fm})$ for η_8 for $\tau/a \in [-20, 20]$ on cB211.072.64 for two orbits. Shown in purple is the full P-disconnected contribution with the strange current correlator, in green the disconnected contribution involving a disconnected light quark and the strange current correlator ("l × s corr.", corresponds to mixed disconnected II) and in turquoise the one involving only strange quarks ("s × s corr.", corresponds to strange disconnected). More momentum orbits are shown in App. D.2.

3.6 η- and η'-meson Wick contractions contributing in $C^{(2)}$

For the η- and η'-meson contributions to $C^{(2)}$, both diagrams in Fig. 3.2 need to be considered. The same pseudoscalar operator as in the last section is used, i.e.

$$\eta(\epsilon) = \eta_l + \epsilon\eta_s, \tag{3.136}$$

where $\epsilon = -2$ for η_8 and $\epsilon = 1$ for η_1. Note that the 2pt amplitudes built here need an additional normalization factor of $1/\sqrt{6}$ for each involved η_8 operator and of $1/\sqrt{3}$ for each involved η_1 operator.

3.6.1 Connected contraction

The connected pseudoscalar 2pt function in terms of quark propagators, given in Eq. (3.91), can be written as

$$PP^F(\vec{p},\Gamma_f,\Gamma_i) = \sum_{\vec{x},\vec{y}} e^{i\vec{p}\vec{y}} e^{-i\vec{p}\vec{x}} \operatorname{Tr}\left[S^F_{fi}\Gamma_i S^F_{if}\Gamma_f\right], \tag{3.137}$$

since the amplitudes relevant here come in flavour pairs. Again suppressing the Dirac structure, the connected contraction takes the form

$$\langle\eta(\epsilon,t_f)\eta(\epsilon,t_i)\rangle_{\text{conn.}} = PP^u(\vec{p}) + PP^d(\vec{p}) + \frac{\epsilon^2}{2}\left(PP^{s_+}(\vec{p}) + PP^{s_-}(\vec{p})\right), \tag{3.138}$$

with a factor $1/2$ due to the Osterwalder-Seiler strange quarks. The d- and s_--quark contributions are related to the u- and s_+-quark contributions, respectively, by γ_5-hermiticity as usual, while twisted parity transforms the amplitudes into their charge conjugated partners and flips all momenta, such that

$$\begin{aligned}
&\frac{1}{2}\left(\mathbb{1} + P\tau^1\right)\langle\eta(\epsilon,t_f)\eta(\epsilon,t_i)\rangle_{\text{conn.}} = \\
&\qquad = \frac{1}{2}\left[PP^u(\vec{p}) + PP^d(\vec{p}) + \frac{\epsilon^2}{2}\left(PP^{s_+}(\vec{p}) + PP^{s_-}(\vec{p})\right)\right. \\
&\qquad\quad \left. + PP^d(-\vec{p}) + PP^u(-\vec{p}) + \frac{\epsilon^2}{2}\left(PP^{s_-}(-\vec{p}) + PP^{s_+}(-\vec{p})\right)\right] \\
&\qquad = \operatorname{Re}\left[PP^u(\vec{p}) + PP^u(-\vec{p}) + \frac{\epsilon^2}{2}\left(PP^{s_+}(\vec{p}) + PP^{s_+}(-\vec{p})\right)\right].
\end{aligned} \tag{3.139}$$

Thus the connected $\eta(\epsilon)$ 2pt function with $\vec{p}=0$ is given by

$$\langle\eta(\epsilon,t_f)\eta(\epsilon,t_i)\rangle_{\text{conn.}} = 2\text{Re}\left[PP^u(\vec{0}) + \frac{\epsilon^2}{2}\left(PP^{s_+}(\vec{0})\right)\right]. \tag{3.140}$$

For the cross-correlator this translates to

$$\langle\eta(\epsilon_f,t_f)\eta(\epsilon_i,t_i)\rangle_{\text{conn.}} = 2\text{Re}\left[PP^u(\vec{0}) + \frac{\epsilon_f\epsilon_i}{2}\left(PP^{s_+}(\vec{0})\right)\right]. \tag{3.141}$$

3.6.2 Disconnected contraction

In terms of quark loops, cf. Eq. (3.118), the disconnected contribution to the 2pt amplitude reads

$$\begin{aligned}\langle \eta(\epsilon, t_f, \vec{p})\ \eta(\epsilon, t_i, -\vec{p})\rangle_{\text{disc.}} = \\ \Big(L^u(\vec{p},\Gamma_f) - L^d(\vec{p},\Gamma_f) + \frac{\epsilon}{2}\left[L^{s_+}(\vec{p},\Gamma_f) - L^{s_-}(\vec{p},\Gamma_f)\right]\Big) \\ \cdot \Big(L^u(-\vec{p},\Gamma_i) - L^d(-\vec{p},\Gamma_i) + \frac{\epsilon}{2}\left[L^{s_+}(-\vec{p},\Gamma_i) - L^{s_-}(-\vec{p},\Gamma_i)\right]\Big)\,, \quad (3.142)\end{aligned}$$

with factors of $1/2$ again due to Osterwalder-Seiler. Converting all d- and s_--quark contributions using γ_5-hermiticity and directly going to $\vec{p}=0$ yields

$$\begin{aligned}\langle \eta(\epsilon, t_f)\ \eta(\epsilon, t_i)\rangle_{\text{disc.}} = \\ \Big(2i\mathrm{Im}L^u(\vec{0},\Gamma_f) + 2i\frac{\epsilon}{2}\mathrm{Im}L^{s_+}(\vec{0},\Gamma_f)\Big) \\ \cdot \Big(2i\mathrm{Im}L^u(\vec{0},\Gamma_i) + 2i\frac{\epsilon}{2}\mathrm{Im}L^{s_+}(\vec{0},\Gamma_i)\Big) \quad (3.143) \\ = 4i^2\Big(\mathrm{Im}L^u(\vec{0},\Gamma_f)\mathrm{Im}L^u(\vec{0},\Gamma_i) + \frac{\epsilon^2}{4}\mathrm{Im}L^{s_+}(\vec{0},\Gamma_f)\mathrm{Im}L^{s_+}(\vec{0},\Gamma_i) \\ + \frac{\epsilon}{2}\mathrm{Im}L^u(\vec{0},\Gamma_f)\mathrm{Im}L^{s_+}(\vec{0},\Gamma_i) + \frac{\epsilon}{2}\mathrm{Im}L^{s_+}(\vec{0},\Gamma_f)\mathrm{Im}L^u(\vec{0},\Gamma_i)\Big)\,. \quad (3.144)\end{aligned}$$

For the cross-correlator this translates to

$$\begin{aligned}\langle \eta(\epsilon_f, t_f)\ \eta(\epsilon_i, t_i)\rangle_{\text{disc.}} = \\ = 4i^2\Big(\mathrm{Im}L^u(\vec{0},\Gamma_f)\mathrm{Im}L^u(\vec{0},\Gamma_i) + \frac{\epsilon_f\epsilon_i}{4}\mathrm{Im}L^{s_+}(\vec{0},\Gamma_f)\mathrm{Im}L^{s_+}(\vec{0},\Gamma_i) \\ + \frac{\epsilon_i}{2}\mathrm{Im}L^u(\vec{0},\Gamma_f)\mathrm{Im}L^{s_+}(\vec{0},\Gamma_i) + \frac{\epsilon_f}{2}\mathrm{Im}L^{s_+}(\vec{0},\Gamma_f)\mathrm{Im}L^u(\vec{0},\Gamma_i)\Big)\,. \quad (3.145)\end{aligned}$$

Illustrations for the η_8 and η_1 2pt amplitudes with $\vec{p}=0$ can be found in Fig. 3.12.

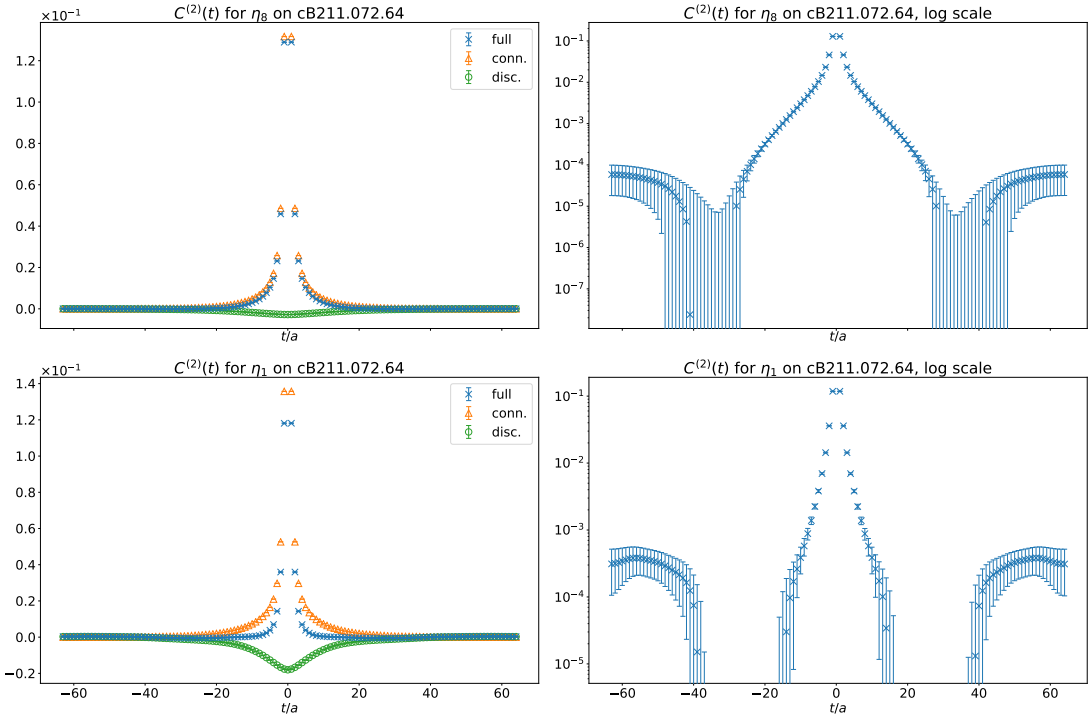

Figure 3.12: $C^{(2)}(t)$ on cB211.072.64 for η_8 (top row) and η_1 (bottom row). In contrast to the charged pion 2pt functions, and especially for the η_1 operator, there is no region of exponential decay clearly dominated by just one decay constant.

3.6.3 Fitting the η- and η'-meson 2pt functions

As seen in Fig. 3.12, it is quite challenging to extract the overlap factors and masses for η_8 and η_1. The same fit function as in Sec. 3.4.1 was used, but the choice of fit window is much more delicate, especially for η_1.
Promising fit windows can be identified by determining plateaus in the effective mass m_{eff}. Assuming that the 2pt function $C^{(2)}(t)$ of interest is dominated by a state with energy E, it is described by an exponential decay

$$C^{(2)}(t) = Ae^{-Et}. \tag{3.146}$$

This is in general a reasonable approximation for sufficiently large t, with E being the energy of the ground state. The standard definition of m_{eff} is then given by

$$m_{\text{eff}} = \log\left[\frac{C^{(2)}(t)}{C^{(2)}(t+1)}\right] \overset{t\gg 1}{\approx} \log\left[e^{-Et+E(t+1)}\right] = \log[e^{E}] = E. \tag{3.147}$$

If the periodic boundary conditions are taken into account, the expression for m_{eff} becomes

$$m_{\text{eff}} \overset{t\gg 1}{=} \log\left[\frac{C^{(2)}(t)}{C^{(2)}(t+1)} \cdot \frac{1+e^{-E(L_t-2(t+1))}}{1+e^{-E(L_t-2t)}}\right], \tag{3.148}$$

cf. App. B.5. Note that E on the r.h.s of Eq. (3.148) is a priori not known. Thus, an initial guess for E is made using Eq. (3.147) and then iteratively improved according to Eq. (3.148), see Lst. 1 for an example implementation in `python`. For the pion 2pt function, there is a significant contribution from the backwards propagating state, see Fig. D.4, while for the η_8 and η_1 2pt functions the effective masses from Eq. (3.147) and Eq. (3.148) almost coincide due to the heavy η-meson mass, cf. Fig 3.13.
It is often useful to consider definitions of the effective mass obtained using trigonometric relations for the 2pt function while including backwards propagation and shifts of the 2pt function in the temporal direction such as

$$\frac{C^{(2)}(t+\tau)+C^{(2)}(t-\tau)}{2C^{(2)}(t)} = \cosh E\tau, \tag{3.149}$$

giving

$$m_{\text{eff}}(t,\tau) = \frac{1}{\tau}\text{arccosh}\left(\frac{C^{(2)}(t+\tau)+C^{(2)}(t-\tau)}{2C^{(2)}(t)}\right), \tag{3.150}$$

```python
# Function for extracting the effective mass,
# including backwards propagation.
# t : integer, specifies timeslice
# c : array storing the (symmetrized) 2pt function per timeslice
# Lt: float, temporal extent of the lattice
import numpy as np
def M_eff_wrap(t, c, Lt):
  mass = np.log(c[t]) - np.log(c[t+1])
  res = 1
  counter = 0
  while res > 1e-12:
    u = 1. + np.exp(-mass*(Lt - 2.*float(t) - 2.))
    d = 1. + np.exp(-mass*(Lt - 2.*float(t)))
    tmp_mass = np.log(c[t])-np.log(c[t+1])+np.log(u)-np.log(d)
    res = abs(tmp_mass - mass)
    mass = tmp_mass
    counter += 1
  return mass, counter
```

Listing 1: Example implementation of the iterative procedure used to extract m_{eff} while including backwards propagation, cf. Eq. (3.148).

or

$$\frac{C^{(2)}(t-2\tau)-C^{(2)}(t+2\tau)}{2(C^{(2)}(t-\tau)-C^{(2)}(t+\tau))}=\cosh E\tau, \tag{3.151}$$

and thus

$$m_{\text{eff}}(t,\tau)=\frac{1}{\tau}\text{arccosh}\left(\frac{C^{(2)}(t-2\tau)-C^{(2)}(t+2\tau)}{2(C^{(2)}(t-\tau)-C^{(2)}(t+\tau))}\right). \tag{3.152}$$

Note that this uses only differences of the 2pt function. Should the 2pt function of interest have a significant vacuum expectation value (vev), it is useful to consider shifted 2pt functions $C'(t;s)=C^{(2)}(t)-C^{(2)}(t+s)$ for the construction of m_{eff}, since they allow for a cancellation of the vev in m_{eff}. Illustrations for the η_8 and η_1 effective mass can be found in Fig. 3.13. In particular, one sees that the η_8 effective mass obtained using the different methods presented above converges to the same plateau, starting at $t/a\approx 11$, while this does not happen for the η_1 effective mass due to the smaller overlap between the η_1 operator and the η-meson state, cf. Sec. 4.3.7.3.

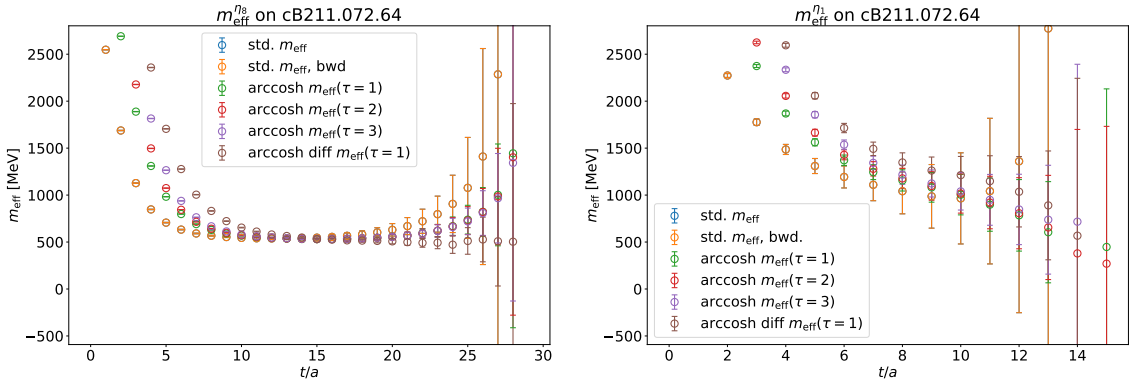

Figure 3.13: Effective η_8 mass $m_{\text{eff}}^{\eta_8}$ (left) and effective η_1 mass $m_{\text{eff}}^{\eta_1}$ (right), std. m_{eff} is calculated according to Eq. (3.147), std. m_{eff}, bwd according to Eq. (3.148), arccosh m_{eff} according to Eq. (3.150) and arccosh diff m_{eff} according to Eq. (3.152). In the case of $m_{\text{eff}}^{\eta_8}$ a plateau around 550 MeV is visible, while $m_{\text{eff}}^{\eta_1}$ decays much slower due to the smaller overlap between the η_1 operator and the η-meson state, cf. Sec. 4.3.7.3, and does not reach a plateau.

3.6.4 η-meson $\tilde{A}$

As discussed in Sec. 3.4.2, the approximation of the limit where the pseudoscalar is removed to asymptotically large Euclidean times in the construction of $\tilde{A}(\tau)$, cf. Eq. (3.37), is done by studying the excited state contamination when increasing the temporal separations between the pseudoscalar and the current at the source. While in comparison to the pion shorter temporal separations can be used for the η-meson, due to its faster decay rate caused by the large η-meson mass, the signal-to-noise ratio in the disconnected contributions rapidly deteriorates with increasing temporal separation. Thus, a delicate balance between excited state contamination and signal quality needs to be found. Here, three values for t_f were considered. While the lowest of the three clearly gave the best signal-to-noise ratio it at the same time suffered from excited state contamination when compared to the larger t_f, especially for the lower momentum orbits. Since the excited states were suppressed best for the largest value of t_f, it was used in Sec. 4.3. An illustration of this can be found in Fig. 3.14, see also the discussion in Sec. 4.3.

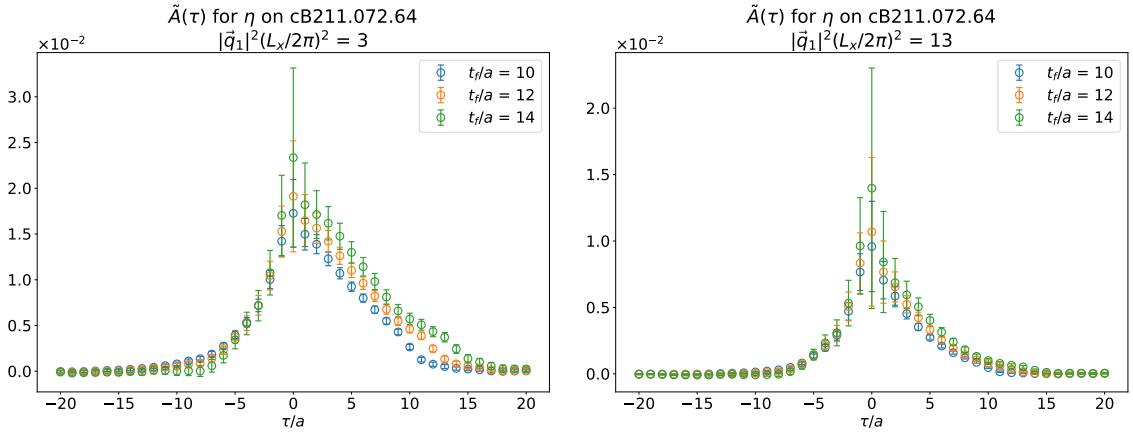

Figure 3.14: Momentum orbit averaged η-meson $\tilde{A}(\tau)$ using $t_f \in \{0.80, 0.96, 1.11\}$ fm for $\tau/a \in [-20, 20]$ on cB211.072.64 for two orbits. Note the clear excited state contamination visible for the lower momentum (left) which becomes smaller for the higher momentum (right). Other examples can be found in App. D.2.

3.7 Extending $\tilde{A}(\tau)$ and extraction of the TFFs

To extract the transition form factors $\mathcal{F}_{P\to\gamma^*\gamma^*}$, $\tilde{A}(\tau)e^{\omega_1\tau}$ is integrated over the whole temporal axis, cf. Eq. (3.30). The contribution from one of the tails is enhanced exponentially by the factor $e^{\omega_1\tau}$, this effect is significant for choices of ω_1 resulting in kinematics close to the singly virtual axis for the charged pion and, due to the large η-meson mass, significant for all ω_1 for the η-meson. In addition, since the pseudoscalar operator is placed at some finite Euclidean time, not all data has the correct time ordering needed for the approximation of $\tilde{A}(\tau)$ in Eq. (3.37). Further, the signal-to-noise ratio deteriorates exponentially with increasing $|\tau|$, which significantly hinders the extraction of the TFFs wherever the exponential enhancement of one of the tails is significant.

As presented in Ch. 4 and 5, following [66, 67], joint fits to all $\vec{q}_1$ momentum orbits using the Vector Meson Dominance (VMD) and Lowest Meson Dominance (LMD) models are performed to determine the asymptotic behaviour of $\tilde{A}(\tau)$. The models are used to replace the lattice data $A^{(\text{latt.})}(\tau)$ for $|\tau| > \tau_{\text{cut}}$ when performing the integration in Eq. (3.30). Note that τ_{cut} can be chosen independently for the two tails, which can be useful to maximize the amount of included lattice data. The

integration in Eq. (3.30) gets replaced by

$$\mathcal{F}_{P\to\gamma^*\gamma^*}(q_1^2,q_2^2) = \int_{-\tau_{\text{cut}}}^{\tau_{\text{cut}}} d\tau\, \tilde{A}^{(\text{latt.})}(\tau)e^{\omega_1\tau} + \int_{\tau_{\text{cut}}}^{\infty} d\tau\, \tilde{A}^{(\text{fit})}(\tau)e^{\omega_1\tau} + \int_{-\infty}^{-\tau_{\text{cut}}} d\tau\, \tilde{A}^{(\text{fit})}(\tau)e^{\omega_1\tau}. \tag{3.153}$$

To get a handle on the model dependence, the lattice data content

$$\Delta_{\text{latt.}} = \frac{\int_{-\tau_{\text{cut}}}^{\tau_{\text{cut}}} d\tau\, \tilde{A}^{(\text{latt.})}(\tau)e^{\omega_1\tau}}{\mathcal{F}_{P\to\gamma^*\gamma^*}(q_1^2,q_2^2)}, \tag{3.154}$$

is stored when performing the integration in Eq. (3.153), allowing the exclusion of TFF values which depend too strongly on the used model in the further steps.
The LMD fit function for the scalar amplitude defined from Eq. (3.37) is given by

$$\tilde{A}^{\text{LMD}}(\tau \gtrless 0) = \pm\frac{1}{2}\Bigg[\frac{\alpha M_V^4 + \beta(2M_V^2 + m_P^2 \mp 2m_P\sqrt{M_V^2+|\vec{q}_1|^2})}{m_P\sqrt{M_V^2+|\vec{q}_1|^2}(2\sqrt{M_V^2+|\vec{q}_1|^2} \mp m_P)} e^{\mp\sqrt{M_V^2+|\vec{q}_1|^2}\tau} - \frac{\alpha M_V^4 + \beta(2M_V^2 + m_P^2 \pm 2m_P\sqrt{M_V^2+|\vec{q}_1|^2})}{m_P\sqrt{M_V^2+|\vec{q}_1|^2}(2\sqrt{M_V^2+|\vec{q}_1|^2} \pm m_P)} e^{-(m_P\pm\sqrt{M_V^2+|\vec{q}_1|^2})\tau}\Bigg], \tag{3.155}$$

with M_V, α and β fit parameters, cf. [66, 118, 124, 125]. The energy of the modelled vector meson is $E_V \equiv \sqrt{M_V^2+|\vec{q}_1|^2}$. The VMD fit function is obtained by setting $\beta = 0$.
The LMD fit function can be integrated analytically and independently for all choices of ω_1. Directly integrating gives for the two tails

$$\begin{aligned}\int_{-\infty}^{-\tau_{\text{cut}}} d\tau\, \tilde{A}^{\text{LMD}}(\tau)e^{\omega_1\tau} = \\ -\frac{1}{2}\Bigg[&\frac{\alpha M_V^4 + \beta(2M_V^2 + m_P^2 + 2m_P\sqrt{M_V^2+|\vec{q}_1|^2})}{m_P\sqrt{M_V^2+|\vec{q}_1|^2}(2\sqrt{M_V^2+|\vec{q}_1|^2} + m_P)} e^{(+\sqrt{M_V^2+|\vec{q}_1|^2}+\omega_1)\tau} \\ &\cdot \frac{1}{\sqrt{M_V^2+|\vec{q}_1|^2}+\omega_1} \\ &- \frac{\alpha M_V^4 + \beta(2M_V^2 + m_P^2 - 2m_P\sqrt{M_V^2+|\vec{q}_1|^2})}{m_P\sqrt{M_V^2+|\vec{q}_1|^2}(2\sqrt{M_V^2+|\vec{q}_1|^2} - m_P)} e^{(-(m_P-\sqrt{M_V^2+|\vec{q}_1|^2})+\omega_1)\tau} \\ &\cdot \frac{1}{-(m_P-\sqrt{M_V^2+|\vec{q}_1|^2})+\omega_1}\Bigg]\Bigg|_{\tau=-\tau_{\text{cut}}},\end{aligned} \tag{3.156}$$

$$\int_{\tau_{\text{cut}}}^{\infty} d\tau\, \tilde{A}^{\text{LMD}}(\tau) e^{\omega_1 \tau} =$$
$$+\frac{1}{2}\Bigg[\frac{\alpha M_V^4 + \beta(2M_V^2 + m_P^2 - 2m_P\sqrt{M_V^2+|\vec{q}_1|^2})}{m_P\sqrt{M_V^2+|\vec{q}_1|^2}(2\sqrt{M_V^2+|\vec{q}_1|^2} - m_P)} e^{(-\sqrt{M_V^2+|\vec{q}_1|^2}+\omega_1)\tau}$$
$$\cdot \frac{1}{\sqrt{M_V^2+|\vec{q}_1|^2}-\omega_1}$$
$$- \frac{\alpha M_V^4 + \beta(2M_V^2 + m_P^2 + 2m_P\sqrt{M_V^2+|\vec{q}_1|^2})}{m_P\sqrt{M_V^2+|\vec{q}_1|^2}(2\sqrt{M_V^2+|\vec{q}_1|^2} + m_P)} e^{(-(m_P+\sqrt{M_V^2+|\vec{q}_1|^2})+\omega_1)\tau}$$
$$\cdot \frac{1}{(m_P+\sqrt{M_V^2+|\vec{q}_1|^2})-\omega_1}\Bigg]\Bigg|_{\tau=\tau_{\text{cut}}}, \tag{3.157}$$

where $\tau_{\text{cut}} > 0$. Because of the restrictions on ω_1 due to the hadron production threshold, these integrals should converge for all valid choices of ω_1. Non-converging integrals are a sign that there is some on-shell intermediate state, which would violate the assumptions under which the Wick rotation in Sec. 3.1.3 was performed. Some examples for integrands $\tilde{A}(\tau)e^{\omega_1\tau}$ are shown in Fig. 3.15.

Positive and negative τ can be related analytically by using the symmetry $\tilde{A}(\tau) = e^{-m_P\tau}\tilde{A}(-\tau)$. This allows one to express the TFFs using only data from the tail without the pseudoscalar insertion at $t_f > 0$, which should be less susceptible to excited state contaminations. Fixing all spatial momenta leaves ω_1 as the remaining free parameter as described in Sec. 3.1.3, such that one can write $\mathcal{F}_{P\to\gamma^*\gamma^*}(q_1^2, q_2^2) \equiv \mathcal{F}_{P\to\gamma^*\gamma^*}(\omega_1)$. The TFFs using only $\tau < 0$ data are given by

$$\begin{aligned}\mathcal{F}_{P\to\gamma^*\gamma^*}(\omega_1) &= \int_{-\infty}^{\infty} d\tau\, e^{\omega_1\tau}\tilde{A}_{\mu\nu}(\tau) \\ &= \int_{-\infty}^{0} d\tau\, e^{\omega_1\tau}\tilde{A}_{\mu\nu}(\tau) + \int_{-\infty}^{0} d\tau\, e^{(m_P-\omega_1)\tau}\tilde{A}_{\mu\nu}(\tau) \\ &= \frac{1}{2}\left[\mathcal{F}^{\text{left}}_{P\to\gamma^*\gamma^*}(\omega_1) + \mathcal{F}^{\text{left}}_{P\to\gamma^*\gamma^*}(m_P-\omega_1)\right], \end{aligned} \tag{3.158}$$

where

$$\mathcal{F}^{\text{left}}_{P\to\gamma^*\gamma^*}(\omega) = 2\int_{-\infty}^{0} d\tau\, e^{\omega\tau}\tilde{A}_{\mu\nu}(\tau). \tag{3.159}$$

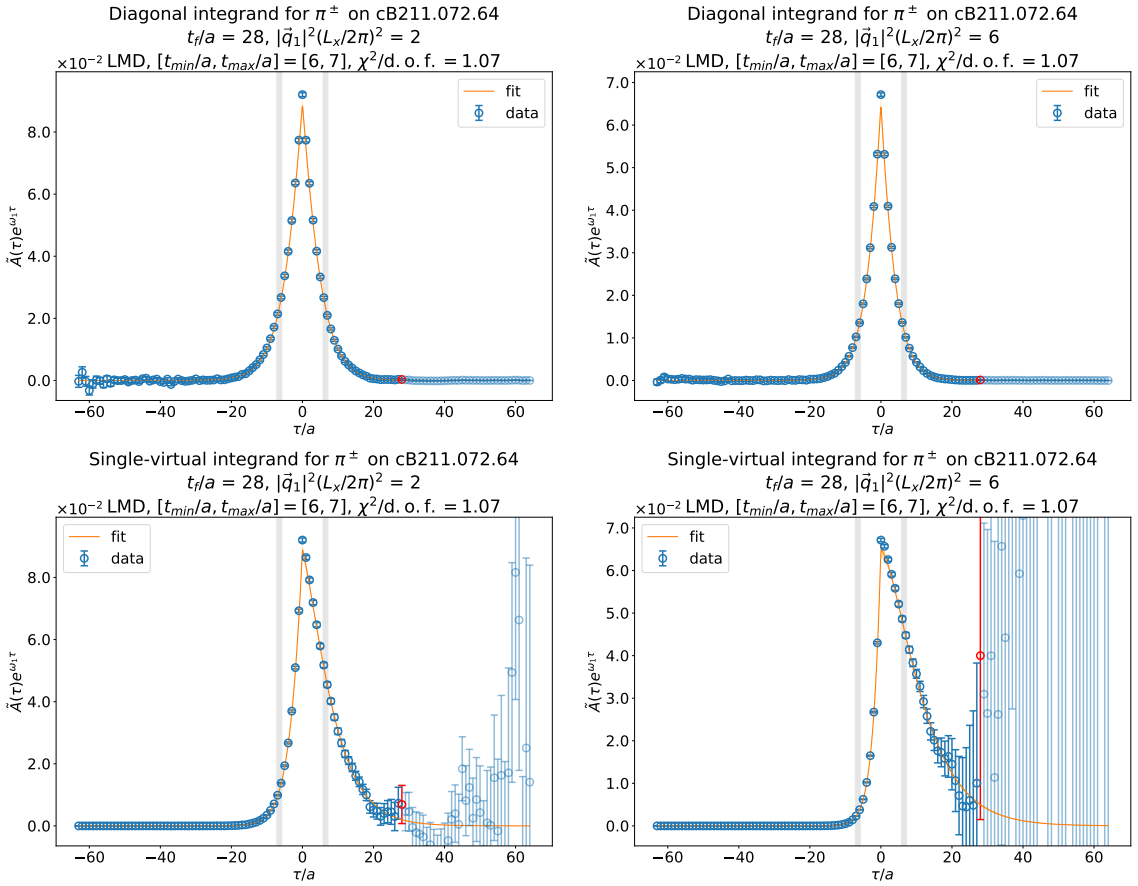

Figure 3.15: Charged pion integrands $\tilde{A}(\tau)e^{\omega_1\tau}$ on cB211.072.64, diagonal kinematics $q_1^2 = q_2^2$ (top row) and single-virtual kinematics $q_2^2 = 0$ (bottom row). Shown is the integrand from lattice data in blue and from a correlated LMD fit to $\tilde{A}(\tau)$ in orange. The fit was done across all momentum orbits $(2\pi/L_x)^2 \leq |\vec{q}_1|^2 \leq 32(2\pi/L_x)^2$ with fit range $[-t_{max}, -t_{min}] \cup [t_{min}, t_{max}]$, indicated by the grey bands. The red point indicates the pseudoscalar timeslice t_f, the greyed out points to the right of it do not have the correct timeordering to approximate Eq. (3.37).
For the diagonal kinematics, $a\omega_1 = am_\pi/2 \approx 0.028$. For the single-virtual kinematics, $a\omega_1 = a|\vec{q}_1| \approx 0.14$ for $|\vec{q}_1|^2 = 2(2\pi/L_x)^2$ (left) and $a\omega_1 \approx 0.24$ for $|\vec{q}_1|^2 = 6(2\pi/L_x)^2$ (right).

The used symmetry follows from the q_1^2–q_2^2 exchange symmetry in the TFFs, equivalent to $\omega_1 \leftrightarrow m_P - \omega_1$. Defining

$$\tilde{A}(\tau) = \frac{2E_P}{Z_P} e^{m_P t_P} e^{-m_P \tau} C(\tau), \tag{3.160}$$

$$\tilde{A}'(\tau) = \frac{2E_P}{Z_P} e^{m_P t_P} C(-\tau), \tag{3.161}$$

and

$$\mathcal{F}_{P\to\gamma^*\gamma^*}(\omega_1) = \int d\tau\, e^{\omega_1 \tau} \tilde{A}(\tau), \tag{3.162}$$

$$\mathcal{F}'_{P\to\gamma^*\gamma^*}(\omega_1) = \int d\tau\, e^{\omega_1 \tau} \tilde{A}'(\tau), \tag{3.163}$$

one finds

$$\begin{aligned}
\mathcal{F}_{P\to\gamma^*\gamma^*}(m_P - \omega_1) &= \int d\tau\, e^{(m_P-\omega_1)\tau} \tilde{A}(\tau) \\
&= \int d\tau\, e^{(\omega_1-m_P)\tau} \tilde{A}(-\tau) \\
&= \int d\tau\, e^{\omega_1 \tau} \tilde{A}'(\tau) \\
&= \mathcal{F}'_{P\to\gamma^*\gamma^*}(\omega_1).
\end{aligned} \tag{3.164}$$

In particular, this allows for time reversal in $\tilde{A}(\tau)$ not only by flipping $\tau \to -\tau$ but also by applying a factor of $e^{-m_P\tau}$ and implies that $\mathcal{F}_{P\to\gamma^*\gamma^*}(q_1^2, q_2^2)$ and $\mathcal{F}_{P\to\gamma^*\gamma^*}(q_2^2, q_1^2)$ differ by numerical fluctuations when using $\tilde{A}^{(\text{latt.})}(\tau)$.

3.8 Details on the employed ensembles, correlators and loops

An overview of the employed ensembles and their most important properties is given in Tab. 3.1, for an introduction to the used lattice setup see Sec. 2.2.
In the pion calculation, 8 or 16 point sources per configuration are used for the evaluation of the connected Wick contractions of the 3pt function, depending on the ensemble, for a total of $\mathcal{O}(10^3 - 10^4)$ inversions. The pseudoscalar 2pt functions

Ensemble	V/a^4	N_{conf}	β	$a\,[\text{fm}]$	$a\mu_l$	$M_\pi^{\text{2pt}}\,[\text{MeV}]$	$L\,[\text{fm}]$	$M_\pi L$
cB211.072.64	$64^3 \cdot 128$	748	1.778	0.07961(13)	0.00072	140.27(12)	5.09	3.62
cC211.060.80	$80^3 \cdot 160$	397	1.836	0.06821(12)	0.00060	136.88(12)	5.46	3.78
cD211.054.96	$96^3 \cdot 192$	495	1.900	0.05692(10)	0.00054	141.57(19)	5.46	3.90

Table 3.1: Parameters of the ETMC ensembles used in this work, adapted from [40]. Other paramters can be found in [40, 100, 103–105]. For the η-meson form factor calculation, $N_{\text{conf}} = 1539$ configurations of the cB211.072.64 ensemble were used, yielding $M_\eta^{\text{2pt}} = 550(20)\,\text{MeV}$. M_π^{2pt} and M_η^{2pt} are the pion and η-meson masses determined in this work from a two-state fit to the 2pt function, see Sec. 3.4.1 and 3.6.3.

are evaluated using either 8 point sources or 128 stochastic sources [126–128] per configuration. The current-pseudoscalar correlator in the V-disconnected contraction of the 3pt function is evaluated using 8 point sources per configuration. Finally, the evaluation of the current loop in the V-disconnected contraction uses differing numbers of stochastic sources. For the numerically most sizeable one, the light current loop, 128 stochastic sources per configuration are used, with usually 4 sources for the strange and 1 source for the charm current loops. Deflation of low-modes [129] and hierarchical probing [130] are used to improve the signal-to-noise ratio of the disconnected loops.

In the η-meson calculation, 16 point sources per configuration are used for the evaluation of the connected Wick contractions of the 3pt function, for a total of 24 624 inversions. The connected pseudoscalar 2pt function and the current-current correlator in the P-disconnected contraction to the 3pt function are evaluated using 200 point sources per configuration. Finally, the evaluation of the pseudoscalar loop in the P-disconnected contraction uses 128 stochastic sources per configuration.

Chapter 4

Publications

In this chapter, the publications written as part of this work are collected. Sec. 4.1 reproduces the proceedings of the 2021 lattice conference, published as [68]. It reports on the current status of the calculation of the pion-pole contribution to HLbL at this point in time. Sec. 4.2 reproduces the proceedings of the 2022 lattice conference, published as [69]. It contains an update on the pion-pole calculation, with the most notable differences to Sec. 4.1 being the inclusion of an additional ensemble as well as the inclusion of all possible disconnected Wick contractions. Further, it reports first preliminary results for the η-pole contribution to HLbL at a single lattice spacing. An extensive draft further updating the pion-pole calculation can be found in Ch. 5. Finally, Sec. 4.3 reproduces the preprint published on arXiv as [71], which was submitted to PRL in January 2023. Presented there are first results for the η-pole contribution to HLbL, the partial decay width $\Gamma(\eta \to \gamma\gamma)$ and the slope parameter b_η at a single lattice spacing.
Note that the introductory and methodology parts of these three sections are similar, since they are all part of the same project. The discussion in Sec. 4.2 is the most extensive without giving details on the partial decay width and slope parameter, which are discussed in Sec. 4.3.

4.1 Pion-pole contribution to HLbL from twisted mass lattice QCD at the physical point

This section reproduces [68] and was published as part of the proceedings of the 2021 lattice conference.

4.1.1 Abstract

We report on our computation of the pion transition form factor $\mathcal{F}_{\pi\to\gamma^*\gamma^*}$ from twisted mass lattice QCD in order to determine the numerically dominant light pseudoscalar pole contribution in the hadronic light-by-light scattering contribution to the anomalous magnetic moment of the muon $a_\mu = (g-2)_\mu$. The pion transition form factor is computed directly at the physical point. We present first results for our estimate of the pion-pole contribution with kinematic setup for the pion at rest.

4.1.2 Introduction

In this project we aim to compute the pseudoscalar transition form factors $\mathcal{F}_{P\to\gamma^*\gamma^*}$ from twisted mass lattice QCD for the three pseudoscalar states $P = \pi^0, \eta$ and η' in order to determine the corresponding pseudoscalar pole contributions in the hadronic light-by-light (HLbL) scattering contribution to the anomalous magnetic moment of the muon $a_\mu = (g-2)_\mu$. Our computation is done on two ensembles with the pion mass at its physical value. For our calculations we are using twisted-mass clover-improved lattice QCD at maximal twist, so that we have automatic $\mathcal{O}(a)$-improvement in place. The generation of the two ensembles was done in the context of the Extended Twisted Mass Collaboration (ETMC) where the $N_f = 2+1+1$ simulations include the two mass-degenerate light u- and d-quark flavours at their physical quark-mass values and the heavier s- and c-quark flavours at quark masses close to their physical values. At the moment, the analysis is done on two physical point ensembles at two different lattice spacings as decribed in Table 4.1. For further details on the simulations we refer to Refs. [104, 115].

ensemble	$L^3 \cdot T/a^4$	m_π [MeV]	a [fm]	L [fm]	$m_\pi \cdot L$
cB072.64	$64^3 \cdot 128$	136.8(6)	0.082	5.22	3.6
cC060.80	$80^3 \cdot 160$	134.2(5)	0.069	5.55	3.8

Table 4.1: Description of ensembles used for the analysis presented in these proceedings.

The assumption of hadronic light-by-light scattering being dominated by single pseudoscalar meson exchange can be used to calculate the correspondingly leading pseudoscalar pole contributions $a_\mu^{P\text{-pole}}$ to the muon anomly at next-to-leading order (NLO), cf. Figure 4.1. The pole contributions are given by a three-dimensional integral derived in Ref. [50]. It takes the form

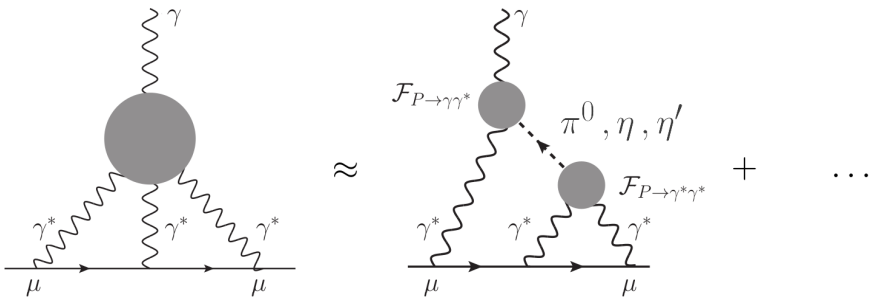

Figure 4.1: Pseudoscalar pole contribution to hadronic light-by-light scattering in the muon $(g-2)_\mu$. Adapted from Ref. [66].

$$a_\mu^{P\text{-pole}} = \left(\frac{\alpha}{\pi}\right)^3 \int_0^\infty dQ_1 \int_0^\infty dQ_2 \int_{-1}^{+1} d\tilde{\tau} \Big[w_1(Q_1,Q_2,\tilde{\tau}) \mathcal{F}_{P\to\gamma^*\gamma^*}(-Q_1^2,-(Q_1+Q_2)^2) \mathcal{F}_{P\to\gamma^*\gamma^*}(-Q_2^2,0) + w_2(Q_1,Q_2,\tilde{\tau}) \mathcal{F}_{P\to\gamma^*\gamma^*}(-Q_1^2,-Q_2^2) \mathcal{F}_{P\to\gamma^*\gamma^*}(-(Q_1+Q_2)^2,0) \Big], \tag{4.1}$$

where the nonperturbative information is encapsulated in the transition form factors $\mathcal{F}_{P\to\gamma^*\gamma^*}$ of the pseudoscalar mesons $P = \pi^0, \eta, \eta'$ to two virtual photons. The evaluation of the integrands in Eq. (4.1) requires the knowledge of the transition form factors (TFFs) at space-like momenta, both in the single and double virtual case. It turns out that these TFFs can indeed be obtained from a QCD calculation on a Euclidean lattice. The relevant kinematic region is determined by the positive weight

functions w_1 and w_2 which depend on the absolute values of the photon momenta, the kinematic variable $\tilde{\tau} = \cos\theta \in [-1, +1]$, with θ being the angle between the photon momenta, and the mass of the pseudoscalar meson P. In these proceedings we focus on the pion-pole contribution for which first lattice results were obtained in [66, 67].

4.1.3 The transition form factors on the lattice

In the continuum Minkowski space the TFFs are defined via the matrix element of two electromagnetic currents j_μ and j_ν and the pseudoscalar state P with four-momentum p,

$$\begin{aligned} M_{\mu\nu}(p, q_1) &= i \int d^4x \, e^{iq_1 x} \langle 0 \left| T\{j_\mu(x) j_\nu(0)\} \right| P(p) \rangle \\ &= \varepsilon_{\mu\nu\alpha\beta} q_1^\alpha q_2^\beta \mathcal{F}_{P\to\gamma^*\gamma^*}(q_1^2, q_2^2) \, . \end{aligned}$$

For virtualities below the threshold for hadron production, the transition form factors can be analytically continued to Euclidean space, cf. Ref. [66], and are therefore accessible on the lattice. The Euclidean matrix element $M^E_{\mu\nu}(p, q_1)$ can be calculated via an integral over the temporal separation $\tau = t_i - t_f$ of the two currents,

$$M^E_{\mu\nu} = \int_{-\infty}^{\infty} d\tau \, e^{\omega_1 \tau} \tilde{A}_{\mu\nu}(\tau), \quad i^{n_0} M^E_{\mu\nu}(p, q_1) = M_{\mu\nu}(p, q_1). \tag{4.2}$$

Here, n_0 denotes the number of temporal indices in $M_{\mu\nu}$, q_1 and q_2 are the photon virtualities, $p = q_1 + q_2$ is the on-shell pseudoscalar momentum, ω_1 is a real-valued free parameter with $q_1 = (\omega_1, \vec{q}_1)$, and

$$\tilde{A}_{\mu\nu}(\tau) = \langle 0 \left| T\{j_\mu(\vec{q}_1, \tau) j_\nu(\vec{p} - \vec{q}_1, 0)\} \right| P(p) \rangle \ .$$

On the lattice this function is recovered from the three-point function

$$C_{\mu\nu}(\tau, t_P) = a^6 \sum_{\vec{x}, \vec{z}} \langle j_\mu(\vec{x}, t_i) j_\nu(\vec{0}, t_f) P^\dagger(\vec{z}, t_0) e^{i\vec{p}\vec{z}} \rangle e^{-i\vec{x}\vec{q}_1} \equiv \langle j_\mu j_\nu P^\dagger \rangle \, , \tag{4.3}$$

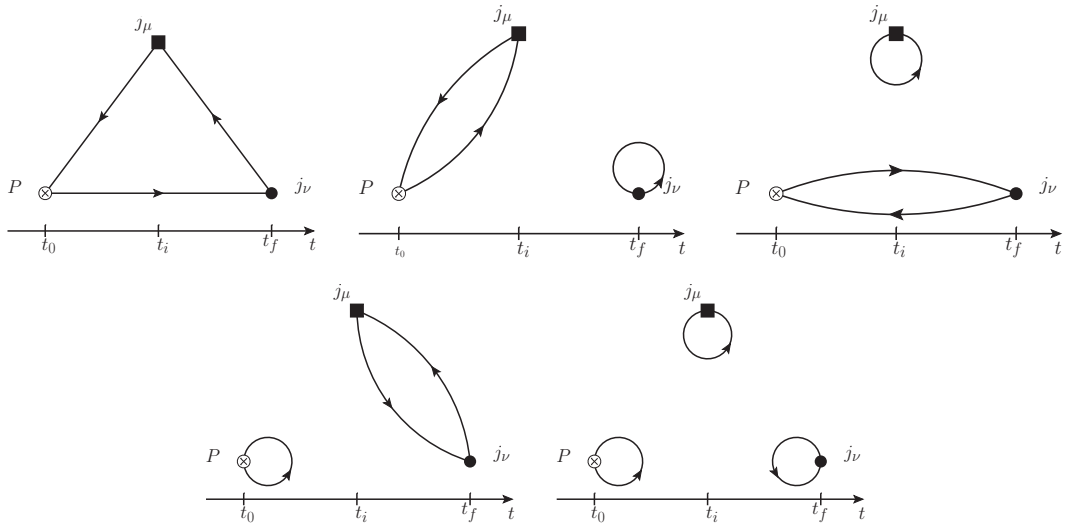

Figure 4.2: Contributions to the three-point function $C_{\mu\nu}$: Connected (top left), vector current disconnected (top middle and right), pseudoscalar disconnected (bottom left) and fully disconnected (bottom right).

via

$$\tilde{A}_{\mu\nu}(\tau) = \frac{2E_P}{Z_P} \lim_{t_P \to \infty} e^{E_P(t_f - t_0)} C_{\mu\nu}(\tau, t_P)\,, \tag{4.4}$$

where $t_P = \min(t_f - t_0, t_i - t_0)$ is the minimal temporal separation between the pseudoscalar and the two vector currents. The pseudoscalar meson energy E_P and the factors Z_P are determined through appropriate pseudoscalar two-point functions. Before integrating over τ, one can contract the Lorentz structure of the matrix elements. The function $\tilde{A}_{\mu\nu}$ with one or more temporal indices vanishes for the pseudocalar at rest, and the spatial components can be written as $\tilde{A}(\tau) = im_P^{-1}\varepsilon_{ijk}\frac{\vec{q}_1^{\,i}}{\vec{q}_1^{\,2}}\tilde{A}_{jk}(\tau)$, and analogously for $C(\tau)$.

The amplitude $C_{\mu\nu}$ contains connected, vector current disconnected, pseudoscalar disconnected, and fully disconnected diagrams as illustrated in Figure 4.2. For Wilson fermions the pseudoscalar disconnected diagrams on the second line are zero for $P = \pi_0$ by the exact cancellation between the up and down quark loops. For $P = \eta$ and η' this is not the case and these disconnected diagrams must be included. This is so also for $P = \pi_0$ in the twisted mass Wilson fermion discretization, where the diagrams on the second line are nonzero due to the broken isospin symmetry. Since this isospin breaking is a lattice artefact, we consider an isospin rotation

$\pi^0 \to -i \cdot (\pi^+ + \pi^-)$ with a corresponding transformation of the isospin decomposed light quark electromagnetic currents $j_\mu^{0,0} \to j_\mu^{0,0}$ and $j_\mu^{1,0} \to i \cdot (j_\mu^{1,+} - j_\mu^{1,-})$, which allows us to relate the neutral and charged pion form factors. The difference between the two at finite lattice spacing is a lattice artefact of order $O(a^2)$.

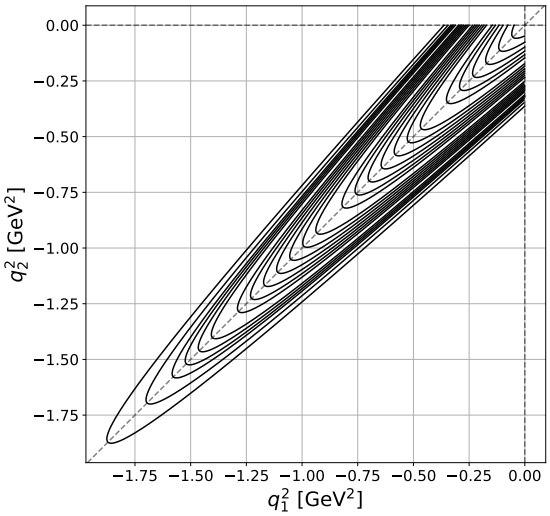

Figure 4.3: Range of photon virtualities spanned in our calculation on the ensemble cB072.64.

A further simplification is achieved by restricting the considerations to the kinematic situation where the pseudoscalar is at rest, i.e., $\vec{p} = \vec{0}$. Then, the expressions for the photon virtualities simplify to

$$q_1^2 = \omega_1^2 - \vec{q}_1^{\,2}\,, \quad q_2^2 = (m_P - \omega_1)^2 - \vec{q}_1^{\,2}\,. \tag{4.5}$$

As a consequence, for each choice of spatial momentum $\vec{q}_1$ one obtains a continuous set of combinations of q_1 and q_2 which form an orbit in the (q_1^2, q_2^2)-plane as illustrated in Figure 4.3 for m_P set to the physical pion mass. There we show the orbits for all the momenta calculated on the ensemble cB072.64. From Eqs. (4.5) it becomes clear that the shape of the orbits becomes squeezed along the diagonal as the pseudoscalar mass m_P is lowered. This feature makes it particularly challenging to extract single virtual pion transition form factors $\mathcal{F}_{\pi\to\gamma^*\gamma^*}(q_1^2, 0) = \mathcal{F}_{\pi\to\gamma^*\gamma^*}(0, q_2^2)$ at large momenta q_i^2 on physical point ensembles if one uses only pions at rest. However, the problem can be circumvented by using moving frames, cf. [67]. For $P = \eta$ and η' the problem is less eminent due to the larger values of the meson masses m_P.

4.1.4 First results at the physical point

After this theoretical discussion we are now in the position to present first results for the transition form factor $\mathcal{F}_{\pi\to\gamma^*\gamma^*}$ of the pion obtained for the ensembles cB072.64 and cC060.80 at the physical point. First, we illustrate the quality of our data with sample results for the amplitude $\tilde{A}(\tau)$ defined in Eq. (4.4). In Figure 4.4 we show the full amplitude and separately the fully connected and the vector current disconnected contributions for two of the momentum orbits on the ensemble cB072.64. The vector current disconnected amplitude is multiplied by a factor -50 in order to facilitate comparison with the connected contribution and the full amplitude. The

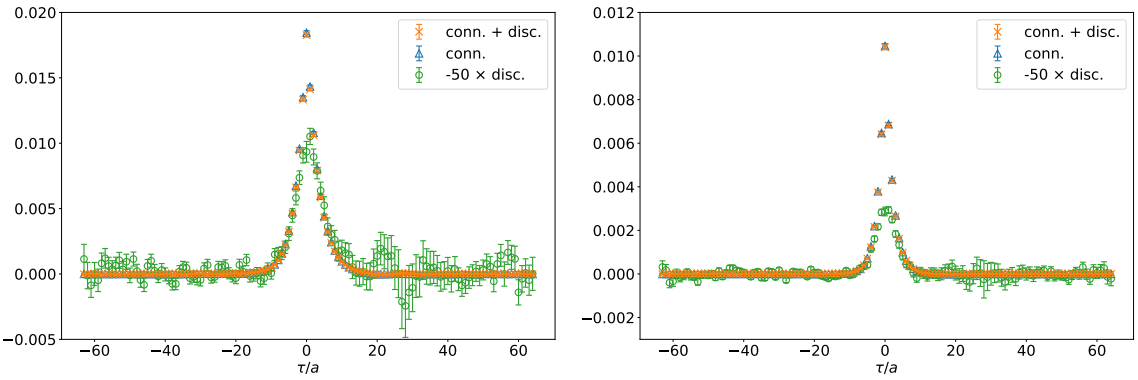

Figure 4.4: Amplitude $\tilde{A}(\tau)$ for momentum orbit $|\vec{q}^2|= 10\,(2\pi/L)^2$ (left) and $|\vec{q}^2|= 29\,(2\pi/L)^2$ on cB072.64. Shown in orange is the full contribution to $\tilde{A}(\tau)$, in blue the connected contribution and in green the vector current disconnected contribution multiplied by -50.

examples illustrate that the disconnected contribution is very small, but significant. More generally, we find that in the peak region it is suppressed w.r.t. the connected contribution by a factor between 50 and 200 depending on the orbit. We also conclude from our data that the statistical error on the disconnected contribution is sufficiently well under control on the physical point ensembles.

To obtain the form factor we need to integrate $\tilde{A}(\tau)$ weighted by the factor $\exp(\omega_1\tau)$ over the whole temporal axis, cf. Eq. 4.2. In order to control the statistical error in the exponentially enhanced tail and to be able to integrate up to $\tau\to\infty$, we proceed as follows. First, we fit the lattice data by a model function $\tilde{A}^{(\mathrm{fit})}(\tau)$ in a range $\tau_{\min}\leq|\tau|\leq\tau_{\max}$, and then we replace the lattice data $\tilde{A}^{(\mathrm{latt.})}(\tau)$ by the data

from the fit for $\tau > \tau_{\text{cut}}$,

$$\mathcal{F}_{\pi\to\gamma^*\gamma^*}(q_1^2, q_2^2) = \int_{-\infty}^{\tau_{\text{cut}}} d\tau\, \tilde{A}^{(\text{latt.})}(\tau) e^{\omega_1 \tau} + \int_{\tau_{\text{cut}}}^{\infty} d\tau\, \tilde{A}^{(\text{fit})}(\tau) e^{\omega_1 \tau}. \tag{4.6}$$

Following Ref. [66] we use both a vector meson dominance (VMD) model and the lowest meson dominance (LMD) model to estimate the model dependence. We perform global fully correlated fits, i.e., we simultaneously fit all momentum orbits in the range $\tau_{\text{min}} \leq |\tau| \leq \tau_{\text{max}}$ and take into account the correlation between all fitted data. In Figure 4.5 we illustrate the procedure by showing the result for the

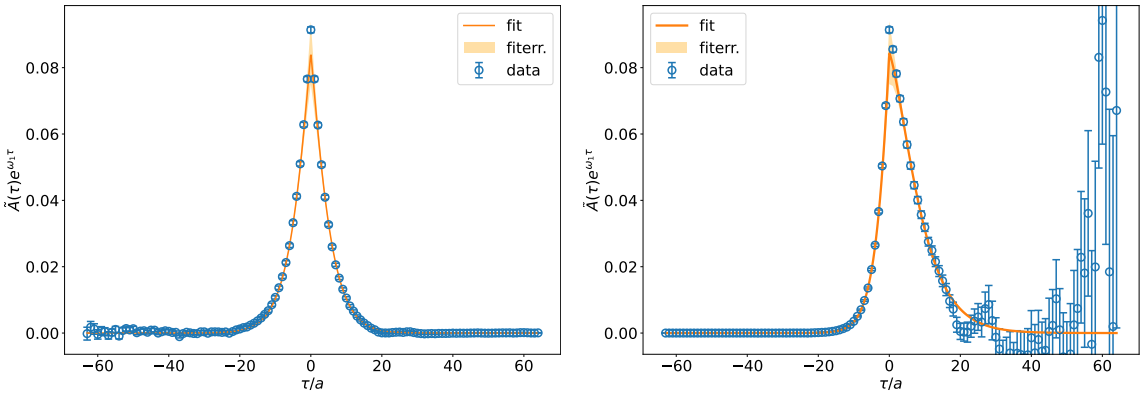

Figure 4.5: Integrand $\tilde{A}(\tau)e^{\omega_1\tau}$ on cB072.64 with LMD model fits for momentum orbit $|\vec{q}^2| = 2\,(2\pi/L)^2$. Diagonal kinematics with $a\omega_1 = am_\pi/2 \approx 0.0284$ (left), single virtual kinematics with $a\omega_1 = a|\vec{q}_1| \approx 0.1388$ (right).

integrand $\tilde{A}(\tau)e^{\omega_1\tau}$ of a typical global fit to $\tilde{A}(\tau)$ in the range $9 \leq |\tau/a| \leq 12$ with $\chi^2/\text{dof} = 1.20$ on the ensemble cB072.64 using the LMD model. The plot on the left shows the resulting integrand for the diagonal kinematics $q_1^2 = q_2^2$, while the plot on the right shows it for the single virtual kinematics with $q_1^2 = 0$. The transition form factors obtained from the integration over the lattice data and the fitted data depend of course on the choice of the model, the fit range and the value τ_{cut}. The variations resulting from these choices are carried through all further analysis steps and are included in the systematic error estimate of the final result for a_μ. The typical values of τ_{cut} we use in our analysis result in a data content of well above 98% for most of the TFFs. However, for TFFs with (close to) single virtual kinematics, the data content is sometimes also less for higher momentum orbits. Here, the data content is defined as the fraction of the TFF coming from the first term in Eq. (4.6).

Once the form factors are obtained in the whole kinematic region as described by the yield plot in Figure 4.3, we parameterize them using a modified z-expansion of the form

$$P(Q_1^2, Q_2^2) \cdot \mathcal{F}_{\pi\gamma^*\gamma^*}(-Q_1^2, -Q_2^2) = \sum_{m,n=0}^{N} c_{nm} \left(z_1^n - (-1)^{N+n+1} \frac{n}{N+1} z_1^{N+1} \right) \left(z_2^m - (-1)^{N+m+1} \frac{m}{N+1} z_2^{N+1} \right) \quad (4.7)$$

where $z_k = z(Q_k^2)$ are modified four-momenta and $P(Q_1^2, Q_2^2)$ is a polynomial, see Ref. [67] and references therein for further details. We determine the coefficients c_{nm} by fitting Eq. (4.7) to samples of $\mathcal{F}_{\pi\to\gamma^*\gamma^*}(-Q_1^2, -Q_2^2)$ in the (Q_1^2, Q_2^2)-plane. The sample points are given by a set of fixed values of Q_2^2/Q_1^2 on all momentum orbits, and we ensure that all included data points pass a certain threshold for the data content. In Figure 4.6 we show the result of such a (fully correlated) fit with $\chi^2/\text{dof} = 0.96$ using $Q_2^2/Q_1^2 = 1.0, 0.59, 0.0$, and $N = 2$ to the TFFs obtained from a global LMD fit with $\{\tau_{\min}/a, \tau_{\max}/a\} = \{9, 12\}$, $\chi^2/\text{dof} = 1.20$, $\tau_{\text{cut}}/a = 20$ and a threshold of 90% on the ensemble cB072.64. As a crosscheck for the quality of

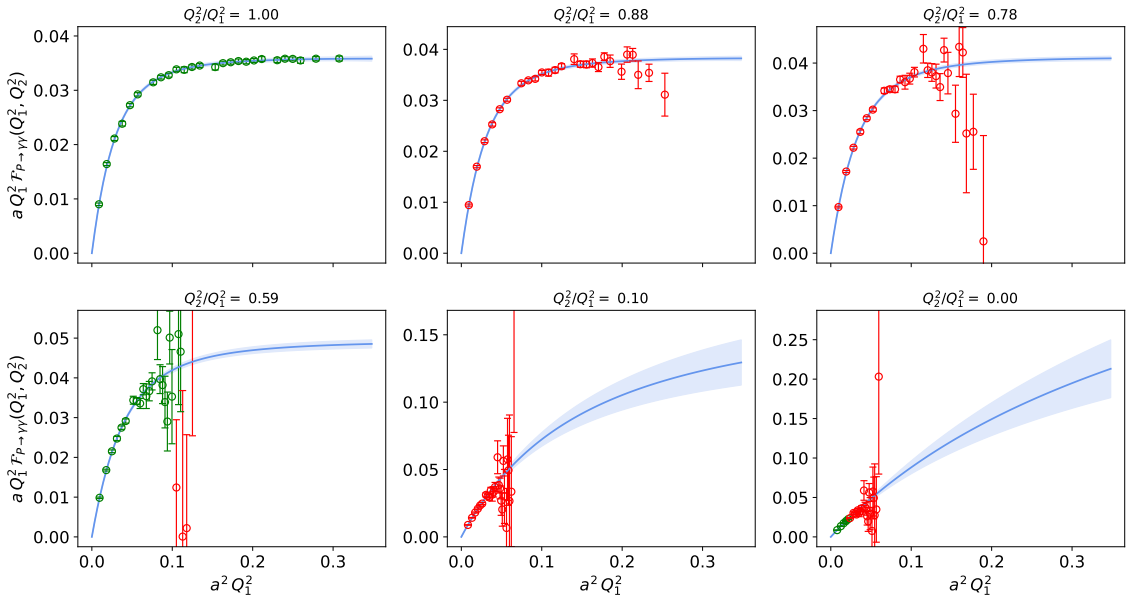

Figure 4.6: Illustration of transition form factors and their parameterization using the fitted modified z-expansion. Only the data coloured in green is included in the fit.

the fit we also show the data for three other ratios $Q_2^2/Q_1^2 = 0.88$, 0.78, and 0.10

not included in the fit together with the fitted modified z-expansion. The variations resulting from varying the sampling of $\mathcal{F}_{\pi\to\gamma^*\gamma^*}(-Q_1^2, -Q_2^2)$ in the momentum plane are also included in the systematic error estimate of the final result for a_μ.

Finally, having the parameterization of the TFFs at hand, we can use it in the three-dimensional integral representation in Eq. (4.1) and calculate the bare pion-pole contribution $a_\mu^{\pi\text{-pole, bare}}$ to the anomalous magnetic moment. In Figure 4.7 we show the results for $a_\mu^{\pi\text{-pole, bare}}$ on the two ensembles at the physical point as a function of τ_{cut}/a. Each data point is a weighted average of $O(100)$ results from different fits for $\tilde{A}$ using VMD or LMD with different fit ranges and different fits using the modified z-expansion on different samplings in the momentum plane. The weighted average is obtained using weights inspired by the Akaike information criterion (AIC). The error therefore includes the variation w.r.t. the fitting of $\tilde{A}$ and the sampling of $\mathcal{F}_{\pi\to\gamma^*\gamma^*}$ in the (Q_1^2, Q_2^2)-plane. The variation of the final result with τ_{cut} indicates a residual

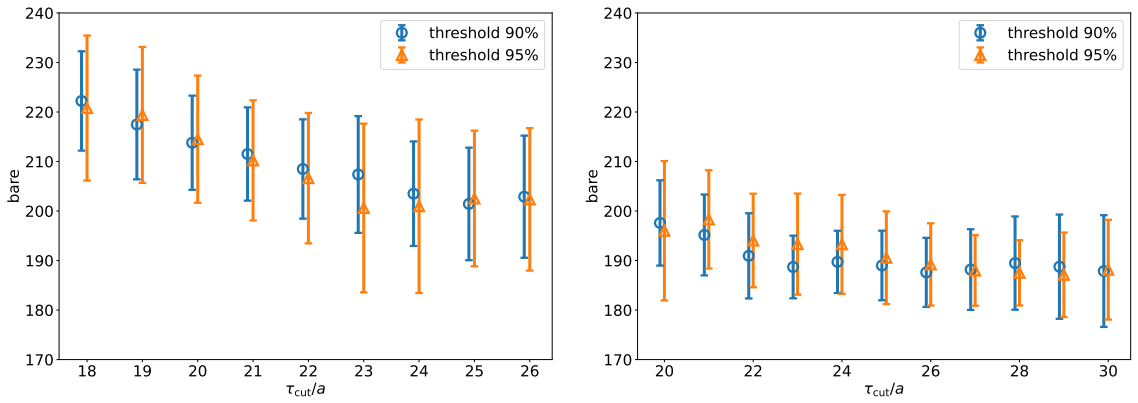

Figure 4.7: AIC averaged data for a range of τ_{cut}/a for the ensembles cB072.64 (left) and cC060.80 (right).

dependence on the specific procedure of variance reduction in the large-τ tail of $\tilde{A}$. In principle, this dependence is removed in the limit $\tau_{\text{cut}} \to \infty$, but if τ_{cut} is chosen too large the z-expansion fits become unstable and hence the final result unreliable. Our results in Figure 4.7 indicate that choosing $\tau_{\text{cut}} \in [1.8, 2.1]$ fm seems a safe choice and we perform a further AIC averaging over this range. This yields the bare results shown in Table 4.2 for the two physical point ensembles, with total errors in the 5%-8% range. Since we use local iso-vector and iso-vector axial current operators in our amplitude $C_{\mu\nu}$, instead of conserved (point-split) current operators, we need to renormalize the bare results by the corresponding renormalization constants.

$a_\mu^{\pi-\text{pole, bare}} \cdot 10^{-11}$	threshold 90%	threshold 95%
cB072.64	208.9(10.1)(7.8)[12.8]	204.5(14.2)(6.3)[15.6]
cC060.80	188.9(9.9)(2.7)[10.2]	187.9(9.0)(1.9)[9.2]

Table 4.2: Bare results using the AIC procedure on the two physical point ensembles. The first error is the statistical error, the second the systematic error and the third the total error.

Preliminary values are available for our setup from a calculation within ETMC.

4.1.5 Conclusion and outlook

After applying the renormalization factors and performing a rough estimate of the continuum limit, we obtain a preliminary value $a_\mu^{\pi-\text{pole}} = 53.7(2.6)(3.1)[4.0] \cdot 10^{-11}$. This can be compared to the recent lattice result $a_\mu^{\pi-\text{pole}} = 59.7(3.6) \cdot 10^{-11}$ from Ref. [67] and the dispersive result $a_\mu^{\pi-\text{pole}} = 63.0^{+2.7}_{-2.1} \cdot 10^{-11}$ from Refs. [3, 63, 64], and we find agreement within 1 to 2 standard deviations. Finalizing the analysis might result in a slightly different central value, however, we expect that the relative total error will stay below the 10% level. We plan to analyze a third physical point ensemble at a finer lattice spacing which will result in a more robust continuum limit extrapolation. We also plan to calculate the form factors for the pion in a moving frame and to perform the analysis of the η- and η'-pole contributions, and to include ensembles with larger pion masses.

4.2 Pseudoscalar-pole contributions to the muon $g-2$ at the physical point

This section reproduces [69] and was published as part of the proceedings of the 2022 lattice conference.

4.2.1 Abstract

Pseudoscalar-pole diagrams are an important component of estimates of the hadronic light-by-light (HLbL) contribution to the muon $g-2$. We report on our computation of the transition form factors $\mathcal{F}_{P\to\gamma^*\gamma^*}$ for the neutral pseudoscalar mesons $P=\pi^0$ and η. The calculation is performed using twisted-mass lattice QCD with physical quark masses. On the lattice, we have access to a broad range of (space-like) photon four-momenta and therefore produce form factor data complementary to the experimentally accessible single-virtual direction, which directly leads to an estimate of the pion- and η-pole components of the muon $g-2$. For the pion, our result for the $g-2$ contribution in the continuum is comparable with previous lattice and data-driven determinations, with combined relative uncertainties below 10%. For the η meson, we report on a preliminary determination from a single lattice spacing.

4.2.2 Introduction

Here we report on the progress of the calculation originally presented in Ref. [68]. We aim to compute the pseudoscalar transition form factors $\mathcal{F}_{P\to\gamma^*\gamma^*}$ from twisted-mass lattice QCD for the three pseudoscalar states $P=\pi^0,\eta$ and η' in order to determine the corresponding pseudoscalar-pole contributions to the hadronic light-by-light (HLbL) scattering in the anomalous magnetic moment of the muon, $a_\mu=(g_\mu-2)/2$. Presented here are the recent developments of our calculation for the states $P=\pi^0$ and η. We employ twisted-mass lattice QCD at maximal twist, so that we profit from automatic $\mathcal{O}(a)$ improvement of observables [78, 79]. The pion-pole calculation is performed using three $N_f=2+1+1$ ensembles with varying lattice spacings,

while the preliminary η-pole calculation uses the ensemble at the coarsest lattice spacing only. The production of these ensembles by the Extended Twisted Mass Collaboration (ETMC) is described in Refs. [100, 104, 115]. The quark masses for all three ensembles are tuned such that the charged-pion mass is fixed to its physical value and the s- and c-quark masses approximate their physical values. A summary of the properties of the three ensembles is presented in Table 4.3.

Under the assumption of pole dominance, the leading contributions to the hadronic light-by-light scattering come from exchanges of a neutral pseudoscalar meson $P \in \{\pi^0, \eta, \eta'\}$. The corresponding contributions to the muon anomalous magnetic moment, $a_\mu^{P\text{-pole}}$, are given by the diagrams shown in Figure 4.8. The nonperturbative information is encapsulated in the transition form factors $\mathcal{F}_{P\to\gamma^*\gamma^*}$ of the pseudoscalar meson P to two virtual photons. The pole contributions are given by a

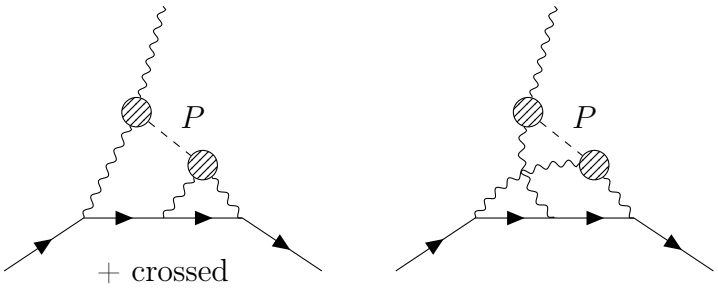

Figure 4.8: The pseudoscalar-pole diagrams contributing to the leading order HLbL scattering in the muon anomalous magnetic moment. Striped circles indicate the nonperturbative $P \to \gamma^*\gamma^*$ transition form factors required to evaluate these contributions.

ensemble	$L^3 \cdot T/a^4$	m_π [MeV]	a [fm]	L [fm]	$m_\pi \cdot L$	Z_V	Z_A
cB072.64	$64^3 \cdot 128$	140.2(2)	0.07961(13)	5.09	3.62	0.706378(16)	0.74284(23)
cC060.80	$80^3 \cdot 160$	136.7(2)	0.06821(12)	5.46	3.78	0.725405(13)	0.75841(16)
cD054.96	$96^3 \cdot 192$	140.8(2)	0.05692(10)	5.46	3.90	0.744105(11)	0.77394(10)

Table 4.3: Description of ETMC ensembles used for the analysis presented in these proceedings, including the lattice geometry, pion mass m_π, lattice spacing a, lattice size L, and the renormalization constants Z_V and Z_A for the vector and axial currents [40, 100, 104, 115].

three-dimensional integral derived in Ref. [50],

$$a_\mu^{P\text{-pole}} = \left(\frac{\alpha}{\pi}\right)^3 \int_0^\infty dQ_1 \int_0^\infty dQ_2 \int_{-1}^1 d\tilde{\tau} \Big[w_1(Q_1, Q_2, \tilde{\tau}) \mathcal{F}_{P\to\gamma^*\gamma^*}(-Q_1^2, -Q_3^2) \mathcal{F}_{P\to\gamma^*\gamma}(-Q_2^2, 0) + w_2(Q_1, Q_2, \tilde{\tau}) \mathcal{F}_{P\to\gamma^*\gamma^*}(-Q_1^2, -Q_2^2) \mathcal{F}_{P\to\gamma^*\gamma}(-Q_3^2, 0) \Big], \quad (4.8)$$

where $Q_3^2 = Q_1^2 + Q_2^2 + 2\tilde{\tau} Q_1 Q_2$ and the weight functions w_1 and w_2 are analytically known functions of the kinematics and muon and pseudoscalar masses. Each term in the integrand in Eq. (4.8) involves two transition form factors (TFFs) at space-like momenta, one at single-virtual kinematics and the other at double-virtual kinematics. First lattice results for the pion-pole contribution were obtained in Refs. [66,67], while for the η-pole contribution preliminary results have so far only been presented using a lattice spacing of $a = 0.1315\,\text{fm}$ and lattice size $L = 4.21\,\text{fm}$ [70]. The pion analysis first presented in Ref. [68] and extended in these proceedings complements prior work by working directly at the physical point and using a different discretization. For the η meson we provide a result at the physical point with a single lattice spacing of $a = 0.0796\,\text{fm}$ with lattice size $L = 5.09\,\text{fm}$; an extension of this result has also now been reported in Ref. [71].

4.2.3 The transition form factors on the lattice

Following Refs. [66,68], the transition form factor in continuum Minkowski space-time is defined via the matrix element of two electromagnetic currents j_μ and j_ν between the vacuum and the pseudoscalar state P,

$$\begin{aligned} M_{\mu\nu}(p, q_1) &= i \int d^4x\, e^{iq_1 x} \langle 0 \,|T\{j_\mu(x) j_\nu(0)\}|\, P(p)\rangle \\ &= \varepsilon_{\mu\nu\alpha\beta} q_1^\alpha q_2^\beta \mathcal{F}_{P\to\gamma^*\gamma^*}(q_1^2, q_2^2)\,. \end{aligned} \quad (4.9)$$

Here $T\{\cdot\}$ indicates time-ordering, p is the pseudoscalar four-momentum, q_1 is the four-momentum of j_μ, and the four-momentum $q_2 = p - q_1$ of j_ν is enforced by momentum conservation. For photon virtualities below the threshold for hadron

production, the transition form factor can be analytically continued to Euclidean space [66] and is thus accessible on the lattice. In Euclidean space-time, the matrix element can be recovered via

$$M_{\mu\nu}(p, q_1) = i^{n_0} M^E_{\mu\nu}(p, q_1), \quad M^E_{\mu\nu} = -\int_{-\infty}^{\infty} d\tau\, e^{\omega_1 \tau} \tilde{A}_{\mu\nu}(\tau), \tag{4.10}$$

where n_0 denotes the number of temporal indices in $M_{\mu\nu}$, ω_1 is the temporal component of the momentum $q_1 = (\omega_1, \vec{q}_1)$, and $\tilde{A}_{\mu\nu}$ is the Euclidean matrix element

$$\tilde{A}_{\mu\nu}(\tau) \equiv \int d^3\vec{x} e^{-i\vec{q}_1 \cdot \vec{x}} \langle 0|T\{j_\mu(\tau, \vec{x}) j_\nu(0)\}|P(\vec{p})\rangle\,. \tag{4.11}$$

On the lattice this function is accessed from the three-point function

$$C_{\mu\nu}(\tau, t_P) \equiv \int d^3\vec{x}\, d^3\vec{y}\, e^{-i\vec{q}_1 \cdot \vec{x}} e^{i\vec{p} \cdot \vec{y}} \langle 0|T\{j_\mu(\tau, \vec{x}) j_\nu(0) \mathcal{O}^\dagger_P(-t_P, \vec{y})\}|0\rangle \tag{4.12}$$

via

$$\tilde{A}_{\mu\nu}(\tau) = \lim_{t_P \to \infty} \frac{2E_P}{Z_P} e^{E_P t_P} C_{\mu\nu}(\tau, t_P), \tag{4.13}$$

where t_P is the pseudoscalar insertion time and $Z_P = \langle 0|\mathcal{O}_P(\vec{0}, 0)|P(p)\rangle$. In this work, the pseudoscalar meson energy E_P and overlap factor Z_P are determined through a separate analysis of two-point functions of the operator $\mathcal{O}_P$.

For the pion, we use the creation operator $\mathcal{O}^\dagger_{\pi^0} = i\bar{\psi}\lambda_3\gamma_5\psi$, while for the η meson, we use the creation operator $\mathcal{O}^\dagger_\eta = i\bar{\psi}\lambda_8\gamma_5\psi$, where $\lambda_3 = \mathrm{diag}(1, -1, 0)$ and $\lambda_8 = \mathrm{diag}(1, 1, -2)/\sqrt{3}$ are Gell-Mann matrices describing the SU(3) flavor structure. The creation operator $\mathcal{O}^\dagger_\eta$ has overlap with the physical η-meson state, meaning the correct η-meson amplitude is projected at large time separations between the operator and currents, independent of η-η' meson mixing. The electromagnetic currents are defined for this $N_f = 2 + 1 + 1$ calculation as

$$j_\mu = \frac{2}{3}\bar{\psi}_u\,\gamma_\mu\,\psi_u - \frac{1}{3}\bar{\psi}_d\,\gamma_\mu\,\psi_d - \frac{1}{3}\bar{\psi}_s\,\gamma_\mu\,\psi_s + \frac{2}{3}\bar{\psi}_c\,\gamma_\mu\,\psi_c. \tag{4.14}$$

The component of the electromagnetic current involving the light quarks can be

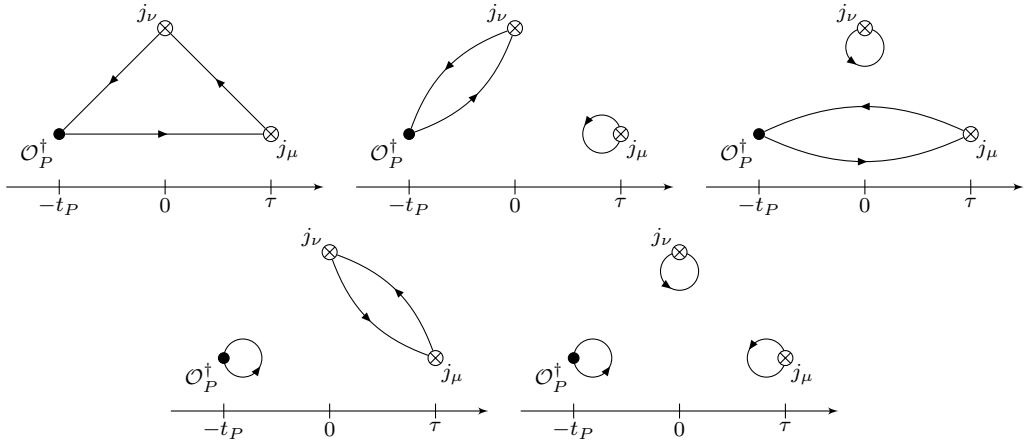

Figure 4.9: Wick contractions contributing to $C_{\mu\nu}(\tau, t_P)$. Connected (top left), vector-current disconnected ("V-disconnected", top middle and right), pseudoscalar disconnected ("P-disconnected", bottom left) and fully disconnected (bottom right). The second connected diagram with quark propagators running in the opposite direction is omitted for brevity.

decomposed into terms with definite isospin, i.e.,

$$\begin{aligned} j_\mu^l \equiv \bar{\psi}_l \, \gamma_\mu \tilde{Q} \, \psi_l &= \frac{1}{6} j_\mu^{0,0} + \frac{1}{2} j_\mu^{1,0}, \\ j_\mu^{0,0} &\equiv \bar{\psi}_l \, \gamma_\mu \, \mathbb{1} \, \psi_l \\ j_\mu^{1,0} &\equiv \bar{\psi}_l \, \gamma_\mu \, \sigma_3 \, \psi_l, \end{aligned} \tag{4.15}$$

where $\psi_l = (\psi_u \quad \psi_d)$ indicates the light-quark doublet and $\tilde{Q} = \mathrm{diag}(+2/3, -1/3)$ is the relevant charge matrix. The current $j_\mu^{0,0}$ has isospin $I = 0$ and $j_\mu^{1,0}$ has isospin $I = 0$, $I_z = 0$. This decomposition allows us to consider only the corresponding isospin preserving parts of the amplitude. These currents also need to be further renormalized by Z_V, due to the use of local currents instead of conserved (point-split) currents in the calculation. The renormalization factors for the ensembles used here have been precisely determined in Ref. [40], as detailed in Table 4.3.

The evaluation of the three-point function $C_{\mu\nu}$ involves connected, vector-current disconnected, pseudoscalar disconnected, and fully disconnected Wick contractions, as illustrated from top left to bottom right in Figure 4.9. In the case of the π^0, the amplitude can be related in the isospin-symmetric limit to a charged-pion amplitude

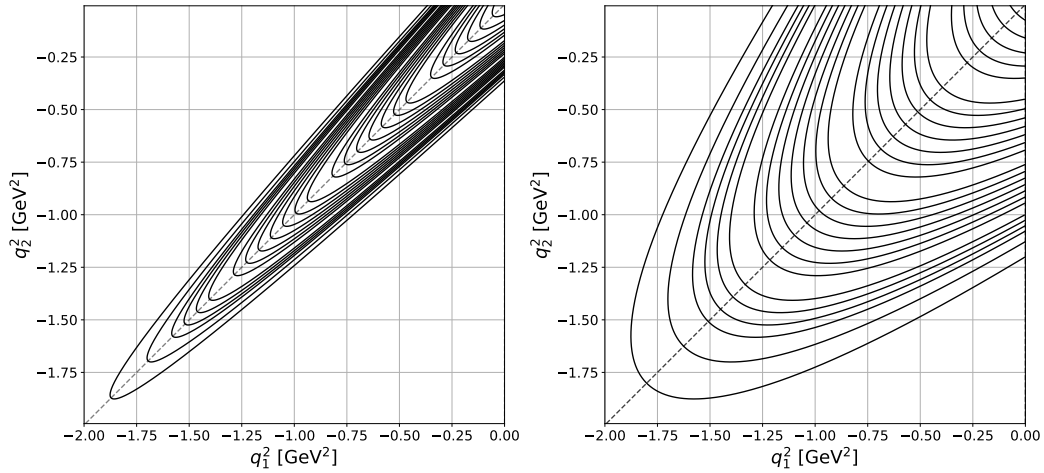

Figure 4.10: Range of photon virtualities for the pion (left) and η meson (right) TFFs spanned in our calculation on the ensemble cB072.64.

by the isospin rotation

$$\begin{aligned} \pi^0 &\to -i \cdot (\pi^+ + \pi^-)\,, \\ j_\mu^{0,0} &\to j_\mu^{0,0}\,, \\ j_\mu^{1,0} &\to i \cdot (j_\mu^{1,+} - j_\mu^{1,-})\,, \end{aligned} \tag{4.16}$$

where $j_\mu^{1,\pm} = \bar{\psi}_l \, \gamma_\mu \, \sigma_\pm \, \psi_l$ with $\sigma_\pm = (\sigma_1 \pm i\sigma_2)/2$. Note that the currents $j_\mu^{1,\pm}$, when working in the twisted basis, need to be renormalized with Z_A rather than Z_V. The values of these renormalization constants are given in Table 4.3. The isospin rotation simplifies the evaluation of the three-point function by removing the pseudoscalar-disconnected diagram and is thus employed in our analysis of the pion TFF. Although isospin symmetry is broken by $O(a^2)$ lattice artifacts in the twisted-mass Wilson fermion discretization, the effect of this rotation is removed in the continuum extrapolation. In the case of the η- and η'-meson states, pseudoscalar-disconnected diagrams do not cancel even in the isospin symmetric limit and indeed play an important role in capturing the physics of these states.

To evaluate the connected diagram, we choose to perform a sequential inversion through the pseudoscalar operator. This makes it computationally convenient to project to various choices of momenta $\vec{q}_1$ for the j_μ current at the cost of having to restrict to only a few momenta $\vec{p}$ for the pseudoscalar meson. The calculation presented here is restricted to pseudoscalar mesons at rest, i.e., $\vec{p} = \vec{0}$. In this

kinematic setup, the expressions for the photon virtualities simplify to

$$q_1^2 = \omega_1^2 - \vec{q}_1^{\,2}\,, \quad q_2^2 = (m_P - \omega_1)^2 - \vec{q}_1^{\,2}\,. \tag{4.17}$$

Thus each choice of spatial momentum $\vec{q}_1$ corresponds to a continuous set of combinations of q_1 and q_2 which form an orbit in the (q_1^2, q_2^2)-plane. The resulting reach in the kinematics of both the pion and η-meson TFFs on the cB072.64 ensemble is shown in Figure 4.10. The narrowness of the orbits available for the pion TFF is due to the relatively small mass of the pion. This illustrates the challenge in extracting single-virtual pion transition form factors $\mathcal{F}_{\pi\to\gamma^*\gamma}(q^2,0) = \mathcal{F}_{\pi\to\gamma\gamma^*}(0,q^2)$ at significantly negative virtualities q^2 on physical point ensembles if one uses only pions at rest. In future extensions of the analysis presented here, it would thus be useful to extend the single-virtual coverage by using moving frames [67]. For the η meson, due to the higher mass, the problem is less eminent.

The rest frame also simplifies the procedure in Eq. (4.9) of extracting the Lorentz-scalar TFF from the components of the transition amplitude. In particular, one finds in the rest frame that $\tilde{A}_{\mu\nu}$, and therefore $M_{\mu\nu}$, vanishes when one or more of the indices are temporal. Meanwhile, the spatial components can be averaged to yield the Lorentz scalar $\tilde{A}(\tau) = im_P^{-1}\varepsilon_{ijk}(\vec{q}_1^{\,i}/|\vec{q}_1|^2)\tilde{A}_{jk}(\tau)$, which is the appropriate combination to yield the TFF after integration,

$$\mathcal{F}_{P\to\gamma^*\gamma^*}(q_1^2, q_2^2)|_{\vec{p}=0} = \int_{-\infty}^{\infty} d\tau e^{\omega_1\tau}\tilde{A}(\tau). \tag{4.18}$$

For the pion, examples for the averaged amplitude $\tilde{A}(\tau)$ are shown in Figure 4.11, illustrating the full amplitude and separately the connected and the vector-current disconnected contributions with disconnected light-, strange- and charm-current loops for two orbits on the ensemble cB072.64. The vector-current disconnected contributions are multiplied by a factor of 50 to make the comparison to the connected contribution and full amplitude easier. While the disconnected contributions are very small, we still are able to extract significant signals across all momentum orbits for the V-disconnected light and strange contributions. The charm contributions are also determined to sufficient precision to constrain their contribution to the amplitude. We find on all three ensembles that the total V-disconnected contribution in the

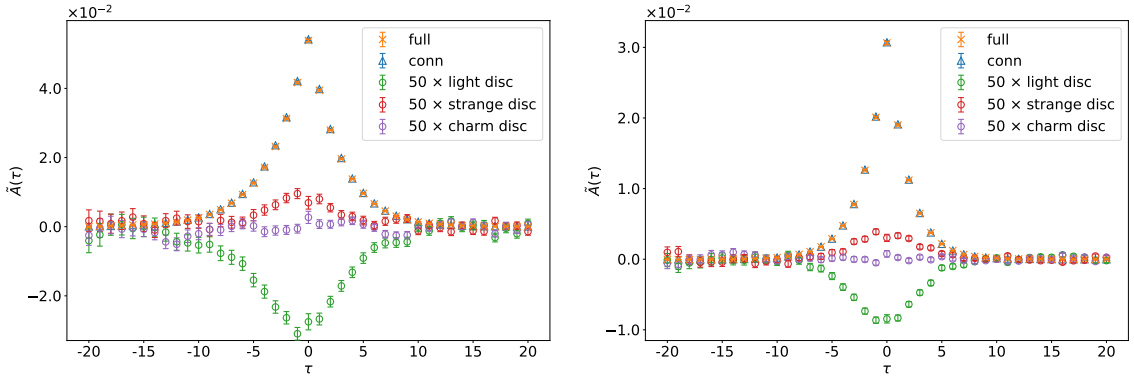

Figure 4.11: Amplitude $\tilde{A}(\tau)$ for the pion for momentum orbit $|\vec{q}^2| = 10\,(2\pi/L)^2$ (left) and $|\vec{q}^2| = 29\,(2\pi/L)^2$ on cB072.64. Shown in orange is the full contribution to $\tilde{A}(\tau)$, in blue the connected contribution and in green, red and purple the V-disconnected contributions multiplied by 50.

peak region is suppressed with respect to the connected contribution by a factor of at least ~ 50. We also find that the statistical error on the V-disconnected contribution is well under control on all three physical point ensembles.

Sample results for the η-meson amplitude $\tilde{A}(\tau)$ as defined in Eq. (4.13) are displayed in Figure 4.12 where we show the full amplitude and separately the different contributions to it considered in our analysis for two orbits on the ensemble cB072.64. The examples show that the contributions involving strange quarks in the currents are suppressed at least by a factor of ~ 10 compared to the corresponding light contributions. Based on the results in the pion case, we expect the contributions involving charm quarks to be more suppressed still. This contribution along with the vector-current disconnected and fully disconnected diagrams are therefore irrelevant at the presently achievable precision, and we do not include them in the further η-meson analysis.

As shown in Eq. (4.18), the transition form factors $\mathcal{F}_{P\to\gamma^*\gamma^*}$ are obtained by integrating $e^{\omega_1\tau}\tilde{A}(\tau)$ over the whole temporal axis. For choices of ω_1 that result in kinematics near the single-virtual axes (cf. Figure 4.10), the exponential factor $e^{\omega_1\tau}$ enhances the contribution from one of the tails exponentially. Meanwhile, the signal-to-noise ratio deteriorates exponentially at large $|\tau|$, presenting a significant obstacle to the extraction of the TFFs in the single-virtual regime. Further, the lattice data for times $\tau < -t_P$ have incorrect time ordering of the operators and do not yield a valid

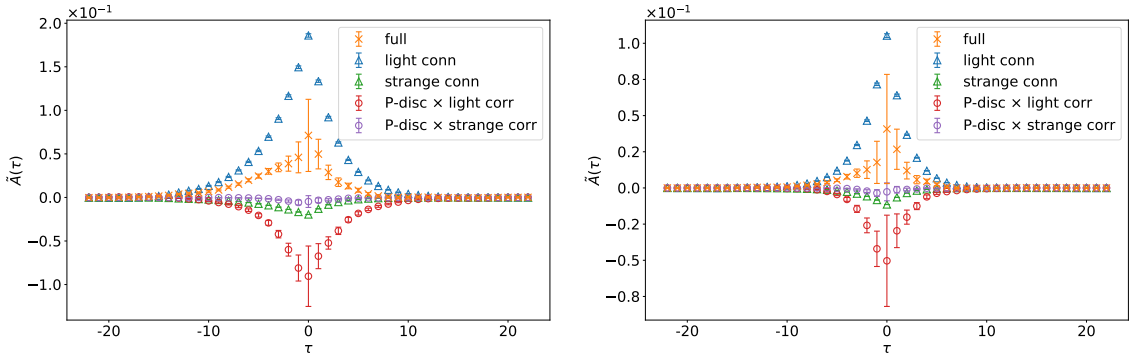

Figure 4.12: Amplitude $\tilde{A}(\tau)$ for the η meson for momentum orbit $|\vec{q}^2|= 10\,(2\pi/L)^2$ (left) and $|\vec{q}^2|= 29\,(2\pi/L)^2$ on cB072.64. Shown is the full value of $\tilde{A}(\tau)$, as well as the decomposition into the light and strange connected contributions and the light and strange P-disconnected contributions.

approximation to $\tilde{A}_{\mu\nu}(\tau)$ in Eq. (4.11).

To address both of these issues, we extend $\tilde{A}(\tau)$ by fitting the lattice data with a model function $\tilde{A}^{(\text{fit})}(\tau)$ in a range $\tau_{\text{min}} \leq |\tau| < \tau_{\text{max}}$, and replacing the lattice data $\tilde{A}^{(\text{latt.})}(\tau)$ by the fit for $|\tau| > \tau_{\text{cut}}$. The integration in Eq. (4.18) is then replaced by

$$\begin{aligned}\mathcal{F}_{P\to\gamma^*\gamma^*}(q_1^2, q_2^2) = &\int_{-\tau_{\text{cut}}}^{\tau_{\text{cut}}} d\tau\, \tilde{A}^{(\text{latt.})}(\tau) e^{\omega_1 \tau} \\ &+ \int_{\tau_{\text{cut}}}^{\infty} d\tau\, \tilde{A}^{(\text{fit})}(\tau) e^{\omega_1 \tau} + \int_{-\infty}^{-\tau_{\text{cut}}} d\tau\, \tilde{A}^{(\text{fit})}(\tau) e^{\omega_1 \tau}. \end{aligned} \tag{4.19}$$

Note that in principle τ_{cut} can be chosen independently in the two tails in order to keep as much of the original lattice data as possible. For the pion, the contributions to $\mathcal{F}_{\pi\to\gamma^*\gamma^*}$ from $\tilde{A}^{\pi,\,(\text{fit})}(\tau)$ are below 2% for most photon virtualities, with the exception of some large virtualities at or close to single-virtual kinematics. In the case of the η meson, the creation operator insertion happens at Euclidean times t_η much closer to zero, as compared to the pion, to control the rapidly deteriorating signal-to-noise ratio for the P-disconnected contribution with increasing t_η and τ. This requires smaller values of τ_{cut} to satisfy correct time-ordering of the amplitude, resulting in larger contributions from $\tilde{A}^{\eta,\,(\text{fit})}(\tau)$ to $\mathcal{F}_{\eta\to\gamma^*\gamma^*}$ despite the much faster exponential decay of the heavier η-meson.

Following the approach of Ref. [66], we consider both the vector-meson dominance

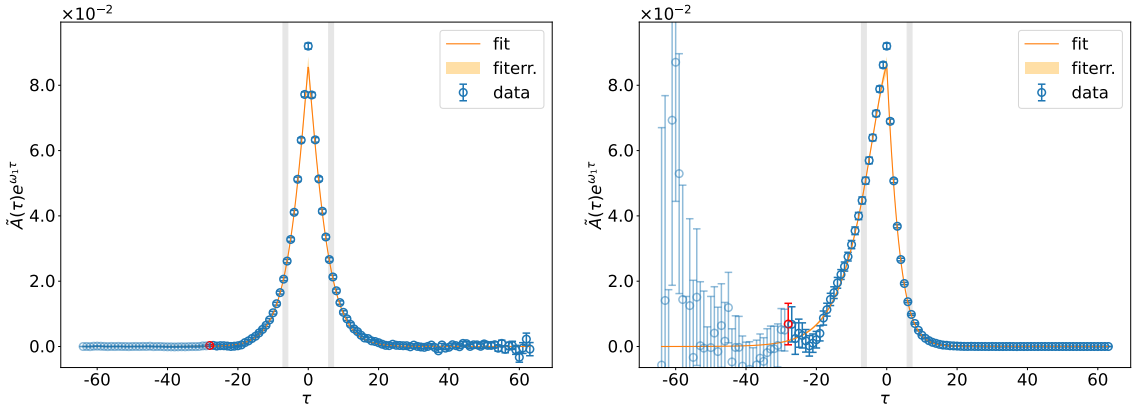

Figure 4.13: Lattice data vs. the LMD model fit of the integrand $\tilde{A}(\tau)e^{\omega_1\tau}$ for the pion on the cB072.64 ensemble with the momentum of the current $|\vec{q}_1^{\,2}| = 2\,(2\pi/L)^2$. The left plot shows the integrand for diagonal kinematics ($q_1^2 = q_2^2$) determined by fixing $a\omega_1 = am_\pi/2 \approx 0.0283$, while the right plot shows the integrand for single-virtual kinematics ($q_2^2 = 0$) determined by fixing $a\omega_1 = a|\vec{q}_1| \approx 0.1388$. The grey bands show the data included in the fit from this choice of $\vec{q}_1$; note, however, that data within these windows are taken across all choices of $\vec{q}_1$ for the fit. The point in red indicates the timeslice where the pseudoscalar creation operator is inserted, with the lighter points to the left of this insertion having incorrect time ordering, as discussed in the main text.

(VMD) model and the lowest-meson dominance (LMD) model to fit the amplitude. The variation between the two then gives an estimate of the model dependence of the results. For the pion we perform global fully correlated fits, i.e., we simultaneously fit all momentum orbits in the range $\tau_{\text{min}} \leq |\tau| < \tau_{\text{max}}$ and take into account the correlations between all fitted data, while for the η meson we consider both global uncorrelated and fully correlated fits. An example of this is shown in Figure 4.13 where we plot the integrand $\tilde{A}(\tau)e^{\omega_1\tau}$ resulting from a fully correlated global fit to $\tilde{A}(\tau)$ using the LMD model in the range $6 \leq |\tau/a| < 8$ with $\chi^2/\text{dof} = 1.08$ for the pion on the ensemble cB072.64. The fit quality and reduced χ^2 are representative of the remaining fits performed for other analysis choices. Shown are the integrands for diagonal kinematics $q_1^2 = q_2^2$ on the left and single-virtual kinematics $q_1^2 = 0$ on the right. Note that the so-obtained values of the TFFs depend on the choice of the model, the fit range and the value of τ_{cut}. These various choices are all independently carried through the further analysis steps and are finally used to estimate the systematic error of $a_\mu^{P\text{-pole}}$.

4.2.4 Results for $a_\mu^{P-\text{pole}}$ at the physical point

To extend the form factors to arbitrary photon momenta for the integration in Eq. (4.8), we parameterize them using a model-independent expansion of the form [67]

$$P(Q_1^2, Q_2^2) \cdot \mathcal{F}_{P\gamma^*\gamma^*}(-Q_1^2, -Q_2^2) \approx \sum_{m,n=0}^{N} c_{nm} \left(z_1^n - (-1)^{N+n+1} \frac{n}{N+1} z_1^{N+1} \right) \left(z_2^m - (-1)^{N+m+1} \frac{m}{N+1} z_2^{N+1} \right), \quad (4.20)$$

termed the "modified z-expansion." Above, $P(Q_1^2, Q_2^2) = 1 + (Q_1^2 + Q_2^2)/M_\rho^2$ preconditions the form of the expansion to more easily reproduce the form factor structure, the coefficients $c_{nm} = c_{mn}$ are required to be symmetric by the Bose symmetry of the TFF, and the z_k are conformal transformations of the four-momenta in the quadrant below the non-analytic cuts at $t_c = 4m_\pi^2$, as given by

$$z_k = \frac{\sqrt{t_c + Q_k^2} - \sqrt{t_c - t_0}}{\sqrt{t_c + Q_k^2} + \sqrt{t_c - t_0}}. \quad (4.21)$$

The parameter t_0 is chosen to be

$$t_0 = t_c \left(1 - \sqrt{1 + Q_{\text{max}}^2 / t_c} \right) \quad (4.22)$$

in order to best reproduce the behavior of the TFF for $Q_{1,2}^2 \lesssim Q_{\text{max}}^2$ [67], with $Q_{\text{max}}^2 = 4.0\,\text{GeV}^2$ chosen for the present study. Analyticity of the TFF below t_c ensures that the z-expansion can fully describe the TFF as $N \to \infty$. To fix the coefficients c_{nm} in the expansion, a fit is performed to the lattice data available at the orbits determined by our choices of three-momenta $\vec{q}_1$ (cf. Figure 4.10). Because the orbits are in principle continuously determined by the free choice of ω_1, we follow Refs. [66, 67] and fix a finite set of inputs $\mathcal{F}_{P\to\gamma^*\gamma^*}(-Q_1^2, -Q_2^2)$ by restricting to kinematics satisfying $Q_2^2/Q_1^2 = \text{const.}$ for several choices of this ratio. We further restrict the inputs in the pion case by removing points for which the model contribution to $\mathcal{F}_{\pi\to\gamma^*\gamma^*}$ from $\tilde{A}^{(\text{fit})}(\tau)$ exceeds a given threshold, thereby minimizing the impact of the choice of fit model at this stage of the analysis. In the following analysis, both a threshold of 5% and 10% are considered. We use the smaller choice of 5% for the final continuum-extrapolated result.

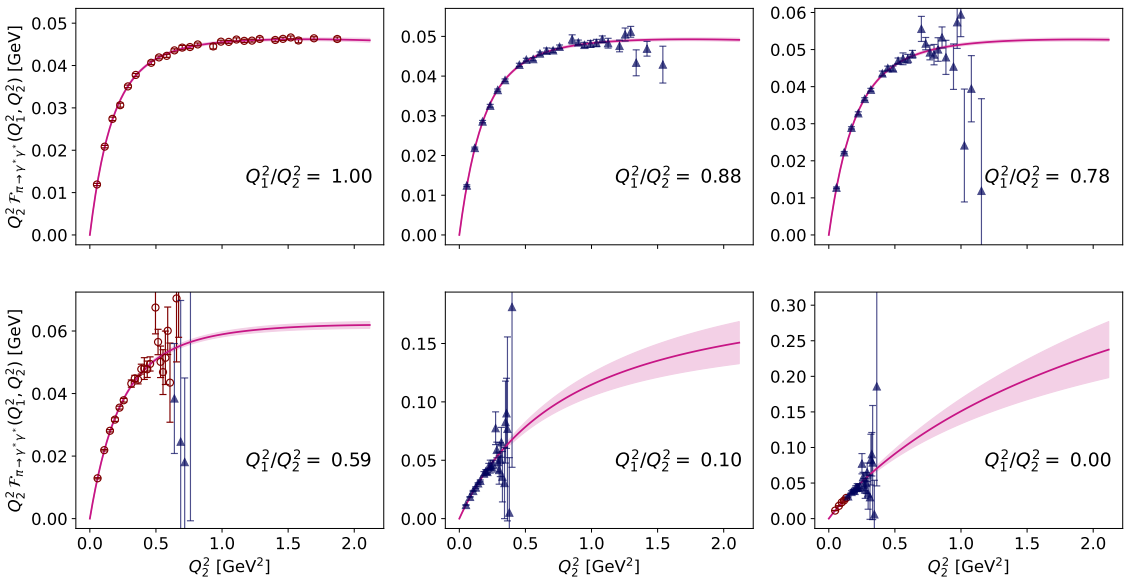

Figure 4.14: Illustration of the pion transition form factor $\mathcal{F}_{\pi\to\gamma^*\gamma^*}$ and its parameterization using the fitted modified z-expansion. Only the data coloured in maroon is included in the fit.

4.2.4.1 Pion

Figure 4.14 shows the example of an $N = 2$ z-expansion fit using TFF data satisfying $Q_2^2/Q_1^2 \in \{1.0, 0.59, 0.0\}$ on the ensemble cB072.64, where the transition form factors are obtained from a global LMD fit with $\{\tau_{\text{min}}/a, \tau_{\text{max}}/a\} = \{9, 12\}$ and integration using $\tau_{\text{cut}}/a = 20$. Here we use a maximal upper limit of a 10% contribution to $\mathcal{F}_{\pi\to\gamma^*\gamma^*}$ from $\tilde{A}^{(\text{fit})}(\tau)$ as a further cut on the input data for the fit. The points marked with maroon in the figure indicate the final data used in the fit, with other points, including the data for the ratios $Q_2^2/Q_1^2 \in \{0.88, 0.78, 0.10\}$, serving as a crosscheck for the quality of the fit. Both the fit to $\tilde{A}(\tau)$ and the fit to the modified z-expansion are fully correlated, with respective $\chi^2_{z-\text{exp}}/\text{dof} = 1.03$ and $\chi^2_{\text{LMD}}/\text{dof} = 1.03$. It is worth noting that the z-expansion fit is most strongly constrained by the precise data available for the ratio $Q_2^2/Q_1^2 = 1.0$. This precision is due to a small dependence on the tails of the integrand $\tilde{A}(\tau)\exp(\omega_1\tau)$ for these kinematics (cf. Figure 4.13).

After extrapolating $\mathcal{F}_{\pi\to\gamma^*\gamma^*}(-Q_1^2, -Q_2^2)$ to arbitrary space-like momenta using the results of the modified z-expansion fits in Eq. (4.20), the three-dimensional integral representation given in Eq. (4.8) can be evaluated to calculate $a_\mu^{\pi\text{-pole}}$. We do so

	cB072.64	cC060.80	cD054.96
$a_\mu^{\pi\text{-pole}} \cdot 10^{11}$	56.8(2.7)(0.3)[2.7]	56.5(2.1)(0.5)[2.2]	54.0(2.1)(0.3)[2.2]

Table 4.4: Preliminary results for estimates of $a_\mu^{\pi\text{-pole}}$ on the three ensembles used in this analysis. The uncertainties shown are statisical, systematic and total, respectively.

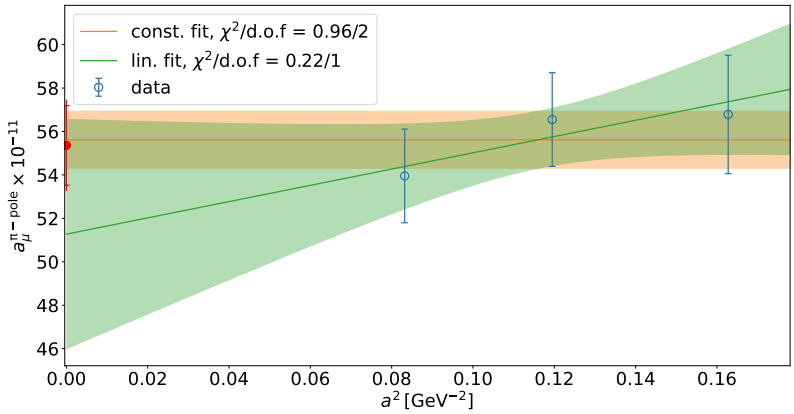

Figure 4.15: Preliminary continuum limit of $a_\mu^{\pi\text{-pole}}$ based on both constant and $\mathcal{O}(a^2)$ extrapolations. The extrapolations are averaged using the procedure from [115], as discussed in the main text, yielding the continuum estimate $a_\mu^{\pi\text{-pole}} = 55.4(1.9)_{\text{fit}}(1.0)_{\text{ctm}-\text{syst.}}[2.1]_{\text{tot}}$ indicated by the red marker at $a^2 = 0$.

for $\mathcal{O}(1000)$ combinations of the choices of fit range and fit model in the $\tilde{A}(\tau)$ fit, the choice of τ_{cut}, and the choices of samplings of $\mathcal{F}_{\pi\to\gamma^*\gamma^*}$ in the (Q_1^2, Q_2^2)-plane as inputs to the modified z-expansion fit. For the pion, the fully correlated z-expansion fits with $N = 2$ give the best reduced χ^2 values, so we restrict to this choice alone. Further, for the pion we consider choices of τ_{cut} satisfying $\tau_{\text{cut}} \in [1.3, 1.6]\,\text{fm}$ in physical units across all three ensembles. We then use a modified version of the Akaike information criterion (AIC) to perform a weighted average across the analysis choices; see Ref. [38] and references therein. Using this procedure we obtain separate estimates of the statistical errors and systematic errors associated with analysis choices described above. The preliminary values for $a_\mu^{\pi\text{-pole}}$ obtained per ensemble are presented in Table 4.4.

Data from these three physical-point ensembles allows a continuum extrapolation to be performed for the value of $a_\mu^{\pi\text{-pole}}$. In the twisted-mass discretization, the leading lattice artifacts are expected to be of $\mathcal{O}(a^2)$. For the continuum limit of $a_\mu^{\pi\text{-pole}}$

we therefore consider both extrapolation with a simple constant fit versus lattice spacing and a linear fit in a^2. As shown in Figure 4.15, both fits are consistent with the lattice data. To determine a preliminary estimate of the continuum value at the present statistics and set of ensembles, we apply the averaging procedure presented in Ref. [115] (see Eqs. (38)–(43) therein) to combine the constant and linear fits. The resulting estimate of the continuum limit is found to be

$$a_\mu^{\pi\text{-pole}} = 55.4(1.9)_{\text{fit}}(1.0)_{\text{ctm}-\text{syst.}}[2.1]_{\text{tot}}, \tag{4.23}$$

where the uncertainties are respectively the average uncertainty from the $\tilde{A}$ and z-expansion fits, the additional systematic uncertainty from variation between the constant and linear continuum extrapolations, and the total uncertainty combined in quadrature.

4.2.4.2 Eta

As in the case of the pion, for the η meson we apply a z-expansion fit to extrapolate TFF results to arbitrary kinematics. Figure 4.16 shows the example of an $N = 2$ z-expansion fit on the ensemble cB072.64 using TFF data satisfying $Q_2^2/Q_1^2 \in \{1.0, 0.88, 0.78, 0.59, 0.1, 0.0\}$, where the transition form factors are obtained from a global VMD fit with $\{\tau_{\text{min}}/a, \tau_{\text{max}}/a\} = \{4, 7\}$ and integration using $\tau_{\text{cut}}/a = 8$. The fit to $\tilde{A}(\tau)$ is performed with correlation taken into account, yielding $\chi^2_{\text{VMD}}/\text{dof} = 0.25$, while the fit to the modified z-expansion is uncorrelated with $\chi^2_{z-\text{exp}}/\text{dof} = 1.03$. Since $m_\eta \gg m_\pi$, in the case of the η meson even the diagonal kinematics include significant contributions from the tails of the integrand $e^{\omega_1 \tau}\tilde{A}(\tau)$ and thus have significant statistical uncertainties. In the single-virtual case, we can compare our results for $\mathcal{F}_{\eta\to\gamma\gamma^*}$, both the data points directly as well as the z-expansion fit, to experimental data from CLEO, CELLO and BaBar, cf. [72–75]. An illustration is shown in Figure 4.17 for the same parameters as in Figure 4.16. We already find relatively good agreement with the experimental data despite working at a single lattice spacing.

Using the results of the modified z-expansion fits to extend the TFF $\mathcal{F}_{\eta\to\gamma^*\gamma^*}(-Q_1^2, -Q_2^2)$ to arbitrary space-like momenta allows us to evaluate

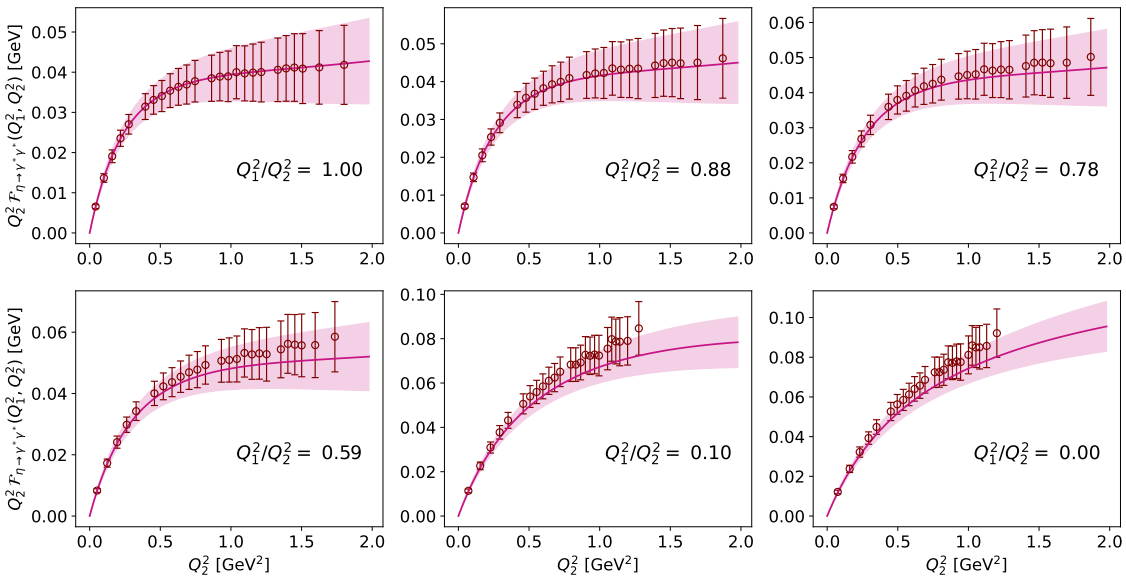

Figure 4.16: Illustration of the η-meson transition form factor $\mathcal{F}_{\eta\to\gamma^*\gamma^*}$ and its parameterization using the fitted modified z-expansion. All data shown is included in the fit.

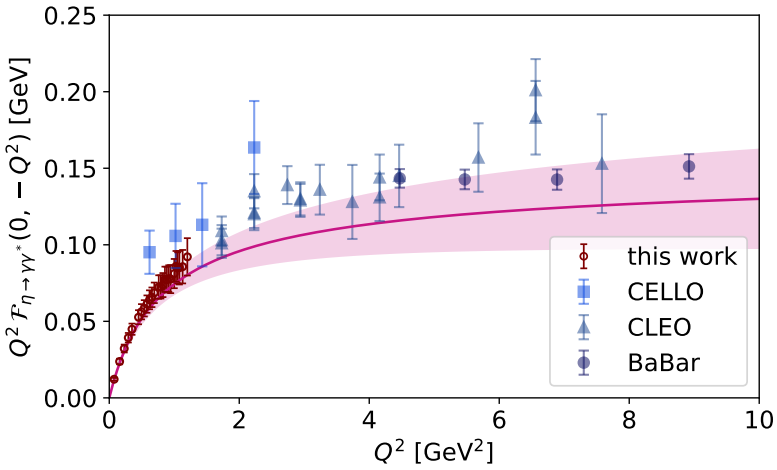

Figure 4.17: Results for the single-virtual η-meson transition form factor $\mathcal{F}_{\eta\to\gamma\gamma^*}$ evaluated using an example set of analysis choices, as described in the main text, versus experimental measurements described in Refs. [72–75]. The red band indicates the result of the z-expansion fit to the lattice data shown in red points. As the lattice data and fit are shown for a single choice of analysis parameters, the uncertainties are purely statistical. A full analysis of the form factor itself has now been presented in Ref. [71].

the three-dimensional integral representation given in Eq. (4.8) to calculate $a_\mu^{\eta\text{-pole}}$, as in the pion case. This is evaluated for each of the $\mathcal{O}(1000)$ combinations of choices of fit range and fit model in the $\tilde{A}(\tau)$ fit, the choice of τ_{cut}, the choices of samplings of $\mathcal{F}_{\eta\to\gamma^*\gamma^*}$ in the (Q_1^2, Q_2^2)-plane as inputs to the modified z-expansion, and the choice of $N \in \{1, 2\}$ for the z-expansion. Further, for the η meson we include all choices of τ_{cut} satisfying $\tau_{\text{cut}} \in [0.16,\, 0.64]\,\text{fm}$. Using the model averaging procedure of Ref. [38], we obtain the preliminary result

$$a_\mu^{\eta\text{-pole}} = 12.7(4.6)_{\text{stat}}(0.7)_{\text{syst}}[4.6]_{\text{tot}} \cdot 10^{-11} \tag{4.24}$$

on the cB072.64 ensemble. We note that the quoted systematic uncertainty in Eq. (4.24) only includes the effects of the analysis choices described above, and in particular does not include uncertainties associated with the continuum and infinite-volume limits.

4.2.5 Conclusion and outlook

Our preliminary result $a_\mu^{\pi\text{-pole}} = 55.4(2.1) \cdot 10^{-11}$ may be compared to the recent lattice result $a_\mu^{\pi\text{-pole}} = 59.7(3.6) \cdot 10^{-11}$ from Ref. [67] and the dispersive result $a_\mu^{\pi\text{-pole}} = 63.0^{+2.7}_{-2.1} \cdot 10^{-11}$ from Refs. [3, 63, 64]. We note that there is a mild tension with the data-driven result, though our analysis is not yet finalized, as discussed below. Our preliminary result $a_\mu^{\eta\text{-pole}} = 12.7(4.6) \cdot 10^{-11}$ on the cB072.64 ensemble can be compared to the estimate $a_\mu^{\eta\text{-pole}} = 16.3(1.4) \cdot 10^{-11}$ from a Canterbury approximant fit to experimental data [65] and $a_\mu^{\eta\text{-pole}} = 15.8(1.2) \cdot 10^{-11}$ and $a_\mu^{\eta\text{-pole}} = 14.7(1.9) \cdot 10^{-11}$ using Dyson-Schwinger and Bethe-Salpeter equations [131, 132]. Within our uncertainties we find good agreement with these various results already at this single lattice spacing. Figure 4.18 compares our results for both $a_\mu^{\pi\text{-pole}}$ and $a_\mu^{\eta\text{-pole}}$ with the aforementioned estimates.

At the moment, the z-expansion fits for the pion on cB072.64 are being finalized. Though this may change the central value of $a_\mu^{\pi\text{-pole}}$ in the continuum slightly we do not expect a drastic shift, and also no significant change in the total error. At the same time, the continuum extrapolation strategy is being developed to avoid either a too-conservative estimate with overestimated errors or an overly aggressive

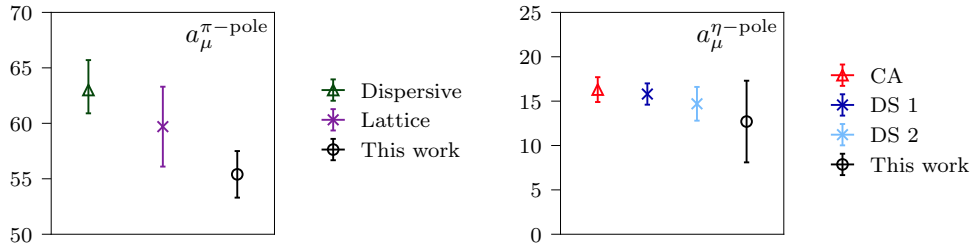

Figure 4.18: Left: Comparison of the estimate of $a_\mu^{\pi\text{-pole}}$ from this work versus an estimate based on dispersion relations [3, 63, 64] and a prior estimate from lattice QCD [67]. Right: Comparison of the estimate of $a_\mu^{\eta\text{-pole}}$ from this work versus a result derived from Canterbury approximant (CA) fits to experimental data [65] and two estimates based on Dyson-Schwinger (DS) equations [131, 132].

estimate dominated by the constant fit. Finally, future calculations on the cC060.80 and cD054.96 ensembles are planned for the analysis of $a_\mu^{\eta\text{-pole}}$, which will allow a continuum estimate of this value directly from ab-initio lattice QCD. An ab-initio value is not yet available for this quantity, so that such a result will provide an important cross-check for data-driven results for $a_\mu^{\eta\text{-pole}}$.

4.2.5.1 Acknowledgments

This work is supported in part by the Sino-German collaborative research center CRC 110 and the Swiss National Science Foundation (SNSF) through grant No. 200021_175761, 200021_208222, and 200020_200424. The authors gratefully acknowledge computing time granted on Piz Daint at Centro Svizzero di Calcolo Scientifico (CSCS) via the projects s849, s982, s1045 and s1133. The authors also gratefully acknowledge the Gauss Centre for Supercomputing e.V. (www.gauss-centre.eu) for funding the project by providing computing time on the GCS supercomputer JUWELS Booster [133] at the Jülich Supercomputing Centre (JSC). Part of the results were created within the EA program of JUWELS Booster also with the help of the JUWELS Booster Project Team (JSC, Atos, ParTec, NVIDIA). Ensemble production and measurements for this analysis made use of tmLQCD [134–137], DD-αAMG [138, 139], and QUDA [140–142]. Some figures were produced using `matplotlib` [143].

4.3 The $\eta \to \gamma^*\gamma^*$ transition form factor and the hadronic light-by-light η-pole contribution to the muon $g-2$ from lattice QCD

This section reproduces [71] and was published as a preprint on arXiv for a paper submitted to PRL in January 2023.

4.3.1 Abstract

We calculate the double-virtual $\eta \to \gamma^*\gamma^*$ transition form factor $\mathcal{F}_{\eta\to\gamma^*\gamma^*}(q_1^2, q_2^2)$ from first principles using a lattice QCD simulation with $N_f = 2+1+1$ quark flavors at the physical pion mass and at one lattice spacing and volume. The kinematic range covered by our calculation is complementary to the one accessible from experiment and is relevant for the η-pole contribution to the hadronic light-by-light scattering in the anomalous magnetic moment $a_\mu = (g-2)/2$ of the muon. From the form factor calculation we extract the partial decay width $\Gamma(\eta \to \gamma\gamma) = 338(87)_{\text{stat}}(17)_{\text{syst}}$ eV and the slope parameter $b_\eta = 1.34(28)_{\text{stat}}(14)_{\text{syst}}$ GeV^{-2}. For the η-pole contribution to a_μ we obtain $a_\mu^{\eta\text{-pole}} = 13.8(5.2)_{\text{stat}}(1.5)_{\text{syst}} \cdot 10^{-11}$.

4.3.2 Introduction

Radiative transitions and decays of the neutral pseudoscalar mesons $P = \pi^0$, η and η' arise through the axial anomaly and are therefore a crucial probe of the nonperturbative low-energy properties of QCD. The simplest transition to two (virtual) photons, $P \to \gamma^*\gamma^*$, is specified through the transition form factor (TFF)

$\mathcal{F}_{P\to\gamma^*\gamma^*}(q_1^2, q_2^2)$ defined by the matrix element

$$i\int d^4x\, e^{iq_1x}\langle 0|T\{j_\mu(x)j_\nu(0)\}|P(q_1+q_2)\rangle = \epsilon_{\mu\nu\rho\sigma}q_1^\rho q_2^\sigma \mathcal{F}_{P\to\gamma^*\gamma^*}(q_1^2, q_2^2), \tag{4.25}$$

where j_μ, j_ν are the electromagnetic currents and q_1, q_2 are the photon momenta. The TFFs determine the partial decay widths to leading order in the fine-structure constant α_{em} through

$$\Gamma(P\to\gamma\gamma) = \frac{\pi\alpha_{\text{em}}^2 m_P^3}{4}\,|\mathcal{F}_{P\to\gamma\gamma}(0,0)|^2, \tag{4.26}$$

where m_P is the pseudoscalar meson mass. $\Gamma(\eta\to\gamma\gamma)$ is of particular interest, since it can be used to extract the $\eta-\eta'$ mixing angles and provides a normalization for many other η partial widths [12]. At the same time, there is a long-standing tension between its different experimental determinations through e^+e^- collisions on the one hand and Primakoff production on the other [144–150]. The TFFs also provide input for determining the electromagnetic interaction radius of the pseudoscalar mesons through the slope parameter

$$b_P = \frac{1}{\mathcal{F}_{P\to\gamma\gamma}(0,0)}\frac{\mathrm{d}\mathcal{F}_{P\to\gamma^*\gamma}(q^2,0)}{\mathrm{d}q^2}\bigg|_{q^2=0}. \tag{4.27}$$

Moreover, the TFFs play a critical role for the leading-order hadronic light-by-light (HLbL) scattering in the anomalous magnetic moment $a_\mu = (g-2)/2$ of the muon. Recent results from the Fermilab E989 and Brookhaven E821 experiments [2, 20] indicate a 4.2σ tension with the consensus on the Standard Model prediction in Refs. [3, 4, 27–30, 32, 33, 51, 64, 65, 67, 151–159]. The uncertainty of the latter is dominated by the Hadronic Vacuum Polarization and the HLbL scattering. The HLbL contribution can be estimated, among other approaches [42–51], by a systematic decomposition into contributions from various intermediate states [52–55]. Lattice QCD can provide ab-initio data for the required form factors and hadron scattering amplitudes within this approach. This is thus complementary to a lattice-QCD calculation of the full HLbL scattering amplitude [56–61].

The pseudoscalar pole diagrams, depicted in Figure 4.19, make the dominant contribution to the HLbL scattering amplitude, with $\mathcal{F}_{P\to\gamma^*\gamma^*}$ as the key nonper-

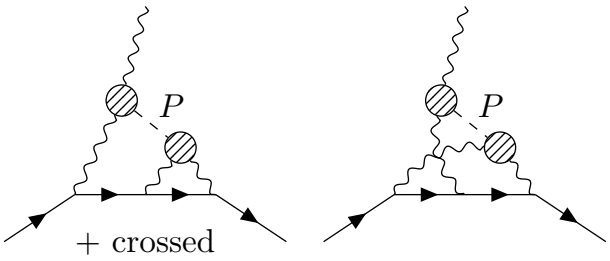

Figure 4.19: The pseudoscalar pole diagrams contributing to the leading order HLbL scattering in the muon anomalous magnetic moment. Each striped blob indicates the insertion of a pseudoscalar meson transition form factor $\mathcal{F}_{P\to\gamma^*\gamma^*}$, where $P \in \{\pi^0, \eta, \eta'\}$.

turbative input. Of these diagrams, the π^0-pole contribution has been estimated based on a dispersive framework [63, 64] and on lattice-QCD calculations of the pion TFF [66–68] while rational approximant fits to experimental TFF data have yielded an estimate of all three contributions [65]. A preliminary calculation of the η- and η'-pole contributions using a coarse lattice was reported in Ref. [70]. Experimental results from CELLO [73], CLEO [72], and BaBar [74, 75] constrain the spacelike single-virtual $\mathcal{F}_{P\to\gamma^*\gamma}(-Q^2, 0)$ in the regime $Q^2 \gtrsim 1\,\mathrm{GeV}^2$, but do not provide data for $0 \leq Q^2 \lesssim 1\mathrm{GeV}^2$ or for general double-virtual kinematics. In contrast, these kinematics are the most accessible in lattice QCD.

In this letter we present an ab-initio calculation of $\mathcal{F}_{\eta\to\gamma^*\gamma^*}(q_1^2, q_2^2)$ and the corresponding η-pole HLbL contribution $a_\mu^{\eta\text{-pole}}$ using lattice QCD simulations at a single lattice spacing and a single volume. We employ $N_f = 2 + 1 + 1$ flavors of twisted-mass quarks [77] tuned to the physical pion mass, physical heavy-quark masses, and maximal twist. The latter guarantees automatic $\mathcal{O}(a)$-improvement of observables [78, 79], which here includes $\mathcal{F}_{P\to\gamma^*\gamma^*}$, $\Gamma(\eta \to \gamma\gamma)$, b_η, and $a_\mu^{\eta\text{-pole}}$.

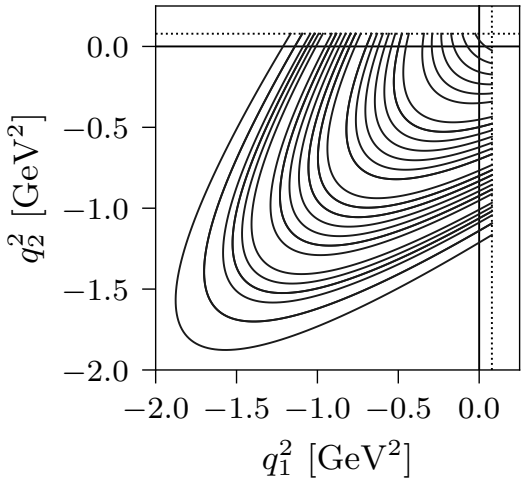

Figure 4.20: Orbits of photon virtualities (q_1^2, q_2^2) accessed in this work. Dotted lines indicate two-pion thresholds at $4m_\pi^2$.

4.3.3 Methods

We apply the method introduced in Refs. [66,67] to the case of the η TFF. In particular, the TFF is related to the Euclidean η-to-vacuum transition amplitude [119]

$$\tilde{A}_{\mu\nu}(\tau) \equiv \int d^3\vec{x} e^{-i\vec{q}_1\cdot\vec{x}} \langle 0|T\{j_\mu(\tau,\vec{x})j_\nu(0)\}|\eta(\vec{p})\rangle \tag{4.28}$$

by

$$\epsilon_{\mu\nu\alpha\beta} q_1^\alpha q_2^\beta \mathcal{F}_{\eta\to\gamma^*\gamma^*}(q_1^2, q_2^2) = -i^{n_0}\int_{-\infty}^{\infty} d\tau e^{\omega_1\tau}\tilde{A}_{\mu\nu}(\tau), \tag{4.29}$$

where $n_0 = \delta_{\mu,0} + \delta_{\nu,0}$ counts the number of temporal indices. The kinematics are determined by the four-momentum $p \equiv (E_\eta, \vec{p})$ of the on-shell η state with energy $E_\eta = \sqrt{m_\eta^2 + \vec{p}^2}$, the four-momentum $q_1 = (\omega_1, \vec{q}_1)$ of the first current, and the momentum conservation constraint $q_2 = p - q_1$. In the lattice setup used here, it is most practical to fix $\vec{p}$ and evaluate the amplitude for a variety of $\vec{q}_1$ and ω_1. The present calculation is restricted to the rest frame, $\vec{p} = (0,0,0)$, and momenta satisfying $|\vec{q}_1|^2 \leq 32(2\pi/L)^2$ and $|q_1^x|, |q_1^y|, |q_1^z| \leq 4(2\pi/L)$. Each choice of finite-volume momentum $\vec{q}_1$ gives access to $\mathcal{F}_{\eta\to\gamma^*\gamma^*}(q_1^2, q_2^2)$ on a particular kinematical orbit, as shown in Figure 4.20. Notably, the $|\vec{q}_1|^2 = (2\pi/L)^2$ orbit lies outside the spacelike quadrant, but still falls below the non-analytic thresholds at $4m_\pi^2$, allowing it to be accessed on the lattice; its proximity to $(0,0)$ makes it particularly helpful in

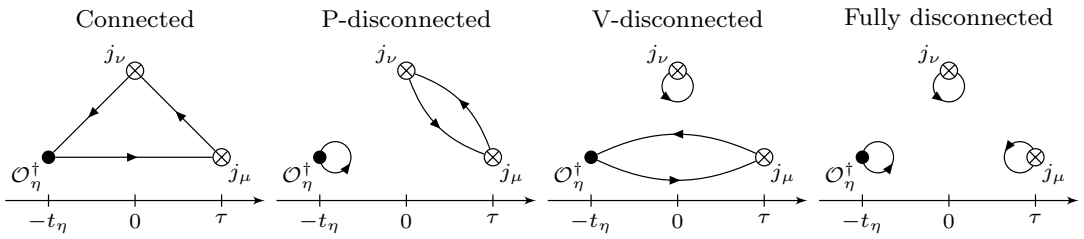

Figure 4.21: Wick contractions contributing to $C_{\mu\nu}(\tau, t_\eta)$. The second connected diagram with quark propagators running in the opposite direction and the second V-disconnected diagram with a loop at $j_\mu(\tau)$ are omitted for brevity.

constraining $\Gamma(\eta \to \gamma\gamma)$ and b_η.

The Euclidean amplitude in Eq. (4.28) is accessed by evaluating the three-point function

$$\begin{aligned} C_{\mu\nu}(\tau, t_\eta) \equiv & \int d^3\vec{x}\, d^3\vec{y}\, e^{-i\vec{q}_1\cdot\vec{x}} e^{i\vec{p}\cdot\vec{y}} \\ & \times \langle T\{j_\mu(\tau, \vec{x}) j_\nu(0) \mathcal{O}_\eta^\dagger(-t_\eta, \vec{y})\}\rangle \,. \end{aligned} \tag{4.30}$$

For any operator $\mathcal{O}_\eta^\dagger$ with overlap onto the η state, the three-point function is projected onto the physical η meson at large time separation, $-t_\eta \ll \min(0, \tau)$, irrespective of $\eta - \eta'$ mixing. Here we use $\mathcal{O}_\eta^\dagger = i\bar{\psi}\lambda_8\gamma_5\psi$, where $\lambda_8 = \mathrm{diag}(1, 1, -2)/\sqrt{3}$ describes the SU(3) flavor structure. The electromagnetic currents are defined by $j_\mu = Z_V\, \bar{\psi}\, \gamma_\mu\, \mathcal{Q}\, \psi$ with $\mathcal{Q} = \mathrm{diag}(+2/3,\, -1/3,\, -1/3)$ and $Z_V = 0.706378\,(16)$ [40].

Evaluating $C_{\mu\nu}$ requires the Wick contractions shown in Figure 4.21. We evaluate all connected (sub-)diagrams with point-to-all quark propagators. In the P-disconnected diagram, we compute the quark-loop at $O_\eta^\dagger$ from propagators based on stochastic volume sources. Unlike in previous lattice QCD studies of the π^0 TFF, here P-disconnected diagrams of the isospin-singlet η operator are non-zero. The projection onto the η state relies on a delicate cancellation between connected and P-disconnected diagram contributions, as shown in Figure 4.22.

The amplitude $\tilde{A}_{\mu\nu}$ is then recovered from $C_{\mu\nu}$ as

$$\tilde{A}_{\mu\nu}(\tau) = \lim_{t_\eta \to \infty} \frac{2E_\eta}{Z_\eta} e^{E_\eta t_\eta} C_{\mu\nu}(\tau, t_\eta), \tag{4.31}$$

where $Z_\eta = \langle 0|\mathcal{O}_\eta(0, \vec{0})|\eta(\vec{p})\rangle$ is the overlap factor associated with the chosen creation

operator. In practice we approximate the limit $t_\eta \to \infty$ by considering three fixed values of t_η in the range 0.80 fm $\lesssim t_\eta \lesssim$ 1.11 fm. Contamination from excited states and the η' meson are suppressed best for the largest value of t_η, thus we report the values for $\Gamma(\eta \to \gamma\gamma)$, b_η, and $a_\mu^{\eta\text{-pole}}$ from $t_\eta \approx 1.11\,\text{fm}$ as the main result and use the remaining choices to check for excited state effects.

Statistical noise significantly hinders evaluation of $\tilde{A}_{\mu\nu}(\tau)$ for large values of $|\tau|$. Following Refs. [66–68], we address this issue by performing joint fits of the asymptotic behavior of $\tilde{A}_{\mu\nu}(\tau)$ for all $\vec{q}_1$ to Vector Meson Dominance and Lowest Meson Dominance functional forms [160] with fit windows defined by $t_i \leq |\tau| \leq t_f$. We then integrate over τ as in Eq. (4.29) using numerical integration of the lattice data within the peak region, $|\tau| \leq \tau_c$, and analytical integration of the fit form in the tail region, $|\tau| > \tau_c$. In this work, we consider several choices of τ_c in the range $0.16\,\text{fm} \lesssim \tau_c \lesssim 0.64\,\text{fm}$.

Access to the partial decay width, the slope parameter, and the η-pole HLbL contribution requires an interpolation of the TFF close to the origin and an extrapolation in the quadrant of non-positive photon virtualities. We apply the model-independent expansion in powers of conformal variables advocated in Ref. [67], termed the z-expansion. Analyticity of the form factor below the two-pion thresholds at $q_1^2 = 4m_\pi^2$ and $q_2^2 = 4m_\pi^2$ guarantees convergence as the highest power N in the expansion is taken to infinity. Moreover, the expansion is restricted to account for the known threshold scaling and contains preconditioning to more easily capture the expected asymptotic behavior as $q_1^2, q_2^2 \to -\infty$. In practice we find that the $N = 2$ fit, consisting of six free parameters, already provides a very accurate fit to all lattice results, so we restrict to $N \in \{1, 2\}$ in all subsequent analyses.

The η-pole HLbL contribution has the integral representation [116, 118]

$$\begin{aligned} a_\mu^{\eta\text{-pole}} = \left(\frac{\alpha}{\pi}\right)^3 \int_0^\infty dQ_1 dQ_2 \int_{-1}^1 dt \Big[\\ w_1(Q_1, Q_2, t) \mathcal{F}_{\eta\to\gamma^*\gamma^*}(-Q_1^2, -Q_3^2) \mathcal{F}_{\eta\to\gamma^*\gamma}(-Q_2^2, 0) \\ + w_2(Q_1, Q_2, t) \mathcal{F}_{\eta\to\gamma^*\gamma^*}(-Q_1^2, -Q_2^2) \mathcal{F}_{\eta\to\gamma^*\gamma}(-Q_3^2, 0) \Big] , \end{aligned} \tag{4.32}$$

with $t = \cos\theta$ parameterizing the angle between the four-momenta, so that

$Q_3^2 = Q_1^2 + 2Q_1Q_2\cos\theta + Q_2^2$. The weight functions w_1 and w_2 are peaked such that contributions to Eq. (4.32) mainly come from the region $0 \leq Q_1, Q_2 \lesssim 2\,\text{GeV}$ [118]. Knowledge of the TFF in the regime of relatively small virtualities is thus sufficient to accurately evaluate $a_\mu^{\eta\text{-pole}}$.

Finally, we quantify systematic errors associated with the choices of tail-fit model, the parameters (t_i, t_f), τ_c and the z-expansion order N by the model-averaging procedure detailed in the supplemental material.

4.3.4 Results

Our lattice results are obtained on the gauge ensemble cB211.072.64 produced by the Extended Twisted Mass Collaboration (ETMC) [115]. The sea-quark masses for this ensemble are tuned to reproduce the physical charged-pion mass and the strange- and charm-quark masses, with a lattice spacing of $a \simeq 0.08$ fm and a lattice size of $L \simeq 5.09$ fm ($m_\pi L \simeq 3.62$) [40, 115]. For the valence strange quark we use the mixed action approach in Ref. [79], with valence strange-quark mass tuned such that the η meson has physical mass.

We show in Figure 4.22 an example of the contributions to $C_{\mu\nu}(\tau, t_\eta)$ from the connected and P-disconnected Wick contractions on this ensemble at our largest separation, $t_\eta \simeq 1.11\,\text{fm}$. The contributions involving strange-quark vector currents are suppressed by a factor ~ 10 for the connected and ~ 20 for the P-disconnected contribution compared to those from the light quark vector currents. Contributions from charm-quark vector currents are expected to be even more suppressed [68], as are those from V-disconnected and fully disconnected diagrams (lower two diagrams in Figure 4.21). At the presently achievable accuracy these contributions are hence not relevant and are not included in the analysis.

In Figure 4.23 we show our results for the TFF as a function of the virtuality in the single-virtual case $\mathcal{F}_{\eta\to\gamma^*\gamma}(-Q^2, 0)$ (top row) and in the double-virtual case $\mathcal{F}_{\eta\to\gamma^*\gamma^*}(-Q^2, -Q^2)$ (bottom row) together with our result from the z-expansion fits. The darker inner band indicates only statistical uncertainties while the lighter

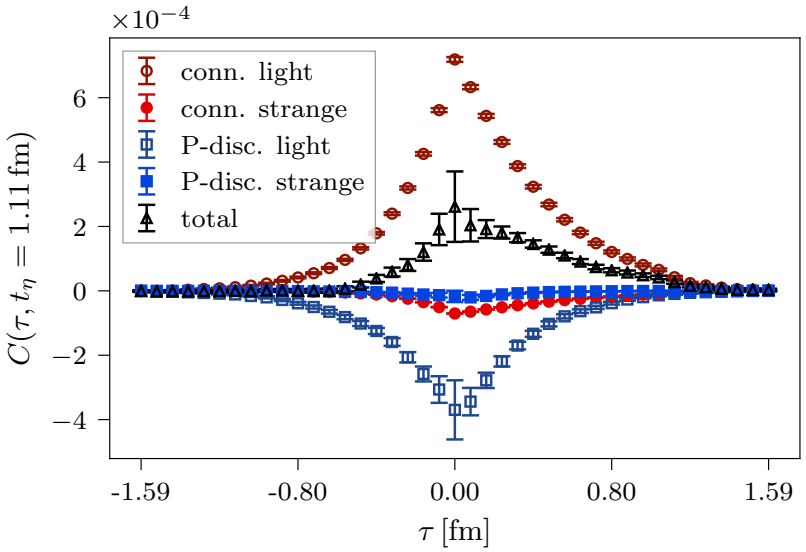

Figure 4.22: Contributions from the connected and P-disconnected Wick contractions in the evaluation of $C(\tau, t_\eta) \equiv (i\epsilon_{ijk}\vec{q}_1^{\,i}/|\vec{q}_1|^2)\, C_{jk}(\tau, t_\eta)$ at $t_\eta = 1.11\,\text{fm}$ and $|\vec{q}_1^{\,2}| = 3(2\pi/L)^2$. The labels "light" and "strange" indicate the quark flavor in the contractions of the electromagnetic currents.

outer band includes systematic uncertainties estimated from the variation of fitting choices discussed above. At all virtualities shown, the statistical errors dominate the total uncertainty. In addition to the available experimental data, we also show the Canterbury approximant (CA) result from Ref. [65]. We observe reasonable agreement between our results, the experimental data and the CA data.

From the parameterization of the momentum dependence of our TFF data we extract the decay width, slope parameter, and $a_\mu^{\eta\text{-pole}}$. As with the TFF itself, we repeat the calculation for all choices of the analysis parameters to determine systematic errors associated with tail fits of $\tilde{A}$ and the z-expansion. A detailed breakdown is given in the supplemental materials. For the decay width the resulting systematic uncertainty stems mainly from the variation in the fits of the tails of $\tilde{A}_{\mu\nu}(\tau)$ and τ_c, while for the slope parameter and the HLbL pole contribution it is mainly due to the conformal fit. The total error, however, is always dominated by the statistical uncertainties. We also observe a mild systematic dependence on t_η, as detailed in the supplemental materials, which points to the fact that excited-state and possibly η'-meson contributions to the transition amplitude are not completely eliminated at the smaller values of t_η. We conservatively quote results obtained at our largest

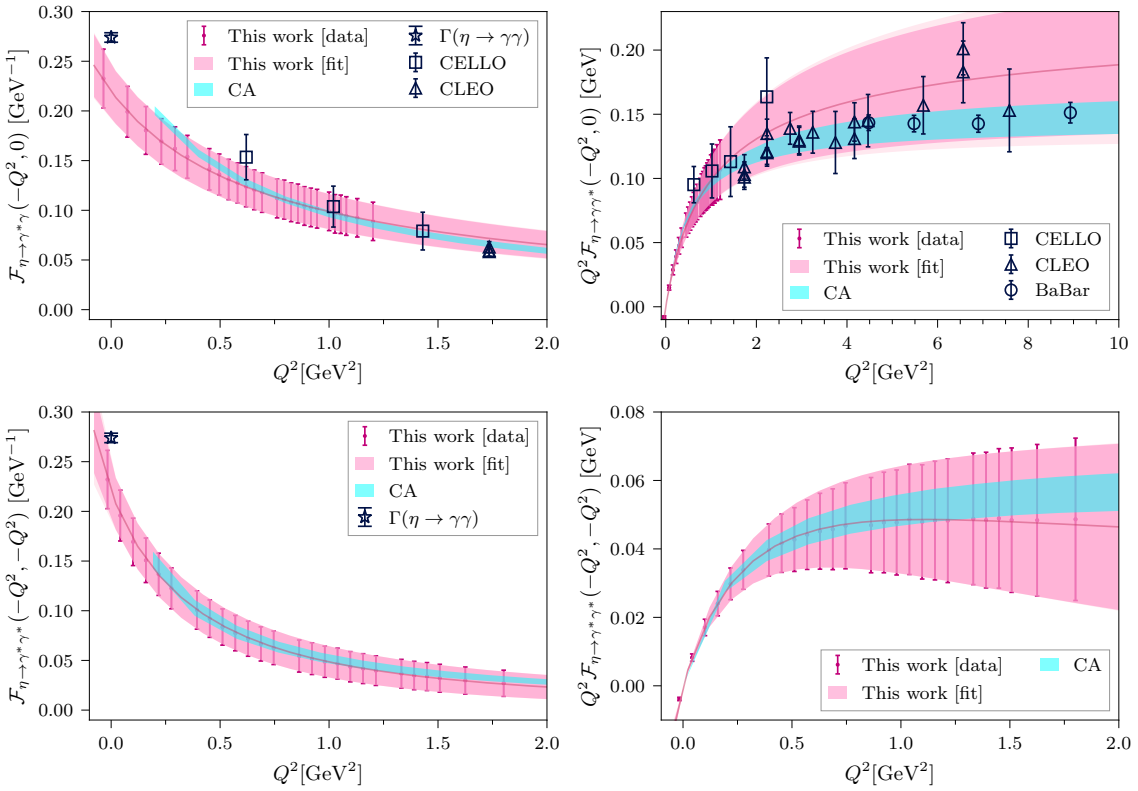

Figure 4.23: Comparison of the TFF estimated from this work (pink curve) versus the available $\mathcal{F}_{\eta\to\gamma^*\gamma}$ and $\Gamma(\eta \to \gamma\gamma)$ experimental results (blue points) [12, 72–75] and a Canterbury approximant estimate (cyan curve) [65]. For better comparison to features at both small and large Q^2, the TFFs are plotted both with and without a conventional Q^2 prefactor.

value of $t_\eta \simeq 1.11\,\mathrm{fm}$ for which the statistical uncertainty is largest and covers the results at the smaller t_η values.

For the leading-order decay width we obtain

$$\Gamma(\eta \to \gamma\gamma) = 338(87)_{\mathrm{stat}}(17)_{\mathrm{syst}}[88]_{\mathrm{tot}}\,\mathrm{eV} \tag{4.33}$$

in comparison to the experimental average $516(18)\,\mathrm{eV}$ [12, 145–149]. For the slope parameter we find

$$b_\eta = 1.34(28)_{\mathrm{stat}}(14)_{\mathrm{syst}}[31]_{\mathrm{tot}}\,\mathrm{GeV}^{-2} \tag{4.34}$$

to be compared with $b_\eta = 1.92(4)\ \mathrm{GeV}^{-2}$ from a Padé approximant fit to the experimental results [161] and $b_\eta = 1.95(9)\ \mathrm{GeV}^{-2}$ from a dispersive calculation [162]. Finally, we use the parameterization of our TFF data to perform the integration in Eq. (4.32) and obtain

$$a_\mu^{\eta\text{-pole}} = 13.8(5.2)_{\mathrm{stat}}(1.5)_{\mathrm{syst}}[5.5]_{\mathrm{tot}} \cdot 10^{-11} \tag{4.35}$$

in comparison to a Canterbury approximant fit to experimental results yielding $16.3(1.4) \cdot 10^{-11}$ [65], the VMD model value $14.5(3.4) \cdot 10^{-11}$ [118], and estimates $15.8(1.2) \cdot 10^{-11}$ [131] and $14.7(1.9) \cdot 10^{-11}$ [132] based on the Dyson-Schwinger equations.

We emphasize that our results are obtained at a fixed lattice spacing and a fixed volume. The present estimates therefore exclude systematic errors associated with finite-volume effects and lattice artifacts. The latter are expected to be of $\mathcal{O}\left(a^2\Lambda_{\mathrm{QCD}}^2\right)$ with the lattice discretization used here. Lattice artifacts contribute through the bare TFFs, the vector-current renormalization factors (except in b_η) and through the setting of the lattice scale required to convert m_μ to lattice units. Both Z_V and the lattice scale are determined independently of the quantities considered here [40, 115]. A quantitative estimate of the lattice artifacts present in $a_\mu^{\eta\text{-pole}}$ can therefore be obtained by considering the scheme of fixing the renormalization by the physical decay width instead of the hadronic scheme. This gives $a_{\mu;\Gamma-\mathrm{renorm}}^{\eta\text{-pole}} = 20.7\,(4.5)_{\mathrm{stat}}(2.3)_{\mathrm{syst}} \cdot 10^{-11}$, which differs from $a_\mu^{\eta\text{-pole}}$ in Eq. (4.35) by $6.9 \cdot 10^{-11}$, which is of similar size to our total error.

4.3.5 Conclusions and outlook

The results of our lattice QCD calculation of the transition form factor $\mathcal{F}_{\eta\to\gamma^*\gamma^*}(q_1^2, q_2^2)$ at physical pion mass have a precision comparable to experimental results in the range where both are available, and demonstrate nice agreement, cf. Figure 4.23. Our results provide single-virtual data at lower photon virtuality than currently accessible by experiments. This includes the region around zero virtuality necessary to study the decay width and slope parameter. The results for these quantities in Eqs. (4.33) and (4.34) undershoot the experimental (and for b_η also theoretical) results by 1.5–2.0 standard deviations.

Our lattice computation also provides TFF data for double-virtual (space-like) photon kinematics, which is difficult to access by experiment. We have made use of this advantage and calculated the η-pole contribution to the anomalous magnetic moment of the muon, $a_\mu^{\eta\text{-pole}} = 13.8(5.2)_{\text{stat}}(1.5)_{\text{syst}}[5.5]_{\text{tot}} \cdot 10^{-11}$. Our result confirms the currently available data-driven Canterbury approximant estimate [65] and the theoretical model estimates [118, 131, 132], but does not yet reach the same precision. Nevertheless, it provides important independent support of these estimates. The main shortcoming of our calculation is the use of a single lattice spacing, which will be removed in the future by computations with ETMC gauge ensembles on finer lattices [104, 115].

4.3.6 Acknowledgments

We thank Martin Hoferichter, Simon Holz, and Bastian Kubis for helpful discussions. We are also grateful to the authors of Ref. [65] for sharing form factor data produced in their work. This work is supported in part by the Sino-German collaborative research center CRC 110 and the Swiss National Science Foundation (SNSF) through grant No. 200021_175761, 200020_208222, and 200020_200424. We gratefully acknowledge computing time granted on Piz Daint at Centro Svizzero di Calcolo

Scientifico (CSCS) via the projects s849, s982, s1045 and s1133. Some figures were produced using `matplotlib` [143].

4.3.7 Supplementary material

4.3.7.1 Error estimation and model averaging

All statistical errors reported in this work are given as 1σ confidence intervals derived from $N_{\text{boot}} = 2000$ bootstrap resamplings of the ensemble of configurations. We find virtually no autocorrelation between the relevant primary data taken on a subset of configurations constituting the ensemble, and the bootstrap bin size is therefore fixed to 1.

During our analysis, we make several choices corresponding to fits of the large-$|\tau|$ tails of the amplitude $\tilde{A}_{\mu\nu}(\tau)$ and of the finite-volume TFF orbits. In particular, the following analysis parameters are varied:

1. The choice between using the Vector Meson Dominance (VMD) or Lowest Meson Dominance (LMD) model to the fit the tail behavior;
2. The window (t_i, t_f), determining which regions of the amplitude $\tilde{A}_{\mu\nu}(\tau)$ are used as inputs to fit the asymptotic tail behavior;
3. The integration cutoff τ_c, distinguishing the region $|\tau| \leq \tau_c$ in which the lattice data is integrated from the region $|\tau| > \tau_c$ in which the analytical tail model is integrated; and
4. The order N of the conformal expansion used to fit the TFFs.

The variation of our estimates with these model choices gives estimates of the systematic errors associated with these steps. We apply the approach of Refs. [38,163] to construct cumulative distribution functions (CDFs) of all final quantities with various subsets of models and with two choices of rescaling parameter λ applied to the systematic error. The various total error estimates, given by the difference

between the 16th and 84th percentiles of the CDF in each case, allow an extraction and decomposition of the total uncertainty into statistical, total systematic, and various individual sources.

In this approach, weights must be assigned to each model included in the CDF. Weights based on the Akaike Information Criterion [164] derived from χ^2 values of each fit have previously been employed. For the tail of the amplitude, we perform a fit to values of $\tilde{A}_{\mu\nu}(\tau)$ over sequential choices of τ and across all momentum orbits. For the z-expansion, we perform a fit to values of $\mathcal{F}_{\eta\to\gamma^*\gamma^*}(-Q_1^2, -Q_2^2)$ across all orbits at several fixed choices of the ratio Q_1^2/Q_2^2. This input data is highly correlated, and determining the correlated χ^2 therefore requires a very precise estimate of nearly degenerate covariance matrices of both the tail fits and z-expansion fits. Even for fits to small windows (t_i, t_f) and few choices of orbits, we did not find estimates of the χ^2 values to be accurate in our preliminary investigations. Instead, in this work we perform fits using much more stable uncorrelated fits and make the conservative choice to use a uniform weighting of all possible models in the CDF method. This can be expected to overestimate the systematic error associated with model variation. The decomposition of uncertainties is detailed in Table 4.5 for all three final physical

	$10^{11} \cdot a_\mu^{\eta\text{-pole}}$	$\Gamma(\eta \to \gamma\gamma)$ [eV]	b_η [GeV^{-2}]
Tail model vs data cut (τ_c)	0.22	10.1	0.020
Tail fit windows (t_i, t_f)	0.18	6.5	0.009
Fit model (VMD vs. LMD)	0.31	11.6	0.034
Conformal fit order (N)	1.44	1.8	0.123
Total systematic	1.53	17.2	0.135
Statistical	5.24	86.7	0.279
Total	5.46	88.4	0.310

Table 4.5: Decomposition of uncertainties in the reported values of the three quantities studied at the single lattice spacing and volume used in this work. The results and uncertainties are based on the conservative choice $t_\eta/a = 14$ corresponding to $t_\eta = 1.11$ fm.

quantities studied in this work. Due to correlations between the total error estimates in each case, the decomposition does not simply add in quadrature, but nevertheless gives an estimate of which components of the error dominate the error budget. Unsurprisingly, the dominant sources of systematic errors vary depending on the observable considered. For the η-pole contribution to the HLbL, the biggest source

of systematic error is the conformal fit used to extrapolate the TFF $\mathcal{F}_{\eta\to\gamma^*\gamma^*}(q_1^2, q_2^2)$ from the low-virtuality orbits accessible on the lattice to the full plane of spacelike (q_1^2, q_2^2). This indicates that, despite the important contributions to $a_\mu^{\eta\text{-pole}}$ from low virtualities, the large uncertainties in the nearly unconstrained higher virtualities can still affect the estimate of $a_\mu^{\eta\text{-pole}}$ from lattice data alone. Incorporating some information about asymptotic scaling of the TFF at large virtualities is therefore an interesting prospect for future work. The other two quantities, $\Gamma(\eta\to\gamma\gamma)$ and b_η are directly related to the behavior of the TFF at $q_1^2 = q_2^2 = 0$. In the case of $\Gamma(\eta\to\gamma\gamma)$, the choices used to fit the tails of the amplitude $\tilde{A}_{\mu\nu}(\tau)$ dominate the systematic errors, while for b_η the systematic uncertainties are still set by the conformal expansion fit. Nonetheless, we find that the uncertainties in all three quantities are almost entirely given by the statistical error, which always far outweighs the systematic errors.

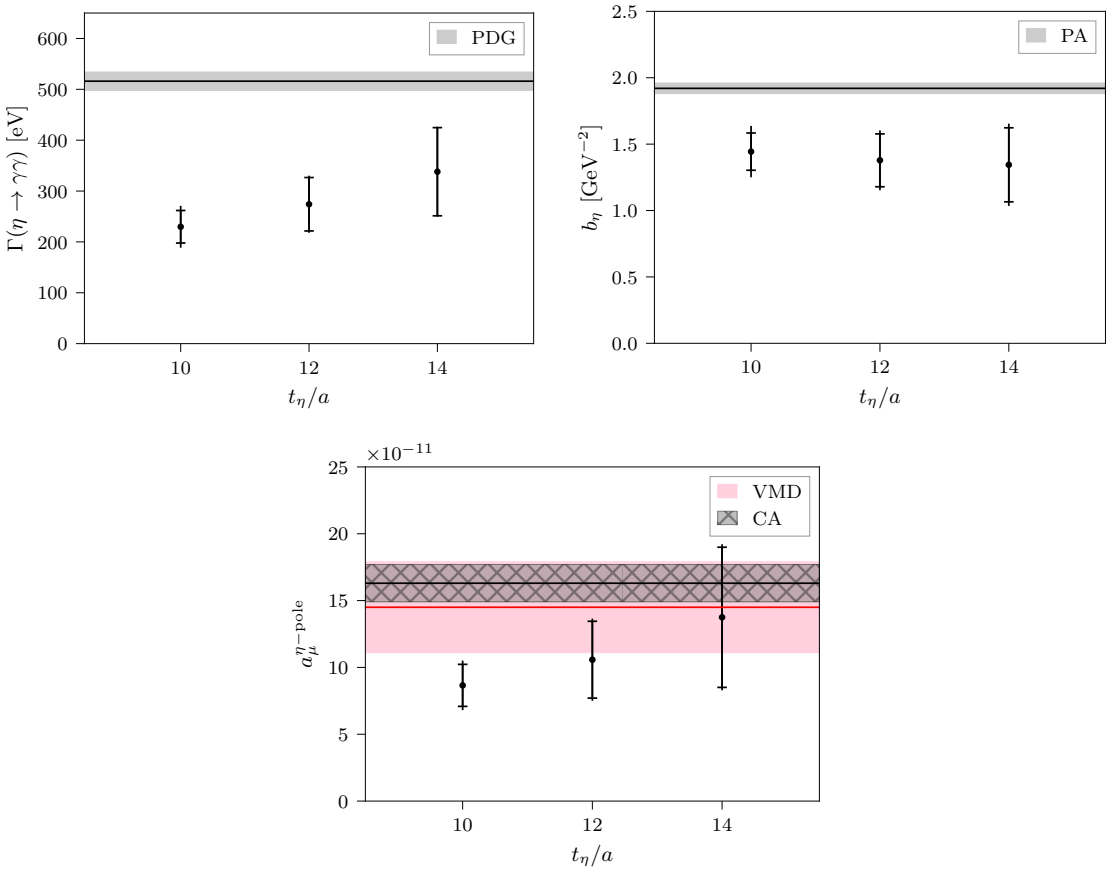

Figure 4.24: Comparison of the partial decay width $\Gamma(\eta \to \gamma\gamma)$, the slope parameter b_η, and the η-pole contribution $a_\mu^{\eta\text{-pole}}$ from three choices of $t_\eta/a = 10, 12, 14$ corresponding to $t_\eta = 0.80, 0.96, 1.11$ fm. For reference, the values are respectively compared against estimates from the PDG [12], Padé approximant (PA) fits to experimental data [161], and the VMD model [118] and Canterbury approximant (CA) experimental fits [65].

4.3.7.2 Dependence on t_η

In Fig. 4.24 we show the dependence of the partial decay width $\Gamma(\eta \to \gamma\gamma)$, the slope parameter b_η, and the η-pole contribution $a_\mu^{\eta\text{-pole}}$ on the choice of t_η which denotes the imaginary time location of the creation operator $\mathcal{O}_\eta^\dagger(-t_\eta)$ for the η meson, to be compared with imaginary time coordinates of the currents $j_\mu(\tau)$ and $j_\nu(0)$. The outer error bar denotes the total error, while the inner one shows the statistical error only. It is clear that the total error is dominated by the statistical one in all cases and for all t_η considered in this calculation. For all three quantities we observe a mild systematic trend with growing t_η which may be an indication that excited state and η'-meson contributions to the transition amplitude, and hence to the quantities shown here, may still be present at the smaller values of t_η. Since we are interested in the limit $t_\eta \to \infty$ we conservatively quote the results for the largest available t_η for which the statistical error is largest and covers the results at the smaller values of t_η.

4.3.7.3 Interpolation of the η state

The η-meson state is the lowest-lying eigenstate of the twisted mass lattice Hamiltonian in the channel with quantum numbers $I^G\left(J^{PC}\right) = 0^+\,(0^{-+})$. The exact interpolating field to project onto the η eigenstate in the lattice calculation is unknown. However, it is sufficient that it can be written as a linear combination of the quark-model octet- and singlet-pseudoscalar operators

$$\begin{aligned} O_\eta^{\text{exact}} &= \alpha\,\bar{\psi}\lambda_8\gamma_5\psi + \beta\,\bar{\psi}\gamma_5\psi + \ldots \\ &= \alpha\,\frac{1}{\sqrt{3}}\left(\bar{u}\gamma_5 u + \bar{d}\gamma_5 d - 2\bar{s}\gamma_5 s\right) + \beta\,\left(\bar{u}\gamma_5 u + \bar{d}\gamma_5 d + \bar{s}\gamma_5 s\right) + \ldots\,, \end{aligned} \tag{4.36}$$

where the ellipsis denotes further linearly independent operators. Using the octet operator

$$O_8 = i\bar{\psi}\lambda_8\gamma_5\psi = \frac{i}{\sqrt{3}}\left(\bar{u}\gamma_5 u + \bar{d}\gamma_5 d - 2\bar{s}\gamma_5 s\right) \tag{4.37}$$

as the interpolating operator means that the projection is imperfect, i.e., the creation operator will produce a tower of Hamiltonian eigenstates from the vacuum,

$$O_8^\dagger \,|\, 0\rangle = Z_\eta \,|\eta\rangle + Z_{\eta'} \,|\eta'\rangle + \dots \,, \tag{4.38}$$

with increasing mass or energy and with $Z_\eta = \langle 0 \,|\, O_8(0) \,|\, \eta\rangle$, $Z_{\eta'} = \langle 0 \,|\, O_8(0) \,|\, \eta'\rangle$. Nevertheless, the η-meson state is the unique ground state of lowest mass, and propagation in Euclidean time systematically suppresses the contribution of the η'-meson and excited states lying higher in the spectrum. This suppression scales exponentially as $\exp\left(-(M - m_\eta)t\right)$, in terms of the Euclidean time evolution t and the relative energy gap between the mass M of the higher state and m_η. This applies to all two- and three-point correlation functions used in this work. Thus for sufficiently long Euclidean time propagation, the projection onto the η-meson state is achieved by our choice of $O_8^\dagger$ as the creation operator for the three-point function.

Chapter 5

Pion Transition Form Factor from Twisted Mass Lattice QCD for the Hadronic Light-by-Light Contribution to Muon $g-2$

This chapter is a draft for a publication in preparation about the computation of the pion transition form factor and its utilization in calculating the pion pole contribution $a_\mu^{\pi-\text{pole}}$ to the hadronic light-by-light scattering in the muon $g-2$, the two-photon decay width $\Gamma(\pi \to \gamma\gamma)$ and the slope parameter b_π.
In the time between handing in this thesis and the defense, it was published as a preprint on arXiv as [165].

5.1 Abstract

The neutral pion generates the leading pole contribution to the hadronic light-by-light tensor, which is given in terms of a transition form factor $\mathcal{F}_{\pi^0\gamma\gamma}(q_1^2, q_2^2)$ and which must be computed non-perturbatively. Recently this form factor has been computed on the lattice with Wilson quarks, staggered quarks and using dispersive methods.

Here we present an independent lattice calculation of this quantity determined in the continuum and at the physical point using twisted mass lattice QCD. We provide a parametrization of the transition form factor for arbitrary single-virtual and space-like kinematics and compare it with experimental measurements of the single-virtual form factor, the two-photon decay width and the slope parameter. We then use the transition form factors to compute the pion pole contribution to the hadronic light-by-light scattering in the muon $g-2$, finding $a_\mu^{\pi-\text{pole}} = 56.7(3.1) \times 10^{-11}$.

5.2 Introduction

The anomalous magnetic moment of the muon provides a stringent test of the Standard Model at high precision and the possibility to glimpse subtle effects of new physics beyond the Standard Model. First results from the Fermilab experiment [2] in combination with the Brookhaven result [20] have yielded a new experimental world average $a_\mu(\text{exp}) = 116592061(41) \times 10^{-11}$ (0.35ppm). A comparable precision has been strived for on the theoretical side as summarized in a recent white paper [3].

The leading hadronic contributions to the muon anomalous magnetic moment come from diagrams involving the hadronic vacuum polarization (HVP) and the hadronic light-by-light scattering (HLbL) tensors. Both make significant contributions at the level of precision achieved by the experimental results. It is important to improve the theoretical determinations of both contributions to match future targets of experimental precision.

In the determination of the hadronic light-by-light contribution, lattice calculations most frequently analyze the complete tensor [56–62]. On the other hand, the data-driven dispersive approach first decomposes the hadronic tensor into contributions from single- or multi-particle exchanges. Contributions from heavier intermediate states are suppressed, allowing one to compute the light-by-light tensor in a controlled expansion [52–55].

The leading single-pole contributions to the HLbL arise from the exchange of neutral pseudoscalar mesons, cf. Fig 5.1, which may be expressed in terms of the non-

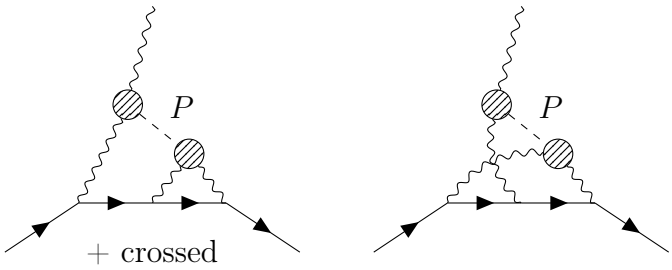

Figure 5.1: Pseudoscalar-pole diagrams contributing to the leading order hadronic light-by-light scattering. Each striped circle indicates a non-perturbative $P \to \gamma^*\gamma^*$ transition form factor required to evaluate these contributions, where "P" stands for the pseudoscalar.

perturbative transition form factors [50],

$$\begin{aligned} M_{\mu\nu}(p, q_1) &= i \int d^4x e^{iq_1 x} \langle 0|T\{j_\mu(x) j_\nu(0)\}|P(p)\rangle \\ &= \epsilon_{\mu\nu\alpha\beta} q^\alpha p^\beta \mathcal{F}_{P\gamma\gamma}(q_1^2, q_2^2), \end{aligned} \tag{5.1}$$

where the pseudoscalar "P" is on shell, $p^2 = M_P^2$, and the photon momenta q_1 and $q_2 = p - q_1$ may be either on-shell or virtual. The pseudoscalar pole contributions to the hadronic light-by-light tensor are given in terms of the transition form factor as

$$\begin{aligned} \Pi^{(P)}_{\mu\nu\lambda\rho}(q_1, q_2, q_3) = i &\frac{\mathcal{F}_{P\gamma\gamma}(q_1^2, q_2^2)\mathcal{F}_{P\gamma\gamma}(q_3^2, (q_1+q_2+q_3)^2)}{(q_1+q_2)^2 + M_P^2} \\ &\times \epsilon_{\mu\nu\alpha\beta} q_1^\alpha q_2^\beta \epsilon_{\lambda\rho\gamma\delta} q_3^\gamma (q_1+q_2)^\delta + (\text{cyclic}), \end{aligned} \tag{5.2}$$

with the dominant contributions arising from the lightest neutral pseudoscalars, $P \in \{\pi^0, \eta, \eta'\}$.

Because of its light mass, the π^0 pole contribution is larger than those of the η and η' by roughly a factor of four. This feature, together with the relative simplicity of accessing the pion transition form factor in both lattice and data-driven approaches, means that the study of this transition form factor is farthest advanced at this point. On one hand, the pion transition form factor has been determined in a data-driven dispersive approach [63–65]. On the other hand, an ab-initio determination is desirable to remove dependence on experimental inputs. As such, the neutral pion transition form factor has also been computed on the lattice by the Mainz group using Wilson

quarks [66,67] and by the BMW collaboration using staggered quarks [166].The major source of uncertainty in the latter approaches is the extrapolation to the continuum and physical pion mass limits. This motivates the present work, which evaluates the pion transition form factor from twisted mass lattice QCD using ensembles directly at the physical pion mass. We note that the computation in [166] has also been done at physical pion mass.

The structure of this paper is as follows. In Sec. 5.3, we present the theoretical background for the extraction of the required amplitudes from lattice QCD simulations and their extension to arbitrary Euclidean times. In Sec. 5.4, we describe the calculation of the transition form factors and their extension to arbitrary photon virtualities. Furthermore, we discuss the sampling used for this extension as well as details of the renormalization. In Sec. 5.5 and 5.6, we present the calculation of $a_\mu^{\pi-\mathrm{pole}}$ from the transition form factors and introduce the decay width $\Gamma(\pi \to \gamma\gamma)$ and the slope parameter b_π. Next, in Sec. 5.7, we discuss the Akaike Information Criterion as a tool to estimate statistical and systematic errors before presenting our model averaged results in Sec. 5.8, comparing them to experimental and theoretical predictions. Then, in Sec. 5.9, we make some concluding remarks and give an outlook on possible future directions for improving the calculation presented here. In App. A.1, we list the operators used in our calculation, along with their behavior under some transformations and the gamma matrix conventions we use. In App. A.2, we give more details on the integral representation introduced in Sec. 5.5.

5.3 Methodology

By analytic continuation, the Minkowski space neutral pion transition form factor in Eq. (5.1) is related to the amplitude in Euclidean space [119–121]

$$M_{\mu\nu}(p, q_1) = i^{n_0} M^E_{\mu\nu}(p, q_1), \quad M^E_{\mu\nu} = \int_{-\infty}^{\infty} d\tau \, e^{\omega_1 \tau} \tilde{A}_{\mu\nu}(\tau), \tag{5.3}$$

where $n_0 = \delta_{\mu,0} + \delta_{\nu,0}$, ω_1 is the temporal component of q_1, and the integrand is given by the Euclidean matrix element

$$\tilde{A}_{\mu\nu}(\tau) = \left\langle 0|T\{j_\mu(\vec{q}_1,\tau)j_\nu(\vec{p}-\vec{q}_1,0)\}|\pi^0(p)\right\rangle . \tag{5.4}$$

The lattice evaluation of the transition form factor proceeds by first extracting this matrix element from a lattice three-point function, then integrating Eq. (5.3) for various choices of ω_1, as we now discuss.

5.3.1 Three-point Function

We will access the matrix element $\tilde{A}_{\mu\nu}(\tau)$ through the following lattice three point correlation function

$$\begin{aligned} C_{\mu\nu}(\tau,t_P) &= \sum_{\vec{x}_f,\vec{x}_c} \langle T\{\pi^0(x_f)j_\nu^\dagger(x_c)j_\mu^\dagger(x_i)\}\rangle e^{i\vec{p}\vec{x}_f}e^{-i\vec{q}_1\vec{x}_c} \\ &= \langle T\{\pi^0(\vec{p},t_f)j_\nu^\dagger(\vec{q}_1,t_c)j_\mu^\dagger(\vec{x}_i=\vec{0},t_i)\}\rangle, \end{aligned} \tag{5.5}$$

where the pseudoscalar has an outgoing momentum $\vec{p}$ at late times t_f, and the vector current at the insertion t_c has an incoming momentum $\vec{q}_1$. The vector current at the source t_i is at position $\vec{x}_i$ and automatically picks up an incoming momentum $\vec{p}-\vec{q}_1$ by translation invariance, or equivalently conservation of momentum. $\tau = t_c - t_i$ is the temporal separation of the vector currents, and $t_P = \min(t_f - t_i, t_f - t_c)$ is the minimal temporal separation between the pseudoscalar and the nearest vector current.

In the limit that the pion annihilation operator $\pi^0(\vec{p},t_f)$ is in the distant future, $t_f \gg t_i, t_c$, the Euclidean matrix element in Eq. (5.4) can be recovered from the three-point function. In the following, we will suppress the dependence on momenta and spatial positions, and find for $\tau > 0$

$$\begin{aligned} C_{\mu\nu} &\approx e^{-E_\pi(t_f-t_c)}\frac{Z_\pi}{2E_\pi}\left\langle \pi^0(\vec{p})\left|j_\mu^\dagger(0)j_\nu^\dagger(-\tau)\right|0\right\rangle \\ &= e^{-E_\pi(t_f-t_i)}\frac{Z_\pi}{2E_\pi}\left\langle \pi^0(\vec{p})\left|j_\mu^\dagger(\tau)j_\nu^\dagger(0)\right|0\right\rangle \end{aligned} \tag{5.6}$$

and for $\tau < 0$

$$\begin{aligned} C_{\mu\nu} &\approx e^{-E_\pi(t_f - t_i)} \frac{Z_\pi}{2E_\pi} \left\langle \pi^0(\vec{p}) \left| j_\nu^\dagger(0) j_\mu^\dagger(\tau) \right| 0 \right\rangle \\ &= e^{-E_\pi(t_f - t_c)} \frac{Z_\pi}{2E_\pi} \left\langle \pi^0(\vec{p}) \left| j_\nu^\dagger(-\tau) j_\mu^\dagger(0) \right| 0 \right\rangle \end{aligned} \tag{5.7}$$

where

$$Z_\pi \equiv \left\langle 0 | \pi^0(\vec{0}, 0) | \pi^0(\vec{p}) \right\rangle \tag{5.8}$$

Given these limiting expressions, we define

$$\tilde{\mathcal{A}}_{\mu\nu} = \frac{2E_\pi}{Z_\pi} e^{E_p(t_f - t_c)} C_{\mu\nu} \tag{5.9}$$

This amplitude is related to that in Eq. (5.3) via a time reversal transformation as we will show.

The vector current can be decomposed into definite isospin combinations.

$$j_\mu = \frac{1}{6} j_\mu^{0,0} + \frac{1}{2} j_\mu^{1,0} \tag{5.10}$$

Keeping only the isospin preserving pieces of the amplitude $C_{\mu\nu}$, we have

$$\begin{aligned} C_{\mu\nu} &= \frac{1}{12} \left(\left\langle \pi^0 j_\nu^{1,0\dagger} j_\mu^{0,0\dagger} \right\rangle + \left\langle \pi^0 j_\nu^{0,0\dagger} j_\mu^{1,0\dagger} \right\rangle \right) \\ &= \frac{1}{6} \left\langle \pi^0 j_\nu^{1,0\dagger} j_\mu^{0,0\dagger} \right\rangle \end{aligned} \tag{5.11}$$

At finite lattice spacing, isospin symmetry is broken in Wilson twisted mass lattice QCD, which is an $\mathcal{O}(a^2)$ effect independently of the twist angle, cf. Ref. [81]. By only considering the isospin preserving pieces of the amplitude, these artefacts can be avoided.

Next we study how the amplitudes defined in our conventions are related to time reversed counterparts. The twisted time reversal transformation of our operators is given in App. A.1.4. Let us take the neutral-pion isospin-projected amplitude for

$C_{\mu\nu}$. The twisted time reversal transformation symmetry means that it is equal to

$$\begin{aligned} C_{\mu\nu} &= \frac{1}{6}\left\{ \begin{array}{ll} \langle \pi^0(t_f) j_\nu^{0,0}(t_c)^\dagger j_\mu^{1,0}(t_i)^\dagger \rangle, & \tau > 0 \\ \langle \pi^0(t_f) j_\mu^{1,0}(t_i)^\dagger j_\nu^{0,0}(t_c)^\dagger \rangle, & \tau < 0 \end{array} \right\} \\ &= \frac{1}{6}\left\{ \begin{array}{ll} -\langle j_\mu^{1,0}(-t_i) j_\nu^{0,0}(-t_c) \pi^0(-t_f)^\dagger \rangle, & \tau > 0 \\ -\langle j_\nu^{0,0}(-t_c) j_\mu^{1,0}(-t_i) \pi^0(-t_f)^\dagger \rangle, & \tau < 0 \end{array} \right\} \end{aligned} \tag{5.12}$$

Then for large time separations $t_f \gg t_c, t_i$, the three-point amplitude takes the form

$$C_{\mu\nu} \to -\frac{Z_\pi^*}{2E_\pi} e^{-E_\pi t_f} \frac{1}{6}\left\{ \begin{array}{ll} \langle 0 | j_\mu^{1,0}(-t_i) j_\nu^{0,0}(-t_c) | \pi^0(\vec{p}) \rangle, & \tau > 0 \\ \langle 0 | j_\nu^{0,0}(-t_c) j_\mu^{1,0}(-t_i) | \pi^0(\vec{p}) \rangle, & \tau < 0 \end{array} \right\} \tag{5.13}$$

$$= -\frac{Z_\pi^*}{2E_\pi} e^{-E_\pi (t_f - t_c)} \frac{1}{6}\left\{ \begin{array}{ll} \langle 0 | j_\mu^{1,0}(\tau) j_\nu^{0,0}(0) | \pi^0(\vec{p}) \rangle, & \tau > 0 \\ \langle 0 | j_\nu^{0,0}(0) j_\mu^{1,0}(\tau) | \pi^0(\vec{p}) \rangle, & \tau < 0 \end{array} \right\} \tag{5.14}$$

Therefore we find in the limit $t_f \gg t_i, t_c$

$$\tilde{\mathcal{A}}_{\mu\nu} = -\frac{Z_\pi^*}{Z_\pi} \tilde{A}_{\mu\nu} \tag{5.15}$$

I.e. our definition of $\tilde{\mathcal{A}}_{\mu\nu}$ differs from the standard Mainz definition $\tilde{A}_{\mu\nu}$ by at most a phase. For the pion, the overlap factor is set to be $Z_\pi = Z_\pi^* = F_\pi m_\pi^2 / m_{\mathrm{PCAC}} > 0$ by the PCAC relation with the choice of pion operator used here, cf. [66, 67, 123]. Thus our definition of $\tilde{\mathcal{A}}_{\mu\nu}$ differs from the standard Mainz definition by a sign only, which is always included going forward such that the amplitude with contracted Lorentz indices, given in Eq. (5.25), is real and positive.

One then constructs

$$\tilde{A}_{\mu\nu}(\tau) = \frac{2E_\pi}{Z_\pi} \lim_{t_P \to \infty} e^{E_\pi (t_f - t_0)} C_{\mu\nu}(\tau, t_P). \tag{5.16}$$

We use gauge ensembles produced by the Extended Twisted Mass Collaboration (ETMC) in isospin-symmetric QCD (isoQCD) with $N_f = 2+1+1$ flavours of Wilson Clover twisted mass quarks are used, with quark masses tuned very close to their physical values. Some properties of the used ensemble can be found in Tab. 5.1, for more details see Refs. [40, 100, 103–105].

Ensemble	V/a^4	N_{conf}	β	a [fm]	$a\mu_l$	M_π [MeV]	L [fm]	$M_\pi L$
cB211.072.64	$64^3 \cdot 128$	748	1.778	0.07961(13)	0.00072	140.2(2)	5.09	3.62
cC211.060.80	$80^3 \cdot 160$	397	1.836	0.06821(12)	0.00060	136.7(2)	5.46	3.78
cD211.054.96	$96^3 \cdot 192$	495	1.900	0.05692(10)	0.00054	140.8(2)	5.46	3.90

Table 5.1: Parameters of the ETMC ensembles for the analysis presented in this work, adapted from [40]. Further paramters can be found in [40, 100, 103–105].

We perform our calculation for fermion fields in the twisted basis denoted χ related to the usual light fermion doublet $\psi = (u, d)$ through the twist transformation $(\psi, \bar{\psi}) = (e^{i\pi\gamma_5\tau^3/4}\chi, \bar{\chi}e^{i\pi\gamma_5\tau^3/4})$ which removes the twisted mass term in the action. We define the normalization of our operators to be convenient in the twisted basis, as shown in App. A.1.

In the twisted mass formulation, the three point amplitude Eq. (5.5) contains disconnected contributions in which the pion contracts with itself. These include a singly disconnected contribution which correlates the neutral pion loop with the connected vector-vector two point function, as well as a doubly disconnected contribution with three loops. For this reason, we instead consider the isospin-rotated amplitude

$$C^{\pm}_{\mu\nu} = -\frac{1}{6}\left\langle \pi^- j^{1,+\dagger}_\nu j^{0,0\dagger}_\mu \right\rangle + \frac{1}{6}\left\langle \pi^+ j^{1,-\dagger}_\nu j^{0,0\dagger}_\mu \right\rangle, \tag{5.17}$$

which does not contain a pion loop disconnected contribution. This amplitude only contains connected and vector current disconnected ("V-disconnected") contributions, depicted in Fig. 5.2. The rotated amplitude is related to Eq. (5.5) by lattice artifacts of order $O(a^2)$ due to isospin breaking away from the continuum limit in twisted mass lattice QCD. These artifacts are accounted for in the final continuum extrapolation.

To confirm the relation between Eq. (5.11) and Eq. (5.17), note that the vectorial isospin transformation acts on fields in the twisted basis as

$$\chi(x) \to e^{-i\omega\gamma_5\tau_3/2}e^{i\theta_a\tau_a/2}e^{i\omega\gamma_5\tau_3/2}\chi(x), \tag{5.18}$$

$$\bar{\chi}(x) \to \bar{\chi}(x)e^{i\omega\gamma_5\tau_3/2}e^{-i\theta_a\tau_a/2}e^{-i\omega\gamma_5\tau_3/2}. \tag{5.19}$$

where we have $\omega = \pi/2$ for maximal twist. Consider the rotation $\theta_1 = \theta_3 = 0$,

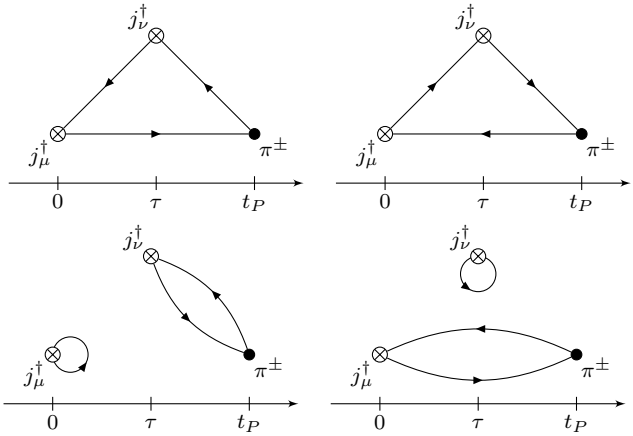

Figure 5.2: Wick contractions contributing to $C^{\pm}_{\mu\nu}(\tau, t_P)$. These are the connected (top row), and pseudoscalar disconnected ("P-disconnected", bottom row) diagrams. Note that the connected diagrams only involve light quarks, while the disconnected current loop in the P-disconnected diagrams can also be a strange or charm current loop, since s and c charms are present in the sea quarks.

$\theta_2 = \pi/2$, call this transformation I_y. For the neutral pion, one finds

$$\pi^0 = \bar{\chi}(x)\chi(x) \xrightarrow{I_y} -i\bar{\chi}(x)\gamma_5(\tau^+ + \tau^-)\chi(x) = -i(\pi^+ + \pi^-). \tag{5.20}$$

Similarly the vector current operators transform as

$$j_\mu^{0,0} \xrightarrow{I_y} j_\mu^{0,0}, \tag{5.21}$$

$$j_\mu^{1,0} \xrightarrow{I_y} ij_\mu^{1,+} - ij_\mu^{1,-}. \tag{5.22}$$

Applying this to Eq. (5.11), the amplitude in Eq. (5.17) is recovered.

5.3.2 Kinematics

The pion momentum $\vec{p}$ is set through the pseudoscalar interpolating operator in Eq. (5.5), with the energy E_π imposed by the on-shell condition. Momentum conservation $\vec{p} = \vec{q}_1 + \vec{q}_2$ allows us to freely vary one of the two vector current momenta, for example $\vec{q}_1$, from the available finite-volume momenta $\vec{q}_1 = \frac{2\pi}{L}\vec{n},\ \vec{n} \in \mathbb{Z}^3$. In Eq. (5.3) we can also continuously vary ω_1, while ω_2 is given by energy conservation $E_\pi = \omega_1 + \omega_2$. The kinematical range accessible on the lattice can then be

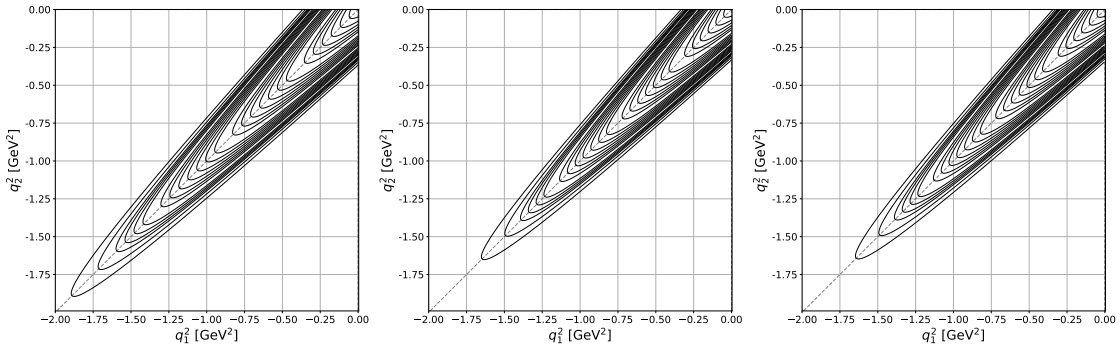

Figure 5.3: Range of photon virtualities spanned in our calculation on the ensembles cB211.072.64 (left) and cC211.060.80 (middle) and cD211.054.96 (right).

parametrized by the accessible virtualities of the electromagnetic currents,

$$\begin{aligned} q_1^2 &= \omega_1^2 - \vec{q}_1^2, \\ q_2^2 &= (E_\pi - \omega_1)^2 - (\vec{p} - \vec{q}_1)^2. \end{aligned} \tag{5.23}$$

For a resting pseudoscalar $\vec{p} = 0$, it holds that $E_\pi = m_\pi$ and $\vec{q}_2 = -\vec{q}_1$. In this case, the photon virtualities simplify to

$$\begin{aligned} q_1^2 &= \omega_1^2 - \vec{q}_1^2, \\ q_2^2 &= (m_\pi - \omega_1)^2 - \vec{q}_1^2. \end{aligned} \tag{5.24}$$

The condition $q_i^2 < 4m_\pi^2$, or equivalently $\sqrt{4m_\pi^2 + \vec{q}_1^2} + m_\pi < \omega_1 < \sqrt{4m_\pi^2 + \vec{q}_1^2}$ prevents the off-shell photon from turning into a real hadron state [119]. Fig. 5.3 depicts the kinematical range for 26 different choices of $|q_1|^2$ with $(2\pi/L)^2 \leq |\vec{q}_1|^2 \leq 32(2\pi/L)^2$ for the finite volumes accessible on the three distinct ensembles used in this work. For all three ensembles, the maximum momentum used in the evaluation of the three-point correlation function gives access to virtualities up to $|q_{1,2}^2| \approx 1.7\,\mathrm{GeV}^2$. Using Eqs. (5.1), (5.3) and (5.24) it is straightforward to show that the rest-frame $\tilde{A}_{\mu\nu}(\tau)$ vanishes when one or both Lorentz indices are temporal, while the spatial components can be written as

$$\tilde{A}_{ij}(\tau) = -im_\pi \epsilon_{ijk} q_1^k \tilde{A}(\tau). \tag{5.25}$$

Inverting the relation gives

$$\tilde{A}(\tau) = i\epsilon_{ijk}\frac{q_1^k}{m_\pi \vec{q}_1^2}\tilde{A}_{ij}(\tau), \tag{5.26}$$

where $\tilde{A}(\tau)$ is a scalar under the spatial rotation group. Since the full amplitude can be extracted from the scalar $\tilde{A}(\tau)$ in the rest frame, we focus on the evaluation of this scalar function for the remainder of this work.

We start from the lattice data $C_{\mu\nu}(\tau)$ by constructing $C(\tau)$ and averaging over equivalent momenta through the cubic group to increase statistics. Let

$$\mathcal{Q} = \{\{\vec{q}_{(i)}\} : \vec{q}_{(i)}^2 = \vec{q}^2, \vec{q}_{(i)} \neq -\vec{q}_{(j)} \forall i \neq j\} \tag{5.27}$$

be half the orbit of momentum $\vec{q}^2$ (i.e. to avoid double counting, it only contains $\vec{q}$ or $-\vec{q}$, not both). Then one takes

$$C(\tau) = \frac{1}{2|\mathcal{Q}|}\sum_{\vec{q}\in\mathcal{Q}} i\epsilon_{ijk}\frac{\vec{q}_k}{m_\pi q^2}C_{ij}(\tau), \tag{5.28}$$

which is related to $\tilde{A}(\tau)$ by Eq. (5.16).

5.3.3 Finite-time Extent Corrections

With periodic temporal boundaries, an operator inserted at a specified time may create or destroy states which will have or have wrapped around the lattice, i.e. backward propagating pions may contribute to the three-point correlation function. We study the asymptotic behaviour of the three-point correlation function of the backwards propagating pions, again considering the limit that the pion is in the distant future, $t_f \gg t_i, t_c$, with $\tau = t_c - t_i$ and hiding the dependence on momenta and spatial positions. We have for $\tau > 0$

$$C_{\mu\nu} \approx e^{-E_\pi(T-(t_f-t_c)-\tau)}\frac{Z_\pi(\vec{p})}{2E_\pi}\left\langle \pi^0(\vec{p}) \left| j_c^\dagger(0) j_i^\dagger(-\tau) \right| 0 \right\rangle \tag{5.29}$$

and for $\tau < 0$

$$C_{\mu\nu} \approx e^{-E_\pi(T-(t_f-t_i)+\tau)} \frac{Z_\pi(\vec{p})}{2E_\pi} \left\langle \pi^0(\vec{p}) \left| j_i^\dagger(0) j_c^\dagger(\tau) \right| 0 \right\rangle , \tag{5.30}$$

such that

$$\begin{aligned} \tilde{A}_{\mu\nu}(\tau > 0) &= \frac{2E_\pi}{Z_\pi} \lim_{t_P \to \infty} e^{E_\pi(t_f - t_0)} C_{\mu\nu}(\tau, t_P) \left[1 - e^{-E_\pi(T-2t_P-\tau)}\right]^{-1} , \\ \tilde{A}_{\mu\nu}(\tau < 0) &= \frac{2E_\pi}{Z_\pi} \lim_{t_P \to \infty} e^{E_\pi(t_f - t_0)} C_{\mu\nu}(\tau, t_P) \left[1 - e^{-E_\pi(T-2t_P+\tau)}\right]^{-1} . \end{aligned} \tag{5.31}$$

Examples for $\tilde{A}(\tau)$ including finite time corrections are shown in Fig. 5.4.

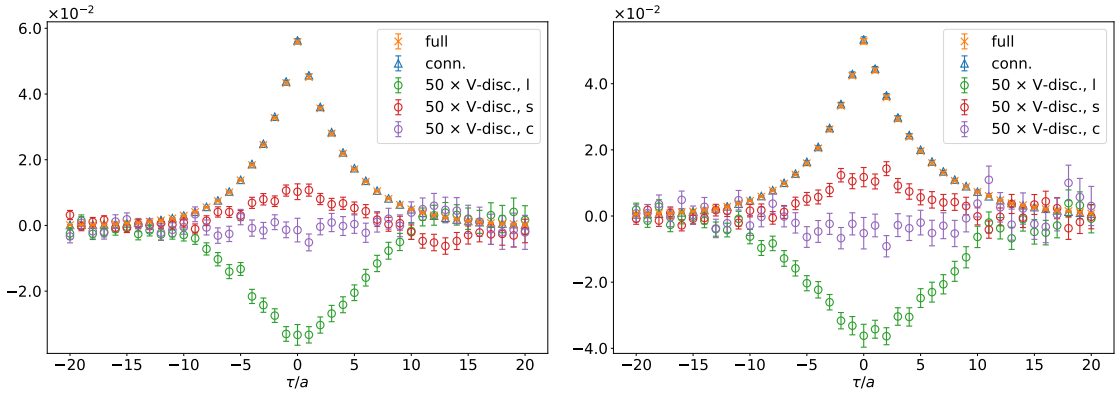

Figure 5.4: $\tilde{A}(\tau)$ for $\tau/a \in [-20, 20]$ with $|\vec{q}_1|^2 = 10(2\pi/L)^2$ including finite-time extent corrections on the ensembles cC211.060.80 (left) and cD211.054.96 (right). Show in orange is the full $\tilde{A}(\tau)$, in blue the connected contribution, and in green, red and purple the V-disconnected contributions (multiplied by 50 for easier comparison) with a light, strange and charm current loop, respectively.

5.3.4 Tail Fits

The extraction of the transition form factor in principle require access to $\tilde{A}(\tau)$ for arbitrary τ, cf. Eq. (5.3). To estimate the amplitude over the whole temporal range we use two phenomenological models, namely the VMD and the LMD model, cf. [118, 124, 125]. They were chosen since they allow global fits to all momenta in our data simultaneously and since they reproduce certain constraints explained in the following. In the chiral limit and at low energy, a fermionic triangle diagram

contributes an extra term, the so-called Adler-Bell-Jackiw (ABJ) anomaly [167, 168], to the PCAC relation, this restrains the form factor to

$$\mathcal{F}_{\pi^0\gamma\gamma}(0,0) = \frac{1}{4\pi^2 F_\pi}, \tag{5.32}$$

with $F_\pi = 92.3(1)\,\text{MeV}$ the pion decay constant [12]. The Brodsky-Lepage behaviour constrains the single-virtual form factor at large Euclidean (spacelike) momentum [169–171]. At leading order in α_s, one finds

$$\mathcal{F}_{\pi^0\gamma\gamma}(-Q^2,0) \overset{Q^2\to\infty}{\longrightarrow} \frac{2F_\pi}{Q^2}. \tag{5.33}$$

This behaviour is reproduced by the VMD model, but the LMD model tends to a constant at large Eucidean momenta in the single-virtual form factor. Finally, the operator product expansion (OPE) at short distances [172, 173] restricts the doubly-virtual form factor where both momenta become large at the same time, one finds in the chiral limit

$$\mathcal{F}_{\pi^0\gamma\gamma}(-Q^2,-Q^2) \overset{Q^2\to\infty}{\longrightarrow} \frac{2F_\pi}{3}\left[\frac{1}{Q^2} + \mathcal{O}\left(\frac{1}{Q^4}\right)\right]. \tag{5.34}$$

This behaviour is reproduced by the LMD model, but the VMD model in this case falls off as $1/Q^4$ [66].
The VMD and LMD form factors are given by

$$\mathcal{F}^{VMD}_{\pi^0\gamma\gamma} = \frac{\alpha M_V^4}{(M_V^2 - q_1^2)(M_V^2 - q_2^2)} \tag{5.35}$$

and

$$\mathcal{F}^{LMD}_{\pi^0\gamma\gamma} = \frac{\alpha M_V^4 + \beta(q_1^2 + q_2^2)}{(M_V^2 - q_1^2)(M_V^2 - q_2^2)}, \tag{5.36}$$

respectively, where $\alpha = \alpha_{th} = 1/(4\pi^2 F_\pi) = 0.274\,\text{GeV}^{-1}$ to reproduce the ABJ anomaly, M_V usually is set to the ρ meson mass and $\beta = \beta^{OPE} = -F_\pi/3 = -0.0308\,\text{GeV}$ to reproduce the leading OPE prediction [66, 124, 125]. We will treat α, M_V and β as free model parameters when fitting the models to our data. For the LMD amplitude

fit function one finds

$$\tilde{A}^{LMD}(\tau \gtrless 0) = \pm \frac{1}{2}\Bigg[\frac{\alpha M_V^4 + \beta(2M_V^2 + m_\pi^2 \mp 2m_\pi\sqrt{M_V^2+|\vec{q}_1|^2})}{m_\pi\sqrt{M_V^2+|\vec{q}_1|^2}(2\sqrt{M_V^2+|\vec{q}_1|^2} \mp m_\pi)} e^{\mp\sqrt{M_V^2+|\vec{q}_1|^2}\tau} - \frac{\alpha M_V^4 + \beta(2M_V^2 + m_\pi^2 \pm 2m_\pi\sqrt{M_V^2+|\vec{q}_1|^2})}{m_\pi\sqrt{M_V^2+|\vec{q}_1|^2}(2\sqrt{M_V^2+|\vec{q}_1|^2} \pm m_\pi)} e^{-(m_\pi\pm\sqrt{M_V^2+|\vec{q}_1|^2})\tau}\Bigg] \tag{5.37}$$

using Eqs. (5.3) and (5.36) and noting that $\tilde{A}_{\mu\nu}$ is essentially the Laplace transform of the form factor [66]. The VMD fit function is obtained by setting $\beta = 0$.

In particular the VMD model is not expected to capture the short-distance behavior of $\tilde{A}(\tau)$ well, but both models capture the long-distance behavior accurately. However, we will use the lattice data directly for the short-distance region as discussed in Sec. 5.4.1.

5.4 Transition Form Factor

5.4.1 Numerical Integration

To obtain the transition form factors, we need to evaluate

$$\mathcal{F}_{\pi^0\gamma\gamma}(q_1^2, q_2^2) = \int_{-\infty}^{\infty} d\tau\, \tilde{A}(\tau) e^{\omega_1\tau}, \tag{5.38}$$

where for a given momentum orbit $|\vec{q}_1|^2$ the squared four-momenta q_1^2 and q_2^2 are given by Eq. (5.24). While $\tilde{A}(\tau)$ decreases exponentially quickly for $|\tau| \gg 1$, the exponential factor $e^{\omega_1\tau}$ still probes a tail of $\tilde{A}(\tau)$ if $|\omega_1|$ is sufficiently large. This makes the numerical integration difficult: Since the signal-to-noise ratio decreases when going to larger $|\tau|$, fluctuations in one of the tails due to the small signal-to-noise ratio are exponentially enhanced. We observe that this effect is small for the diagonal case with $q_1^2 = q_2^2 \Rightarrow \omega_1 = m_\pi/2$, mainly since at the physical point, m_π is small, and severe for the single-virtual case $q_1^2 = 0 \Rightarrow \omega_1 = |\vec{q}_1|$ due to the strong dependence of ω_1 on the used momentum orbit, especially for the larger momentum orbits. For

an illustration, see Fig. 5.5. For choices of virtualities between these two cases, the exponential enhancement gets more and more pronounced when going from the diagonal to the single-virtual case. Further, the range of integration over the lattice data is limited naturally due to the finite extent of the lattice.

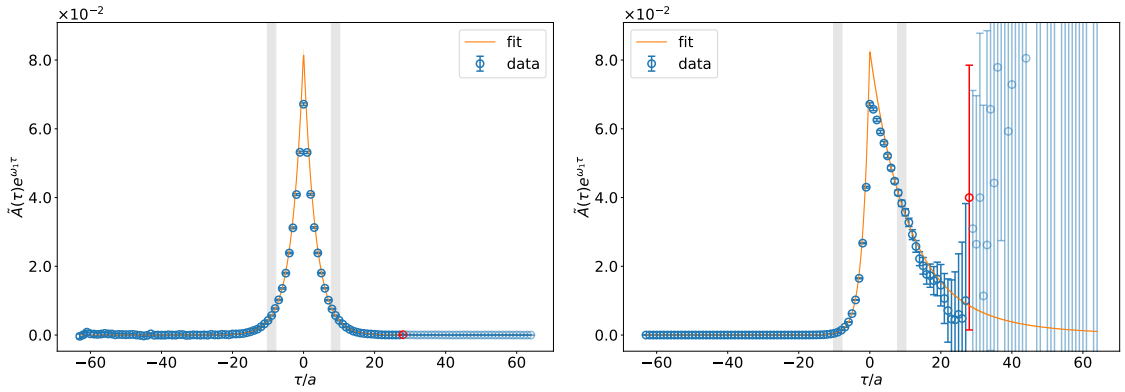

Figure 5.5: Integrands $\tilde{A}(\tau)e^{\omega_1\tau}$ with $|\vec{q}_1|^2 = 6(2\pi/L)^2$ on the ensemble cB211.072.64, comparing diagonal kinematics $q_1^2 = q_2^2$ (left) and single-virtual kinematics $q_2^2 = 0$ (right). Shown in blue is the integrand from lattice data and in orange from a correlated LMD fit to $\tilde{A}(\tau)$ according to Eq. (5.37). The fit was done globally across all momentum orbits $(2\pi/L)^2 \leq |\vec{q}_1|^2 \leq 32(2\pi/L)^2$ with fit range $[-10, -8] \cup [8, 10]$, indicated by the grey bands, giving $\chi^2/\text{d.o.f.} = 1.01$. The red point indicates the timeslice where the pseudoscalar operator is inserted, while the greyed out points are those with a timeordering not satisying the one from Eq. (5.4). For the diagonal kinematics, $a\omega_1 = am_\pi/2 \approx 0.028$, for the single-virtual kinematics, $a\omega_1 = a|\vec{q}_1| \approx 0.31$.

These issues are addressed by the introduction of cutoff times $\tau_{\text{cut}}^{L/R}$, with lattice data replaced by a fitted $\tilde{A}(\tau)$ for $\tau \geq \tau_{\text{cut}}^R$ and $\tau \leq \tau_{\text{cut}}^L$. In our analysis, we perform a global fit per jackknife or bootstrap sample to Eq. (5.37) across data at all available $\vec{q}_1$ and for values of τ selected from symmetrical fit ranges on both sides of the peak, i.e. $\tau \in [-\tau_{\text{max}}, -\tau_{\text{min}}] \cup [\tau_{\text{min}}, \tau_{\text{max}}]$. The left and right cutoff times are selected depending on the sign of ω_1 to include as much data as possible on the exponentially suppressed tail of the integrand, in particular by fixing $\tau_{\text{cut}}^L = T/2$ or $\tau_{\text{cut}}^R = T/2$ when $\omega_1 \geq 0$ or $\omega_1 < 0$, respectively. The choice of the remaining cutoff time is varied to assess the systematic error associated with this fitting choice.

Finally, we filter the choices of cutoff times and kinematics to demand that for a given momentum orbit and ω_1 a certain percentage of $\mathcal{F}_{\pi^0\gamma\gamma}(q_1^2, q_2^2)$ must come from

the lattice data. This is done to minimize the introduction of a model dependence in the final result.

5.4.2 z-Expansion

Integrating the amplitude for various choices of ω_1 in principle gives access to the form factor for any of the kinematics on the discrete orbits shown in Fig. 5.3. We then use the z-expansion proposed in [67] to extrapolate this data to the whole kinematical range. This is a model-independent way of extending the transition form factor to arbitrary photon momenta which is preconditioned to more easily reproduce the form factor structure. Following [67], the model independent fit form is constructed by first defining the conformal variables z_1 and z_2 [174]

$$z_k = \frac{\sqrt{t_c + Q_k^2} - \sqrt{t_c - t_0}}{\sqrt{t_c + Q_k^2} + \sqrt{t_c - t_0}}, \quad k \in \{1, 2\}, \tag{5.39}$$

where $t_c = 4m_\pi^2$, indicating the position of the branch cut due to the two-pion threshold. t_0 is a free parameter which can be tuned to optimize the rate of convergence. The optimal choice of t_0 for a given Q^2_{max} is

$$t_0 = t_c \left(1 - \sqrt{1 + Q^2_{max}/t_c}\right), \tag{5.40}$$

which reduces the maximum value of $|z_k|$ in the range $[0, Q^2_{max}]$. We use $Q^2_{max} = 4\,\mathrm{GeV}^2$ in the present study.

In terms of these conformal variables, one can write

$$\mathcal{F}_{\pi^0\gamma\gamma}(-Q_1^2, -Q_2^2) = \sum_{n,m=0}^{\infty} c_{nm} z_1^n z_2^m, \tag{5.41}$$

since the transition form factor is analytic for $|z_k| < 1$. The coefficients $c_{nm} = c_{mn}$ are symmetric due to the Bose symmetry. Note that $|z_k| < 1$, such that a fast convergence of the sum is expected. In practise, this means that it is sufficient to restrict the sum to $m, n \leq N$, where the maximum order N is chosen to reach a given accuracy. The transition form factor can be multiplied by an arbitrary analytical function

$P(Q_1^2, Q_2^2)$ and the resulting product expanded in powers of z_k. This allows for the preconditioning to more easily reproduce the form factor structure. As shown in [67], the choice

$$P(Q_1^2, Q_2^2) = 1 + \frac{Q_1^2 + Q_2^2}{M_V^2}, \tag{5.42}$$

where $M_V = 775.26(23)\,\mathrm{MeV}$ [12] is the ρ meson mass, leads to a parametrization of the transition form factor which decreases asymptotically as $1/Q^2$ in all directions in the momentum plane even at finite values of N, thus satisfying the momentum dependence of Eqs. (5.33) and (5.34). As shown in [175], to enforce the appropriate scaling at the two-pion threshold, the derivatives of the transition form factors with respect to z_k at $z_k = -1$ need to be fixed to zero, giving the expansion [67]

$$\begin{aligned} &P(Q_1^2, Q_2^2)\mathcal{F}_{\pi^0\gamma\gamma}(-Q_1^2, -Q_2^2) \\ &\qquad = \sum_{m,n=0}^{N} c_{nm} \left(z_1^n - (-1)^{N+n+1} \frac{n}{N+1} z_1^{N+1} \right) \\ &\qquad\qquad \times \left(z_2^m - (-1)^{N+m+1} \frac{m}{N+1} z_2^{N+1} \right). \end{aligned} \tag{5.43}$$

One possibility to obtain results in the continuum limit is to perform a combined fit to all three ensembles with a correction term for $\mathcal{O}(a^2)$ lattice artefacts by modifying the coefficients as

$$c_{nm}(a) = c_{nm}(0) + \delta_{nm} \left(\frac{a}{a_{\mathrm{ref.}}} \right)^2, \tag{5.44}$$

where we use the cC211.060.80 lattice spacing for $a_{\mathrm{ref.}}$.

In contrast to [67] and the recently published [166] we perform fully correlated fits to the modified z-expansion. We are using $N = 1, 2$ and variations $N = 1$ plus one additional coefficient, since usually at least two of the $N = 2$ coefficients are correlated with c_{11}, see Sec. 5.4.3. While we can only include $\mathcal{O}(10^2)$ data points per ensemble, we find that the resulting fits describe the lattice data well, even the cuts not included in the fit, as seen in the example in Fig. 5.6.

Note that the transition form factors obtained from Eq. (5.43) multiplied by Q^2 tend to a constant by construction, with predictions for the single-virtual and diagonal case, cf. Eqs. (5.33) and (5.34). We exclude analyses where the single-virtual transition

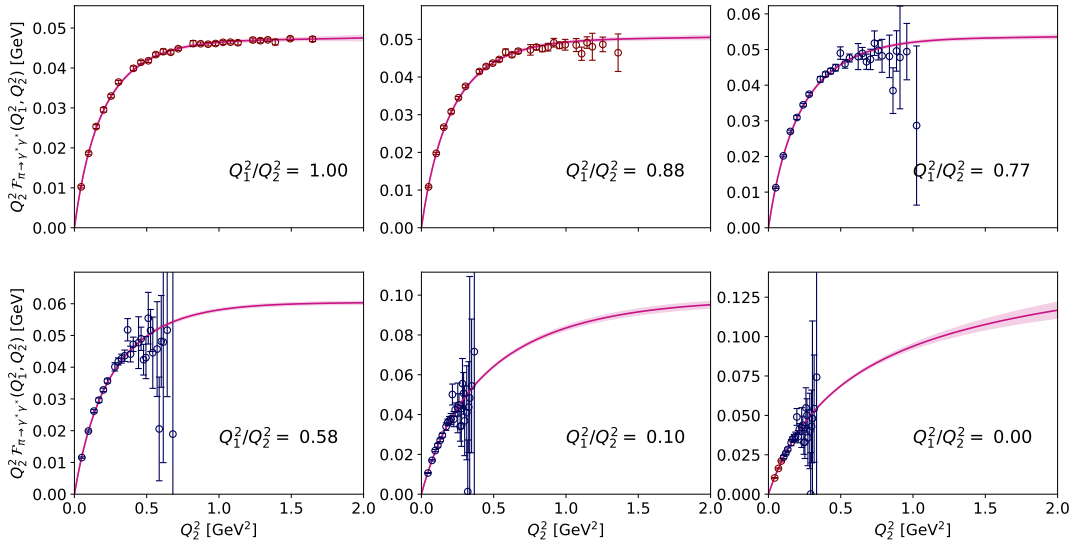

Figure 5.6: Correlated z-expansion fit to $\frac{q_2^2}{q_1^2} \in \{1.0, 0.88, 0.0\}$ on cC211.060.80, using c_{00}, c_{10}, c_{11} and c_{22}. Only TFF data points where at least 95% of the transition form factors come from lattice data (colored red for the used cuts) are included, for $\tilde{A}(\tau)$ a global LMD fit with fit range $[20, 21]$ and $\tau_{\text{cut}} = 23$ in lattice units is used. The reduced χ^2 are $\chi^2_{\tilde{A}}/\text{d.o.f} = 0.86$ and $\chi^2_{z-\text{exp.}}/\text{d.o.f} = 1.00$. Data in blue are shown for illustration only. The whole sampling is shown in Fig. 5.8.

form factor multiplied by Q^2 tends to a constant smaller than zero, since this clearly violates those predictions.

5.4.3 Sampling in the Momentum Plane

As illustrated in Fig. 5.3, the transition form factor obtained from the lattice is a continuous function of ω_1 for each spatial momentum orbit $|\vec{q}_1|^2$. In order to fit to the z-expansion, we need to sample choices of ω_1 to determine our input data first. In this work, we do so by selecting ω_1 corresponding to fixed choices of the ratio q_2^2/q_1^2, i.e. by finding the intersection between our available orbits and several diagonal "cuts" through the (q_1^2, q_2^2) plane. Because the underlying lattice data are identical for all choices of ω_1 within each orbit, data at nearby values of ω_1 are strongly correlated. A relatively sparse sampling is therefore possible without sacrificing useful inputs to the z-expansion fits. Both $q_2^2/q_1^2 = 0$ and $q_2^2/q_1^2 = 1$ are useful choices of ratio to include, the former since the single-virtual transition form factor plays an important

role later, and the latter since we get the best signal-to-noise ratio in the transition form factor there.

We found that correlated z-expansion fits with both $N = 1$ and $N = 2$ lead to a good quality of fit when including three or four such cuts. However, for $N = 2$, at least two of the coefficients c_{nm} are correlated in this case. Even when including only one of the $N = 2$ coefficients in conjunction with all three $N = 1$ coefficients, we find slight correlations between some of them. See Fig. 5.7 for an example using $c_{nm} = \{c_{00}, c_{10}, c_{11}, c_{22}\}$ with the corresponding correlation matrix given by

$$\mathrm{cor}(c_{nm}) = \begin{pmatrix} +1.00 & -0.30 & -0.39 & +0.31 \\ -0.30 & +1.00 & -0.05 & -0.14 \\ -0.39 & -0.05 & +1.00 & -0.88 \\ +0.31 & -0.14 & -0.88 & +1.00 \end{pmatrix}, \tag{5.45}$$

To get reliable estimates of the individual coefficients, it is desirable to only use a subset of the coefficients which are not strongly correlated. Furter, with $N \geq 3$ the fits in general do not converge.

We used the following procedure for the sampling in the momentum plane. For however many cuts we want to make we determine ω_1 such that $q_2^2/q_1^2 \in \{0, 1\}$ are included and that the arc length of the curve parametrized by ω_1 between neighbouring samples on $|\vec{q}_1|^2 = 32(2\pi/L)^2$ is constant. This fixes the ratios q_2^2/q_1^2 which we then use to determine the needed ω_1 on the other spatial momentum orbits. To better cover the close to single-virtual region, we also include a cut $q_2^2/q_1^2 = 0.1$ together with five cuts with equal arc length, cf. Fig. 5.8. We do correlated z-expansion fits per jackknife or bootstrap sample for a number of choices of three cuts (all combinations from the ones with equal arc length which include both the diagonal and single-virtual case, as well as the diagonal and closest to diagonal case plus the $q_2^2/q_1^2 = 0.1$ cut) from the six shown in Fig. 5.8 and for four cuts (with the diagonal, closest to diagonal, closest to single-virtual and single-virtual cut), while imposing a threshold for a minimal data content in the transition form factor of 95% to minimize the VMD and LMD model dependence as mentioned in Sec. 5.4.1.

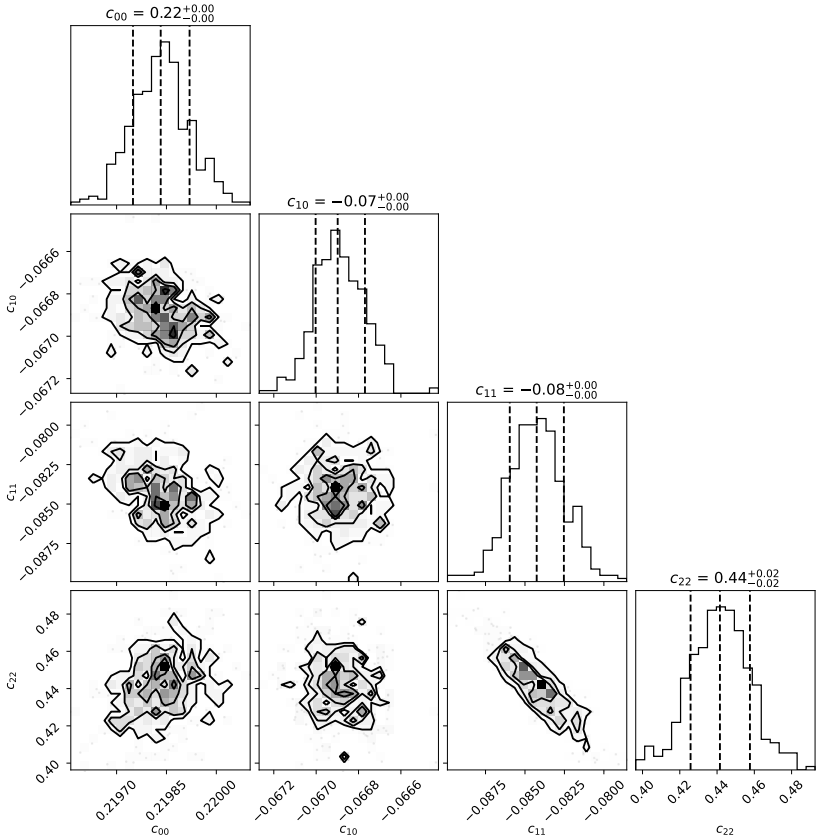

Figure 5.7: Cornerplot of a correlated z-expansion fit to $(q_2^2/q_1^2) \in \{1.0, 0.88, 0.0\}$ on cC211.060.80, using coefficients c_{00}, c_{10}, c_{11} and c_{22}. Only TFF data points where at least 95% of the transition form factors come from lattice data are included, for $\tilde{A}(\tau)$ a global LMD fit with fit range $[20, 21]$ and $\tau_{\text{cut}} = 23$ in lattice units is used. The reduced χ^2 are $\chi^2_{\tilde{A}}/\text{d.o.f} = 0.86$ and $\chi^2_{z-\text{exp.}}/\text{d.o.f} = 1.00$. Notice the clear (anti)correlation between c_{11} and c_{22} and the less severe (anti)correlations between all other coefficients except for c_{10} and c_{11} which are almost completely uncorrelated. The corresponding correlation matrix is given in Eq. (5.45). When including all $N = 2$ coefficients, it turns out that c_{20} and c_{21} are strongly correlated with c_{11} for almost all choices of parameters.

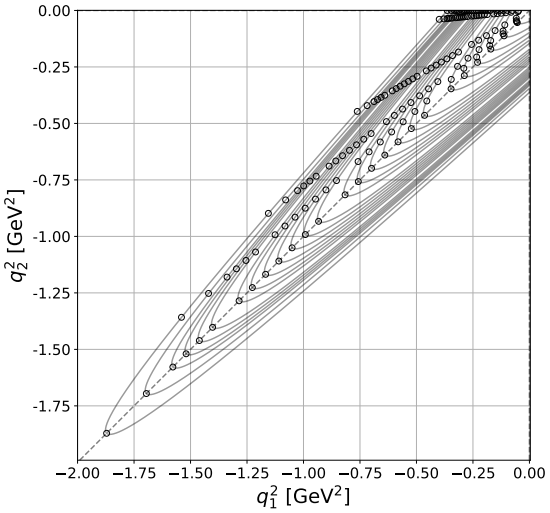

Figure 5.8: Sampling in the momentum plane used to extract $\mathcal{F}_{\pi^0\gamma\gamma}(q_1^2, q_2^2)$ over the whole kinematical range. Cuts $(q_2^2/q_1^2) \in \{1.0, 0.88, 0.78, 0.59, 0.1, 0.0\}$ on ensemble cB211.072.64.

5.4.4 Renormalization

As detailed in App. A.1, we use point-like (local) bare current operators instead of the exactly conserved one-point split vector currents $\tilde{j}_\mu{}^{0,0}$ and $\tilde{j}_\mu{}^{1,0}$ and the one-point split axial current $\tilde{j}_\mu{}^{1,\pm}$. The vector currents $\tilde{j}_\mu{}^{0,0}$ and $\tilde{j}_\mu{}^{1,0}$ are Noether currents associated with the flavor global vector transformations, i.e. they follow from Ward-Takahashi Identities (WIs), and the axial current $\tilde{j}_\mu{}^{1,\pm}$ follows from the axial WI. It is computationally much cheaper and easier to use the nonconserved local operators instead of the point split operators, but this must then be renormalized as discussed in the following.

As shown in [176–178], for LQCD with Wilson fermions, the conserved vector currents do not require renormalization, i.e. $Z_{\tilde{V}} = 1$, because of the existence of an exact WI, which at the same time implies that the local vector currents $j_\mu^{0,0}$ and $j_\mu^{1,0}$ are not conserved. However, the matrix elements of the local vector current coincide with those from the point split vector current in the continuum. It is further shown that the renormalization constant (RC) of the local vector current, Z_V, is finite and that it can only depend on the bare gauge coupling β (which controls the lattice spacing), i.e. $Z_V(\beta) \neq 1$. It is then shown in [40] that for our lattice setup, both $j_\mu^{0,0}$ and $j_\mu^{1,0}$

Ensemble	Z_V	Z_A
cB211.072.64	0.706378(16)	0.74284(23)
cC211.060.80	0.725405(13)	0.75841(16)
cD211.054.96	0.744105(11)	0.77394(10)

Table 5.2: Values of Z_V and Z_A for the ETMC ensembles which were used in this work, cf. [40].

are renormalized with the same RC.

Because of the chiral symmetry breaking Wilson term in the action, it is less straightforward to implement the axial symmetry, however, the PCAC is recovered in the continuum by using suitable renormalization conditions [177, 178]. It is shown in [176] that the WI for the one-point split axial current contains an additional term compared to the vector current case, coming from the variation of the Wilson term under axial transformations. Still, the local axial current can be used since $\hat{j}_\mu^{1,\pm} = \lim_{a\to 0} Z_{\tilde{A}} \tilde{j}_\mu^{1,\pm} = \lim_{a\to 0} Z_A j_\mu^{1,\pm}$ holds, with $\hat{j}_\mu$ the PCAC and $Z_{\tilde{A}}(\beta)$ and $Z_A(\beta)$ the point split and local axial current RCs, respectively.

For the ensembles used in this work, the RCs were calculated in [40] using a hadronic method based on the WI, employing a high statistics determination of the needed correlators. The resulting Z_V and Z_A are found in Tab. 5.2, and the corresponding renormalized local current operators are given by

$$j_{\mu,R}^{0,0} = Z_V j_\mu^{0,0}, \tag{5.46}$$

$$j_{\mu,R}^{1,0} = Z_V j_\mu^{1,0}, \tag{5.47}$$

$$j_{\mu,R}^{1,\pm} = Z_A j_\mu^{1,\pm}. \tag{5.48}$$

Note that the TFFs and the pion pole contributions to a_μ, after the transformation I_y, are renormalized with $Z_V Z_A$ and $Z_V^2 Z_A^2$, respectively. Further note that the errors on the RCs are negligible compared to the errors on the bare TFFs, such that we only use the central values of the RCs.

5.5 3d Integral Representation of the Contribution to a_μ

We follow [118] and use the three-dimensional integral representation for the pion pole contribution

$$a_\mu^{\pi-\text{pole}} = \left(\frac{\alpha}{\pi}\right)^3 \left[a_\mu^{\pi-\text{pole}(1)} + a_\mu^{\pi-\text{pole}(2)}\right], \tag{5.49}$$

where α is the fine structure constant,

$$\begin{aligned} a_\mu^{\pi-\text{pole}(1)} = &\int_0^\infty dQ_1 \int_0^\infty dQ_2 \int_{-1}^1 d\tau \\ &w_1(Q_1, Q_2, \tau)\mathcal{F}_{\pi^0\gamma\gamma}(-Q_1^2, -Q_3^2)\mathcal{F}_{\pi^0\gamma\gamma}(-Q_2^2, 0), \end{aligned} \tag{5.50}$$

and

$$\begin{aligned} a_\mu^{\pi-\text{pole}(2)} = &\int_0^\infty dQ_1 \int_0^\infty dQ_2 \int_{-1}^1 d\tau \\ &w_2(Q_1, Q_2, \tau)\mathcal{F}_{\pi^0\gamma\gamma}(-Q_1^2, -Q_2^2)\mathcal{F}_{\pi^0\gamma\gamma}(-Q_3^2, 0). \end{aligned} \tag{5.51}$$

The integration is performed over the magnitudes Q_1, Q_2 of two of the four-momenta and $\tau = \cos\theta$ describing the angle θ between them, with the third four-momentum fixed by $Q_3^2 = Q_1^2 + Q_2^2 + 2Q_1Q_2\tau$. The weight functions w_1 and w_2 are given by

$$w_1(Q_1, Q_2, \tau) = \left(-\frac{2\pi}{3}\right)\sqrt{1-\tau^2}\frac{Q_1^3 Q_2^3}{Q_2^2 + m_\pi^2} I_1(Q_1, Q_2, \tau), \tag{5.52}$$

$$w_2(Q_1, Q_2, \tau) = \left(-\frac{2\pi}{3}\right)\sqrt{1-\tau^2}\frac{Q_1^3 Q_2^3}{(Q_1+Q_2)^2 + m_\pi^2} I_2(Q_1, Q_2, \tau), \tag{5.53}$$

where the functions $I_{1,2}$ are given in App. A.2. Note that $w_{1,2}$ are both dimensionless and $w_{1,2}(Q_1, Q_2, \tau) \to 0$ for $Q_{1,2} \to 0$ and for $\tau \to \pm 1$. Further, w_2 is symmetric under the exchange of Q_1 and Q_2. In [118], the weight functions for the pion are studied and discussed in detail. One finds that the momentum region $Q_{1,2} \leq 0.5\,\text{GeV}$ is the most important in Eqs. (5.50) and (5.51) for $a_\mu^{\pi-\text{pole}}$. For some examples, see Fig. 5.9. In particular, note that $w_2(Q_1, Q_2, \tau)$ is roughly an order of magnitude smaller than $w_1(Q_1, Q_2, \tau)$.

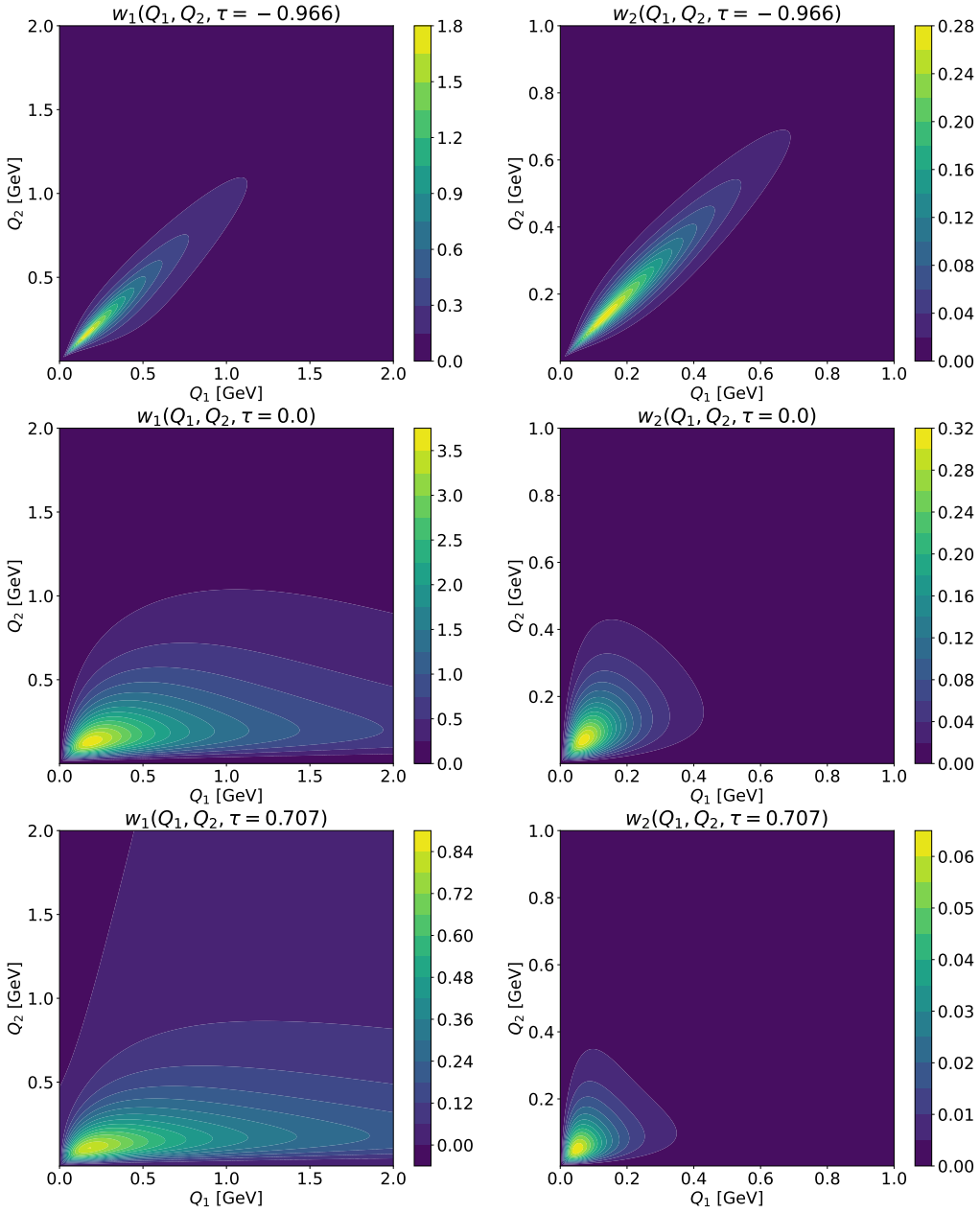

Figure 5.9: Weight functions $w_1(Q_1, Q_2, \tau)$ (left) and $w_2(Q_1, Q_2, \tau)$ (right) for the pion for momenta Q_1 and Q_2 with a selection of $\tau = \cos\theta$, corresponding from top to bottom to $\theta \in \{165°, 90°, 45°\}$. Note the different momentum range for and magnitude of w_2 as well as its symmetry with respect to $Q_1 \leftrightarrow Q_2$.

By introducing a momentum cutoff Λ, i.e. by replacing

$$\int_0^\infty dQ_{1,2} \longrightarrow \int_0^\Lambda dQ_{1,2} \tag{5.54}$$

in Eqs. (5.50) and (5.51), one can estimate the importance of various momentum bins. Though the cutoffs are only directly imposed on $Q_{1,2}$, they imply a cutoff of $Q_3 \leq 2\Lambda$ on the third momentum as well. We find that the integrals saturate rapidly, such that we get around 85% of the total result with $\Lambda = 1\,\text{GeV}$ and around 90% with $\Lambda = 1.5\,\text{GeV}$, i.e. from momentum regions with strong data support from our lattice calculation. An example of this is shown in Fig. 5.10. Again, we integrate separately for each jackknife or bootstrap sample to consistently propagate the errors.

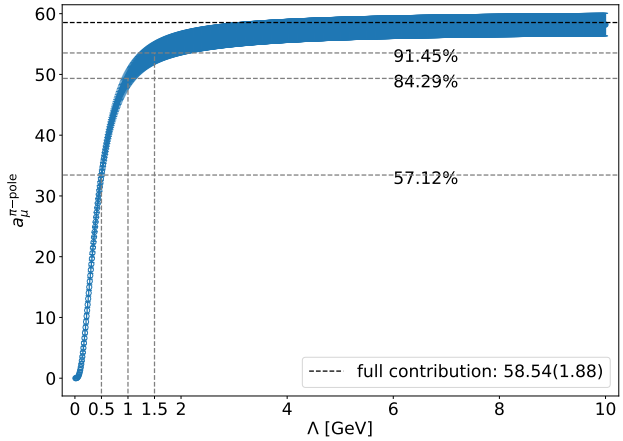

Figure 5.10: Contribution to $a_\mu^{\pi-\text{pole}}$ for increasing cutoff Λ for ensemble cC211.060.80, using a $N = 2$ correlated z-expansion fit to $(q_2^2/q_1^2) \in \{1.0, 0.88, 0.1, 0.0\}$. Only TFF data points where at least 95% of the transition form factors come from lattice data are included, for $\tilde{A}(\tau)$ a global LMD fit with fit range $[7, 8]$ and $\tau_{\text{cut}} = 26$ in lattice units is used. The reduced χ^2 are $\chi^2_{\tilde{A}}/\text{d.o.f} = 0.85$ and $\chi^2_{z-\text{exp.}}/\text{d.o.f} = 1.02$. Indicated is the saturation at $\Lambda \in \{0.5, 1.0, 1.5\}$ GeV as well as the value of the full contribution for this particular choice of parameters.

5.6 Decay Width and Slope Parameter

To leading order in the fine structure constant α, the transition form factors determine the partial decay width through

$$\Gamma(\pi \to \gamma\gamma) = \frac{\pi\alpha^2 m_\pi^3}{4} \left|\mathcal{F}_{\pi^0\gamma\gamma}(0,0)\right|^2 . \tag{5.55}$$

The neutral pion decay width has been measured in the PrimEx and PrimEx-II experiments [179,180] with a combined result of $\Gamma(\pi \to \gamma\gamma) = 7.802(52)_{\text{stat}}(105)_{\text{sys}}\,\text{eV}$.

Further, the transition form factors can be used to extract the slope parameter

$$b_\pi = \frac{1}{\mathcal{F}_{\pi^0\gamma\gamma}(0,0)} \frac{\mathrm{d}\mathcal{F}_{\pi^0\gamma\gamma}(q^2,0)}{\mathrm{d}q^2}\bigg|_{q^2=0}, \tag{5.56}$$

thus providing input for determining the electromagnetic interaction radius. The averaged experimental result for the slope parameter is $b_\pi = 1.84(17)\,\text{GeV}^{-2}$ [12].

These quantities are easily extracted from the form of the z-expansion fit at $(q_1^2, q_2^2) = (0,0)$. The value of $\mathcal{F}_{\pi^0\gamma\gamma}(0,0)$ comes directly from the z-expansion fit, while the derivative can be acquired by differentiating the form of the z-expansion in Eq. (5.43) with respect to $-Q_1^2$, yielding the slope parameter

$$\begin{aligned}
b_\pi &= -\frac{d}{dQ_1^2} \ln \mathcal{F}_{\pi^0\gamma\gamma}(-Q_1^2, 0)|_{Q_1^2=0} \\
&\approx \frac{d}{dQ_1^2} \ln P(Q_1^2, 0)|_{Q_1^2=0} \\
&\quad - \frac{d}{dQ_1^2} \ln \Big[\sum_{m,n=0}^{N} c_{nm} \left(z_1^n - (-1)^{N+n+1} \frac{n}{N+1} z_1^{N+1} \right) \\
&\qquad\qquad \times \left(z_2^m - (-1)^{N+m+1} \frac{m}{N+1} z_2^{N+1} \right) \Big]_{Q_{1,2}^2=0} \\
&= \frac{1}{M_V^2} - \frac{1}{z_1} \frac{dz_1}{dQ_1^2} \Big[\sum_{\substack{m=0 \\ n=1}}^{N} n c_{nm} \left(z_1^n - (-1)^{N+n+1} z_1^{N+1} \right) \\
&\qquad\qquad \times \left(z_2^m - (-1)^{N+m+1} \frac{m}{N+1} z_2^{N+1} \right) \Big]_{Q_{1,2}^2=0} .
\end{aligned} \tag{5.57}$$

The term in square brackets can be directly evaluated, and the derivative of the conformal parameter is given by

$$\frac{1}{z_1}\frac{dz_1}{dQ_1^2}\bigg|_{Q_1^2=0} = \frac{1}{t_0}\sqrt{1-t_0/t_c}. \tag{5.58}$$

5.7 AIC Information Criterion

Due to different choices for the parameters, each analysis chain, defined by all considered choices of parameters for a given set of cuts in the momentum plane, yields $\mathcal{O}(10^3 - 10^4)$ values for $a_\mu^{\pi-\text{pole}}$, $\Gamma(\pi \to \gamma\gamma)$ and b_π. The parameters we can choose are the fit range and fit model in the fit to $\tilde{A}(\tau)$, τ_{cut} when constructing the transition form factors and finally the included cuts in the momentum plane in the fit to the modified z-expansion. For the remainder of this section such a choice of parameters is called an "analysis". A priori, only fits with χ^2/d.o.f close to 1 are included in an analysis chain for the single ensemble analyses. For the combined z-expansion fits the input $\tilde{A}(\tau)$ fit ranges and τ_{cut} were chosen to be similar in physical units across all ensembles, using $t_{min} \in [0.48, 1.27]$ fm, $t_{max} \in [0.64, 1.43]$ fm and $\tau_{\text{cut}} \in [1.35, 2.07]$ fm on cB211.072.64 as a reference and remaining within 10% of these physical-units values for the cC211.060.80 and cD211.054.96 ensembles. The fits across all ensembles are of relatively good quality, with χ^2 values in the range $1 \lesssim \chi^2_{\tilde{A}}/\text{d.o.f} \lesssim 2.4$. We calculate the statistical errors for each analysis using the jackknife resampling procedure, with configurations spaced far enough such that there is virtually no autocorrelation between the input data $\tilde{A}(\tau)$.

To take a weighted average of estimates under various analysis choices in an analysis chain, we use a modified version of the Akaike Information Criterion (AIC) [164, 181]. Closely following the method introduced in [163] and [38], the model averaging proceeds as follows. For a target observable y, here $a_\mu^{\pi-\text{pole}}$, $\Gamma(\pi \to \gamma\gamma)$ or b_π, we build a histogram from the different analyses, assigning to each analysis a weight given by the AIC. This criterion is derived from the Kullback-Leibler divergence, which measures the distance of a fit function from the true distribution of the points.

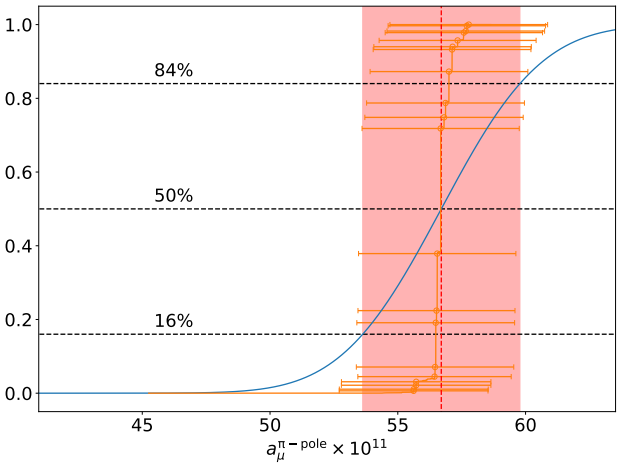

Figure 5.11: Cumulative distribution functions (CDF) of $a_\mu^{\pi-\mathrm{pole}}$ for the combined fit using $c_{nm} = \{c_{00}, c_{10}, c_{11}, c_{22}\}$. The orange curve shows the CDF of ≈15'000 different analyses obtained from their AIC weights, the errors on the orange point show the statistical errors for some analyses with a significant weight in the model averaging. This curve corresponds to $P(y; \lambda = 0)$ while the blue curve corresponds to $P(y; \lambda = 1)$, as defined in Eq. (5.61). Indicated in red is the total error obtained as described in Eq. (5.62). To separate the statistical and systematic part of the error, we further calculate $P(y; \lambda = 2)$, as described in the main text.

For a derivation see [163]. We use the the modified AIC introduced in [38],

$$\mathrm{AIC} \sim \exp\left[-\frac{1}{2}\left(\chi^2 + 2n_{\mathrm{par}} - n_{\mathrm{data}}\right)\right], \tag{5.59}$$

where the χ^2, the number of fit parameters n_{par} and the number of data points n_{data} describe the fit of interest. The first two terms in the exponent correspond to the standard AIC, and the last term is needed to weigh fits with different lengths in the fit ranges when fitting to $\tilde{A}(\tau)$ or to weight z-expansion fits with a differing number of cuts in the momentum plane when sampling the transition form factors. In general, two fitting steps are involved in the determination of each of $a_\mu^{\pi-\mathrm{pole}}$, $\Gamma(\pi^0 \to \gamma\gamma)$, and b_π on a given ensemble: the global fit to $\tilde{A}(\tau)$ and the z-expansion fit to the transition form factor. A combined weight can be assigned to each combination of fitting choices across both of these steps by multiplying together the respective AIC weights given in Eq. (5.59). In the alternative simultaneous continuum and z-expansion fit procedure described in Sec. 5.4.2, the model averaging step is instead performed globally across all three ensembles, and therefore a combined AIC weight

is assigned by multiplying together the weights of the fits to $\tilde{A}(\tau)$ across all three ensembles as well as the weight of the final global z-expansion fit with lattice artifacts included. In either case, the result is one unnormalized weight $\tilde{w}_i$ per analysis.

To perform model averaging, the weights across all included analyses must first be normalized, to give

$$w_i = \tilde{w}_i / \sum_j \tilde{w}_j. \tag{5.60}$$

The weights w_i may then be interpreted as a probability. Noting that due to the central limit theorem, the statistical uncertainties follow a Gaussian distribution $N(y; m_i, \sigma_i)$, with central value m_i and standard deviation σ_i, one can include the statistical uncertainties. The central value and standard deviation are given by the jackknife resampling procedure for each analysis. We then define the cumulative distribution function (CDF)

$$P(y; \lambda) = \int_{-\infty}^{y} dy' \sum_i w_i N(y'; m_i, \sigma_i \sqrt{\lambda}), \tag{5.61}$$

where the rescaling of the statistical error by λ is introduced to later separate statistical and systematic error. For an illustration, see Fig. 5.11.

We choose the median of the CDF as the central value of y and the total error is given by the 16% and 84% percentiles of the CDF, i.e.

$$\sigma^2_{\text{total}} \equiv \left[\frac{1}{2} \left(y_{84} - y_{16} \right) \right]^2, \tag{5.62}$$

where $P(y_{16}; 1) = 0.16$ and $P(y_{84}; 1) = 0.84$. The systematic error could then be defined by evaluating the 16% and 84% percentiles of the $P(y; 0)$ since fixing $\lambda = 0$ removes the contribution of the statistical errors to the distribution. However, since $P(y; 0)$ as a function of step functions is a step function itself, the definition of the systematic error would be highly sensitive to the value of the chosen percentile. A more robust choice for the systematic error can be made by first demanding

$$\sigma^2_{\text{total}} \equiv \sigma^2_{\text{stat}} + \sigma^2_{\text{sys}}, \tag{5.63}$$

and noticing that the rescaling of each σ_i^2 by λ is expected to increase σ^2_{stat} by the

same factor, i.e.

$$\lambda\sigma^2_{\text{stat}} + \sigma^2_{\text{sys}} \equiv \left[\frac{1}{2}\left(\tilde{y}_{84} - \tilde{y}_{16}\right)\right]^2 \equiv \tilde{\sigma}^2_{\text{total}}, \tag{5.64}$$

where $P(\tilde{y}_{16};\lambda) = 0.16$ and $P(\tilde{y}_{84};\lambda) = 0.84$. The systematic and statistic errors can then be separated by a second choice of λ:

$$\sigma^2_{\text{stat}} = \frac{\sigma^2_{\text{total}} - \tilde{\sigma}^2_{\text{total}}}{1-\lambda}, \qquad \sigma^2_{\text{sys}} = \frac{\tilde{\sigma}^2_{\text{total}} - \lambda\sigma^2_{\text{total}}}{1-\lambda}. \tag{5.65}$$

In particular, the CDF is smooth for big enough λ and the procedure is insensitive to the choice of λ.

For a better understanding on the composition of the systematic error, we follow the error budgeting procedure suggested in [38]. For one of the choices made during the analysis chain, e.g. the choice between the VMD or LMD fit to $\tilde{A}(\tau)$ or the different fit ranges, we first determine the total error for each possible option, varying all other components of the analysis. We then construct a second CDF as in Eq. (5.61), with m_i the average of the 16% and 84% percentiles, σ_i the total error and w_i the sum of the weights coming from this choice. Using this CDF, we derive the systematic error as described above for the original CDF, this is our result for the systematic error corresponding to the choice. Note that the estimated systematic errors associated with each of the steps of the analysis by this procedure are correlated, thus they do not sum up quadratically to the full systematic error.

5.8 Results

Here, our results using the model averaging described in Sec. 5.7 are summarized. Comparing to our earlier publication [69] we have refined the analysis by systematically studying different z-expansion fits and by excluding analyses leading to unphysical transition from factors as described in Sec. 5.4.2. We include cut-off times $\tau_{\text{cut}} \approx [1.3, 2.0]\,\text{fm}$ on all three ensembles with a matching as described in Sec 5.7 for the combined fits.

For the single ensemble analyses, an AIC averaging over different choices of z-

expansion fits was performed. We then use the continuum limit extrapolation method described in Ref. [115] (see Eqs. (38) – (43) therein). The results including error budgeting are summarized in Tab. 5.3.

For the z-expansion fits we considered in the combined fitting it turns out that the set $c_{nm} = \{c_{00}, c_{10}, c_{11}, c_{22}\}$ leads to the least correlation amongst the coefficients and gives a fully correlated chi-squared per degree of freedom of 1.36. This is our preferred continuum result. We find

$$a_\mu^{\pi-\text{pole}} = 56.7(3.1)_{\text{stat}}(0.4)_{\text{sys}}[3.1]_{\text{tot}} \times 10^{-11}, \tag{5.66}$$

$$\Gamma(\pi \to \gamma\gamma) = 7.50(0.48)_{\text{stat}}(0.07)_{\text{sys}}[0.48]_{\text{tot}}\,\text{eV}, \tag{5.67}$$

$$b_\pi = 2.16(0.07)_{\text{stat}}(0.01)_{\text{sys}}[0.07]_{\text{tot}}\,\text{GeV}^{-2}. \tag{5.68}$$

These values including error budgeting are summarized in Tab. 5.4, an illustration is show in Fig. 5.12.

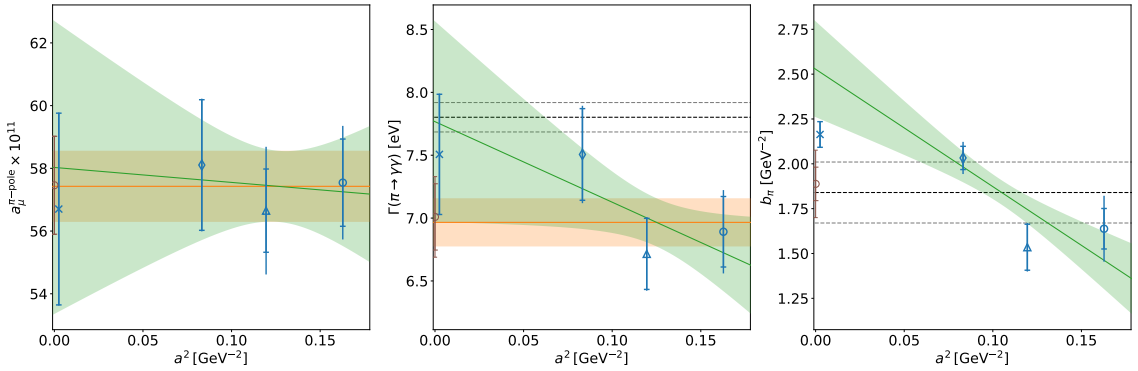

Figure 5.12: Combined fit, single ensemble and continuum extrapolated results from Tabs. 5.3 and 5.4: $a_\mu^{\pi-\text{pole}}$ (left), $\Gamma(\pi \to \gamma\gamma)$ (middle) and b_π (right). Indicated are the statistical and total errors as well as constant and linear fits in a^2 used in the continuum extrapolation. In each plot, the points from left to right correspond to the continuum extrapolation in brown, the combined fit (blue cross), the cD211.054.96 (blue diamond), the cC211.060.80 (blue triangle) and the cB211.072.64 (blue circle) result. In the $\Gamma(\pi \to \gamma\gamma)$ and b_π plots, dashed black and grey lines show the experimental values and their errors, namely $\Gamma(\pi \to \gamma\gamma) = 7.802(117)\,\text{eV}$ [180] and $b_\pi = 1.84(17)\,\text{GeV}^{-2}$ [12].

We note that our result for $a_\mu^{\pi-\text{pole}}$ is compatible both with our earlier analysis [69], where we used the continuum extrapolated result instead of one coming from a

cB211.072.64	$a_\mu^{\pi-\text{pole}} \times 10^{11}$	$\Gamma(\pi \to \gamma\gamma)$ [eV]	b_π [GeV^{-2}]
value	57.54(1.81)	6.89(0.33)	1.63(0.18)
σ_{stat}	1.39	0.28	0.11
σ_{sys}	1.16	0.18	0.15
fit model	0.09	0.01	0.01
fit range	0.00	0.00	0.00
τ_{cut}	0.17	0.06	0.03
sampling	0.20	0.06	0.04
z-exp.	1.15	0.17	0.14
cC211.060.80	$a_\mu^{\pi-\text{pole}} \times 10^{11}$	$\Gamma(\pi \to \gamma\gamma)$ [eV]	b_π [GeV^{-2}]
value	56.65(2.04)	6.72(0.29)	1.54(0.14)
σ_{stat}	1.33	0.28	0.13
σ_{sys}	1.54	0.08	0.04
fit model	0.01	0.00	0.00
fit range	0.07	0.01	0.00
τ_{cut}	0.36	0.03	0.02
sampling	0.50	0.03	0.03
z-exp.	1.51	0.04	0.02
cD211.054.96	$a_\mu^{\pi-\text{pole}} \times 10^{11}$	$\Gamma(\pi \to \gamma\gamma)$ [eV]	b_π [GeV^{-2}]
value	58.11(2.12)	7.51(0.39)	2.03(0.09)
σ_{stat}	2.08	0.36	0.06
σ_{sys}	0.37	0.13	0.06
fit model	0.00	0.00	0.00
fit range	0.01	0.00	0.00
τ_{cut}	0.19	0.08	0.03
sampling	0.10	0.05	0.03
z-exp.	0.29	0.10	0.06
continuum limit	$a_\mu^{\pi-\text{pole}} \times 10^{11}$	$\Gamma(\pi \to \gamma\gamma)$ [eV]	b_π [GeV^{-2}]
value	57.46(1.58)	7.01(0.32)	1.89(0.20)
σ_{stat}	1.57	0.26	0.10
σ_{sys}	0.15	0.17	0.17

Table 5.3: Resulting values including error budgeting on the single ensembles and extrapolated continuum limit results according to [115]. Note the small error budgets from fit model and fit range, indicating that by restricting the transition form factors in the z-expansion to have at least a 95% contribution from lattice data indeed leads to no strong dependence on the model used to extend $\tilde{A}(\tau)$.

combined fit	$a_\mu^{\pi-\text{pole}} \times 10^{11}$	$\Gamma(\pi \to \gamma\gamma)\,[\text{eV}]$	$b_\pi\,[\text{GeV}^{-2}]$
value	56.70(3.08)	7.50(0.48)	2.16(0.07)
σ_{stat}	3.06	0.48	0.07
σ_{sys}	0.35	0.07	0.01
fit model	0.00	0.00	0.00
fit range	0.00	0.00	0.00
τ_{cut}	0.33	0.07	0.00
sampling	0.19	0.05	0.01

Table 5.4: Preferred continuum result from the combined fit using $c_{nm} = \{c_{00}, c_{10}, c_{11}, c_{22}\}$ and $\delta_{nm} = \{\delta_{00}, \delta_{10}\}$.

combined fit, as well as the recent lattice result $a_\mu^{\pi-\text{pole}} = 57.8 \pm 1.8_{\text{stat}} \pm 0.9_{\text{sys}} \times 10^{-11}$ from Ref. [166]. Comparing to the dispersive result $a_\mu^{\pi-\text{pole}} = 63.0^{+2.7}_{-2.1} \cdot 10^{-11}$ from Refs. [3, 63, 64], we find that our result is compatible at the level of $1.7\,\sigma$.

For $\Gamma(\pi \to \gamma\gamma)$, we find agreement with $\Gamma(\pi \to \gamma\gamma) = 7.11 \pm 0.44_{\text{stat}} \pm 0.21_{\text{sys}}\,\text{GeV}^{-2}$ from Ref. [166]. Our result is also compatible with the experimental value $\Gamma(\pi \to \gamma\gamma) = 7.802(52)_{\text{stat}}(105)_{\text{sys}}\,\text{eV}$ from Ref. [180].

Finally, for b_π, we are compatible with the experimental result $b_\pi = 1.84(17)\,\text{GeV}^{-2}$ from Ref. [12] at the level of $1.7\,\sigma$. However, we find a tension of $2.75\,\sigma$ with $b_\pi = 1.78(12)\,\text{GeV}^{-2}$ from the extraction based on Padé approximants [182] and a disagreement of $5\,\sigma$ with the dispersive result $b_\pi = 1.73(5)\,\text{GeV}^{-2}$ from Refs. [63, 64].

We note that from the continuum extrapolated values, cf. Tab. 5.3, we would find for the same comparison a tension of $2.1\,\sigma$ with the dispersive result for $a_\mu^{\pi-\text{pole}}$ and a tension of $2.3\,\sigma$ with the experimental value for $\Gamma(\pi \to \gamma\gamma)$, while finding agreement with all other mentioned quantities. However, as illustrated in Fig. 5.12, the used continuum limit procedure from [115] is quite aggressive when using data points from only three ensembles, and the single ensemble data for b_π leads to a constant fit with $\chi^2/\text{d.o.f} \approx 5$ and is thus clearly not compatible with the assumption of having only small $\mathcal{O}(a^2)$ discretization effects.

The z-expansion coefficients for the combined fit are given by

c_{00}	c_{10}	c_{11}	c_{22}
0.2220(48)	-0.0596(59)	-0.050(18)	0.27(14)

with correlation matrix

$$\mathrm{cor}(c_{nm}) = \begin{pmatrix} +1.00 & -0.46 & -0.07 & +0.07 \\ -0.46 & +1.00 & +0.03 & -0.08 \\ -0.07 & +0.03 & +1.00 & -0.83 \\ +0.07 & -0.08 & -0.83 & +1.00 \end{pmatrix}, \tag{5.69}$$

the corresponding cornerplot is given in Fig. 5.13. The resulting transition form

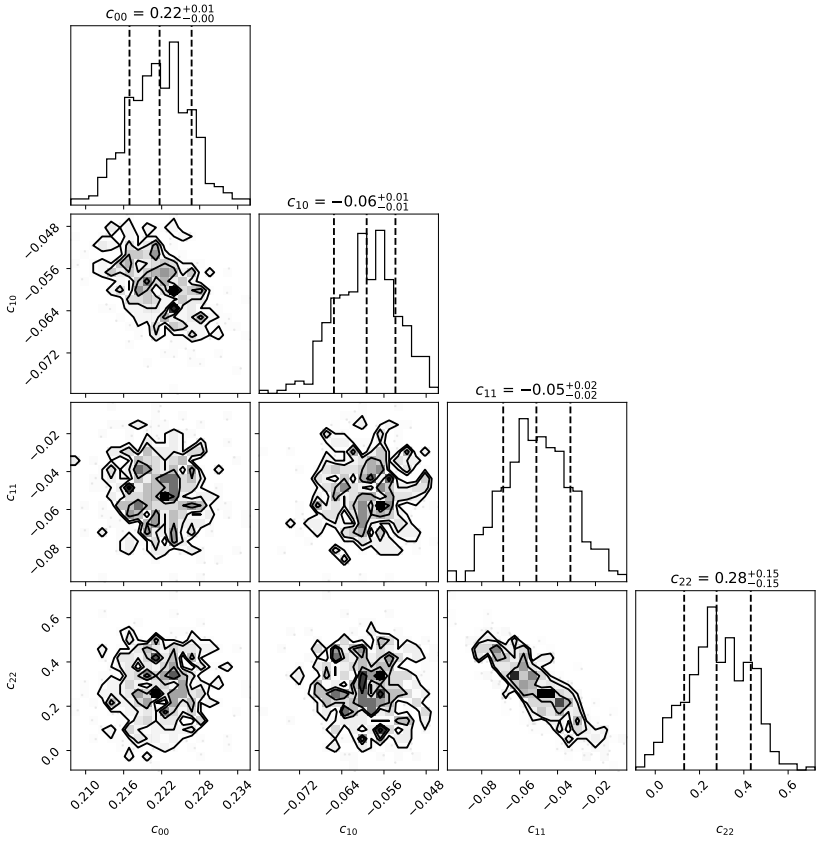

Figure 5.13: Cornerplot of the AIC averaged coefficients of the combined correlated z-expansion fit, using c_{00}, c_{10}, c_{11} and c_{22}. Notice the anticorrelation between c_{11} and c_{22} and the less severe anticorrelation between c_{00} and c_{10}. All other coefficients are virtually uncorrelated. The corresponding correlation matrix is given in Eq. (5.69).

factors for diagonal and single-virtual kinematics are shown in Fig. 5.14. We find

good agreement with the smallest CELLO [73] bin, i.e. close to the momentum region covered by lattice data, for the single-virtual kinematics, while we tend to lower values compared to the experiment at larger momenta.

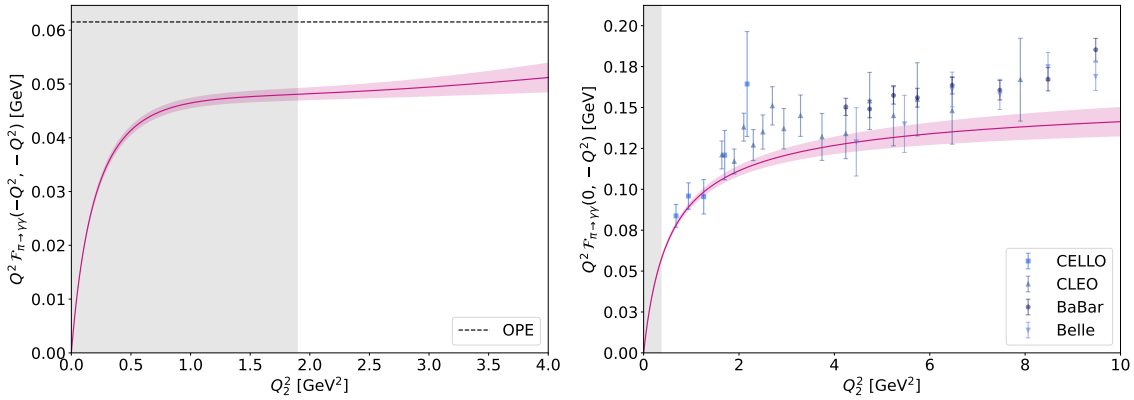

Figure 5.14: Transition form factors from the combined fit using diagonal (left) and single-virtual (right) kinematics. For the diagonal kinematics, the OPE prediction is indicated by the dashed black line while for the single-virtual kinematics, experimental values from CELLO [73], CLEO [72], BaBar [74, 75] and Belle [76] are shown. The region with direct support from lattice data is shaded in grey.

5.9 Conclusion

We have presented an independent ab-initio computation of the pion transition form factors at the physical point in twisted mass lattice QCD, covering the kinematic range relevant for the extraction of the pion pole contribution to the HLbL. We are able to include all disconnected Wick contractions contributing to the amplitudes relevant for the calculation of the form factors.

We find agreement between the calculated pion form factor and the experimental data in the single-virtual regime, also with compatible values for the experimental values of the decay with and the slope parameter.

The main result of this paper, namely the pion pole contribution to HLbL,

$$a_\mu^{\pi-\text{pole}} = 56.7(3.1)_{\text{stat}}(0.4)_{\text{sys}}[3.1]_{\text{tot}} \times 10^{-11}, \tag{5.70}$$

is compatible with the recent lattice result $a_\mu^{\pi-\text{pole}} = 57.8 \pm 1.8_{\text{stat}} \pm 0.9_{\text{sys}} \times 10^{-11}$ from Ref. [166] and compatible at the $1.7\,\sigma$ level with the dispersive result $a_\mu^{\pi-\text{pole}} = 63.0^{+2.7}_{-2.1} \cdot 10^{-11}$ from Refs. [3, 63, 64].

In the future, we plan to also use pions in the moving frame to get a better coverage of the single-virtual axis. In addition, a fourth physical point ensemble with approximately the same volume as the three used here, but with an even smaller lattice spacing, is currently in production and could then also be included in this calculation.

Chapter 6

Conclusions and outlook

The aim of this thesis was the computation of the π^0- and η-pole contributions to the anomalous magnetic moment of the muon by an ab-initio calculation using twisted mass lattice QCD at the physical point. The results can be used to cross-check other data-driven and lattice calculations in the effort to reduce the uncertainty in the Standard Model prediction of a_μ. At the time this thesis was started, there was no lattice calculation of $a_\mu^{\pi-\text{pole}}$ at the physical point and no lattice calculation of $a_\mu^{\eta-\text{pole}}$ had been published at all.

To estimate the π^0- and η-pole contributions, a model independent parametrization of the momentum dependence of the transition form factors $\mathcal{F}_{P\to\gamma^*\gamma^*}(q_1^2, q_2^2)$ is computed from lattice QCD at physical light and heavy quark masses for the pseudoscalars $P = \pi^0$ and η first. On the lattice, one has access to a wide range of space-like photon four-momenta and thus TFFs complementary to the experimentally accessible single-virtual $\mathcal{F}_{P\to\gamma\gamma^*}(q^2, 0)$. In the single-virtual case, the lattice provides data at lower photon virtuality than the experiment. In and close to the region where both lattice and experimental data are available for $\mathcal{F}_{P\to\gamma\gamma^*}(q^2, 0)$, the presented π^0 lattice result has a precision better than the experimental results, cf. Ch. 5, while the η lattice result has a comparable precision, cf. Sec. 4.3.
Using these TFFs as input, the π^0- and η-pole contributions to the anomalous magnetic moment of the muon as well as the decay widths $\Gamma(P \to \gamma\gamma)$ and slope parameter b_P are calculated. In the case of the π^0-pole contribution, agreement within

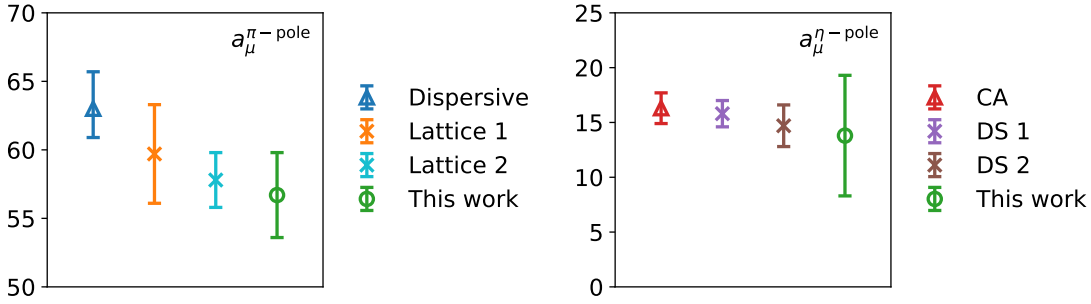

Figure 6.1: Left: Comparison of the estimate of $a_\mu^{\pi\text{-pole}}$ from this work versus an estimate based on dispersion relations [3, 63, 64] and two estimates from lattice QCD [67, 166]. Right: Comparison of the estimate of $a_\mu^{\eta\text{-pole}}$ from this work versus a result derived from Canterbury approximant (CA) fits to experimental data [65] and two estimates based on Dyson-Schwinger (DS) equations [131, 132].

within $1.7\,\sigma$ with the dispersive result of Refs. [3,63,64] is found while agreeing within errors with the recent lattice results of Refs. [67, 166], cf. Fig 6.1. The continuum limit estimate of $a_\mu^{\pi-\text{pole}} = 56.7(3.1)_{\text{stat}}(0.4)_{\text{sys}}[3.1]_{\text{tot}} \times 10^{-11}$ presented here has a relative error of $\sim$5%, competitive with the above references.
For the decay width, $\Gamma(\pi^0 \to \gamma\gamma) = 7.50(0.48)_{\text{stat}}(0.07)_{\text{sys}}[0.48]_{\text{tot}}\,\text{eV}$ is in agreement with the experimental value from Ref. [180] and the recent lattice result from Ref. [166], while the result for $b_{\pi^0} = 2.16(0.07)_{\text{stat}}(0.01)_{\text{sys}}[0.07]_{\text{tot}}\,\text{GeV}^{-2}$ agrees within $1.7\,\sigma$ with the PDG experimental result [12].
The result for the η-pole contribution $a_\mu^{\eta-\text{pole}} = 13.8(5.2)_{\text{stat}}(1.5)_{\text{sys}}[5.5]_{\text{tot}} \times 10^{-11}$ confirms the data-driven Canterbury approximant estimate [65] and the model estimates [118, 131, 132], albeit with a significantly larger error and not yet estimated in the continuum limit, see Fig 6.1 for an illustration. As the result presented here comes from an independent ab-initio lattice QCD calculation, it still provides important independent support for these estimates.
The results for both the decay width $\Gamma(\eta \to \gamma\gamma) = 338(87)_{\text{stat}}(17)_{\text{sys}}[88]_{\text{tot}}\,\text{eV}$ and the slope parameter $b_\eta = 1.34(28)_{\text{stat}}(14)_{\text{sys}}[31]_{\text{tot}}\,\text{GeV}^{-2}$ are in tension with the experimental results by approximately $2\,\sigma$.

The work on this project is far from over! First of all, a fourth physical point ensemble at a finer lattice spacing is in production which could also be used in this analysis to obtain a more robust continuum limit extrapolation for $a_\mu^{\pi-\text{pole}}$. For the analysis of $a_\mu^{\eta-\text{pole}}$, the next steps are to extend the calculation to the other two ensembles used

in this work to allow for a continuum estimate of this value. The measurements on cC211.060.80 are underway. Also, in order to obtain a result for $a_\mu^{\eta'-\text{pole}}$, the quality of the data needs to be improved in order to take into account the η-η' mixing, which is not possible with the currently available data. It is also planned to calculate the form factors in a moving frame to provide better data support in the single-virtual region.

In conclusion, twisted mass lattice QCD at the physical point, using the ETMC ensembles, proves to be a reliable way to extract the π^0- and η-pole contributions to the anomalous magnetic moment of the muon. The estimate for the π^0-pole contribution is an independent result from first principles confirming other data-driven and lattice results, while the presented η-pole contribution is a first ab-initio result, serving as an important cross-check for the data-driven estimates.
There are still many open avenues to improve the calculation presented in this work, with numerous possible directions for interesting future research.

Appendix A

Appendix of the draft in Chapter 5

This appendix is part of the paper draft presented in Ch. 5. Since it is referenced from other parts of this thesis, in particular Ch. 3, it is reproduced separately here and not as part of Ch. 5.

A.1 Operators and Conventions

Our interpolating operators are defined as follows: For the pseudoscalars in the physical basis we have

$$P^0 = i\overline{\psi}\gamma_5\tau^3\psi, \tag{A.1}$$

$$P^{\pm} = i\overline{\psi}\gamma_5\tau^{\pm}\psi, \tag{A.2}$$

where the flavor matrices are given by the Pauli matrices

$$\tau^3 = \begin{pmatrix} 1 & 0 \\ 0 & -1 \end{pmatrix}, \quad \tau^+ = \begin{pmatrix} 0 & 1 \\ 0 & 0 \end{pmatrix}, \quad \tau^- = \begin{pmatrix} 0 & 0 \\ 1 & 0 \end{pmatrix}. \tag{A.3}$$

They satisfy the usual Pauli matrix relations

$$[\tau^+, \tau^-] = \tau^3, \tag{A.4}$$
$$[\tau^3, \tau^\pm] = \pm 2\tau^\pm, \tag{A.5}$$
$$\tau^+ + \tau^- = \tau^1, \tag{A.6}$$
$$i(\tau^- - \tau^+) = \tau^2. \tag{A.7}$$

Note that in this convention the charged operators correspond to annihilation operators for the relevant state, i.e. under the conventional electromagnetic charge assignments for u and d, the operators $P^\pm$ transform with the opposite electromagnetic charge, so they destroy the states $\pi^\pm$ respctively.

The local vector currents used in this work are defined as

$$\begin{aligned} J_\mu^Q &= \overline{\psi}\gamma_\mu Q\psi \\ &= (1/6)J_\mu^{0,0} + (1/2)J^{1,0}, \end{aligned} \tag{A.8}$$
$$J_\mu^{0,0} = \overline{\psi}\gamma_\mu \mathbb{1}\psi, \tag{A.9}$$
$$J_\mu^{1,0} = \overline{\psi}\gamma_\mu \tau^3\psi, \tag{A.10}$$
$$J_\mu^{1,\pm} = \overline{\psi}\gamma_\mu \tau^\pm\psi, \tag{A.11}$$

where $Q = \mathrm{diag}(2/3, -1/3)$ is the two flavor charge matrix in flavor space.

Next we write these operators in the twisted basis. At maximal twist, we have the relations

$$\psi(x) = e^{i\omega\gamma_5\tau_3/2}\chi(x)\big|_{\omega=\pi/2} = \frac{1}{\sqrt{2}}(1 + i\gamma_5\tau_3)\chi(x), \tag{A.12}$$
$$\overline{\psi}(x) = \overline{\chi}(x)e^{i\omega\gamma_5\tau_3/2}\big|_{\omega=\pi/2} = \overline{\chi}(x)\frac{1}{\sqrt{2}}(1 + i\gamma_5\tau_3). \tag{A.13}$$

Translating the operators directly to the twisted basis yields

$$P^0 = -\overline{\chi}\chi \tag{A.14}$$
$$P^{\pm} = i\overline{\chi}\gamma_5\tau^{\pm}\chi, \tag{A.15}$$
$$J_\mu^{0,0} = \overline{\chi}\gamma_\mu\mathbb{1}\chi, \tag{A.16}$$
$$J_\mu^{1,0} = \overline{\chi}\gamma_\mu\tau^3\chi, \tag{A.17}$$
$$J_\mu^{1,\pm} = \mp i\overline{\chi}\gamma_\mu\gamma_5\tau^{\pm}\chi. \tag{A.18}$$

By convention, the overall phases on these operators are modified to give the final interpolating operators and currents used in the twisted-basis calculation:

$$\pi^0 = \overline{\chi}\chi = \bar{u}u + \bar{d}d, \tag{A.19}$$
$$\pi^+ = \overline{\chi}\gamma_5\tau^+\chi = \bar{u}\gamma_5 d, \tag{A.20}$$
$$\pi^- = \overline{\chi}\gamma_5\tau^-\chi = \bar{d}\gamma_5 u, \tag{A.21}$$
$$V_\mu^{0,0} = \overline{\chi}\gamma_\mu\mathbb{1}\chi = \bar{u}\gamma_\mu u + \bar{d}\gamma_\mu d, \tag{A.22}$$
$$V_\mu^{1,0} = \overline{\chi}\gamma_\mu\tau^3\chi = \bar{u}\gamma_\mu u - \bar{d}\gamma_\mu d, \tag{A.23}$$
$$A_\mu^{1,+} = \overline{\chi}\gamma_\mu\gamma_5\tau^+\chi = \bar{u}\gamma_\mu\gamma_5 d, \tag{A.24}$$
$$A_\mu^{1,-} = \overline{\chi}\gamma_\mu\gamma_5\tau^-\chi = \bar{d}\gamma_\mu\gamma_5 u. \tag{A.25}$$

A.1.1 Hermition Conjugation

As we have defined them, the operators transform under Hermitian conjugation (†) as

$$(\pi^0)^\dagger = \pi_0, \tag{A.26}$$
$$(\pi^\pm)^\dagger = -\pi^\mp, \tag{A.27}$$
$$(V_\mu^{0,0})^\dagger = (-1)^{\delta_{\mu,0}-1}V_\mu^{0,0}, \tag{A.28}$$
$$(V_\mu^{1,0})^\dagger = (-1)^{\delta_{\mu,0}-1}V_\mu^{1,0}, \tag{A.29}$$
$$(A_\mu^{1,\pm})^\dagger = (-1)^{\delta_{\mu,0}-1}A_\mu^{1,\mp}. \tag{A.30}$$

A.1.2 Charge Conjugation

Charge conjugation may be defined in the twisted basis by (see Ref. [81], Appendix B)

$$\chi(x) \to C^{-1}\bar{\chi}(x)^T, \tag{A.31}$$
$$\bar{\chi}(x) \to -\chi(x)^T C, \tag{A.32}$$

where

$$C\gamma_\mu C^{-1} = -\gamma_\mu^T, \tag{A.33}$$
$$C\gamma_5 C^{-1} = \gamma_5. \tag{A.34}$$

One possible choice for our gamma basis is $C = C^\dagger = C^{-1} = i\gamma_0\gamma_2$. Taking care about the anticommutativity of χ and $\bar{\chi}$, we find the operators defined above for the twisted basis transform as

$$\pi^0 \xrightarrow{C} \pi^0, \tag{A.35}$$
$$\pi^\pm \xrightarrow{C} \pi^\mp, \tag{A.36}$$
$$V_\mu^{0,0} \xrightarrow{C} -V_\mu^{0,0}, \tag{A.37}$$
$$V_\mu^{1,0} \xrightarrow{C} -V_\mu^{1,0}, \tag{A.38}$$
$$A_\mu^\pm \xrightarrow{C} A_\mu^\mp. \tag{A.39}$$

A.1.3 Twisted Parity

The twisted parity transformation (see Ref. [81], Eq 2.35) may be defined by

$$\chi(t,\vec{x}) \xrightarrow{P\tau^1} i\gamma_0\tau^1\chi(t,-\vec{x}), \tag{A.40}$$
$$\overline{\chi}(t,\vec{x}) \xrightarrow{P\tau^1} -i\overline{\chi}(t,-\vec{x})\gamma_0\tau^1. \tag{A.41}$$

Our operators in the twisted basis then transform as

$$\pi^0 \xrightarrow{P\tau^1} \pi^0, \tag{A.42}$$

$$\pi^\pm \xrightarrow{P\tau^1} -\pi^\mp, \tag{A.43}$$

$$V_k^{0,0} \xrightarrow{P\tau^1} -V_k^{0,0}, \tag{A.44}$$

$$V_0^{0,0} \xrightarrow{P\tau^1} V_0^{0,0}, \tag{A.45}$$

$$V_k^{1,0} \xrightarrow{P\tau^1} V_k^{1,0}, \tag{A.46}$$

$$V_0^{1,0} \xrightarrow{P\tau^1} -V_0^{1,0}, \tag{A.47}$$

$$A_k^\pm \xrightarrow{P\tau^1} A_k^\mp, \tag{A.48}$$

$$A_0^\pm \xrightarrow{P\tau^1} -A_0^\mp. \tag{A.49}$$

A.1.4 Twisted Time Reversal

Away from the continuum limit, the time reversal transformation must be combined with a flavor change to be a valid symmetry of the Wilson Twisted Mass Lattice QCD action (see Ref. [81], Section 2.4):

$$\chi(x,t) \xrightarrow{T_F} i\gamma_0\gamma_5\tau_1\chi(x,-t), \tag{A.50}$$

$$\bar{\chi}(x,t) \xrightarrow{T_F} -i\bar{\chi}(x,-t)\gamma_5\gamma_0\tau_1. \tag{A.51}$$

Our interpolating operators transform as follows:

$$\pi^0(x,t) \xrightarrow{T_F} \pi^0(x,-t) = \pi^0(x,-t)^\dagger, \tag{A.52}$$

$$\pi^\pm(x,t) \xrightarrow{T_F} -\pi^\mp(x,-t) = \pi^\pm(x,-t)^\dagger, \tag{A.53}$$

$$V_\mu^{0,0}(x,t) \xrightarrow{T_F} (-1)^{\delta_{\mu,0}} V_\mu^{0,0}(x,-t) = -V_\mu^{0,0}(x,-t)^\dagger, \tag{A.54}$$

$$V_\mu^{1,0}(x,t) \xrightarrow{T_F} (-1)^{1+\delta_{\mu,0}} V_\mu^{1,0}(x,-t) = V_\mu^{1,0}(x,-t)^\dagger, \tag{A.55}$$

$$A_\mu^{1,\pm}(x,t) \xrightarrow{T_F} (-1)^{1+\delta_{\mu,0}} A_\mu^{1,\mp}(x,-t) = A_\mu^{1,\pm}(x,-t)^\dagger. \tag{A.56}$$

A.1.5 Dirac Matrix Conventions

First note the following notation and convention used by ETMC for the Dirac matrices [81]. The Euclidean Dirac matrices are defined in the chiral basis as

$$\gamma_\mu = \begin{pmatrix} 0 & e_\mu \\ e_\mu^\dagger & 0 \end{pmatrix}, \tag{A.57}$$

where $e_0 = -\mathbb{1}$, $e_k = -i\sigma_k$, and σ_k are the standard Pauli matrices:

$$\sigma_1 = \begin{pmatrix} 0 & 1 \\ 1 & 0 \end{pmatrix}, \quad \sigma_2 = \begin{pmatrix} 0 & -i \\ i & 0 \end{pmatrix}, \quad \sigma_3 = \begin{pmatrix} 1 & 0 \\ 0 & -1 \end{pmatrix}. \tag{A.58}$$

These Dirac matrices have the properties of Hermiticity $\gamma_\mu^\dagger = \gamma_\mu$ as well as anticommutation with respect to the Euclidean signature $\{\gamma_\mu, \gamma_\nu\} = 2\delta_{\mu\nu}$. Finally the 5th Dirac matrix is defined as

$$\gamma_5 = \gamma_0\gamma_1\gamma_2\gamma_3 = \begin{pmatrix} \mathbb{1} & 0 \\ 0 & -\mathbb{1} \end{pmatrix}. \tag{A.59}$$

Written explicitly,

$$\gamma_0 = \begin{pmatrix} 0 & 0 & -1 & 0 \\ 0 & 0 & 0 & -1 \\ -1 & 0 & 0 & 0 \\ 0 & -1 & 0 & 0 \end{pmatrix}, \tag{A.60}$$

$$\gamma_1 = \begin{pmatrix} 0 & 0 & 0 & -i \\ 0 & 0 & -i & 0 \\ 0 & i & 0 & 0 \\ i & 0 & 0 & 0 \end{pmatrix}, \tag{A.61}$$

$$\gamma_2 = \begin{pmatrix} 0 & 0 & 0 & -1 \\ 0 & 0 & 1 & 0 \\ 0 & 1 & 0 & 0 \\ -1 & 0 & 0 & 0 \end{pmatrix}, \tag{A.62}$$

$$\gamma_3 = \begin{pmatrix} 0 & 0 & -i & 0 \\ 0 & 0 & 0 & i \\ i & 0 & 0 & 0 \\ 0 & -i & 0 & 0 \end{pmatrix}. \tag{A.63}$$

While $\mu = 0, 2$ are symmetric and real, $\mu = 1, 3$ are antisymmetric and pure imaginary.

A.2 3d Integral Representation Weights

The weight functions $w_{1,2}$ appearing in Eqs. (5.50) and (5.51) presented here are taken from [118] and have been derived in [116] using the method of Gegenbauer polynomials [183–187].

The weight functions are given in Eqs. (5.52) and (5.53) and read

$$w_1(Q_1, Q_2, \tau) = \left(-\frac{2\pi}{3}\right) \sqrt{1-\tau^2} \frac{Q_1^3 Q_2^3}{Q_2^2 + m_\pi^2} I_1(Q_1, Q_2, \tau), \tag{A.64}$$

$$w_2(Q_1, Q_2, \tau) = \left(-\frac{2\pi}{3}\right) \sqrt{1-\tau^2} \frac{Q_1^3 Q_2^3}{(Q_1+Q_2)^2 + m_\pi^2} I_2(Q_1, Q_2, \tau), \tag{A.65}$$

with

$$\begin{aligned} I_1(Q_1, Q_2, \tau) = X(Q_1, Q_2, \tau)[&8P_1P_2Q_1Q_2\tau - 2P_1P_3(Q_2^4/m_\mu^2 - 2Q_2^2) \\ &+ 4P_2P_3Q_1^2 - 4P_2 - 2P_1(2 - Q_2^2/m_\mu^2 + 2Q_1Q_2\tau/m_\mu^2) \\ &- 2P_3(4 + Q_1^2/m_\mu^2 - 2Q_2^2/m_\mu^2) + 2/m_\mu^2] \\ &- 2P_1P_2(1 + (1 - R_{m1})Q_1Q_2\tau/m_\mu^2) \\ &+ P_1P_3(2 - (1 - R_{m1})Q_2^2/m_\mu^2) \\ &+ P_2P_3(2 + (1 - R_{m1})^2 Q_1Q_2\tau/m_\mu^2) \\ &+ P_1(1 - R_{m1})/m_\mu^2 + 3P_3(1 - R_{m1})/m_\mu^2 \end{aligned} \tag{A.66}$$

and

$$
\begin{aligned}
I_2(Q_1,Q_2,\tau) = X(Q_1,Q_2,\tau)[&4P_1P_2Q_1Q_2\tau + 2P_1P_3Q_2^2 - 2P_1 \\
&+ 2P_2P_3Q_1^2 - 2P_2 - 4P_3 - 4/m_\mu^2] \\
&- 2P_1P_2 - 3P_1(1-R_{m2})/(2m_\mu^2) - 3P_2(1-R_{m1})/(2m_\mu^2) \\
&- P_3(2-R_{m1}-R_{m2})/(2m_\mu^2) \\
&+ P_1P_3[2 + 3(1-R_{m2})Q_2^2/(2m_\mu^2) + (1-R_{m2})^2Q_1Q_2\tau/(2m_\mu^2)] \\
&+ P_2P_3[2 + 3(1-R_{m1})Q_1^2/(2m_\mu^2) + (1-R_{m1})^2Q_1Q_2\tau/(2m_\mu^2)],
\end{aligned}
\tag{A.67}
$$

where

$$Q_3^2 = (Q_1+Q_2)^2 = Q_1^2 + 2Q_1Q_2\tau + Q_2^2, \tag{A.68}$$

$$\tau = \cos\theta, \tag{A.69}$$

$$P_i = 1/Q_i^2, i \in \{1,2,3\}. \tag{A.70}$$

Further,

$$X(Q_1Q_2,\tau) = \frac{1}{Q_1Q_2x}\arctan\left(\frac{zx}{1-z\tau}\right), \tag{A.71}$$

$$x = \sqrt{1-\tau^2}, \tag{A.72}$$

$$z = \frac{Q_1Q_2}{4m_\mu^2}(1-R_{m1})(1-R_{m2}), \tag{A.73}$$

$$R_{mi} = \sqrt{1+\frac{4m_\mu^2}{Q_i^2}}, i \in \{1,2\}. \tag{A.74}$$

For a detailed discussion of the behaviour of $w_{1,2}$ in different limits see [118].

Appendix B

Theoretical aspects

In this appendix, definitions relevant for and aspects of the calculations in Ch. 2 and 3 are collected.

B.1 Dirac matrix conventions and definition of lattice derivatives

The following conventions for the gamma matrices in four dimensions are used:

$$\begin{aligned} \{\gamma_\mu, \gamma_\nu\} &= 2\delta_{\mu\nu} \\ \gamma_\mu^\dagger &= \gamma_\mu \\ \gamma_5 &= \gamma_0\gamma_1\gamma_2\gamma_3 \\ \sigma_{\mu\nu} &= \frac{i}{2}[\gamma_\mu, \gamma_\nu], \end{aligned} \tag{B.1}$$

with $\mu, \nu \in \{0, 1, 2, 3\}$. See also App. A.1.5.

The gauge covariant lattice derivatives action on the quark field $\psi(x)$ are given by

$$\begin{aligned}\nabla_\mu \psi(x) &= \frac{1}{a}\left[U_\mu(x)\psi(x+a\hat{\mu}) - \psi(x)\right] \\ \nabla^*_\mu \psi(x) &= \frac{1}{a}\left[\psi(x) - U^\dagger_\mu(x-a\hat{\mu})\psi(x-a\hat{\mu})\right],\end{aligned} \tag{B.2}$$

while the left action is defined by

$$\begin{aligned}\bar{\psi}(x)\overleftarrow{\nabla}_\mu &= \frac{1}{a}\left[\bar{\psi}(x+a\hat{\mu})U^\dagger_\mu(x) - \bar{\psi}(x)\right] \\ \bar{\psi}(x)\overleftarrow{\nabla}^*_\mu &= \frac{1}{a}\left[\bar{\psi}(x) - \bar{\psi}(x-a\hat{\mu})U_\mu(x-a\hat{\mu})\right],\end{aligned} \tag{B.3}$$

where a is the lattice spacing, $U_\mu(x) \equiv \exp(ig_0 a G_\mu(x))$ is the lattice gauge link, depending on the gauge (gluon) field $G_\mu(x)$ and g_0 is the bare coupling constant.

B.2 Equivalence between tmQCD and QCD in the continuum

Here, the equivalence between tmQCD and QCD in the continuum is shown, following e.g. [77, 80–82]. For simplicity, QCD with two degenerate flavours is considered, called up and down quarks. In flavour space, the Dirac spinor is then given by the doublet $\bar{\psi} = (\bar{u}, \bar{d})$, the standard form of the fermionic Lagrangean density by

$$\mathcal{L} = \bar{\psi}\left[\not{D} + m\right]\psi \tag{B.4}$$

and the twisted mass fermionic Lagrangean density by

$$\mathcal{L}_{\mathrm{tm}} = \bar{\chi}\left[\not{D} + m + i\mu\gamma_5\tau^3\right]\chi, \tag{B.5}$$

where $\not{D} = \gamma_\mu D_\mu$ with $D_\mu = \partial_\mu + G_\mu$ the covariant derivative in a given gauge field G_μ (i.e. the gluon field), m a (bare) mass parameter, μ the bare twisted mass parameter, τ^3 the third Pauli matrix in flavour space. Note that for better legibility the indices on the mass parameters found in Sec. 2.1 were dropped. In the twisted basis, the Dirac spinor in flavour space is denoted by $\bar{\chi} = (\bar{u}, \bar{d})$. Redefining the

fermionic fields through chiral transformations in the third direction, i.e.

$$\begin{aligned} \chi \to \chi' &= \exp\left[i\frac{\alpha}{2}\gamma_5\tau^3\right]\chi, \\ \bar{\chi} \to \bar{\chi}' &= \bar{\chi}\exp\left[i\frac{\alpha}{2}\gamma_5\tau^3\right], \end{aligned} \tag{B.6}$$

and using

$$\exp\left[i\alpha\gamma_5\tau^3\right] = \cos(\alpha) + i\sin(\alpha)\gamma_5\tau^3, \tag{B.7}$$

the Lagrangian density transforms as

$$\mathcal{L}_{\text{tm}} \to \mathcal{L}'_{\text{tm}} = \bar{\chi}\left[\not{D} + m\cos(\alpha) - \mu\sin(\alpha) + i\gamma_5\tau^3(m\sin(\alpha) + \mu\cos(\alpha))\right]\chi. \tag{B.8}$$

Thus this transformation leaves the form of the action invariant and merely transforms the two mass parameters, i.e.

$$m \to m' = m\cos(\alpha) + \mu\sin(\alpha), \tag{B.9}$$

$$\mu \to \mu' = -m\sin(\alpha) + \mu\cos(\alpha), \tag{B.10}$$

$$\mathcal{L}_{\text{tm}} \to \mathcal{L}'_{\text{tm}} = \bar{\chi}'\left[\not{D} + m' + i\mu'\gamma_5\tau^3\right]\chi'. \tag{B.11}$$

This means that the changes of field variables and mass definitions does not change the content of the theory, in particular, the standard form of the action is obtained if

$$\tan(\alpha) = \frac{\mu}{m}, \tag{B.12}$$

using

$$\begin{aligned} \cos(\alpha) &= \frac{m}{\sqrt{m^2+\mu^2}}, \\ \sin(\alpha) &= \frac{\mu}{\sqrt{m^2+\mu^2}}, \end{aligned} \tag{B.13}$$

leading to the Lagrangean density

$$\mathcal{L}'_{\text{tm, }\tan(\alpha)=\frac{\mu}{m}} = \bar{\chi}'\left[\not{D} + M_{\text{inv}}\right]\chi', \tag{B.14}$$

where it immediately follows from Eqs. (B.9) and (B.10) that

$$M_{\text{inv}} = \sqrt{m^2+\mu^2} = \sqrt{(m')^2+(\mu')^2} \tag{B.15}$$

for any choice of α. Note that Eq. (B.7) also implies

$$\mathcal{L}_{\text{tm}} = \bar{\chi}\left[\not{D} + M_{\text{inv}} \exp\left[i\omega\gamma_5\tau^3\right]\right]\chi, \tag{B.16}$$

where the twist angle ω is given by $\tan(\omega) = \frac{\mu}{m}$.

B.3 Further details on twisted charge conjugation

Here more explicit expressions for the twisted charge conjugation of the operators presented in App. A.1.2 are given. One finds

$$\pi^0 \xrightarrow{C} -\chi^T C C^{-1} \overline{\chi}^T = \overline{\chi}\chi = \pi^0, \tag{B.17}$$

$$\pi^\pm \xrightarrow{C} -\chi^T \gamma_5 \tau^\pm \overline{\chi}^T = \overline{\chi}\gamma_5(\tau^\pm)^T\chi = \overline{\chi}\gamma_5\tau^\mp\chi = \pi^\mp, \tag{B.18}$$

$$\begin{aligned} V_\mu^{0,0} \xrightarrow{C} & -(\chi^T C)_\alpha (\gamma_\mu)_{\alpha\beta} \mathbb{1} (C^{-1}\overline{\chi}^T)_\beta = \chi_\alpha (\gamma_\mu)_{\beta\alpha} \mathbb{1} \overline{\chi}_\beta \\ & = -\overline{\chi}_\beta (\gamma_\mu)_{\beta\alpha} \mathbb{1} \chi_\alpha = -V_\mu^{0,0}, \end{aligned} \tag{B.19}$$

$$V_\mu^{1,0} \xrightarrow{C} -V_\mu^{1,0}, \text{ analogous to } V_\mu^{0,0}, \tag{B.20}$$

$$\begin{aligned} A_\mu^\pm \xrightarrow{C} & -(\chi^T C)_{\alpha;\rho} (\gamma_\mu\gamma_5)_{\alpha\beta} (\tau^\pm)_{\rho\sigma} (C^{-1}\overline{\chi}^T)_{\beta;\sigma} = -\chi_{\alpha;\rho} (\gamma_\mu\gamma_5)_{\beta\alpha} (\tau^\pm)_{\rho\sigma} \overline{\chi}_{\beta;\sigma} \\ & = \overline{\chi}_{\beta;\sigma} (\gamma_\mu\gamma_5)_{\beta\alpha} (\tau^\mp)_{\sigma\rho} \chi_{\alpha;\rho} = A_\mu^\mp, \end{aligned} \tag{B.21}$$

under twisted charge C, noting that χ and $\overline{\chi}$ anticommute since they are Grassmann-valued fields.

B.4 Inserting states - asymptotic behaviour

In Euclidean space, operators time evolve according to

$$\mathcal{O}(t) = e^{Ht}\mathcal{O}(0)e^{-Ht}, \tag{B.22}$$

$$\mathcal{O}(t)^\dagger = e^{Ht}\mathcal{O}(0)^\dagger e^{-Ht}. \tag{B.23}$$

The creation and destruction operators in momentum space are related to the position space operators as

$$\mathcal{O}(\vec{p},t)^\dagger = a^3 \sum_{\vec{x}} \mathcal{O}(\vec{x},t)^\dagger e^{-i\vec{p}\vec{x}}, \tag{B.24}$$

$$\mathcal{O}(\vec{p},t) = a^3 \sum_{\vec{x}} \mathcal{O}(\vec{x},t) e^{i\vec{p}\vec{x}}. \tag{B.25}$$

As a result of the relativistic normalization of the pseudoscalar state $|P\rangle$, the projector must be written as

$$\hat{P} = \frac{1}{2E_P a^3} |P(\vec{p})\rangle\langle P(\vec{p})|, \tag{B.26}$$

while the overlap factor is defined by

$$Z_P(\vec{p}) = \langle 0|P(\vec{p},t=0)|P(\vec{p})\rangle, \tag{B.27}$$

or equivalently

$$Z_P = \langle 0|P(\vec{0},0)|P(\vec{p})\rangle = e^{-i\vec{p}\vec{x}}\langle 0|P(\vec{x},0)|P(\vec{p})\rangle = e^{-i\vec{p}\vec{x}+E_P t}\langle 0|P(\vec{x},t)|P(\vec{p})\rangle. \tag{B.28}$$

Note that $Z_P^* = \langle P(\vec{p})|P^\dagger(\vec{0},0)|0\rangle$. For the moment suppressing lattice spacing, position and momenta, consider the amplitude

$$C_{\mu\nu} = \left\langle 0 \left| T\left\{ P(t_f) J_\nu^\dagger(t_c) J_\mu^\dagger(t_i) \right\} \right| 0 \right\rangle, \tag{B.29}$$

with source position t_i, the pseudoscalar at sink t_f and current insertion at t_c. Now, let $t_f \gg t_c > t_i \Rightarrow \tau = t_c - t_i > 0$. Then,

$$C_{\mu\nu} \overset{t_f \gg t_c > t_i}{\longrightarrow} \frac{1}{2E_P} \underbrace{\langle 0|P(t_f)|P\rangle}_{Z_p e^{-E_P t_f}} \left\langle P \left| J_\nu^\dagger(t_c) J_\mu^\dagger(t_i) \right| 0 \right\rangle \tag{B.30}$$

$$= \frac{Z_P}{2E_P} \left\langle P \left| e^{Ht_i} J_\nu^\dagger(t_c - t_i) e^{-Ht_i} e^{Ht_i} J_\mu^\dagger(0) e^{-Ht_i} \right| 0 \right\rangle e^{-E_P t_f} \tag{B.31}$$

$$= \frac{Z_P}{2E_P} \left\langle P \left| J_\nu^\dagger(\tau) J_\mu^\dagger(0) \right| 0 \right\rangle e^{-E_P(t_f - t_i)}, \tag{B.32}$$

where $\langle P|e^{Ht_i} = e^{E_P t_i}\langle P|$ and $e^{-Ht_i}|0\rangle = |0\rangle$ was used. Analogous for $\tau < 0$ and for the pseudoscalar to the far Euclidean past.

B.5 Backward propagation - 2pt functions

On a time-torus, an operator inserted at a specified time may create or destroy states which will have or have wrapped wrapped around the lattice. To extract the corresponding amplitude on the infinite Euclidean space, the "method of images" is used. An operator at t has images at $t + nL_t$ where L_t is the time extent and n is an integer. As an example, consider the finite time contribution to the two point correlation function.

$$\left\langle 0 \left| \mathcal{O}(t)\mathcal{O}(0)^\dagger \right| 0 \right\rangle_{\text{Torus}} = \sum_n \left\langle 0 \left| \mathcal{O}(t + nL_t)\mathcal{O}(0)^\dagger \right| 0 \right\rangle, \tag{B.33}$$

where only images for the destruction operator are inserted since images of the creation operator would just generate copies of the same amplitude due to time translation invariance. Keeping the two most dominant terms in the sum on n, i.e. $n = \pm 1$, one arrives at the well known cosh form of the 2pt correlator. Starting from

$$\begin{aligned} \left\langle 0 \left| \mathcal{O}(t)\mathcal{O}(0)^\dagger \right| 0 \right\rangle_{\text{Torus}} = &\left\langle 0 \left| \mathcal{O}(0)^\dagger \mathcal{O}(t - L_t) \right| 0 \right\rangle \\ &+ \left\langle 0 \left| \mathcal{O}(t)\mathcal{O}(0)^\dagger \right| 0 \right\rangle \\ &+ \left\langle 0 \left| \mathcal{O}(t + L_t)\mathcal{O}(0)^\dagger \right| 0 \right\rangle, \end{aligned} \tag{B.34}$$

one finds that insertion of complete sets of states yields

$$\begin{aligned} \left\langle 0 \left| \mathcal{O}(0)^\dagger \mathcal{O}(t - L_t) \right| 0 \right\rangle &= \left\langle 0 \left| \mathcal{O}(0)^\dagger \right| \mathcal{O} \right\rangle \left\langle \mathcal{O} \left| \mathcal{O}(t - L_t) \right| 0 \right\rangle \\ &= \left\langle 0 \left| \mathcal{O}(0)^\dagger \right| \mathcal{O} \right\rangle \underbrace{\left\langle \mathcal{O} \left| e^{H(t-L_t)} \right.}_{e^{E(t-L_t)}\langle \mathcal{O}|} \mathcal{O}(0) \underbrace{\left. e^{-H(t-L_t)} \right| 0 \right\rangle}_{|0\rangle} \\ &= \left\langle 0 \left| \mathcal{O}(0) \right| \mathcal{O} \right\rangle \left\langle \mathcal{O} \left| \mathcal{O}(0)^\dagger \right| 0 \right\rangle e^{E(t-L_t)} \\ &= \left\langle 0 \left| \mathcal{O}(0) \right| \mathcal{O} \right\rangle \left\langle \mathcal{O} \left| \mathcal{O}(0)^\dagger \right| 0 \right\rangle e^{-E(L_t-t)}, \end{aligned} \tag{B.35}$$

$$\begin{aligned}\left\langle 0\left|\mathcal{O}(t)\mathcal{O}(0)^\dagger\right|0\right\rangle &= \left\langle 0\left|\mathcal{O}(t)\right|\mathcal{O}\right\rangle \left\langle \mathcal{O}\left|\mathcal{O}(0)^\dagger\right|0\right\rangle \\ &= \underbrace{\left\langle 0\left|e^{Ht}\right.}_{\langle 0|}\ \mathcal{O}(0)\ \underbrace{\left.e^{-Ht}\right|\mathcal{O}\right\rangle}_{|\mathcal{O}\rangle e^{-Et}} \left\langle \mathcal{O}\left|\mathcal{O}(0)^\dagger\right|0\right\rangle \\ &= \left\langle 0\left|\mathcal{O}(0)\right|\mathcal{O}\right\rangle \left\langle \mathcal{O}\left|\mathcal{O}(0)^\dagger\right|0\right\rangle e^{-Et}, \end{aligned} \tag{B.36}$$

$$\begin{aligned}\left\langle 0\left|\mathcal{O}(t+L_t)\mathcal{O}(0)^\dagger\right|0\right\rangle &= \left\langle 0\left|\mathcal{O}(t+L_t)\right|\mathcal{O}\right\rangle \left\langle \mathcal{O}\left|\mathcal{O}(0)^\dagger\right|0\right\rangle \\ &= \underbrace{\left\langle 0\left|e^{H(t+L_t)}\right.}_{\langle 0|}\ \mathcal{O}(0)\ \underbrace{\left.e^{-H(t+L_t)}\right|\mathcal{O}\right\rangle}_{|\mathcal{O}\rangle e^{-E(t+L_t)}} \left\langle \mathcal{O}\left|\mathcal{O}(0)^\dagger\right|0\right\rangle \\ &= \left\langle 0\left|\mathcal{O}(0)\right|\mathcal{O}\right\rangle \left\langle \mathcal{O}\left|\mathcal{O}(0)^\dagger\right|0\right\rangle e^{-E(t+L_t)}. \end{aligned} \tag{B.37}$$

Defining

$$\mathcal{A} = \left\langle 0\left|\mathcal{O}(0)\right|\mathcal{O}\right\rangle \left\langle \mathcal{O}\left|\mathcal{O}(0)^\dagger\right|0\right\rangle = \left|\left\langle 0\left|\mathcal{O}(0)\right|\mathcal{O}\right\rangle\right|^2 \tag{B.38}$$

and dropping the term proportional to $e^{-E(t+L_t)}$, one arrives at

$$\begin{aligned}\left\langle 0\left|\mathcal{O}(t)\mathcal{O}(0)^\dagger\right|0\right\rangle_{\text{Torus}} &= \mathcal{A}(e^{-Et} + e^{-E(L_t-t)}) \\ &= \mathcal{A}e^{-EL_t/2} 2\cosh\left(E(t-L_t/2)\right). \end{aligned} \tag{B.39}$$

B.6 Backward propagation - 3pt functions

Using the same convention as in the main text, in particular the same time coordinates, but for the moment suppressing lattice spacing, position and momenta, consider the amplitude

$$C_{\mu\nu} = \left\langle 0\left|T\left\{P(t_f) j_\mu^\dagger(-\tau) J_\nu^\dagger(0)\right\}\right|0\right\rangle. \tag{B.40}$$

Following App. B.4, the asymptotic behaviour for $\tau > 0$ is

$$\begin{aligned} C_{\mu\nu} &\overset{t_P\to\infty}{\longrightarrow} \frac{Z_P}{2E_P} e^{-E_P t_f} \left\langle P(p)\left|J_\nu^\dagger(0) j_\mu^\dagger(-\tau)\right|0\right\rangle \\ &= \frac{Z_P}{2E_P} e^{-E_P t_P} \left\langle P(p)\left|J_\nu^\dagger(0) j_\mu^\dagger(-\tau)\right|0\right\rangle, \end{aligned} \tag{B.41}$$

using $t_P = t_f$. Using the method of images again and fixing the position of the pseudoscalar by time translation invariance, the dominant finite-time correction

comes from the amplitude

$$C'_{\mu\nu} = \left\langle 0 \left| T\left\{ P(t_f) j^\dagger_\mu(-\tau + L_t) J^\dagger_\nu(L_t) \right\} \right| 0 \right\rangle . \tag{B.42}$$

Again considering the case $\tau > 0$, i.e. $L_t > -\tau + L_t > t_f$, the amplitude takes the form

$$C'_{\mu\nu} = \left\langle 0 \left| J^\dagger_\nu(L_t) j^\dagger_\mu(-\tau + L_t) P(t_f) \right| 0 \right\rangle , \tag{B.43}$$

i.e. the amplitude has an anti-pseudoscalar in the distant past. Using (twisted) timereversal (or the $\mathcal{PT}$ symmetry of the amplitude) the normal timeordering can be recovered, yielding

$$C'_{\mu\nu} = \left\langle 0 \left| P(-t_f) j^\dagger_\mu(\tau - L_t) J^\dagger_\nu(-L_t) \right| 0 \right\rangle . \tag{B.44}$$

Note that the spatial momenta flip signs under (twisted) time reversal (but not under $\mathcal{PT}$). By inserting complete sets of states and again using $t_P = t_f$, one then finds the asymptotic behaviour

$$C'_{\mu\nu} \overset{t_P \to \infty}{\longrightarrow} \frac{Z_P}{2E_P} e^{-E_P(L_t - t_P - \tau)} \left\langle P(p) \left| J^\dagger_\mu(0) j^\dagger_\nu(-\tau) \right| 0 \right\rangle . \tag{B.45}$$

The calculation for $\tau < 0$ proceeds analogous.

B.7 Epsilon momentum average

Starting from the scalar amplitude $\tilde{A}(\tau)$ defined in Eq. (3.28) and the scalar counterpart $C(\tau)$, i.e.

$$\tilde{A}(\tau) = -\frac{\varepsilon_{ijk}\vec{q}^k}{m_P|\vec{q}^2|}\tilde{A}_{ij}(\tau), \tag{B.46}$$

$$C(\tau) = -\frac{\varepsilon_{ijk}\vec{q}^k}{m_P|\vec{q}^2|}C_{ij}(\tau), \tag{B.47}$$

the average over momentum orbits is constructed as follows. On the lattice, let

$$Q = \{\{\vec{q}_i\} : |\vec{q}_i|^2 = n^2, \vec{q}_i \neq -\vec{q}_j \forall i \neq j, \vec{q}_i^k \in \mathbb{Z}\} \tag{B.48}$$

be half the orbit of momentum n^2 (i.e. it only contains $\vec{q}$ or $-\vec{q}$, not both). Then one takes

$$\tilde{A}(\tau) = -\frac{L_x}{2\pi}\frac{\varepsilon_{ijk}\vec{q}^k}{2m_P|Q|n^2}\tilde{A}_{ij}(\tau), \tag{B.49}$$

$$C(\tau) = -\frac{L_x}{2\pi}\frac{\varepsilon_{ijk}\vec{q}^k}{2m_P|Q|n^2}C_{ij}(\tau), \tag{B.50}$$

with summation over double indices from 1 to 3, $\vec{q} \in Q$ and L_x the spatial extent of the lattice. Note that the discretized momenta take values of $\frac{2\pi}{L_x}\vec{q}^k$ for a $L_t \times L_x^3$ lattice with periodic spatial boundary conditions, which gives the prefactor of $\frac{L_x}{2\pi}$.

B.8 Operators for the η-meson calculation

In the physical basis, let

$$P = i\bar{\psi}\gamma_5 \begin{pmatrix} 1 & 0 & 0 \\ 0 & 1 & 0 \\ 0 & 0 & \epsilon \end{pmatrix} \psi, \tag{B.51}$$

where $\psi = (u, d, s)^T$ and with $\epsilon = -2$ for $P = \eta_8$ and $\epsilon = 1$ for $P = \eta_1$ be the interpolating operator for η_8 and η_1. Equivalently,

$$\eta_l = i\bar{\psi}\gamma_5\psi \text{ with } \psi = (u, d)^T, \tag{B.52}$$

$$\eta_s = i\bar{\psi}\gamma_5\epsilon\psi \text{ with } \psi = s. \tag{B.53}$$

The interpolating current operator is given by

$$J_\mu^Q = \bar{\psi}\gamma_\mu Q\psi, \tag{B.54}$$

with

$$Q = \begin{pmatrix} 2/3 & 0 & 0 \\ 0 & -1/3 & 0 \\ 0 & 0 & -1/3 \end{pmatrix}, \tag{B.55}$$

where $\psi = (u, d, s)^T$. Equivalently,

$$J_\mu^{Q,l} = \bar{\psi}\gamma_\mu Q\psi, \tag{B.56}$$

with

$$Q = \begin{pmatrix} 2/3 & 0 \\ 0 & -1/3 \end{pmatrix}, \tag{B.57}$$

where $\psi = (u, d)^T$, and

$$J_\mu^{Q,s} = \bar{\psi}\gamma_\mu Q\psi, \tag{B.58}$$

with

$$Q = -1/3, \tag{B.59}$$

where $\psi = s$.

Going to the twisted basis at maximal twist, one has the relations

$$\begin{aligned} \psi(x) &= \frac{1}{\sqrt{2}}(1 + i\gamma_5\tau^3)\chi(x), \\ \bar{\psi}(x) &= \bar{\chi}(x)\frac{1}{\sqrt{2}}(1 + i\gamma_5\tau^3), \end{aligned} \tag{B.60}$$

yielding for η_l at maximal twist

$$\begin{aligned} \eta_l &= i\bar{\psi}(x)\gamma_5\psi(x) \\ &\to \frac{1}{2}i\bar{\chi}(x)(1 + i\gamma_5\tau^3)\gamma_5(1 + i\gamma_5\tau^3)\chi(x) \\ &= -\bar{\chi}(x)\tau^3\chi(x), \end{aligned} \tag{B.61}$$

where $\chi = (u, d)^T$. To align with the conventions in the code, the minus sign will be dropped as was the case for the pion, thus

$$\eta_l = \bar{\chi}(x)\tau^3\chi(x). \tag{B.62}$$

For the light currents, one finds

$$J_\mu^{0,0,l} = \bar{\chi}\gamma_\mu \mathbb{1}\chi =: V_\mu^{0,0,l}, \tag{B.63}$$

$$J_\mu^{1,0,l} = \bar{\chi}\gamma_\mu \tau^3 \chi =: V_\mu^{1,0,l}, \tag{B.64}$$

$$J_\mu^{Q,l} = \frac{1}{6} V_\mu^{0,0,l} + \frac{1}{2} V_\mu^{1,0,l}. \tag{B.65}$$

η_s at maximal twist becomes

$$\begin{aligned} \eta_s &= i\bar{\psi}(x)\gamma_5\psi(x) \\ &\to \frac{1}{2} i\bar{\chi}(x)(1 + i\gamma_5\tau^3)\gamma_5\epsilon(1 + i\gamma_5\tau^3)\chi(x) \\ &= -\bar{\chi}(x)\tau^3\epsilon\chi(x), \end{aligned} \tag{B.66}$$

where $\chi = (s_+, s_-)^T$ for Osterwalder-Seiler strange quarks. To align with the conventions in the code, the minus sign will be dropped, thus

$$\eta_s = \bar{\chi}(x)\tau^3\epsilon\chi(x). \tag{B.67}$$

For the current, one finds

$$J_\mu^{Q,s} = -\frac{1}{3}\bar{\chi}\gamma_\mu \mathbb{1}\chi. \tag{B.68}$$

This would correspond to $-\frac{1}{3}V_\mu^{0,0,s}$ since it has the same structure as (B.63).

B.8.1 Twisted parity for the η-meson

Under twisted parity $P\tau^1$,

$$\begin{aligned} \chi(t, \vec{x}) &\xrightarrow{P\tau^1} i\gamma_0\tau^1\chi(t, -\vec{x}), \\ \bar{\chi}(t, \vec{x}) &\xrightarrow{P\tau^1} -i\bar{\chi}(t, -\vec{x})\gamma_0\tau^1, \end{aligned} \tag{B.69}$$

one finds

$$\begin{aligned}\eta(t,\vec{x})_l &= \bar{\chi}(t,\vec{x})\tau^3\chi(t,\vec{x}) \\ &\xrightarrow{P\tau^1} -i^2\bar{\chi}(t,-\vec{x})\gamma_0\underbrace{\tau^1\tau^3\tau^1}_{=-\tau^3}\gamma_0\chi(t,-\vec{x}) \\ &= -\bar{\chi}(t,-\vec{x})\tau^3\chi(t,-\vec{x}) = -\eta_l(t,-\vec{x}),\end{aligned} \tag{B.70}$$

and

$$\eta(t,\vec{x})_s \xrightarrow{P\tau^1} -\eta_s(t,-\vec{x}). \tag{B.71}$$

The currents needed for the light case transform as (dropping the index l)

$$\begin{aligned} V_k^{0,0} &\xrightarrow{P\tau^1} -V_k^{0,0}, \\ V_0^{0,0} &\xrightarrow{P\tau^1} V_0^{0,0}, \\ V_k^{1,0} &\xrightarrow{P\tau^1} V_k^{1,0}, \\ V_0^{1,0} &\xrightarrow{P\tau^1} -V_0^{1,0}, \end{aligned} \tag{B.72}$$

and for the strange case as

$$J_k^{Q,s} \xrightarrow{P\tau^1} -J_k^{Q,s}, \tag{B.73}$$

$$J_0^{Q,s} \xrightarrow{P\tau^1} J_0^{Q,s}, \tag{B.74}$$

i.e. it transforms like the light $V_\mu^{0,0}$. Note that this means that for entries of $C_{\mu\nu}$ where one of the indices is temporal and one spatial the behaviour under twisted parity is different from the case where both are either spatial or temporal (mixed indices give an additional minus sign).

Appendix C

Technical details

In this appendix, technical details complementary to the ones in Ch. 3 are discussed. App. C.1 contains information on the used model averaging procedure, while App. C.2 to C.5 contain information on the employed error calculation and autocorrelation.

C.1 Model averaging

A version of parts of this section is also included in Sec. 5.7, the main difference being the discussion of the effective number of data points not included there.
Due to different choices for the parameters, each analysis chain, defined by a set of parameter choices, yields $\mathcal{O}(10^3 - 10^4)$ values for $a_\mu^{P-\text{pole}}$. These parameters are the choice of fit range and fit model in the fit to $\tilde{A}(\tau)$, the choice of τ_{cut} when constructing the TFFs and finally the included cuts in the momentum plane in the fit to the modified z-expansion. For the remainder of this section such a choice of parameters is called an "analysis". A priori, only fits with χ^2/d.o.f close to 1 are included in an analysis chain for the single ensemble analyses. For the combined z-expansion fits the input $\tilde{A}(\tau)$ fit ranges and τ_{cut} were chosen to be close in physical units. i.e. within 10% of the values on cB211.072.64, with $1 \lesssim \chi^2_{\tilde{A}}/\text{d.o.f} \lesssim 2.4$. To determine which analyses in an analysis chain are important, a modified version of

the Akaike Information Criterion (AIC) [164, 181] is used.
The statistical errors for each analysis are calculated by the jackknife or bootstrap resampling procedure, with configurations spaced far enough such that there is virtually no autocorrelation between the input data $\tilde{A}(\tau)$, see App. C.2 and C.5.
Closely following the method introduced in [163] and [38], the model averaging proceeds as follows. For a target observable y, here $a_\mu^{P-\text{pole}}$, a histogram from the different analyses is built, assigning to each analysis a weight given by the AIC. This criterion is derived from the Kullback-Leibler divergence, which measures the distance of a fit function from the true distribution of the points. For a derivation see [163]. The modified AIC introduced in [38],

$$\text{AIC} \sim \exp\left[-\frac{1}{2}\left(\chi^2 + 2n_{\text{par}} - n_{\text{data}}\right)\right], \tag{C.1}$$

or, equivalently,

$$\text{AIC} \sim \exp\left[-\frac{1}{2}\left(\chi^2 + 2n_{\text{par}} + n_{\text{cut}}\right)\right], \tag{C.2}$$

is used, where the χ^2, the number of fit parameters n_{par} and the number of data points n_{data} describe the fit of interest. The equivalence follows from $n_{\text{data}} = n_{\text{tot}} - n_{\text{cut}}$, since

$$\exp\left[-\frac{1}{2}\left(\chi^2 + 2n_{\text{par}} - n_{\text{data}}\right)\right] = \exp\left[\frac{1}{2}n_{\text{tot}}\right]\exp\left[-\frac{1}{2}\left(\chi^2 + 2n_{\text{par}} + n_{\text{cut}}\right)\right], \tag{C.3}$$

where n_{tot} is the same for each fit and thus the factor $\exp\left[\frac{1}{2}n_{\text{tot}}\right]$ cancels. The first two terms in the exponent correspond to the standard AIC, and the last term is needed to weigh fits with different lengths in the fit ranges when fitting to $\tilde{A}(\tau)$ or to weight z-expansion fits with a differing number of cuts in the momentum plane when sampling the transition form factors. For the i-th analysis, two copies of Eq. (C.1) are applied multiplicatively, one each for both the fit to $\tilde{A}(\tau)$ and the z-expansion in the single ensemble analyses. In the combined z-expansion fit analyses, three copies of Eq. (C.1) are applied for the fit to $\tilde{A}(\tau)$ on the three ensembles. The weights obtained in this way are normalized such that their sum over all analyses equals 1, i.e. let w_i be the weight of the i-th analysis for the quantity y, with $\sum_i w_i = 1$. The weights w_i are interpreted as a probability. Noting that due to the central limit theorem, the statistical uncertainties follow a Gaussian distribution $N(y; m_i, \sigma_i)$, with central value m_i and standard deviation σ_i, one can include the statistical uncertainties.

Central value and standard deviation are given by the jackknife resampling procedure for each analysis. One then defines the cumulative distribution function (CDF)

$$P(y;\lambda) = \int_{-\infty}^{y} dy' \sum_i w_i N(y'; m_i, \sigma_i\sqrt{\lambda}), \tag{C.4}$$

where the rescaling of the statistical error by λ is introduced to later separate statistical and systematic error.
The median of the CDF is chosen as the central value of y and the total error by the 16% and 84% percentiles of the CDF, i.e.

$$\sigma^2_{\text{total}} \equiv \left[\frac{1}{2}\left(y_{84} - y_{16}\right)\right]^2, \tag{C.5}$$

where $P(y_{16};1) = 0.16$ and $P(y_{84};1) = 0.84$. The systematic error could then be defined by evaluating the 16% and 84% percentiles of the $P(y;0)$ since $\lambda = 0$ cancels the statistical contribution to the distribution. Since $P(y;0)$ as a function of step functions is a step function itself, the definition of the systematic error would be highly sensitive to the value of the chosen percentile. A more robust choice for the systematic error can be made by first demanding

$$\sigma^2_{\text{total}} \equiv \sigma^2_{\text{stat}} + \sigma^2_{\text{sys}}, \tag{C.6}$$

and noticing that the rescaling of each σ_i^2 by λ is expected to increase σ^2_{stat} by the same factor, i.e.

$$\lambda\sigma^2_{\text{stat}} + \sigma^2_{\text{sys}} \equiv \left[\frac{1}{2}\left(\tilde{y}_{84} - \tilde{y}_{16}\right)\right]^2 \equiv \tilde{\sigma}^2_{\text{total}}, \tag{C.7}$$

where $P(\tilde{y}_{16};\lambda) = 0.16$ and $P(\tilde{y}_{84};\lambda) = 0.84$. The systematic and statistic errors can then be separated by a second choice of λ:

$$\sigma^2_{\text{stat}} = \frac{\sigma^2_{\text{total}} - \tilde{\sigma}^2_{\text{total}}}{1-\lambda}, \qquad \sigma^2_{\text{sys}} = \frac{\tilde{\sigma}^2_{\text{total}} - \lambda\sigma^2_{\text{total}}}{1-\lambda}. \tag{C.8}$$

In particular, the CDF is smooth for big enough λ and the procedure is insensitive to the choice of λ.
For a better understanding on the composition of the systematic error, the error budgeting procedure suggested in [38] can be used. For one of the choices made during the analysis chain, e.g. the choice between the VMD or LMD fit to $\tilde{A}(\tau)$ or

the different fit ranges, the total error for each possible option is first determined, varying all other components of the analysis. Then a second CDF is constructed as in Eq. (C.4), with m_i the average of the 16% and 84% percentiles, σ_i the total error and w_i the sum of the weights coming from this choice. Using this CDF, the systematic error is derived as described above for the original CDF, this gives the result for the systematic error corresponding to the choice. Note that the estimated systematic errors associated with each of the steps of the analysis by this procedure are correlated, thus they do not sum up quadratically to the full systematic error.

C.1.1 Effective number of data points

As argued in [188–190], the overall sample size may not be the correct quantity to use in the AIC when the data are correlated and the effective number of parameters is unclear.
To that end, consider the AIC with n_{data} replaced by n_{eff}, where the effective sample size n_{eff} is the number with the property that the estimator has the same variance as the estimator one gets by sampling n_{eff} independent measurements [191]. Further following [191], one can show that the upper limit on n_{eff} is given by

$$|R| = \sup\left\{\frac{1}{a^* R a} : a \in \mathbb{R}^n, \sum a_i = 1\right\}, \tag{C.9}$$

where R is the correlation matrix, i.e. the normalized covariance matrix given by

$$R_{ij} = \rho_{Y_i,Y_j} = \text{cov}(Y_i/\sigma_{Y_i}, Y_j/\sigma_{Y_j}), \tag{C.10}$$

with

$$\text{cov}(X_i, X_j) = E\left[(X_i - E\left[X_i\right])(X_j - E\left[X_j\right])\right]. \tag{C.11}$$

Further, E stands for the expected value of its argument, i.e.

$$E[X] = \sum_i x_i p_i \overset{\text{if } p_i = 1/N}{=} \frac{1}{N}\sum_i x_i, \tag{C.12}$$

and the standard deviation σ_{X_i} is given by

$$\sigma_{X_i} = \sqrt{E\left[(X_i - E\left[X_i\right])^2\right]} = \sqrt{E\left[X_i^2\right] - \left(E\left[X_i\right]\right)^2}. \tag{C.13}$$

Note that Eq. (C.9) holds for positive definite matrices. Further, the magnitude $|R|$ of the correlation matrix is calculated by summing up all entries of R^{-1}. The effective number of data points $n_{\text{eff}} = |R|$ is then used as a variant for model averaging.

C.2 Autocorrelation, rebinning, bootstrap and jackknife

The goal of a Markov chain Monte Carlo simulation is the evaluation of an integral of the form

$$\langle O \rangle = \int d\theta \, O[\theta] p(\theta). \tag{C.14}$$

By generating N samples θ_n, $n \in \{1, ..., N\}$ according to the probability density $p(\theta)$, the ensemble average $\langle O \rangle$ is approximated by

$$\langle O \rangle \approx \frac{1}{N} \sum_{n=1}^{N} O(\theta_n), \tag{C.15}$$

assuming that the generated sequence of samples is a representative set of configurations. Following [83], in lattice simulations, the ensemble averages typically are of the form

$$\langle O \rangle = \frac{\int DU \, O[U] e^{-S[U]}}{\int DU \, e^{-S[U]}}, \tag{C.16}$$

where $S[U]$ is a real functional of the link variables. The probability distribution is given by the Boltzmann factor $e^{-S[U]}$ and typically only a small fraction of the possible link configurations contribute significantly to Eq. (C.16).
Further following [83], consider a countable set of states C_n, $n \in \{1, ..., N\}$, of the system of interest, generated sequentially by a stochastic process according to some transition probability $P(C_n \to C_m)$ to go from the system state C_n to the state C_m. At any given simulation time n, the state of the system will then be a random

variable, whose distribution depends only on the state at simulation time $n-1$, which defines a so-called "Markov chain". To approximate the ensemble average $\langle O \rangle$ by

$$\langle O \rangle_N = \frac{1}{N} \sum_{n=1}^{N} O(C_n) \equiv \mu_O, \tag{C.17}$$

it is sufficient for the Markov process to sample the distribution $e^{-S[U]}$ ergodic and that the transition probability satisfies detailed balance for any two states C and C', i.e.

$$e^{-S(C)} P(C \to C') = e^{-S(C')} P(C' \to C). \tag{C.18}$$

If the states C_n were independently drawn from the probability distribution, the sampling variance would be given by

$$\sigma^2 = \frac{1}{N} \sum_{n=1}^{N} (O(C_n) - \mu_O)^2. \tag{C.19}$$

However, since each state in the Markov chain depends on the previous state, the states C_n are not independent by definition and the variance, following [192], is given by

$$\sigma^2 = \frac{\tau_O}{N} \sum_{n=1}^{N} (O(C_n) - \mu_O)^2 \tag{C.20}$$

instead, where τ_O is the integrated autocorrelation time for the given Markov chain. Thus the error decreases as $\sqrt{\tau_O/N}$ instead of $\sqrt{1/N}$ for increasing N, and τ_O can be interpreted as the number of simulation time steps needed for two samples to be uncorrelated, i.e. N/τ_O corresponds to the effective number of samples. The definition of τ_O is

$$\tau_O = \sum_{\tau=-\infty}^{\infty} \rho_O(\tau), \tag{C.21}$$

where $\rho_O(\tau)$ is the normalized autocorrelation function for the observable O. In [192], an exact expression for $\rho_O(\tau)$ is given, in practise one uses the estimator $\hat{\rho}_O(\tau)$ given by

$$\hat{\rho}_O(\tau) = \frac{\hat{c}_O(\tau)}{\hat{c}_O(0)}, \tag{C.22}$$

with the autocorrelation function

$$\hat{c}_O(\tau) = \frac{1}{N-\tau} \sum_{n=1}^{N-\tau} (O(C_n) - \mu_O)(O(C_{n+\tau}) - \mu_O), \tag{C.23}$$

leading to the estimated integrated autocorrelation time $\hat{\tau}_O(M)$

$$\hat{\tau}_O(M) = 1 + 2 \sum_{\tau=1}^{M} \hat{\rho}_O(\tau), \tag{C.24}$$

where $M \ll N$. It is recommended by [192] to choose M such that $M \geq \kappa \hat{\tau}_O(M)$, for a constant $\kappa \approx 5$, which is found to give reliable estimates of the integrated autocorrelation time for $N \geq 1000\, \tau_O$.

If τ_O is bigger than 1, one can do a so-called "rebinning" of the observables $O(C_n)$ by taking averages of blocks of consecutive observables, defining a new and smaller set of observables. With increasing block sizes, the averages become less and less correlated and the set of averages upon reaching $\tau_O \approx 1$ can be treated as independent observables. Too small choices of the block size in the rebinning lead to an underestimation of the variance. Most notably, if the block size is smaller than the integrated autocorrelation time, it is immediately clear from Eq. (C.20) that the naive variance, cf. Eq. (C.19), is smaller than the true variance. Since it is hard to reliably estimate the integrated autocorrelation time for a relatively small number of measurements, one can check the dependence of the variance on the rebinning block size and conclude that the data can be treated as independent once the variance does not increase with increasing block size anymore. This is illustrated in Fig. C.1 using both jackknife and bootstrap resampling, which will be explained in the following, to estimate the variance as well as two different methods for the rebinning. Note that rebinning requires that the observable one wants to do statistics on either is the rebinned observable itself or that its dependence on the rebinned observable is linear. To estimate the variance on the observables, the jackknife and bootstrap methods are used, cf. [194–196]. Both of them are resampling procedures used for estimating the distributions of statistics based on a sample of independent observables $O(C_1), ..., O(C_N)$ by constructing replicas or resamplings from the original sample. Note that as shown in [197], the jackknife is a linear approximation of the bootstrap. As an example, one would like to find confidence intervals on μ_O, the approximation of the ensemble average $\langle O \rangle$. Note that μ_O should converge to the real mean $\langle O \rangle$ in

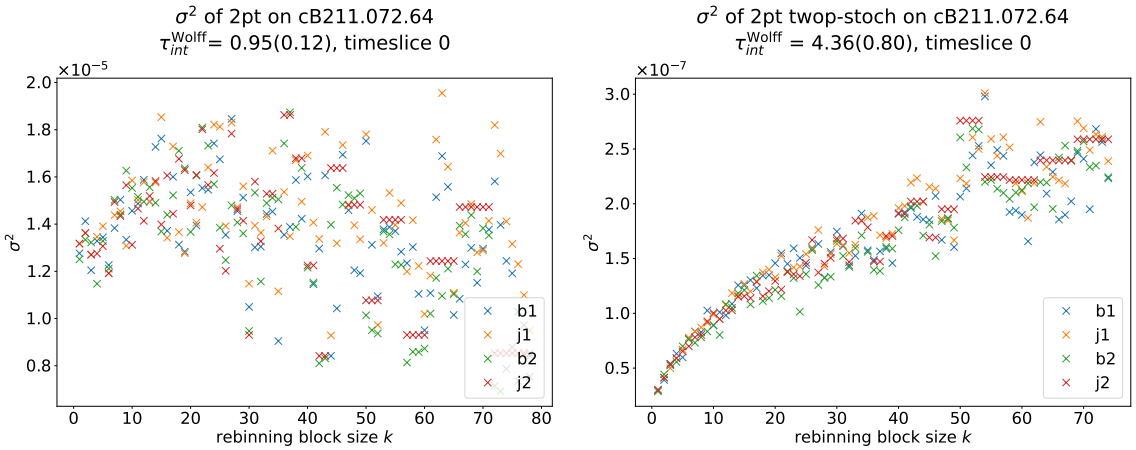

Figure C.1: Variance at $\tau = 0$ with increasing rebinning block size on cB211.072.64 for the charged pion two-point function $C^{(2)}(\tau)$ using local (point-to-all) (left) and stochastic (all-to-all) (right) quark propagators for the pseudoscalar operators [126–128]. The variance was calculated using bootstrap and jackknife resampling (denoted by "b" and "j") and two methods for rebinnig were used. The first method distributes the measurements to blocks of a fixed given size, the last few measurements are dropped if not enough are left to form a block ("1"), the second method distributes the measurements as evenly as possible on blocks of a given minimal size ("2"). Note that this may lead to plateaus in the plots for the jackknife resamplings. Further note the increase in variance on the right with increasing block size, a clear indicator of autocorrelation, while there is no such behaviour on the left, indicating that this observable has no autocorrelation. Also given in the titles are estimates of the autocorrelation time $\tau_{int}^{\text{Wolff}}$ using an implementation of the method presented in [193]. For more details and plots, see App. C.5.

the limit of infinite statistics. Since μ_O is a function of the Markov chain, it also has a probability distribution, which can be approximated using the empirical distribution of the replicas. It is shown in [198] that the bootstrap method holds for t-statistics, in particular, it holds for giving confidence intervals on μ_O.
The jackknife estimator is constructed by systematically leaving out one of the original observables to generate a new sample. In the nth sample S_n one leaves out $O(C_n)$ such that the set of samples is given by

$$S = \{S_n\}_{n=1}^N = \left\{\{O(C_i)\}_{i=1,i\neq n}^N\right\}_{n=1}^N, \tag{C.25}$$

the nth jackknife replica $\bar{O}_n$ is then given by the mean of S_n, i.e.

$$\bar{O}_n = \frac{1}{N-1}\sum_{i=1,i\neq n}^{N} O(C_i). \tag{C.26}$$

It is straightforward to show that the central value of the original sample, μ_O, is equal to the mean of the jackknife replicas

$$\bar{\mu}_O = \frac{1}{N}\sum_{n=1}^{N}\bar{O}_n, \tag{C.27}$$

cf. App. C.3. The jackknife estimate of the variance is then given by

$$\sigma_j^2 = \frac{N-1}{N}\sum_{n=1}^{N}(\bar{O}_n - \bar{\mu}_O)^2. \tag{C.28}$$

The bootstrap estimator is constructed by generating N_b samples of size N by drawing with replacement from the original sample, assigning a weight of $1/N$ to each $O(C_n)$. The set of samples is then given by

$$S = \{S_n\}_{n=1}^{N_b}, \tag{C.29}$$

the nth bootstrap replica $\bar{O}_n$ by the mean of S_n, i.e.

$$\bar{O}_n = \frac{1}{N}\sum_{O(C_i)\in S_n} O(C_i). \tag{C.30}$$

For the bootstrap, the mean of the bootstrap replicas,

$$\bar{\mu}_O = \frac{1}{N_b} \sum_{n=1}^{N_b} \bar{O}_n, \tag{C.31}$$

only coincides with the central value μ_O of the original sample in the limit of infinite statistics, i.e. if $N_b \to \infty$. The bootstrap estimate of the variance is then given by

$$\sigma_b^2 = \frac{1}{N_b - 1} \sum_{n=1}^{N_b} (\bar{O}_n - \bar{\mu}_O)^2. \tag{C.32}$$

C.3 Central value and mean of jackknife samples

Proof of the equivalence of the central value of a dataset and the mean of the jackknife samples:
Suppose the dataset D contains N_c values, i.e.

$$D = \{x_i\}_{i=1}^{N_c}. \tag{C.33}$$

From this one constructs the set of jackknife samples S by leaving out x_n in the nth sample S_n, i.e.

$$S = \{S_n\}_{n=1}^{N_c} = \left\{ \{x_i\}_{i=1, i\neq n}^{N_c} \right\}_{n=1}^{N_c}. \tag{C.34}$$

The central value $\bar{x}$ of D is then given by

$$\bar{x} = \frac{1}{N_c} \sum_{i=1}^{N_c} x_i, \tag{C.35}$$

and the sample mean $\bar{x}_n$ of S_n by

$$\bar{x}_n = \frac{1}{N_c - 1} \sum_{i=1, i\neq n}^{N_c} x_i. \tag{C.36}$$

The mean over all jackknife samples is then

$$\bar{x}_s = \frac{1}{N_c}\sum_{i=1}^{N_c}\bar{x}_n = \frac{1}{N_c}\sum_{i=1}^{N_c}\frac{1}{N_c-1}\sum_{i=1,i\neq n}^{N_c} x_i \tag{C.37}$$

$$= \frac{1}{N_c(N_c-1)}\sum_{i=1}^{N_c}(N_c-1)x_i = \frac{1}{N_c}\sum_{i=1}^{N_c} x_i = \bar{x}. \qquad \square \tag{C.38}$$

C.4 Reconstruction of original data from jackknife samples

Given the set of jackknife replicas

$$\bar{D} = \{\bar{x}_i\}_{i=1}^{N_c}, \tag{C.39}$$

the original data set $D = \{x_i\}_{i=1}^{N_c}$ can be recovered exactly. In matrix form,

$$\bar{\mathcal{D}} = \frac{1}{N_c-1}\begin{pmatrix} 0 & 1 & 1 & \cdots & 1 \\ 1 & 0 & 1 & \cdots & 1 \\ \vdots & \ddots & \ddots & \ddots & \vdots \\ 1 & \cdots & 1 & 0 & 1 \\ 1 & \cdots & 1 & 1 & 0 \end{pmatrix}, \tag{C.40}$$

such that $\bar{\mathcal{D}}D = \bar{D} \Leftrightarrow \bar{\mathcal{D}}^{-1}\bar{D} = D$. Note that the inverse is given by

$$\bar{\mathcal{D}}^{-1} = \begin{pmatrix} -(N_c-2) & 1 & 1 & \cdots & 1 \\ 1 & -(N_c-2) & 1 & \cdots & 1 \\ \vdots & \ddots & \ddots & \ddots & \vdots \\ 1 & \cdots & 1 & -(N_c-2) & 1 \\ 1 & \cdots & 1 & 1 & -(N_c-2) \end{pmatrix}. \tag{C.41}$$

C.5 Plots of variance with increasing rebinning block size

This appendix contains a representative set of plots showing the behaviour of the variance relative to the block size chosen in the rebinning. Shown are two-point (2pt) functions $C^{(2)}(\tau)$ using local (point-to-all), labelled by "twop-local", and stochastic (all-to-all), labelled by "twop-stoch", quark propagators for the pseudoscalar operators [126–128], three-point (3pt) $C(\tau)$ functions using local sources, $\tilde{A}(\tau)$, converted to configurations from jackknife samples as derived in App. C.4, as well as a quantity $\bar{A}(\tau)$, which is related to $\tilde{A}(\tau)$, schematically given by

$$\bar{A}(\tau) \sim \left\langle \frac{\langle 0|T\{j_\mu(\tau,\vec{x})j_\nu(0)\}P^\dagger(-t_P,\vec{p})|0\rangle}{\langle P(0,\vec{0})P^\dagger(-t_P,\vec{0})\rangle} \right\rangle , \tag{C.42}$$

i.e. the ensemble average of the ratio between 3pt and 2pt function, opposed to $\tilde{A}(\tau)$ which is the ratio of the ensemble average of the 3pt and the ensemble average of the 2pt function. Note that the standard method of estimating the autocorrelation on $\tilde{A}(\tau)$ by rebinning the 2pt function, extracting the needed mass and overlap factor and then using the same rebinning on the 3pt function gives, within errors, the same results for the variation, see C.2 for an illustration. This holds trivially by construction for linear quantities, e.g. the 3pt function itself, but for composite quantities, e.g. the mass and overlap factor obtained by fitting the 2pt function, the correspondence is only observed empirically. Also given in the titles are estimates of the autocorrelation time $\tau_{int}^{\text{Wolff}}$ using an implementation of the method presented in [193]. Figs. C.3, C.4 and C.5 show plots for the charged pion on cB211.072.64, cC211.060.80 and cD211.054.96, respectively, Fig. C.6 plots for η_8 on cB211.072.64. The variances were calculated using bootstrap and jackknife resampling (denoted by "b" and "j" in the legends) and two methods for rebinnig were used. The first method distributes the measurements to blocks of a fixed given size, the last few measurements are dropped if not enough are left to form a block ("1" in the legends), the second method distributes the measurements as evenly as possible on blocks of a given minimal size ("2" in the legends). Note that this may lead to plateaus in the plots for the jackknife resamplings. All plots are shown for timeslice $\tau = 5$, i.e. close to the peak where the effects of the autocorrelation are expected to be seen the most

clear due to the good signal-to-noise ratio. They are, however, representative for almost all timeslices. Except for the twop-stoch 2pt functions and the η_8 2pt function, no significant autocorrelation was observed, most notably, the autocorrelation does not show up in $\bar{A}(\tau)$ using the twop-stoch 2pt function and the η_8 $\tilde{A}$.

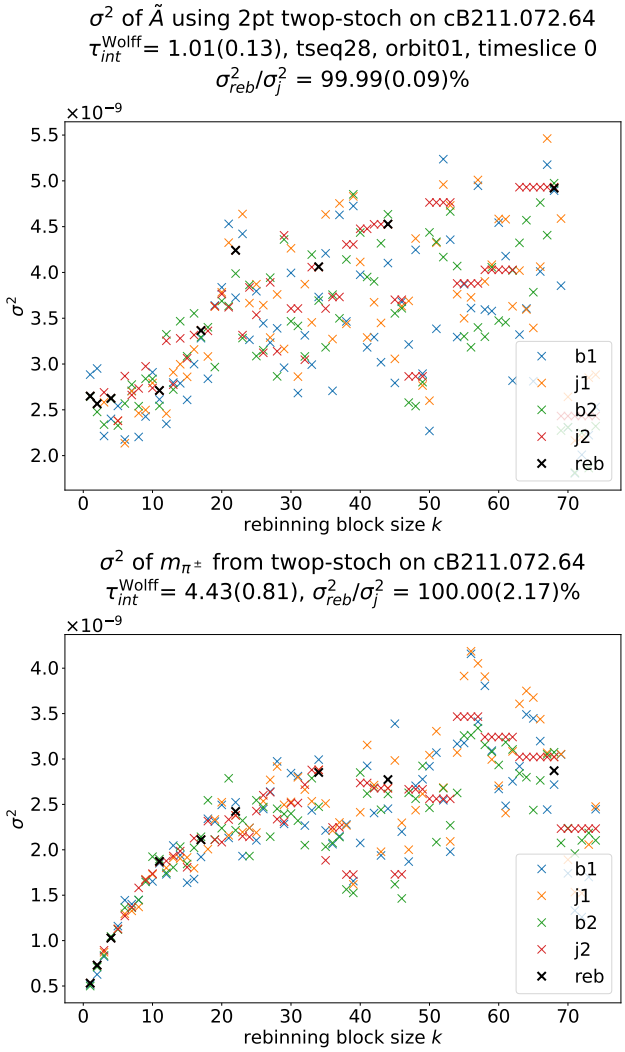

Figure C.2: Variance on $\tilde{A}$ (top) and $m_{\pi^\pm}$ (bottom) for the charged pion on cB211.072.64 with increasing rebinning block size. The points labelled with "j" and "b" were calculated using $\tilde{A}(\tau)$ converted to configurations from jackknife samples, while a separate rebinning of the 2pt and 3pt function was used for the points labelled with "reb". Also indicated is the ratio $\sigma^2_{reb}/\sigma^2_j$, considering only the block sizes used for the "reb" datapoints.

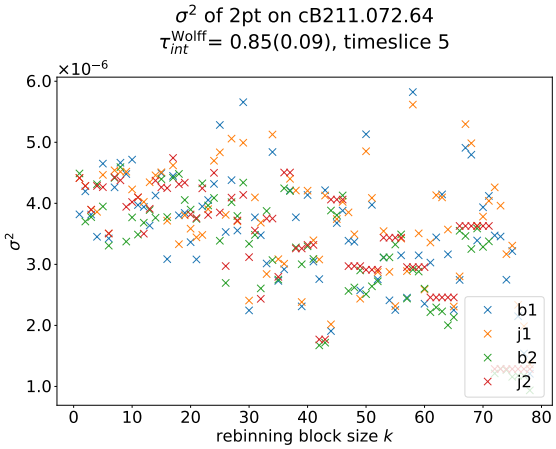

(a) twop-local 2pt function

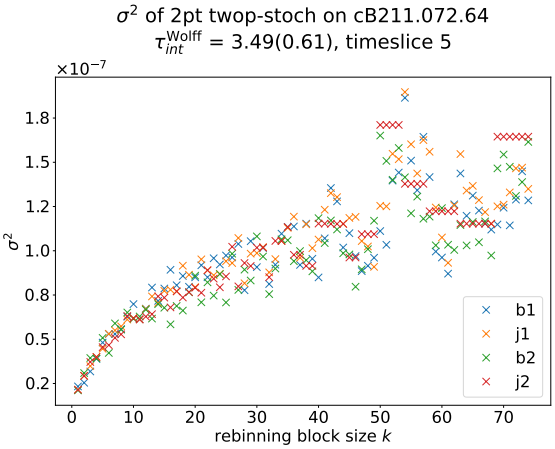

(b) twop-stoch 2pt function

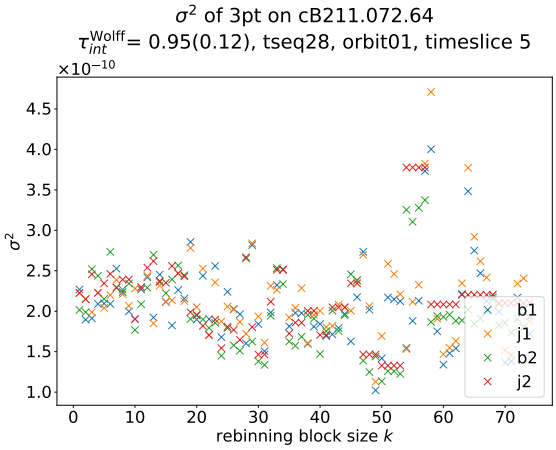

(c) 3pt function

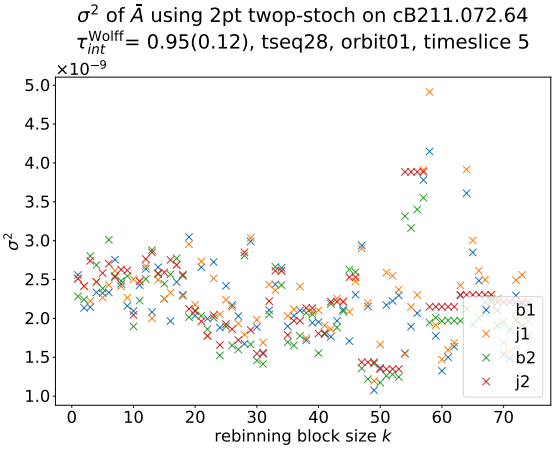

(d) $\bar{A}$ using the twop-stoch 2pt function

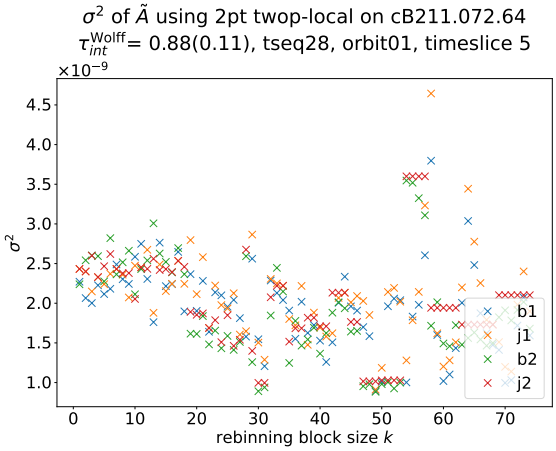

(e) $\tilde{A}$ using the twop-local 2pt function

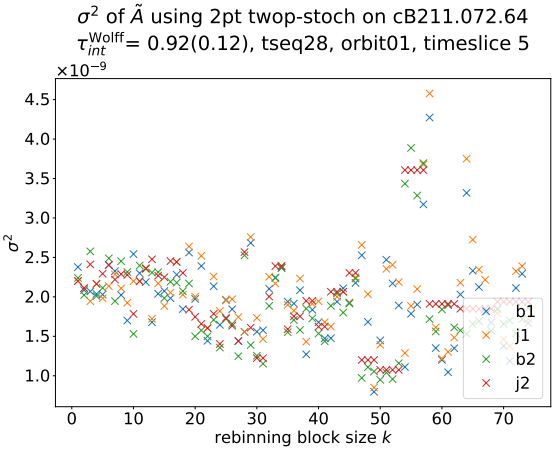

(f) $\tilde{A}$ using the twop-stoch 2pt function

Figure C.3: cB211.072.64 charged pion variance with increasing rebinning block size.

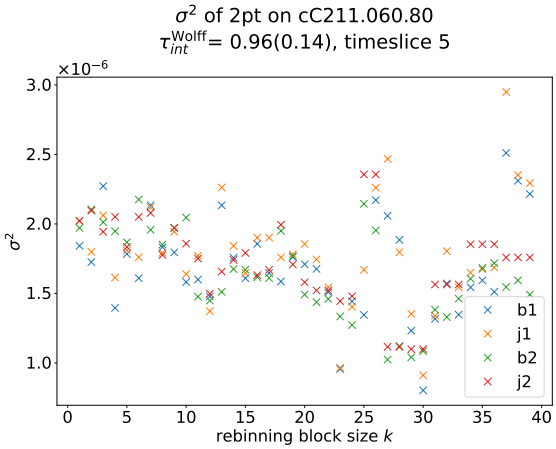

(a) twop-local 2pt function

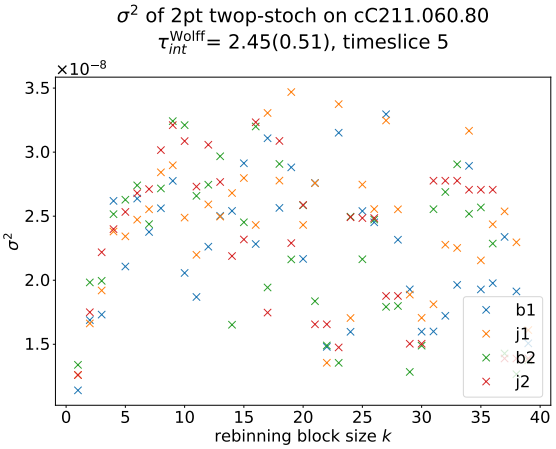

(b) twop-stoch 2pt function

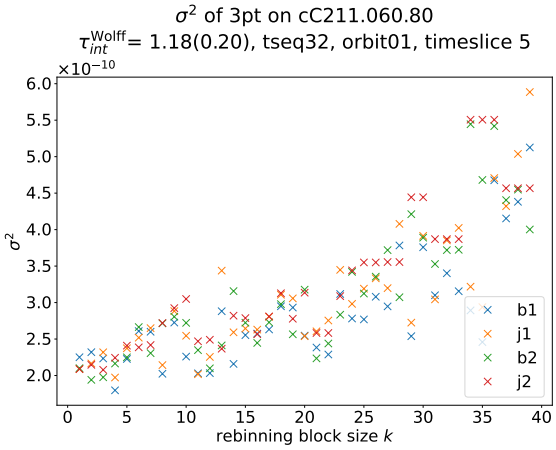

(c) 3pt function

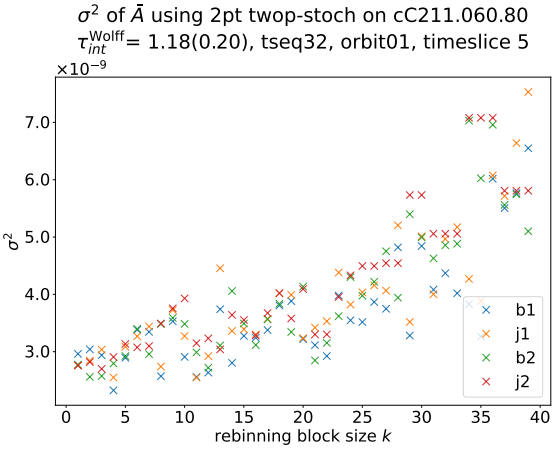

(d) $\bar{A}$ using the twop-stoch 2pt function

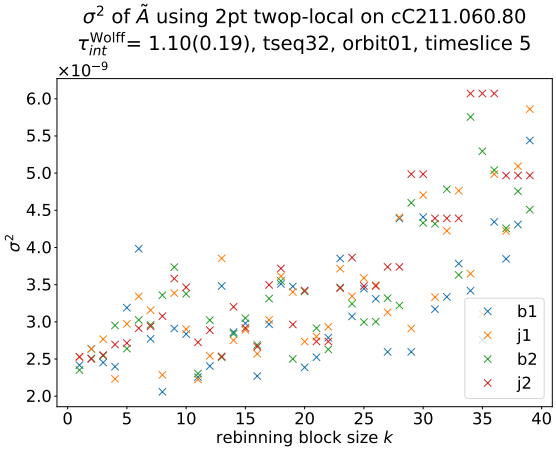

(e) $\tilde{A}$ using the twop-local 2pt function

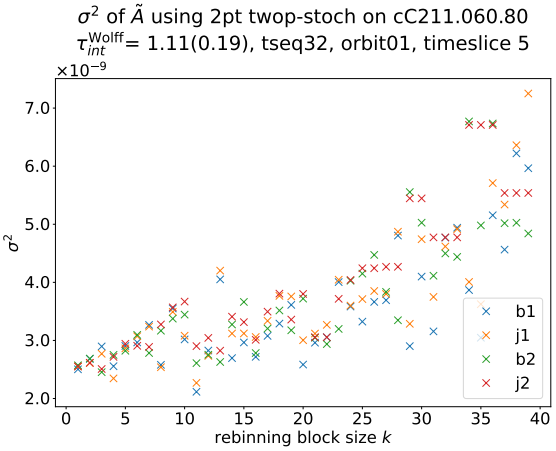

(f) $\tilde{A}$ using the twop-stoch 2pt function

Figure C.4: cC211.060.80 charged pion variance with increasing rebinning block size.

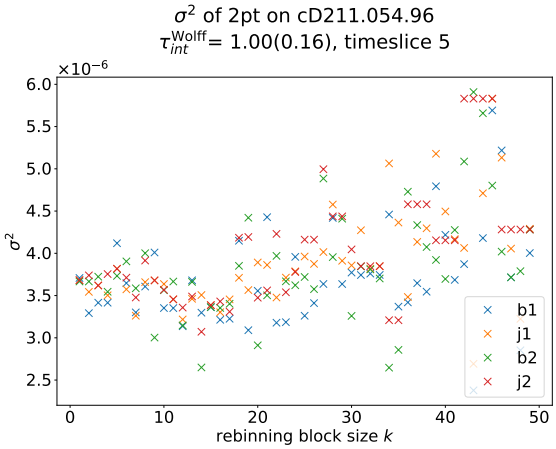

(a) twop-local 2pt function

(b) twop-stoch 2pt function

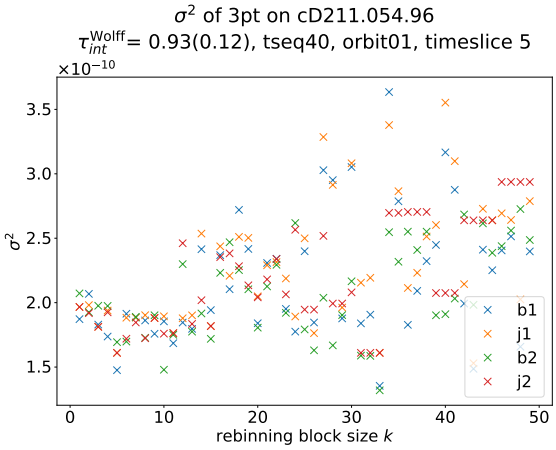

(c) 3pt function

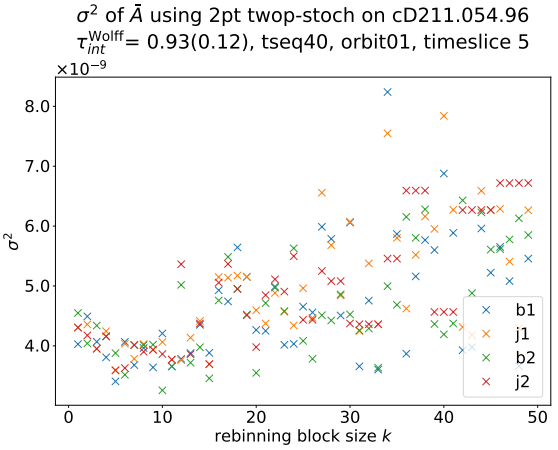

(d) $\bar{A}$ using the twop-stoch 2pt function

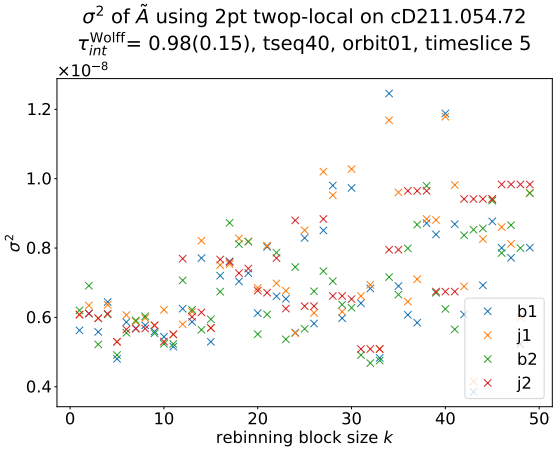

(e) $\tilde{A}$ using the twop-local 2pt function

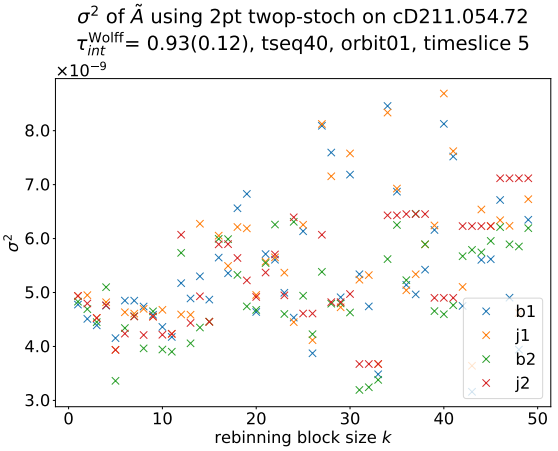

(f) $\tilde{A}$ using the twop-stoch 2pt function

Figure C.5: cD211.054.96 charged pion variance with increasing rebinning block size.

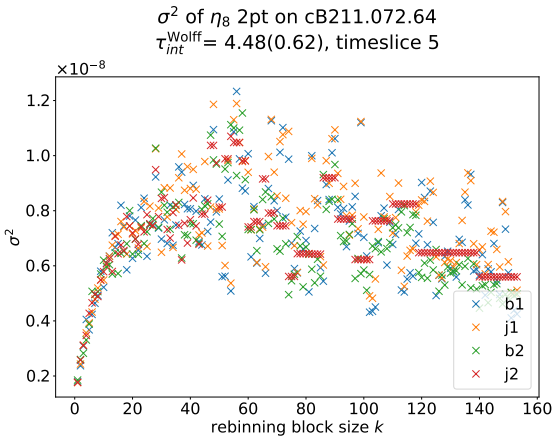

(a) 2pt function

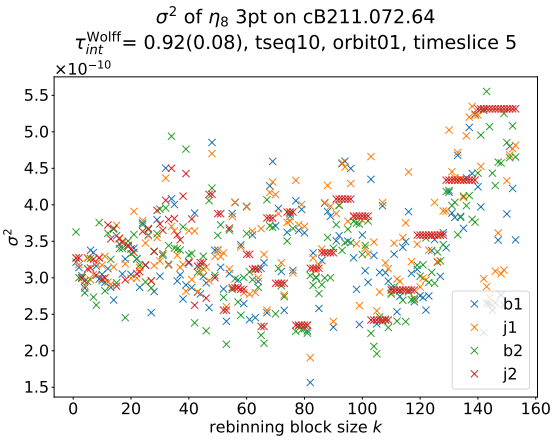

(b) 3pt function

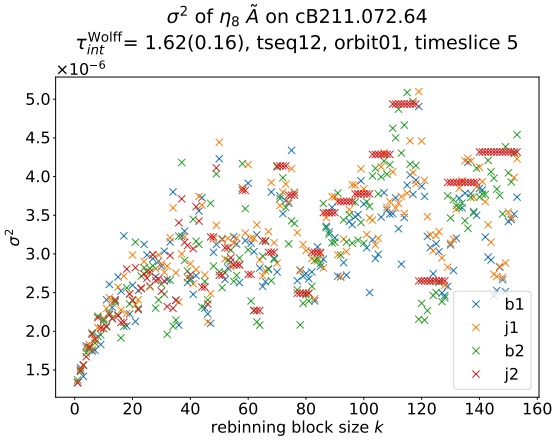

(c) $\tilde{A}$

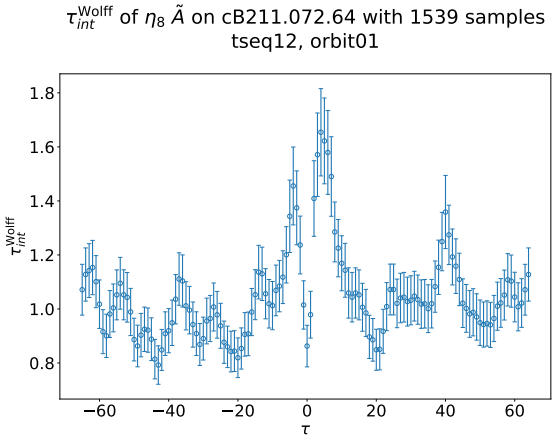

(d) $\tau_{int}^{\text{Wolff}}$ on $\tilde{A}$ per timeslice

Figure C.6: cB211.072.64 η-meson variance with increasing rebinning block size.

Appendix D

Plots and illustrations

In this appendix, plots and illustrations are collected which complement and expand the examples given in the main text. Shown are 3pt and 2pt amplitudes for the pion in App. D.1 and η-meson in App. D.2, the accessible kinematical regions for the pion TFFs on all three ensembles together with a discussion of the sampling in the momentum plane in App. D.3 and D.4 as well as pion transition form factors in App. D.5.

D.1 Plots of pion amplitudes

Here, an overview over the charged pion $C(\tau)$, $\tilde{A}(\tau)$ and $C^{(2)}(t)$ is given. See Sec. 3.3 for the construction of the shown quantities.

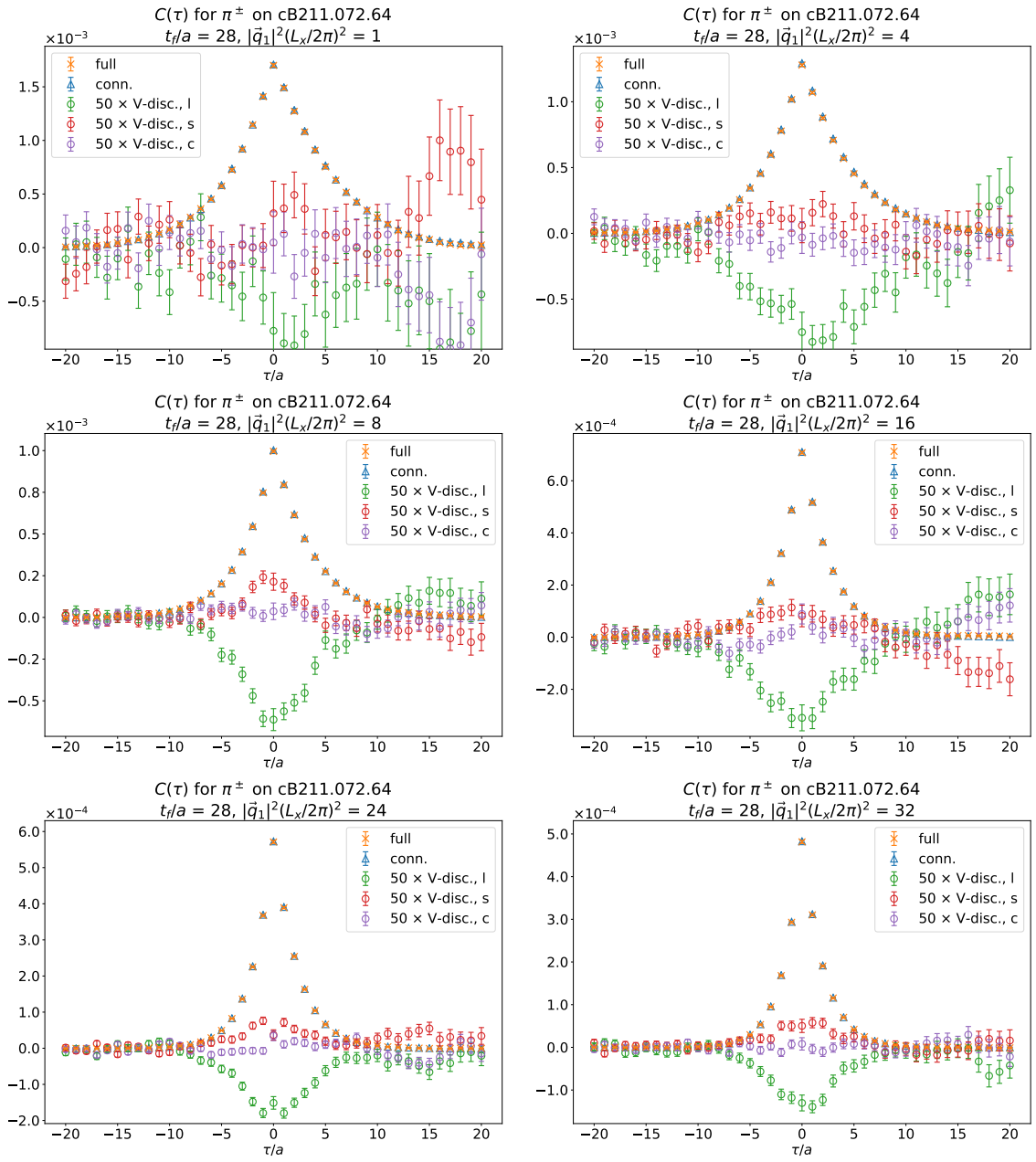

Figure D.1: Momentum orbit averaged $C(\tau, t_f = 2.23\,\mathrm{fm})$ for $\tau/a \in [-20, 20]$ on cB211.072.64 for six orbits. Shown are in orange the full $C(\tau)$, in blue $C^{\mathrm{conn.}}(\tau)$ and in green, red and purple the three $C^{\mathrm{V-disc.}}(\tau)$ multiplied by 50 for easier comparison.

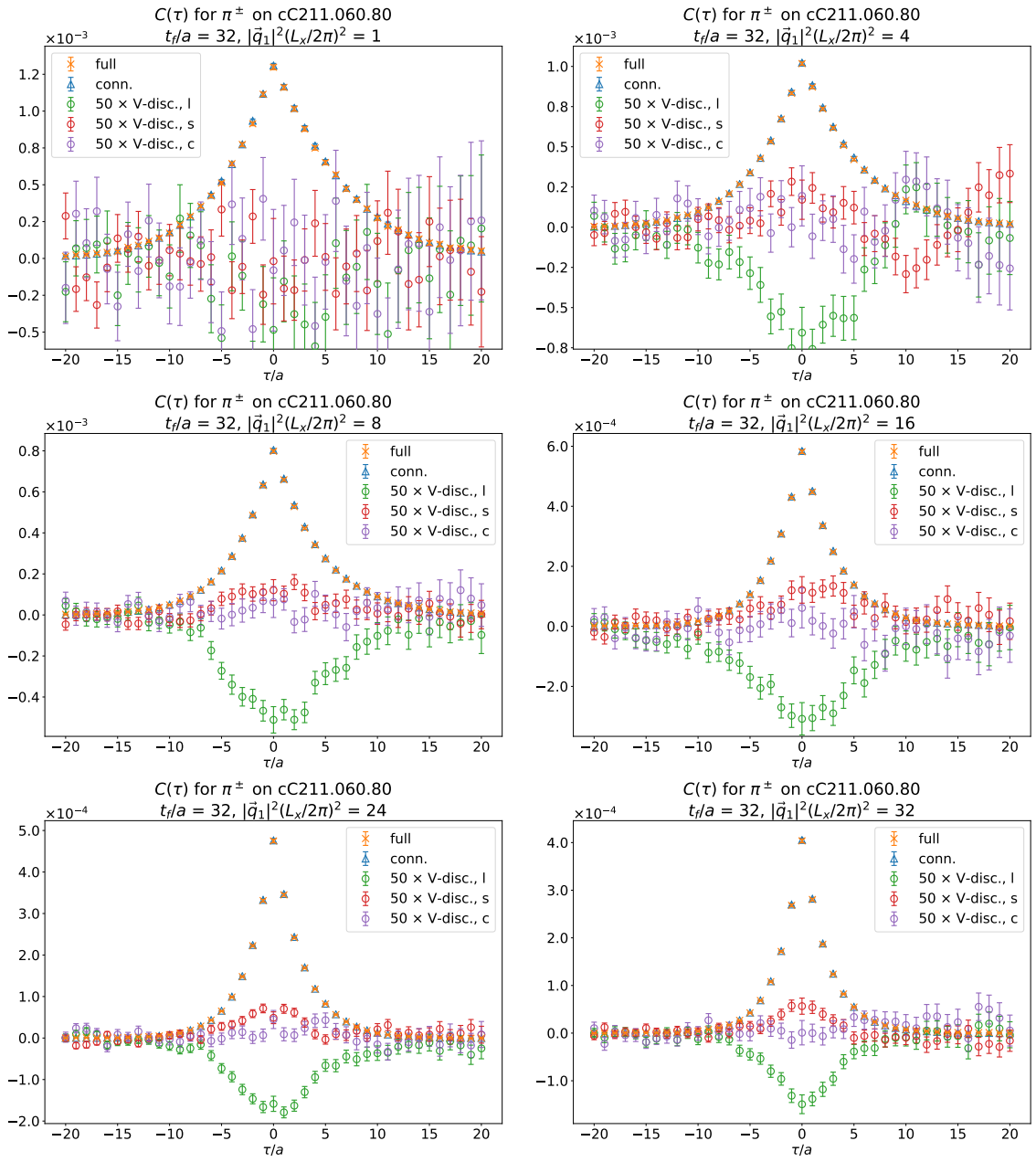

Figure D.2: Momentum orbit averaged $C(\tau, t_f = 2.18\,\mathrm{fm})$ for $\tau/a \in [-20, 20]$ on cC211.060.80 for six orbits. Shown are in orange the full $C(\tau)$, in blue $C^{\mathrm{conn.}}(\tau)$ and in green, red and purple the three $C^{\mathrm{V-disc.}}(\tau)$ multiplied by 50 for easier comparison.

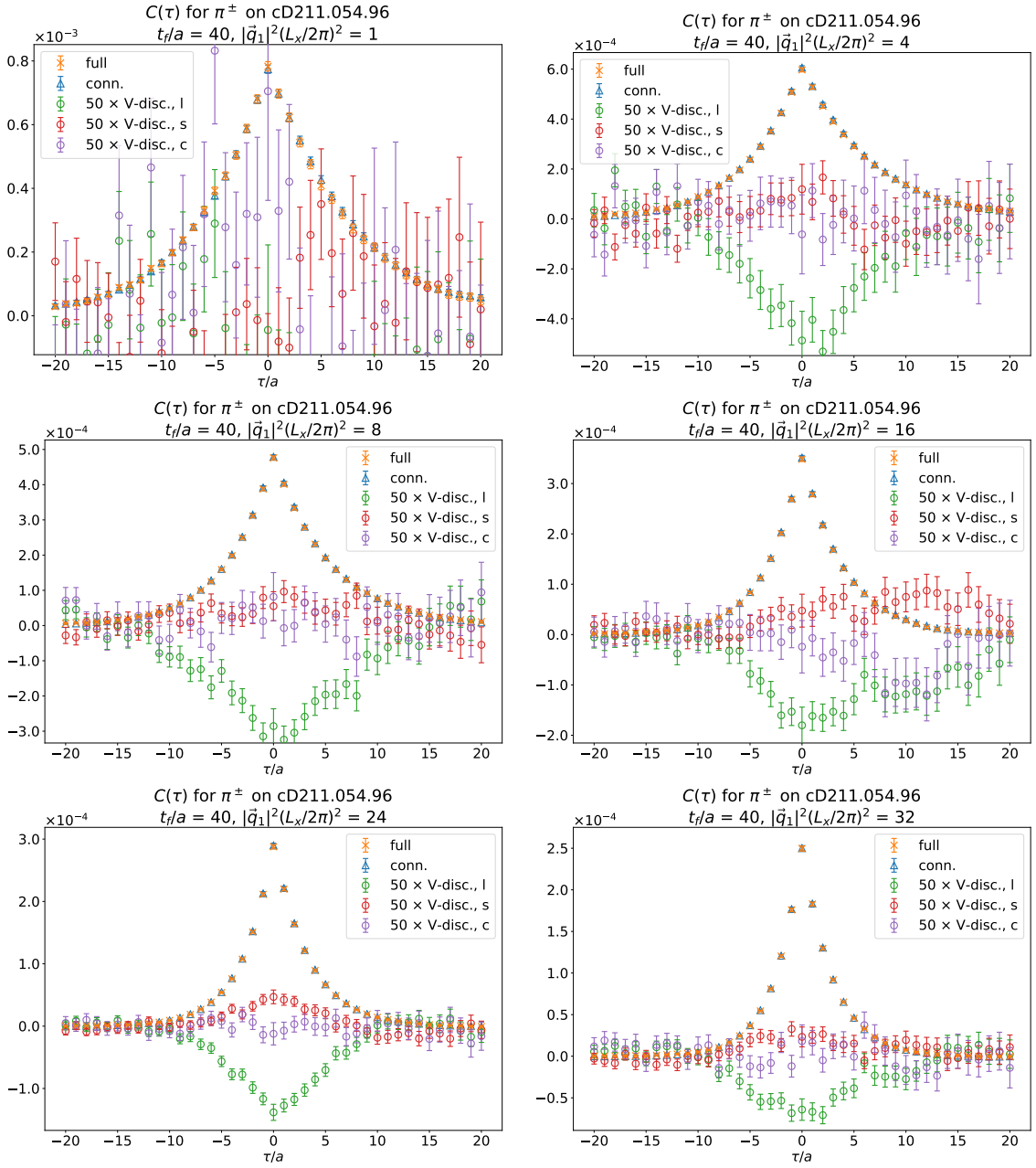

Figure D.3: Momentum orbit averaged $C(\tau, t_f = 2.28\,\mathrm{fm})$ for $\tau/a \in [-20, 20]$ on cD211.054.96 for six orbits. Shown are in orange the full $C(\tau)$, in blue $C^{\mathrm{conn.}}(\tau)$ and in green, red and purple the three $C^{\mathrm{V-disc.}}(\tau)$ multiplied by 50 for easier comparison.

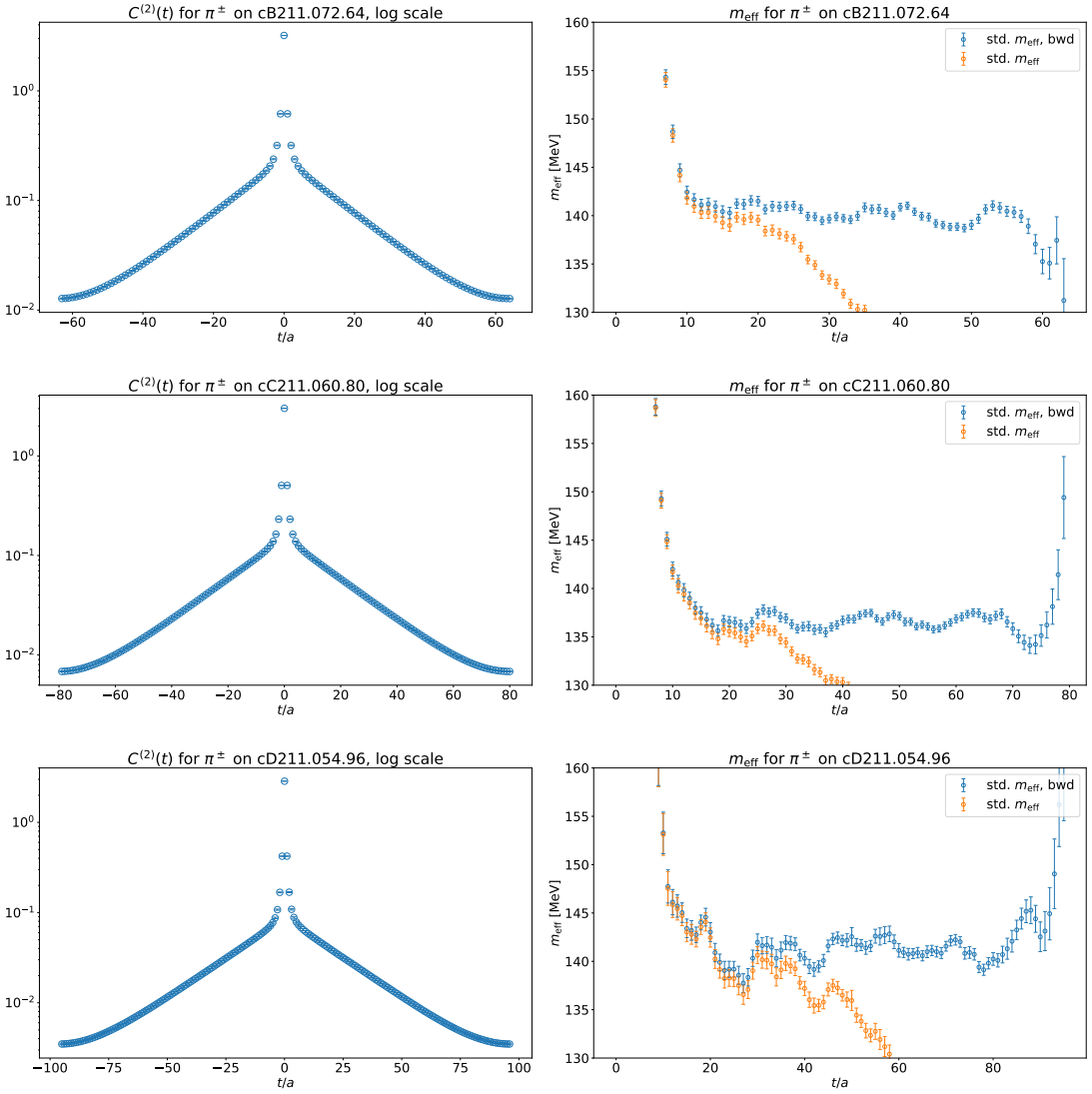

Figure D.4: $C^{(2)}(t)$ (left) and the effective mass m_{eff} in MeV (right) on cB211.072.64 (top), cC211.060.80 (middle) and cD211.054.96 (bottom). On all three ensembles, there is a clean exponential decay with a slope determined by the charged pion mass. The extraction of the effective mass is discussed in Sec. 3.6.3.

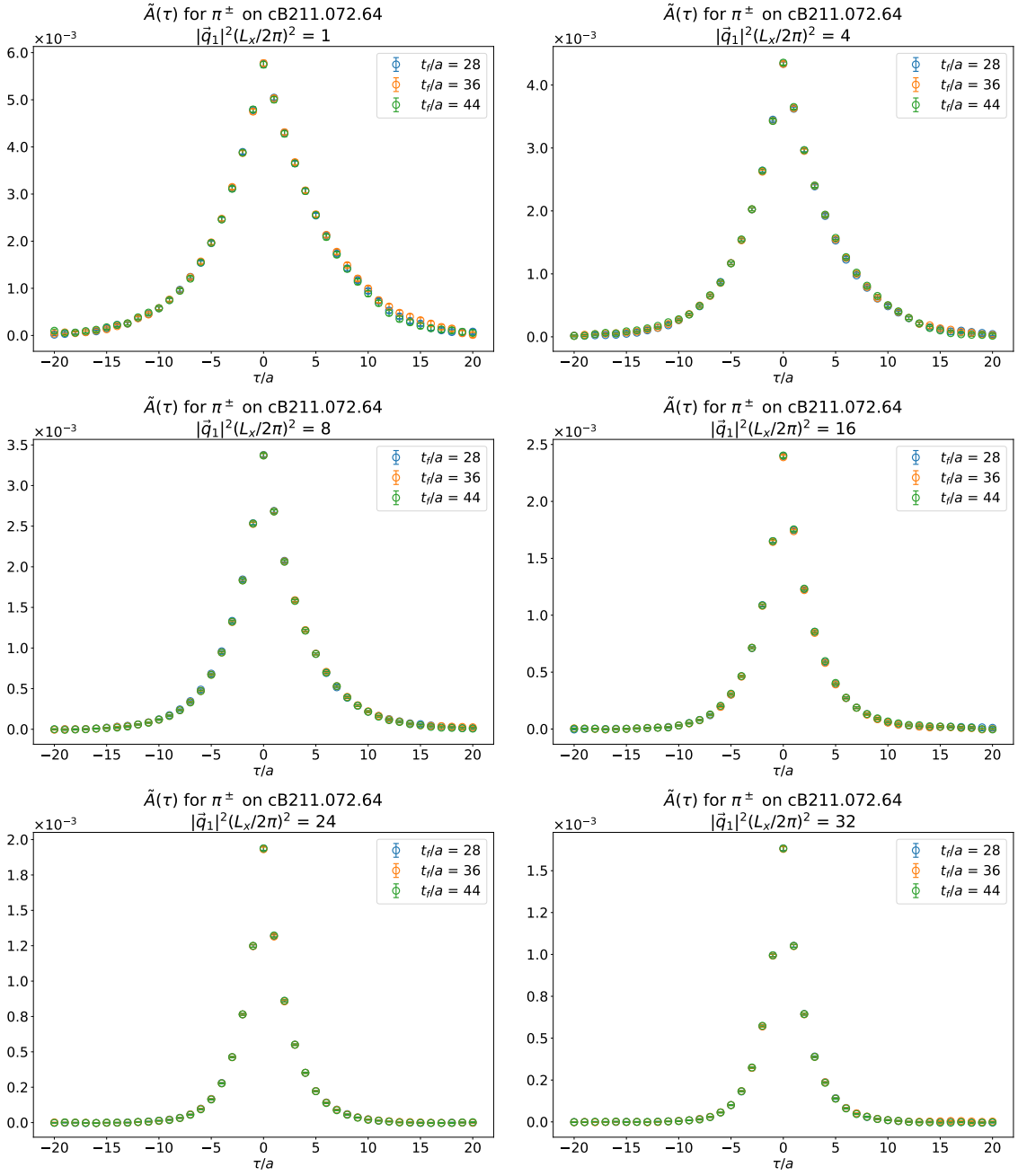

Figure D.5: Momentum orbit averaged $\tilde{A}(\tau)$ using $t_f \in \{2.23, 2.87, 3.50\}$ fm for $\tau/a \in [-20, 20]$ on cB211.072.64 for six orbits. Note the excellent convergence for the different t_f across all orbits $(2\pi/L_x)^2 \leq |\vec{q_1}|^2 \leq 32(2\pi/L_x)^2$, indicating that there is no excited state contamination.

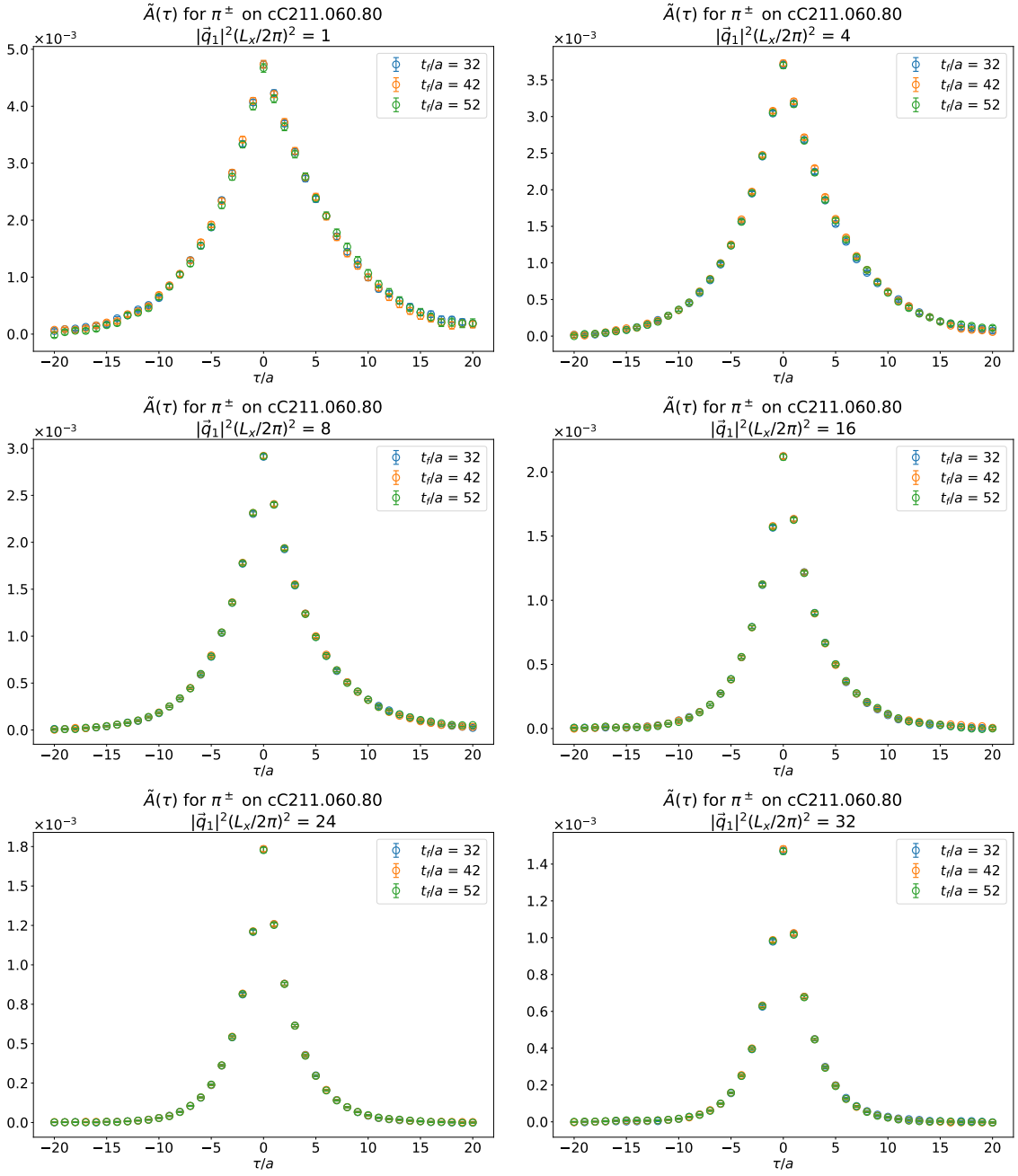

Figure D.6: Momentum orbit averaged $\tilde{A}(\tau)$ using $t_f \in \{2.18, 2.86, 3.55\}$ fm for $\tau/a \in [-20, 20]$ on cC211.060.80 for six orbits. Note the excellent convergence for the different t_f across all orbits $(2\pi/L_x)^2 \leq |\vec{q_1}|^2 \leq 32(2\pi/L_x)^2$, indicating that there is no excited state contamination.

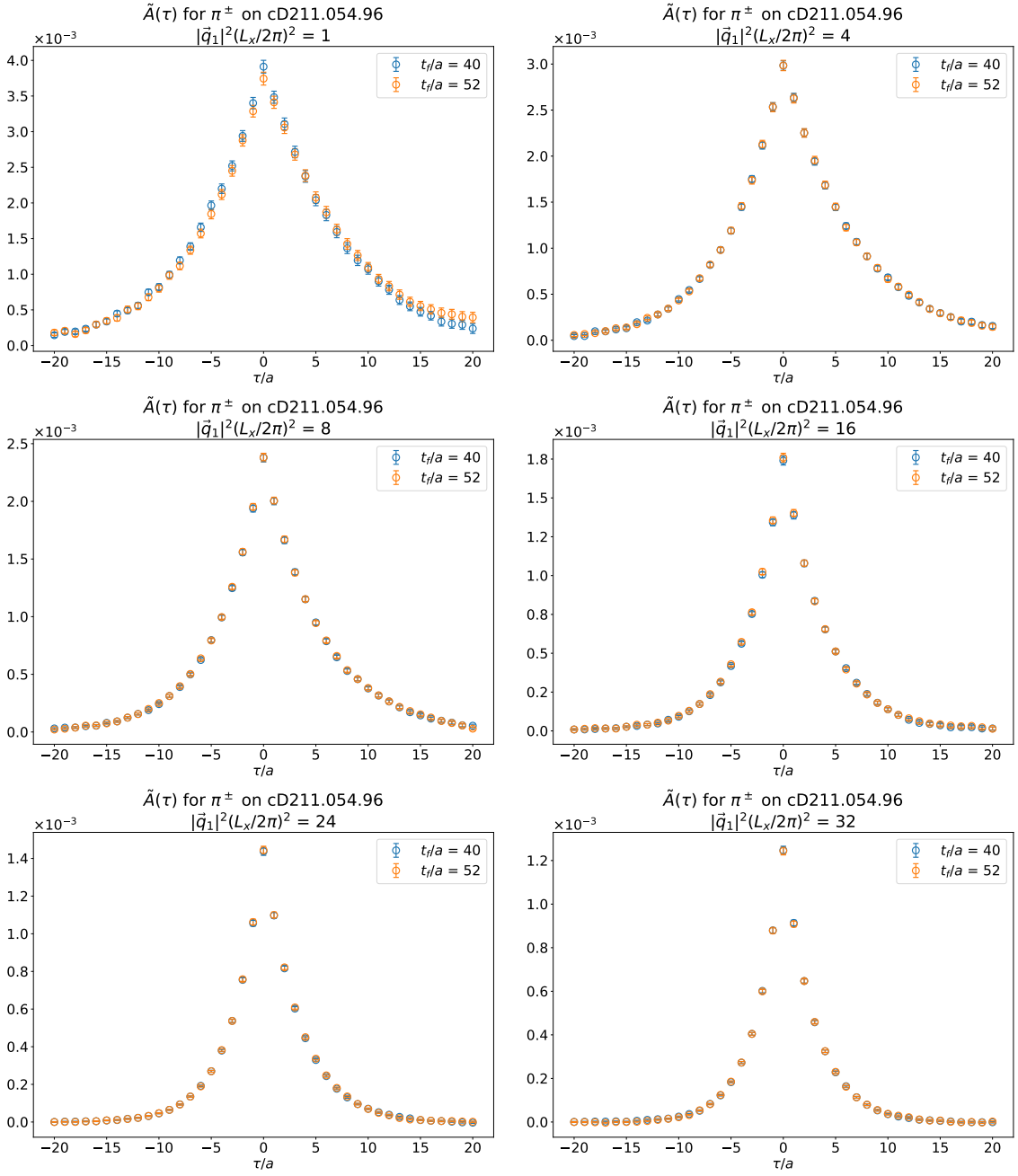

Figure D.7: Momentum orbit averaged $\tilde{A}(\tau)$ using $t_f \in \{2.28, 2.96\}$ fm for $\tau/a \in [-20, 20]$ on cD211.054.96 for six orbits. Note the excited state contamination visible in $|\vec{q}_1|^2 = (2\pi/L_x)^2$, with no excited state contamination in the higher orbits.

D.2 Plots of η-meson amplitudes

Here, an overview over the η-meson $C(\tau)$ and $\tilde{A}(\tau)$ is given. See Sec. 3.5 for the construction of the shown quantities.

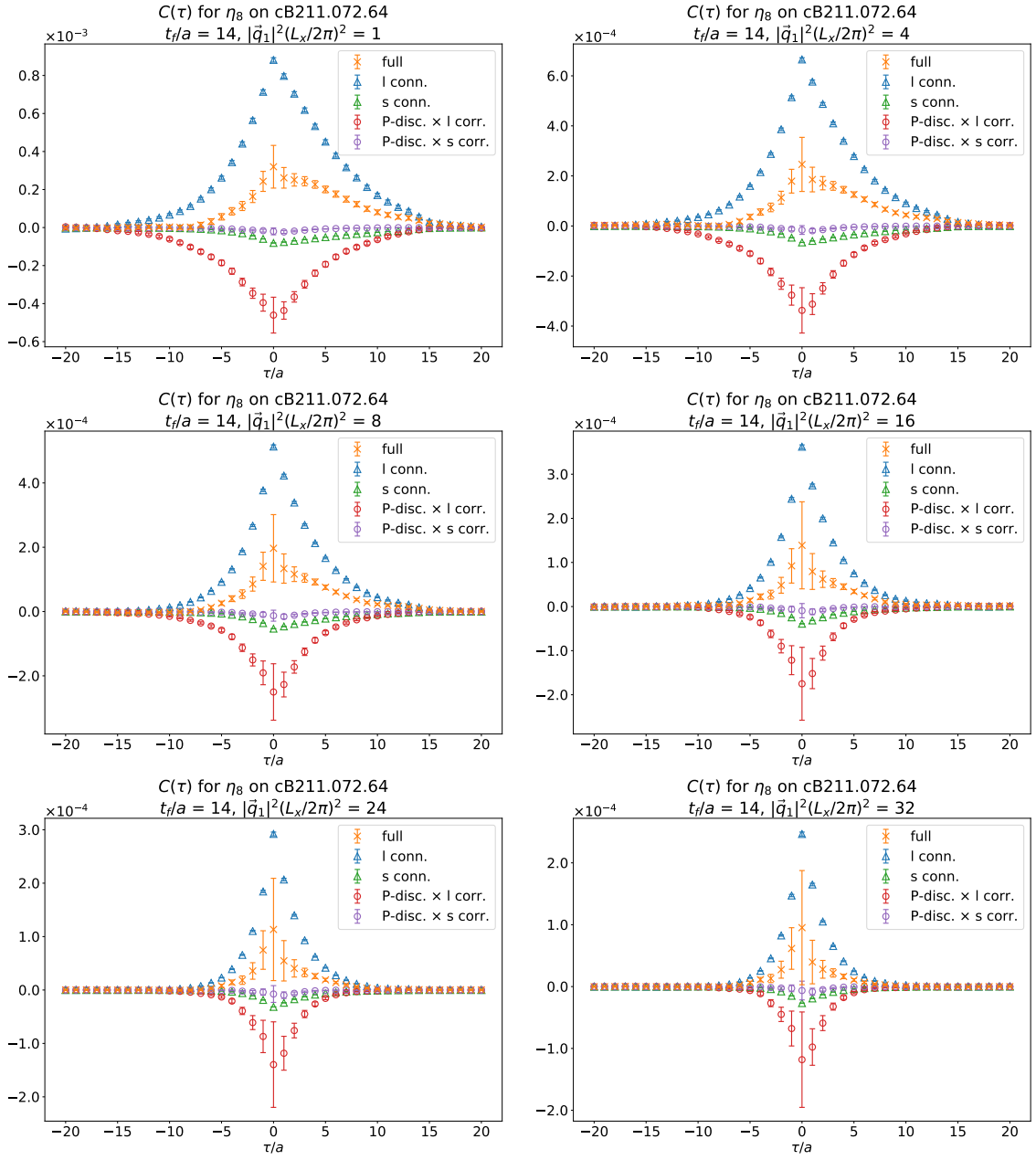

Figure D.8: Momentum orbit averaged $C(\tau, t_f = 1.11\,\mathrm{fm})$ for η_8 for $\tau/a \in [-20, 20]$ on cB211.072.64 for six orbits. Shown are in orange the full $C(\tau)$, in blue and green the fully connected light and strange contributions and in red and purple the P-disconnected contributions with either light or strange current correlators.

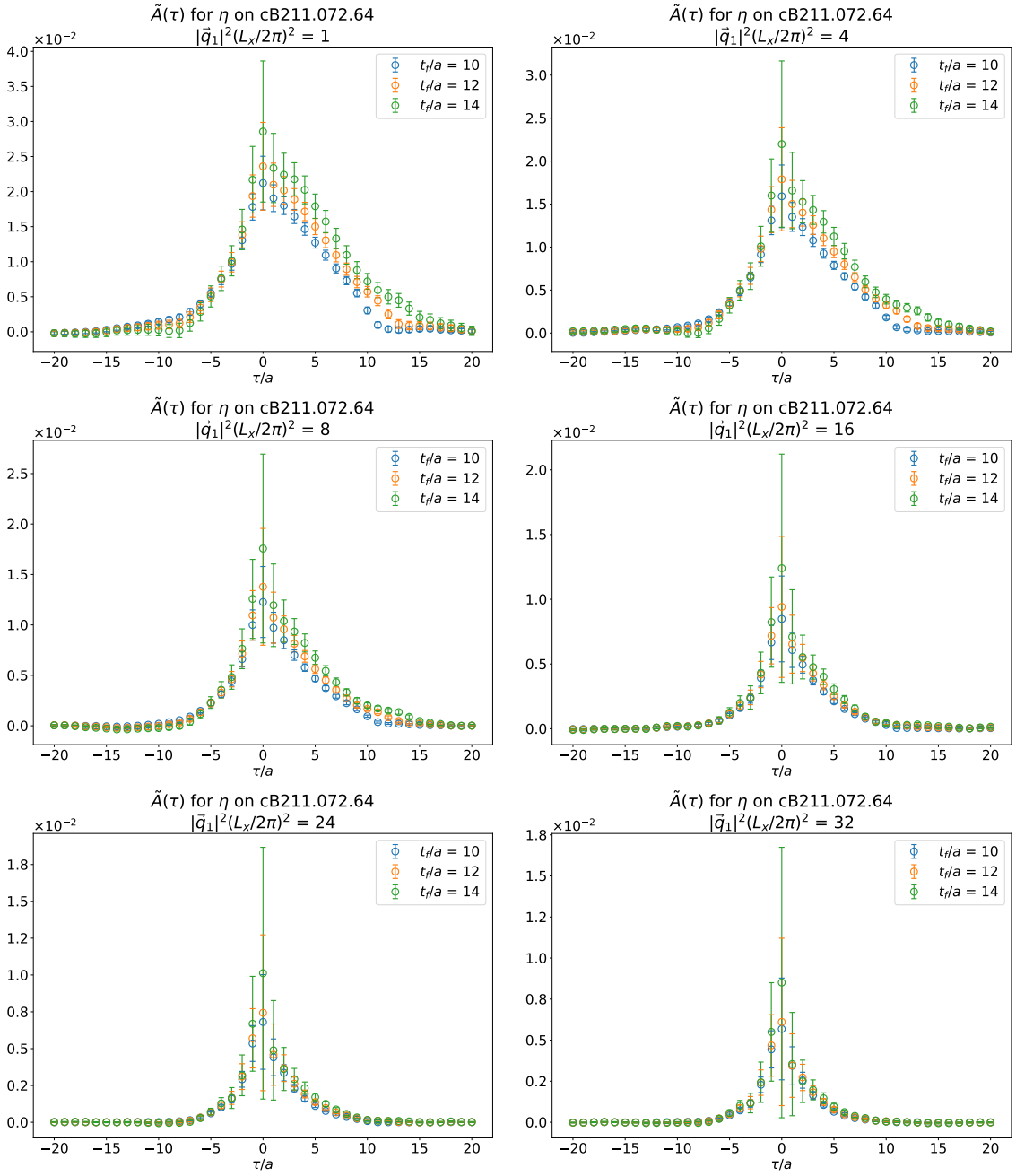

Figure D.9: Momentum orbit averaged η-meson $\tilde{A}(\tau)$ using $t_f \in \{0.80, 0.96, 1.11\}$ fm for $\tau/a \in [-20, 20]$ on cB211.072.64 for six orbits. Note the excited state contamination for the lower orbits.

D.3 Pion kinematical reach

Here the kinematical reach for the resting pion, i.e. $\vec{p} = 0$, on the three ensembles used in this thesis is shown. The kinematical reach in the η-meson calculation is discussed in Sec. 4.2 [69] and Sec. 4.3 [71]. There are in principle three kinematic parameters, the on-shell pseudoscalar momentum p, the inserted current momentum q_1 and the source current momentum q_2. From momentum conservation, q_2 is given by $q_2 = p - q_1$. Since sequential inversion through the pseudoscalar is used in the simulations, changes to $\vec{p}$ require new inversions. The inserted current momentum $\vec{q}_1$ can be varied easily. After fixing the spatial momentum, the inserted current energy ω_1, cf. Eq. (3.30), is the remaining free parameter. The other current energy is the fixed by $\omega_2 = E_P - \omega_1$, with $E_P = \sqrt{m_P^2 + \vec{p}^2}$ the on-shell pseudoscalar energy. The photon virtualities are given by

$$q_1^2 = \omega_1^2 - \vec{q}_1^2, \tag{D.1}$$

$$q_2^2 = (E_P - \omega_1)^2 - (\vec{p} - \vec{q}_1)^2. \tag{D.2}$$

One immediately sees that higher pseudoscalar masses and non-vanishing pseudoscalar momenta lead to a better coverage of the space-like region. Shown in Fig. D.10 is the kinematical reach in the space-like region relevant for the extraction of the TFFs for the setup and ensembles used in this thesis for the charged pion as well as an example for the reach in the case of $\vec{p} \neq 0$. Each curve corresponds to a current momentum $|\vec{q_1}|^2$, with $|\vec{q_1}|^2 \leq 32(2\pi/L_x)^2$ and $|q_1^k| \leq 4(2\pi/L_x)$.

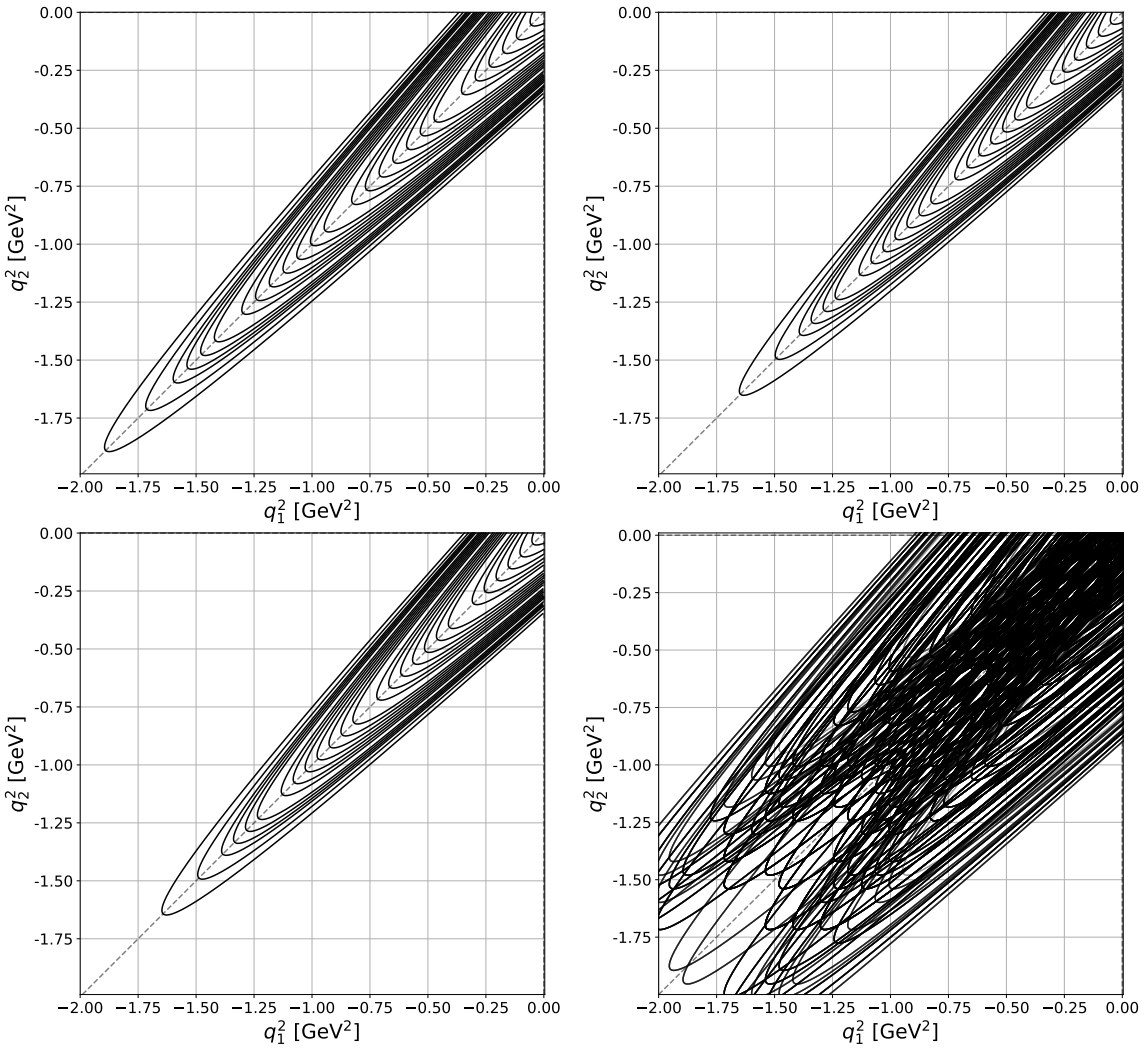

Figure D.10: Kinematical reach on cB211.072.64 (top left), cC211.060.80 (top right) cD211.054.96 (bottom left). The kinematical reach on cB211.072.64 with one unit of momentum for the pseudoscalar in lattice units is shown as well (bottom right).

D.4 Equidistant sampling in the momentum plane

To extend the form factors to arbitrary photon momenta for the integration in Eq. (3.15), the modified z-expansion is used, which is a model independent parametrization of the momentum dependence of the TFFs. More details on this can be found in Ch. 4 to 5 and [67]. Examples of both the pion TFFs and corresponding modified z-expansion fits are shown in App. D.5.

When performing a correlated fit to the modified z-expansion function, only $\mathcal{O}(10^2)$ data points can be included, otherwise the covariance matrix becomes numerically unstable. Since ω_1 is a free parameter, arbitrary kinematics along the accessible momentum orbits can be included, cf. App. D.3.

In this thesis, the TFFs are sampled by splitting the curve parametrized by ω_1 for the highest momentum orbit, $|\vec{q}_1|^2 = 32(2\pi/L_x)^2$ into arcs of equal length in the space-like region. This method is called an "equidistant sampling". The resulting ratios q_2^2/q_1^2 are then kept across all momentum orbits. The sampling was chosen such that the single-virtual and the diagonal kinematics are always included, the former since they appear in each term in Eq. (3.15), the latter since the data is the most precise in this case for the pion calculation. Such a sampling is shown in Fig. D.11. Note that actually only data from half the space-like momentum quadrant needs to be included due to the reflection symmetry of the TFFs along the $q_1^2 = q_2^2$ diagonal. Five such equidistant cuts were used in this thesis, and additionally an independent cut at $q_2^2/q_1^2 = 0.1$ to improve the coverage close to the single-virtual cut.

An (approximately) equidistant sampling on the momentum curves is obtained by

$$\omega_1 = \frac{1}{2}\left(m_P \pm \sqrt{n}\right), \tag{D.3}$$

for equally spaced n, i.e. $n = \alpha k$, $k \in \mathbb{N}, \alpha = const. \in \mathbb{R}_+$.

Approximately means that the spacing is exactly equidistant in the limit $m_P \to 0$ for all n and in the limit $n \to \infty$ independently of m_P. Note that the threshold for hadron production restricts the allowed values for ω_1, but via the choice of α the sampling can be as fine or coarse as desired. Further, for $n = 0$ the diagonal case is covered.

To prove that this choice of ω_1 gives an equidistant sampling, it is sufficient to show

that for $k \to \infty$ the arc length between two points stays finite and constant and the arc length between $k = 0$ and $k = 1$ goes to the same constant for $m_P \to 0$. Defining

$$\omega_i = \frac{1}{2}\left(m_P \pm \sqrt{\alpha i}\right), \quad i \in \mathbb{N}, \tag{D.4}$$

the arc length is given by

$$l(\omega_i, \omega_j) = \int_{\omega_i}^{\omega_j} ds(\omega) d\omega, \tag{D.5}$$

where

$$ds(\omega) = \sqrt{\left(\frac{dq_1^2(\omega)}{d\omega}\right)^2 + \left(\frac{dq_2^2(\omega)}{d\omega}\right)^2} = \sqrt{4(m_P - \omega)^2 + 4\omega^2}. \tag{D.6}$$

Plugging this into Eq. (D.5) yields

$$\begin{aligned} l(\omega_i, \omega_j) = \frac{1}{4}\Bigg(& 2(2\omega_j - m_P)\sqrt{2\omega_j^2 - 2\omega_j m_P + m_P^2} \\ & + \sqrt{2} m_P^2 \ln\left(2\omega_j - m_P + \sqrt{2}\sqrt{2\omega_j^2 - 2\omega_j m_P + m_P^2}\right) \\ & - 2(2\omega_i - m_P)\sqrt{2\omega_i^2 - 2\omega_i m_P + m_P^2} \\ & - \sqrt{2} m_P^2 \ln\left(2\omega_i - m_P + \sqrt{2}\sqrt{2\omega_i^2 - 2\omega_i m_P + m_P^2}\right)\Bigg). \end{aligned} \tag{D.7}$$

Without loss of generality, choose $\alpha = 1$ and $\omega_i = \omega_k = \frac{1}{2}\left(m_P + \sqrt{k}\right)$, $\omega_j = \omega_{k+1} = \frac{1}{2}\left(m_P + \sqrt{k+1}\right)$. The resulting arc length between those two ω is

$$\begin{aligned} l\left(\frac{1}{2}\left(m_P + \sqrt{k}\right), \frac{1}{2}\left(m_P + \sqrt{k+1}\right)\right) = \frac{1}{2\sqrt{2}}\Bigg(& \sqrt{k+1}\sqrt{k+1+m_P^2} \\ & - \sqrt{k}\sqrt{k+m_P^2} + m_P^2 \ln\left(\frac{\sqrt{k+1} + \sqrt{k+1+m_P^2}}{\sqrt{k} + \sqrt{k+m_P^2}}\right)\Bigg). \end{aligned} \tag{D.8}$$

Now the limits $k = 0$ and $k \to \infty$ need to be checked. For $k = 0$ one finds

$$l\left(\frac{1}{2}m_P, \frac{1}{2}\left(m_P + 1\right)\right) = \frac{1}{2\sqrt{2}}\left(\sqrt{1+m_P^2} + m_P^2 \ln\left(\frac{1 + \sqrt{1+m_P^2}}{\sqrt{m_P^2}}\right)\right), \tag{D.9}$$

such that

$$\lim_{m_P \to 0} l\left(\frac{1}{2}m_P, \frac{1}{2}\Big(m_P + 1\Big)\right) = \frac{1}{2\sqrt{2}}. \tag{D.10}$$

For big k the Laurent series expansion (around $k \to \infty$) gives

$$l\left(\frac{1}{2}\Big(m_P + \sqrt{k}\Big), \frac{1}{2}\Big(m_P + \sqrt{k+1}\Big)\right) = \frac{1}{2\sqrt{2}} + \mathcal{O}(1/k), \tag{D.11}$$

thus

$$\lim_{k \to \infty} l\left(\frac{1}{2}\Big(m_P + \sqrt{k}\Big), \frac{1}{2}\Big(m_P + \sqrt{k+1}\Big)\right) = \frac{1}{2\sqrt{2}}. \tag{D.12}$$

Note that by expanding around any $k \in \mathbb{N}$, one can show that the arc length in the limit $m_P \to 0$ stays constant for all k, and that it converges to $1/(2\sqrt{2})$ for small m_P and growing k. □

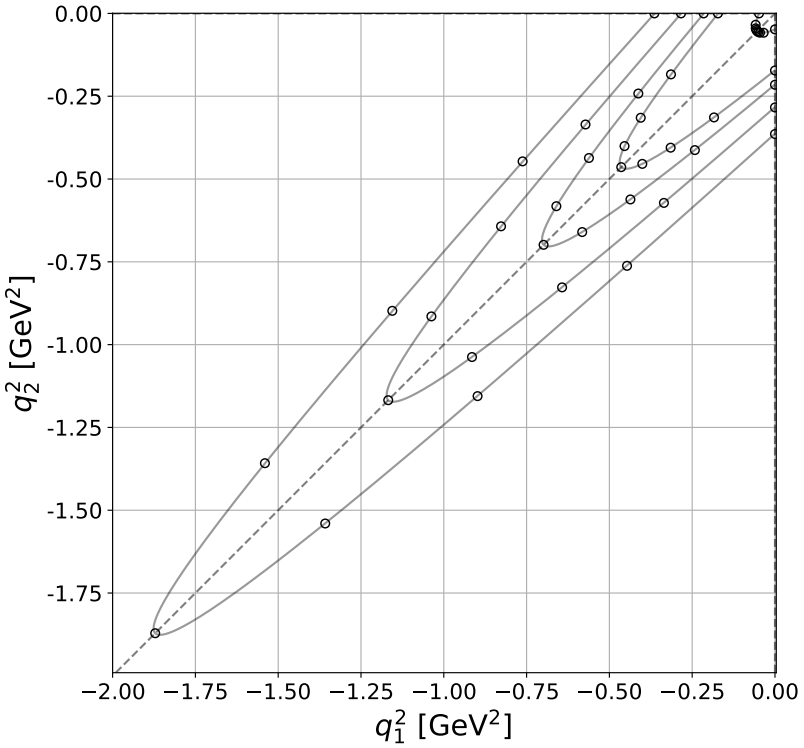

Figure D.11: Sampling of the momentum plane as described in the text, with nine regular arc lengths on the highest momentum orbit, showing momentum orbits $|\vec{q}_1|^2(L_x/2\pi)^2 \in \{1, 8, 12, 20, 32\}$ for the charged pion on cB211.072.64.

D.5 Plots of pion TFFs

Here, a selection of TFFs and modified z-expansions are shown, together with relevant parameters used to perform the z-expansion fit, the model averaging and resulting from the z-expansion fit. See in particular Ch. 5 for details. For the single-virtual experimental data, see [72–76]. For easier comparison, Tab. D.1 reproduces the z-expansion coefficients from [67].

N	c_{00}	c_{10}	c_{11}	c_{20}	c_{21}	c_{22}
1	0.2346(65)	-0.0590(39)	0.074(19)			
2	0.2350(61)	-0.0651(49)	-0.284(68)	0.106(33)	0.109(46)	-0.29(12)

Table D.1: Selection of z-expansion coefficients from [67].

All analyses presented here use $\Delta_{\text{latt.}} \geq 95\%$ (labelled as "threshold 95%"), meaning that only TFF data points with at least a 95% contribution from lattice data are included in the z-expansion fitting, cf. Eq. (3.154). Note that for most data points, the actual data content is higher than 95%, especially for diagonal kinematics or close to diagonal kinematics.

For the single ensemble analyses, TFF data for one choice of parameters is shown together with the corresponding z-expansion fit and the fit parameters are presented in a table and as a so-called cornerplot, which gives an indication of the correlation of the z-expansion fit parameters. Note that the cornerplots are just scatterplots of the fit parameters, as such the single ensemble analysis errors shown in them would need to be adjusted since jackknife resampling was used for the error analysis there. The data included in the z-expansion fit is shown in red, the data shown in blue is there for illustration only.

For the combined analyses, where TFF data for all three ensembles is fitted simultaneously, only an example cornerplot is shown. The errors in these cornerplots need to be adjusted by a factor of $N/(N-1)$, where N is the number of samples, since bootstrap resampling was used for the combined analysis. In both cases, TFF data from the model averaged z-expansion fit parameters and the values of said parameters is also given.

Note that the indicated fit ranges in this section for the $\tilde{A}(\tau)$ fit are given in lattice units and are `python` ranges, meaning that the indicated t_{min} is inclusive and t_{max} is exclusive such that the actual fit range is given by $]-t_{max}, -t_{min}] \cup [t_{min}, t_{max}[$.

D.5.1 cB211.072.64 $N = 1$

c_{00}	c_{10}	c_{11}	$\chi^2_{\tilde{A}}$/d.o.f.	$\chi^2_{z-\text{exp.}}$/d.o.f.
0.2102(13)	-0.0770(21)	0.083(12)	0.84	1.12

Table D.2: z-expansion coefficients and χ^2/d.o.f. of the analysis shown in Figs. D.12 and D.13.

c_{00}	c_{10}	c_{11}	$\chi^2_{z-\text{exp.}}$/d.o.f.
0.2103(12)	-0.0772(21)	0.084(12)	1.13(4)

Table D.3: AIC averaged z-expansion coefficients and χ^2/d.o.f. of Fig. D.14.

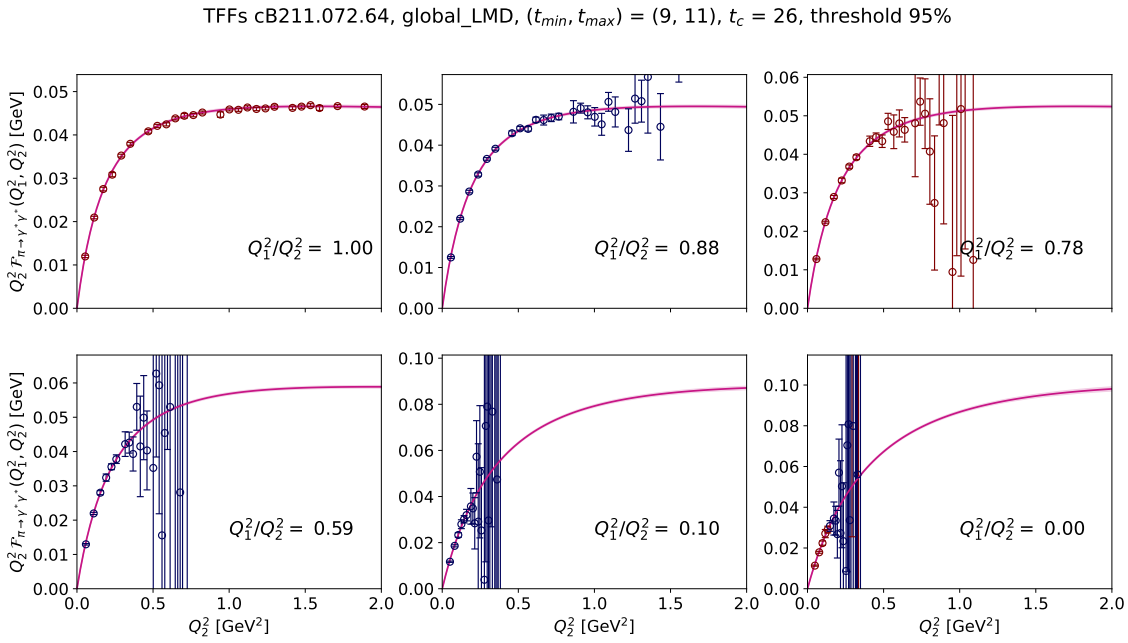

Figure D.12: $N = 1$ single analysis TFFs.

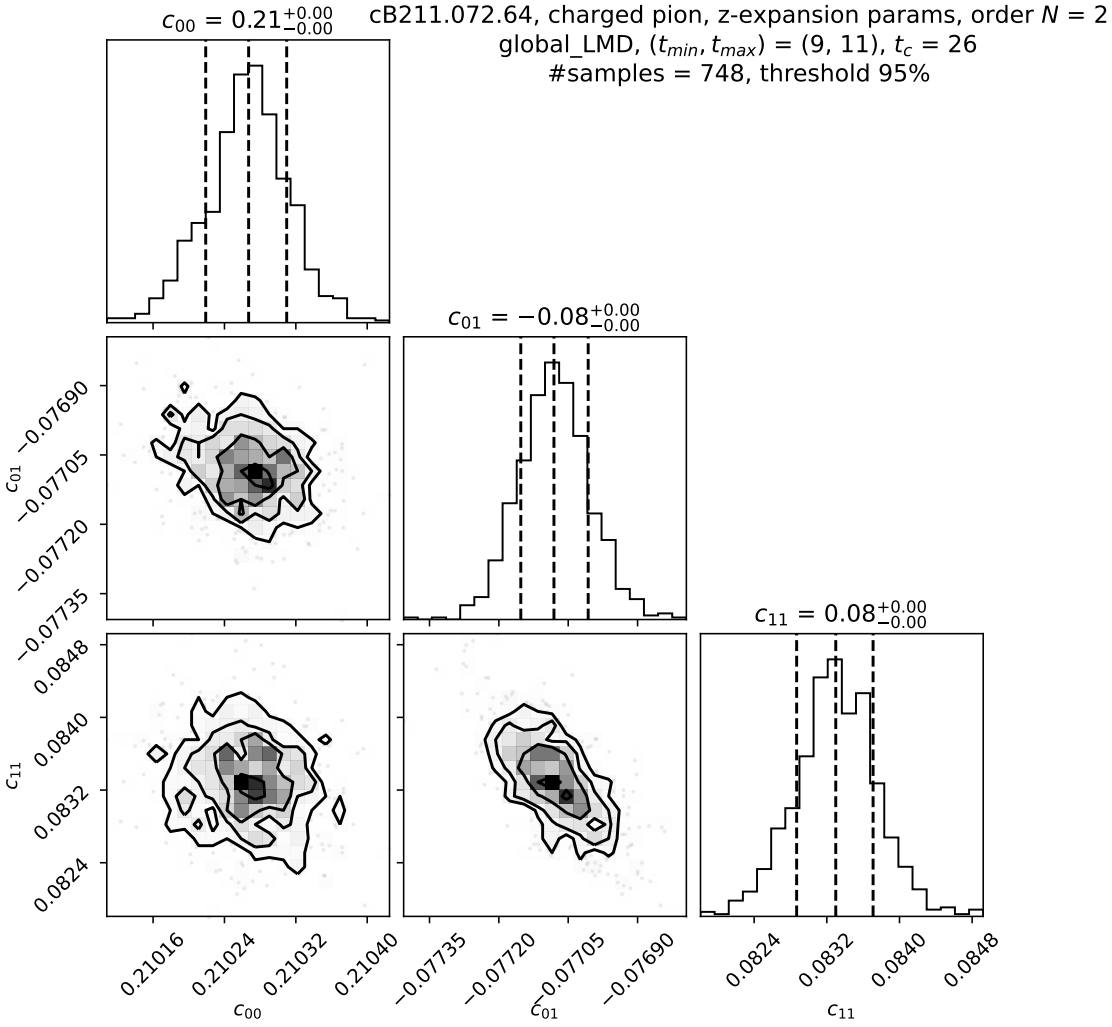

Figure D.13: $N = 1$ single analysis cornerplot.

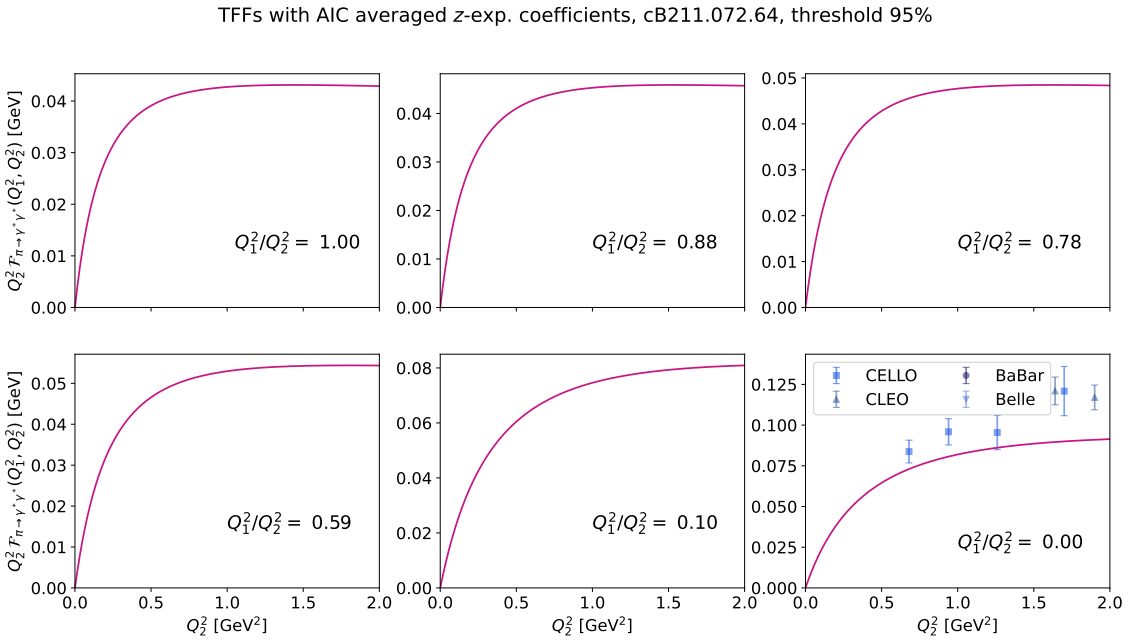

Figure D.14: $N = 1$ AIC averaged TFFs.

D.5.2 cB211.072.64 using c_{00}, c_{10}, c_{11} and c_{22}

c_{00}	c_{10}	c_{11}	c_{22}	$\chi^2_{\tilde{A}}$/d.o.f.	$\chi^2_{z-\text{exp.}}$/d.o.f.
0.2108(13)	-0.0761(20)	-0.028(25)	0.27(20)	0.84	1.20

Table D.4: z-expansion coefficients and χ^2/d.o.f. of the analysis shown in Figs. D.15 and D.16.

c_{00}	c_{10}	c_{11}	c_{22}	$\chi^2_{z-\text{exp.}}$/d.o.f.
0.2108(13)	-0.0760(20)	-0.027(26)	0.25(20)	1.22(5)

Table D.5: AIC averaged z-expansion coefficients and χ^2/d.o.f. of Fig. D.17.

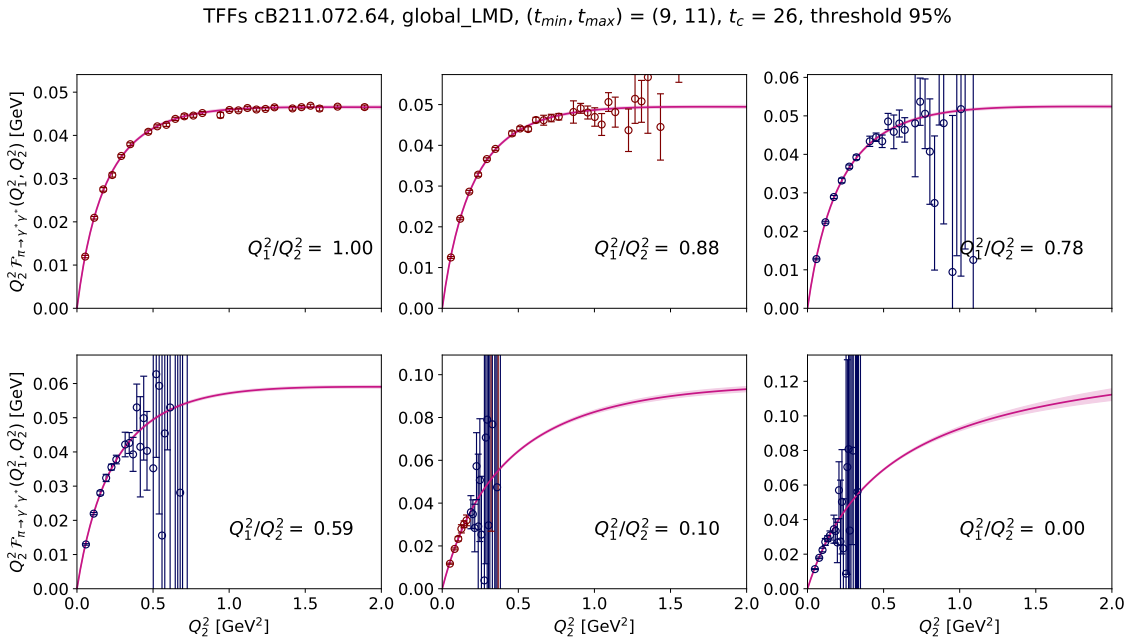

Figure D.15: c_{00}, c_{10}, c_{11} and c_{22} single analysis TFFs.

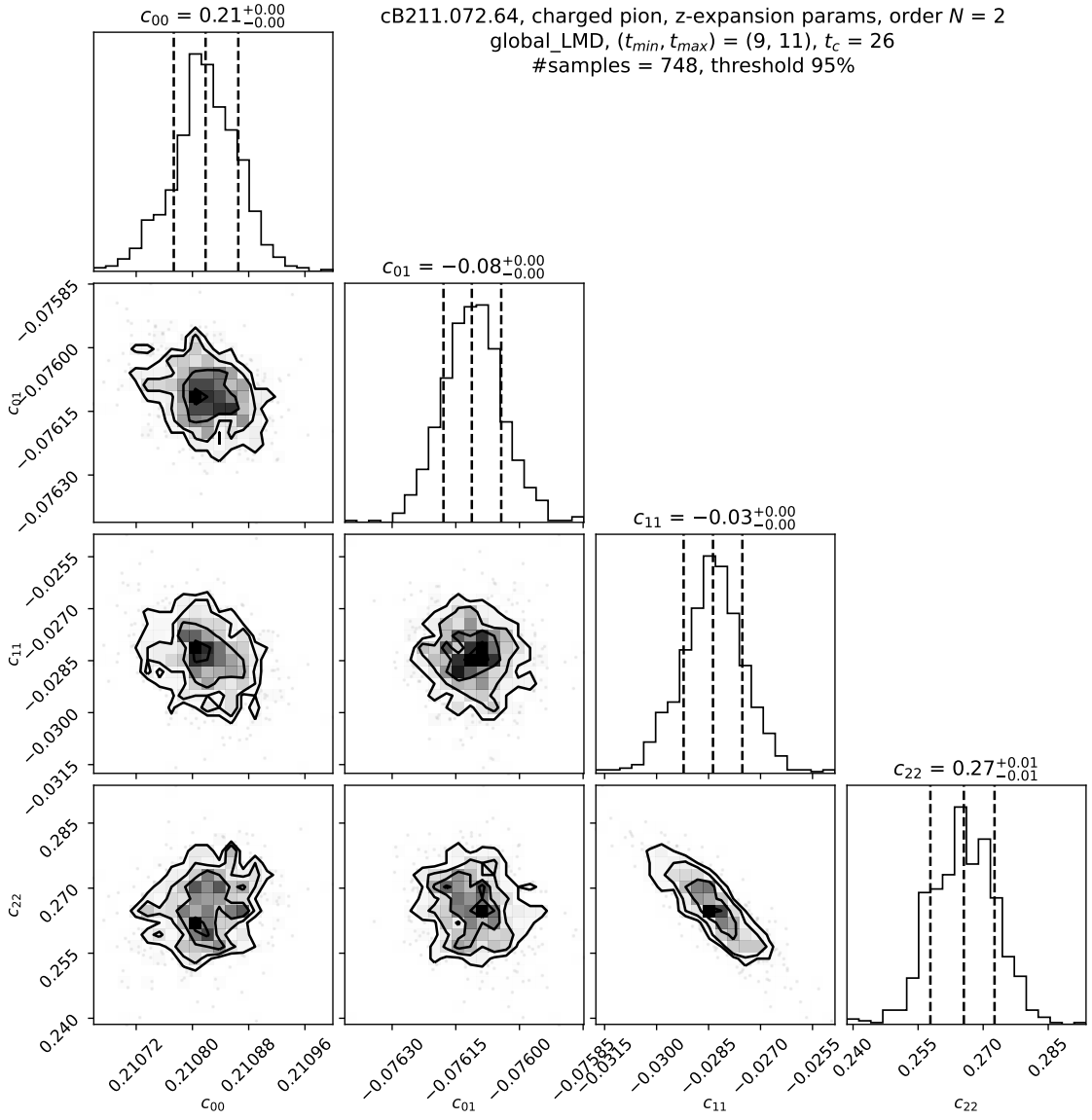

Figure D.16: c_{00}, c_{10}, c_{11} and c_{22} single analysis cornerplot.

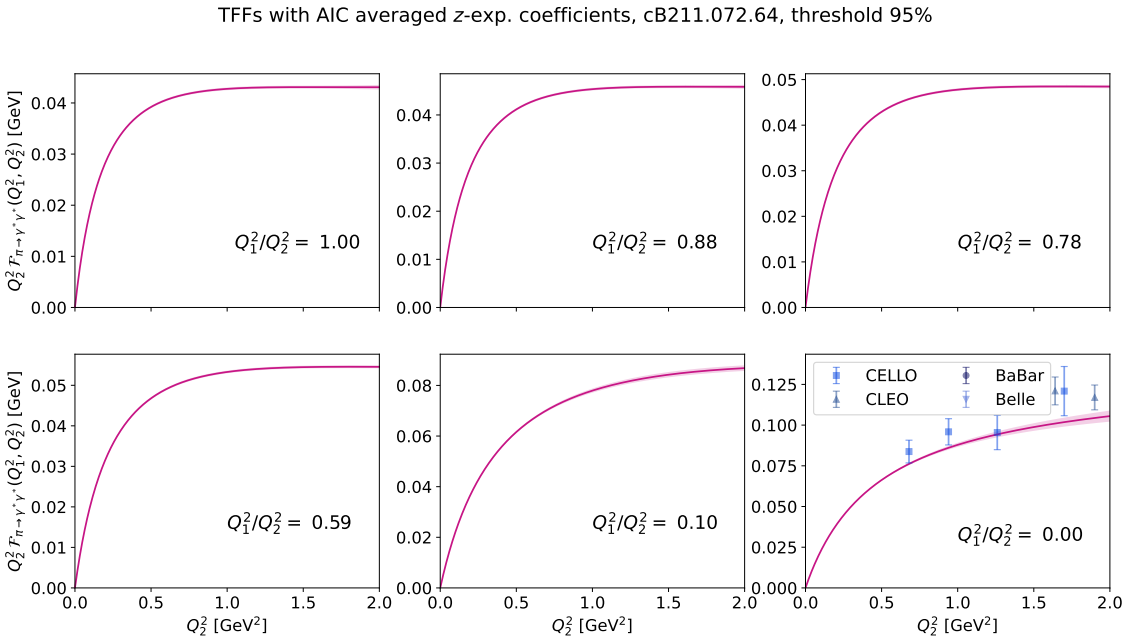

Figure D.17: c_{00}, c_{10}, c_{11} and c_{22} AIC averaged TFFs.

D.5.3 cB211.072.64 $N = 2$

c_{00}	c_{10}	c_{11}	c_{20}	c_{21}	c_{22}	$\chi^2_{\bar{A}}$/d.o.f.	$\chi^2_{z-\text{exp.}}$/d.o.f.
0.2109(13)	-0.0843(30)	-0.39(63)	0.19(32)	0.03(18)	-0.49(39)	0.84	0.84

Table D.6: z-expansion coefficients and χ^2/d.o.f. of the analysis shown in Figs. D.18 and D.19.

c_{00}	c_{10}	c_{11}	c_{20}	c_{21}	c_{22}	$\chi^2_{z-\text{exp.}}$/d.o.f.
0.2109(13)	-0.0837(30)	-0.46(62)	0.23(31)	0.01(18)	-0.55(39)	0.87(4)

Table D.7: AIC averaged z-expansion coefficients and χ^2/d.o.f. of Fig. D.20.

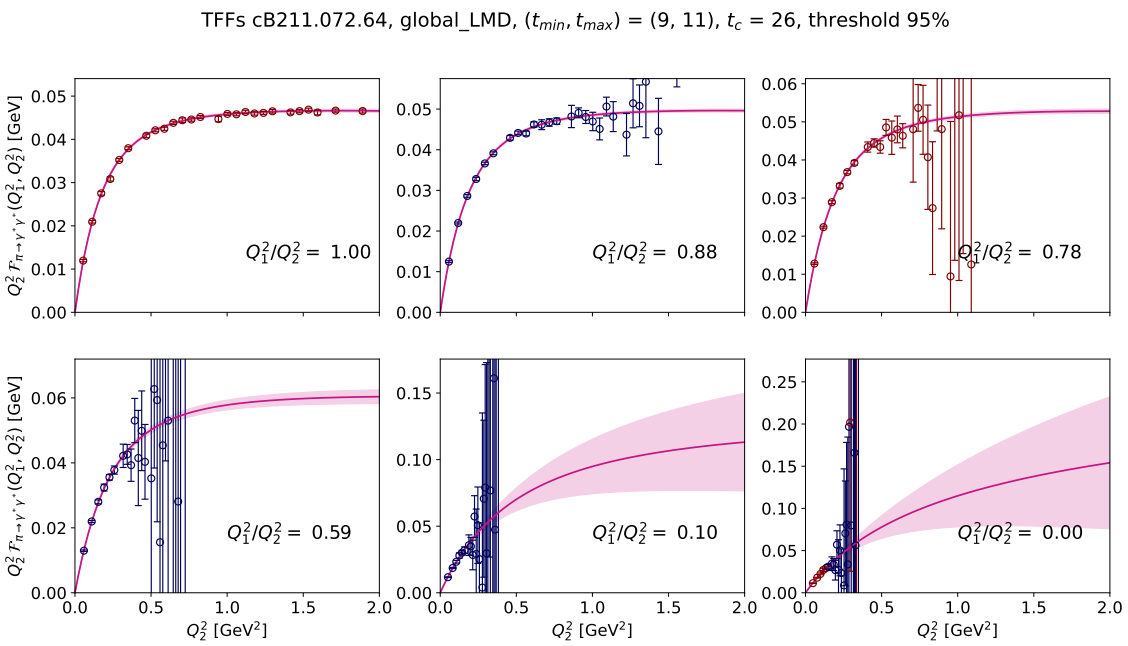

Figure D.18: $N = 2$ single analysis TFFs.

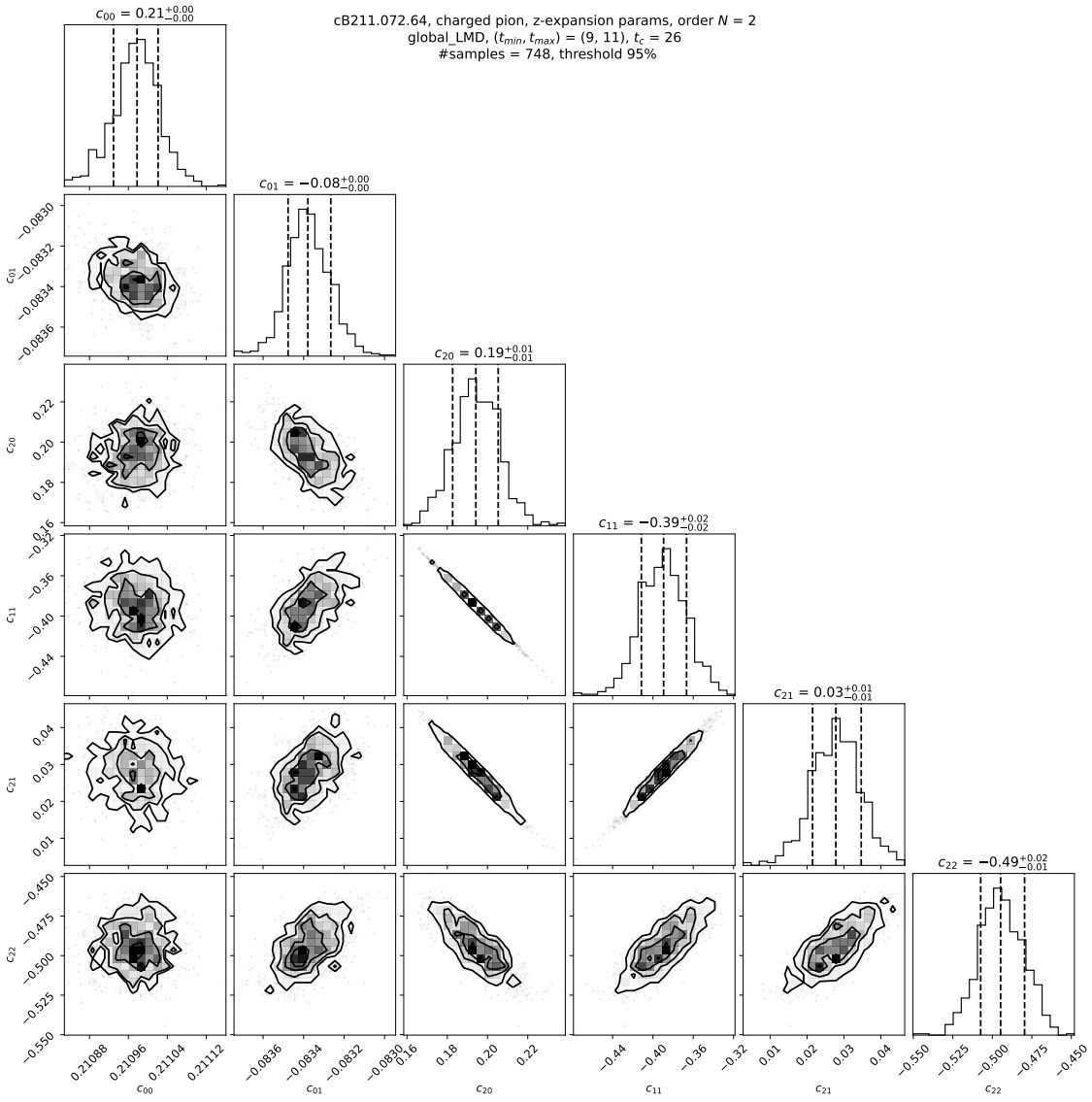

Figure D.19: $N = 2$ single analysis cornerplot.

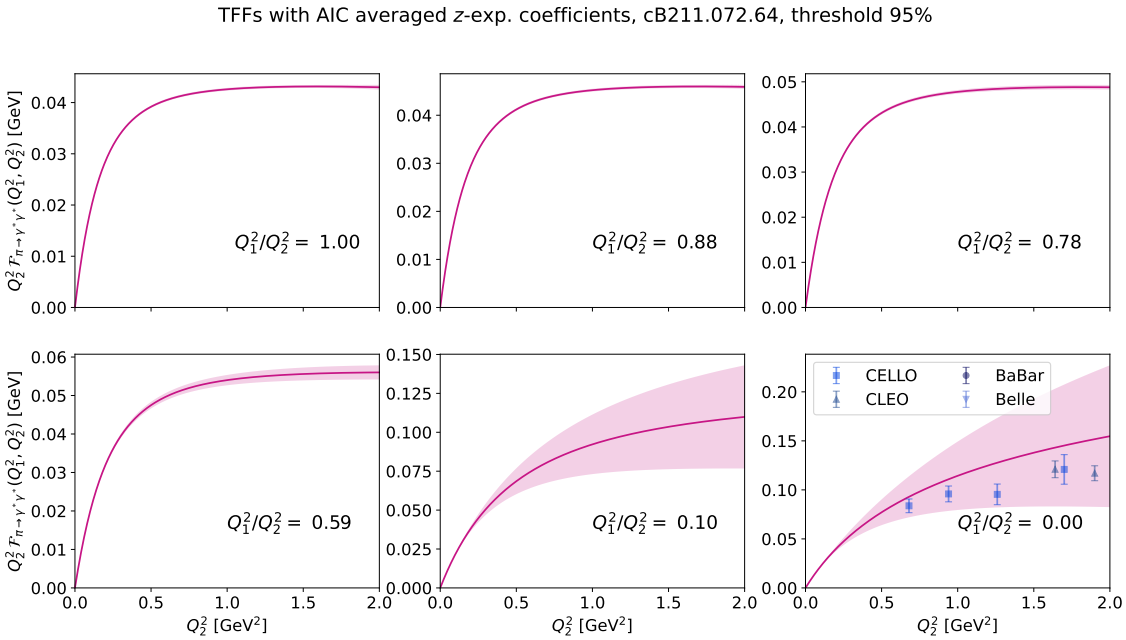

Figure D.20: $N = 2$ AIC averaged TFFs.

D.5.4 cC211.060.80 $N = 1$

c_{00}	c_{10}	c_{11}	$\chi^2_{\tilde{A}}$/d.o.f.	$\chi^2_{z-\text{exp.}}$/d.o.f.
0.2195(17)	-0.0674(27)	0.040(17)	0.86	1.00

Table D.8: z-expansion coefficients and χ^2/d.o.f. of the analysis shown in Figs. D.21 and D.22.

c_{00}	c_{10}	c_{11}	$\chi^2_{z-\text{exp.}}$/d.o.f.
0.2194(17)	-0.0676(29)	0.040(18)	1.01(5)

Table D.9: AIC averaged z-expansion coefficients and χ^2/d.o.f. of Fig. D.23.

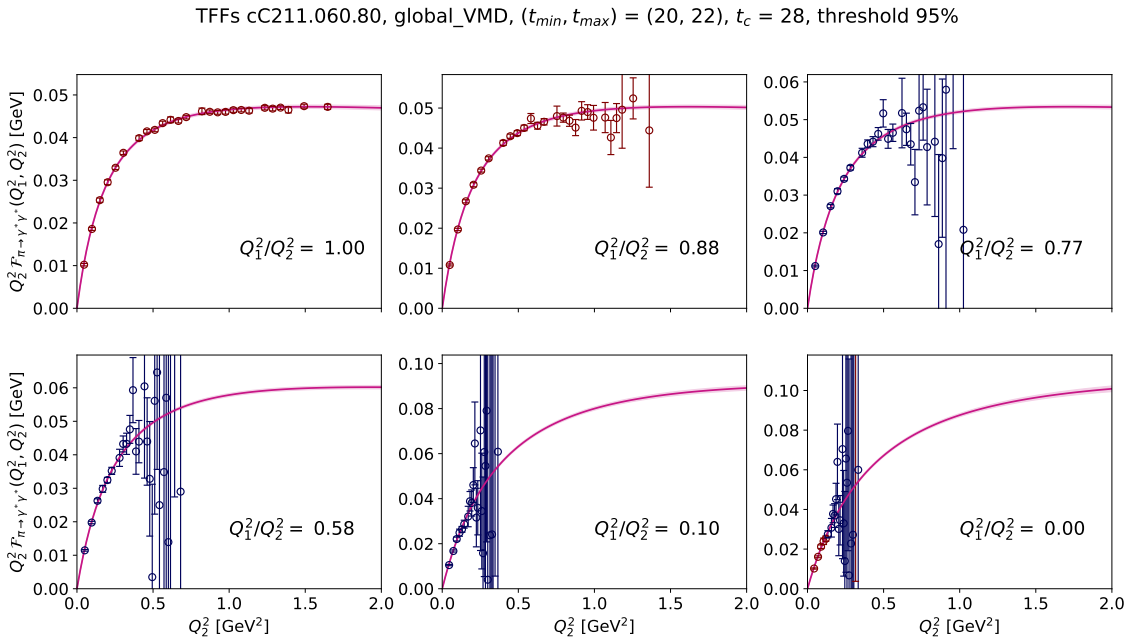

Figure D.21: $N = 1$ single analysis TFFs.

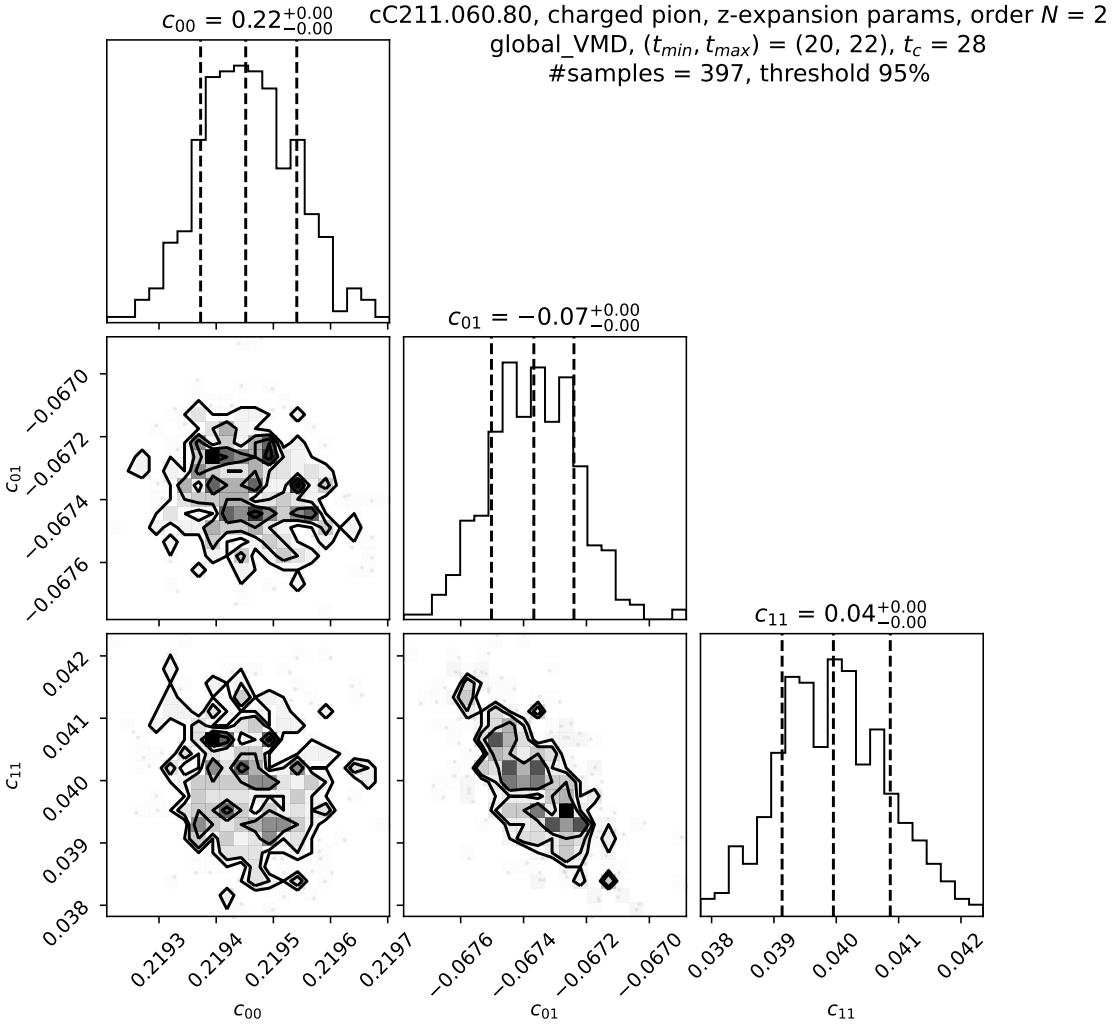

Figure D.22: $N = 1$ single analysis cornerplot.

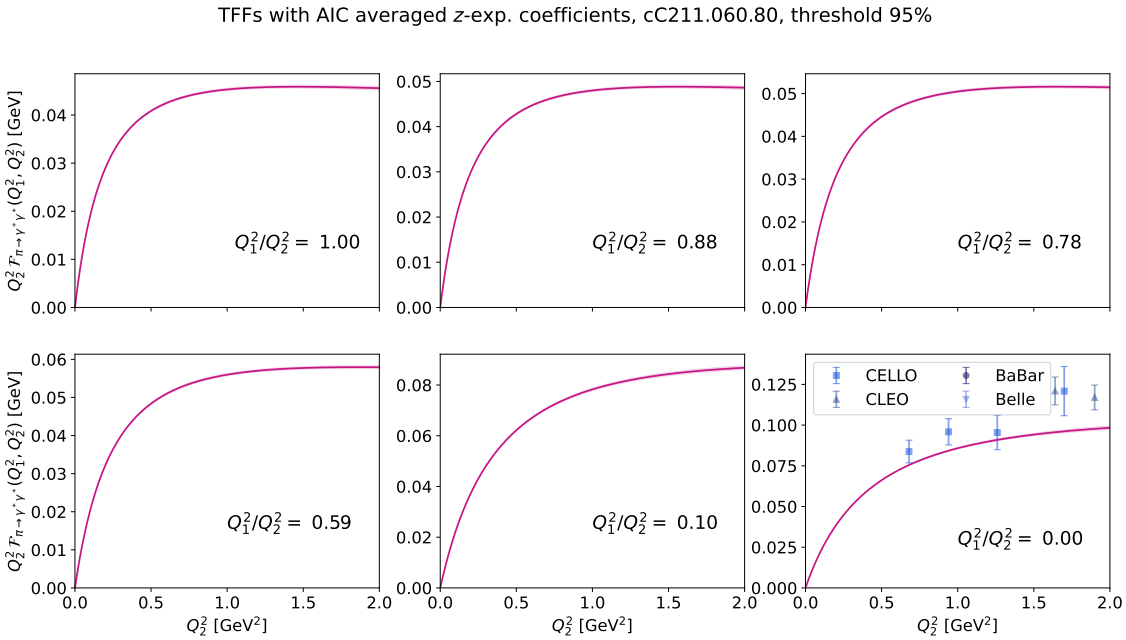

Figure D.23: $N = 1$ AIC averaged TFFs.

D.5.5 cC211.060.80 using c_{00}, c_{10}, c_{11} and c_{22}

c_{00}	c_{10}	c_{11}	c_{22}	$\chi^2_{\tilde{A}}$/d.o.f.	$\chi^2_{z-\text{exp.}}$/d.o.f.
0.2211(17)	-0.0679(25)	-0.103(33)	0.60(32)	0.86	0.94

Table D.10: z-expansion coefficients and χ^2/d.o.f. of the analysis shown in Figs. D.24 and D.25.

c_{00}	c_{10}	c_{11}	c_{22}	$\chi^2_{z-\text{exp.}}$/d.o.f.
0.2206(18)	-0.0676(28)	-0.091(36)	0.519(36)	0.94(6)

Table D.11: AIC averaged z-expansion coefficients and χ^2/d.o.f. of Fig. D.26.

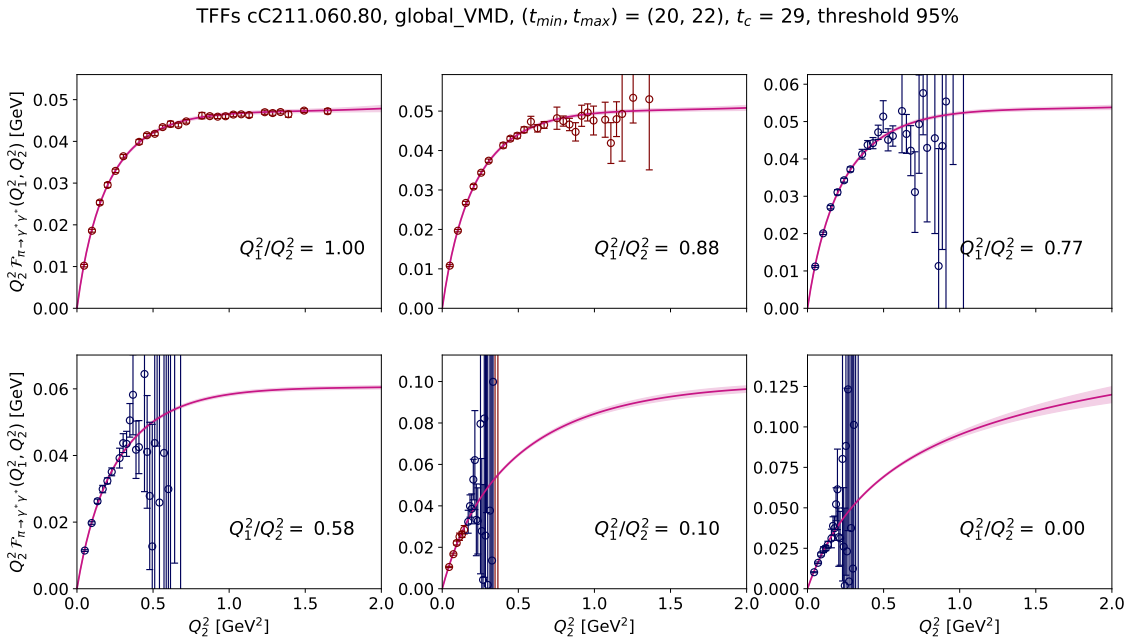

Figure D.24: c_{00}, c_{10}, c_{11} and c_{22} single analysis TFFs.

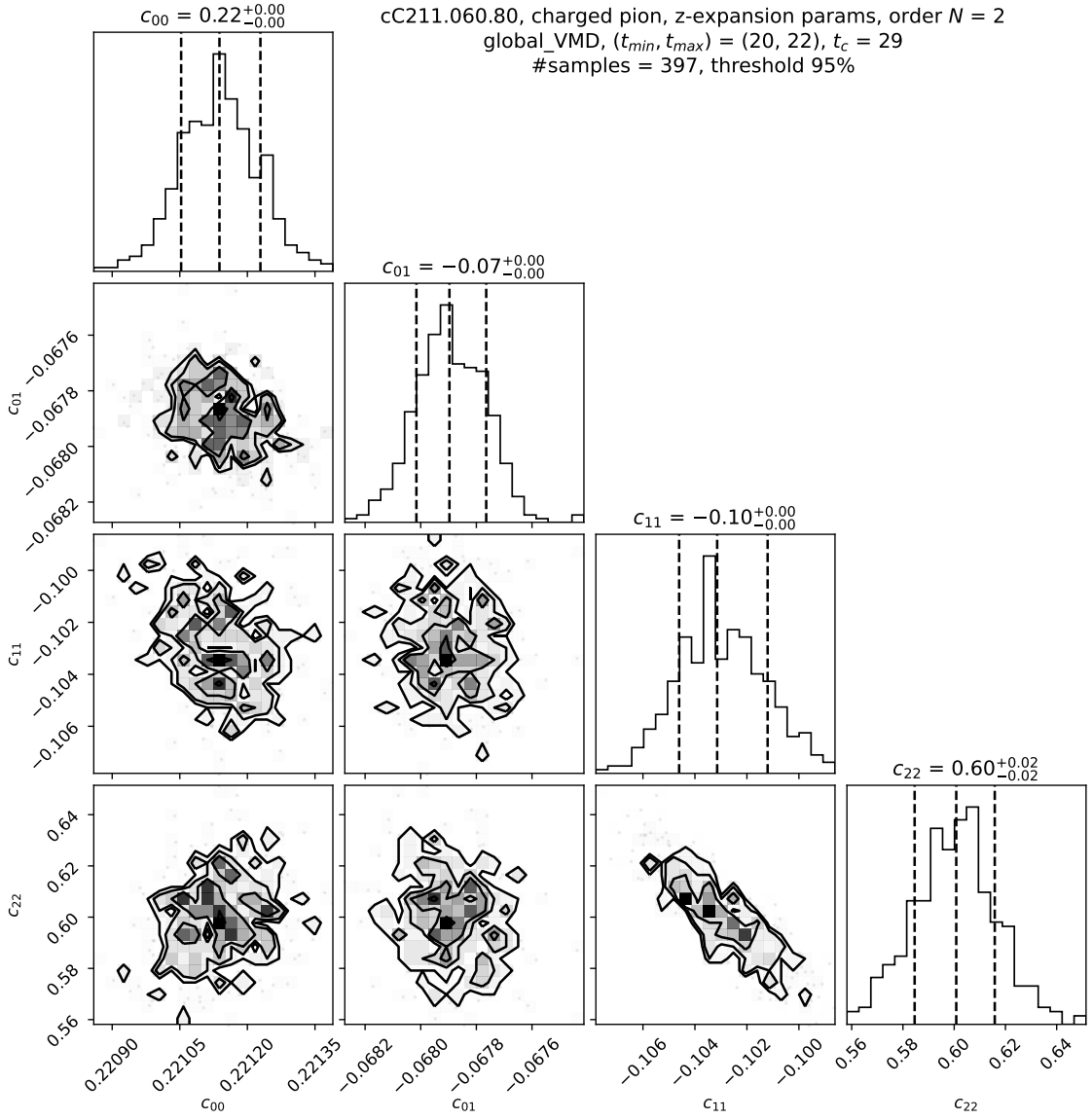

Figure D.25: c_{00}, c_{10}, c_{11} and c_{22} single analysis cornerplot.

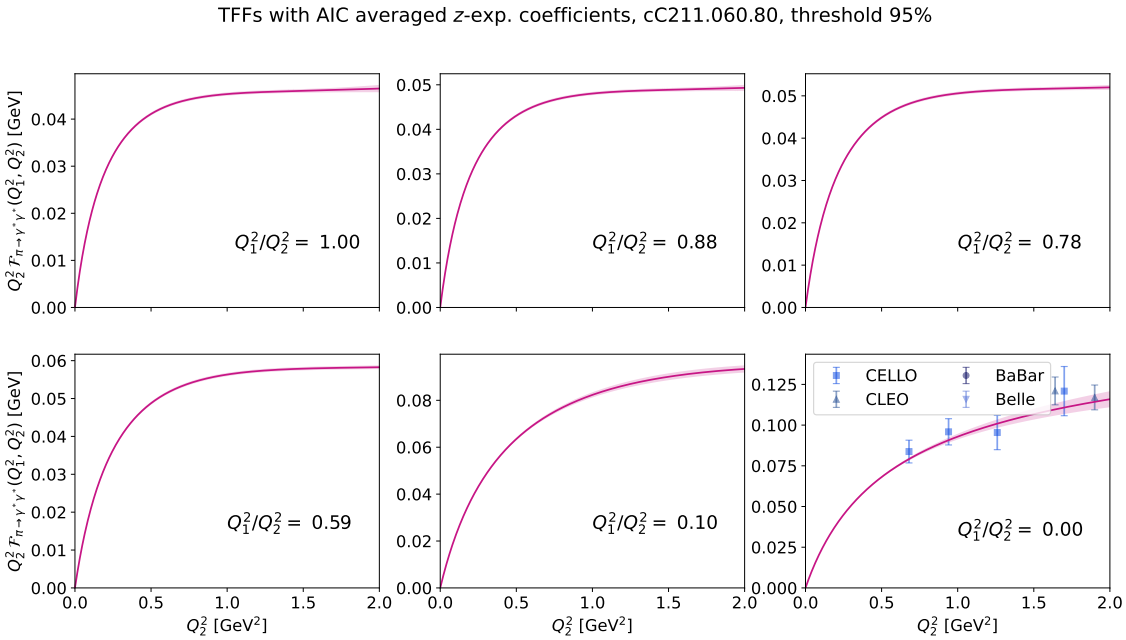

Figure D.26: c_{00}, c_{10}, c_{11} and c_{22} AIC averaged TFFs.

D.5.6 cC211.060.80 $N = 2$

c_{00}	c_{10}	c_{11}	c_{20}	c_{21}	c_{22}	$\chi^2_{\tilde{A}}$/d.o.f.	$\chi^2_{z-\text{exp.}}$/d.o.f.
0.2212(17)	-0.0753(30)	0.18(23)	-0.14(11)	0.218(67)	0.42(23)	0.86	0.66

Table D.12: z-expansion coefficients and χ^2/d.o.f. of the analysis shown in Figs. D.27 and D.28.

c_{00}	c_{10}	c_{11}	c_{20}	c_{21}	c_{22}	$\chi^2_{z-\text{exp.}}$/d.o.f.
0.2211(17)	-0.0755(34)	-0.03(44)	-0.06(23)	0.17(13)	0.25(39)	0.68(3)

Table D.13: AIC averaged z-expansion coefficients and χ^2/d.o.f. of Fig. D.29.

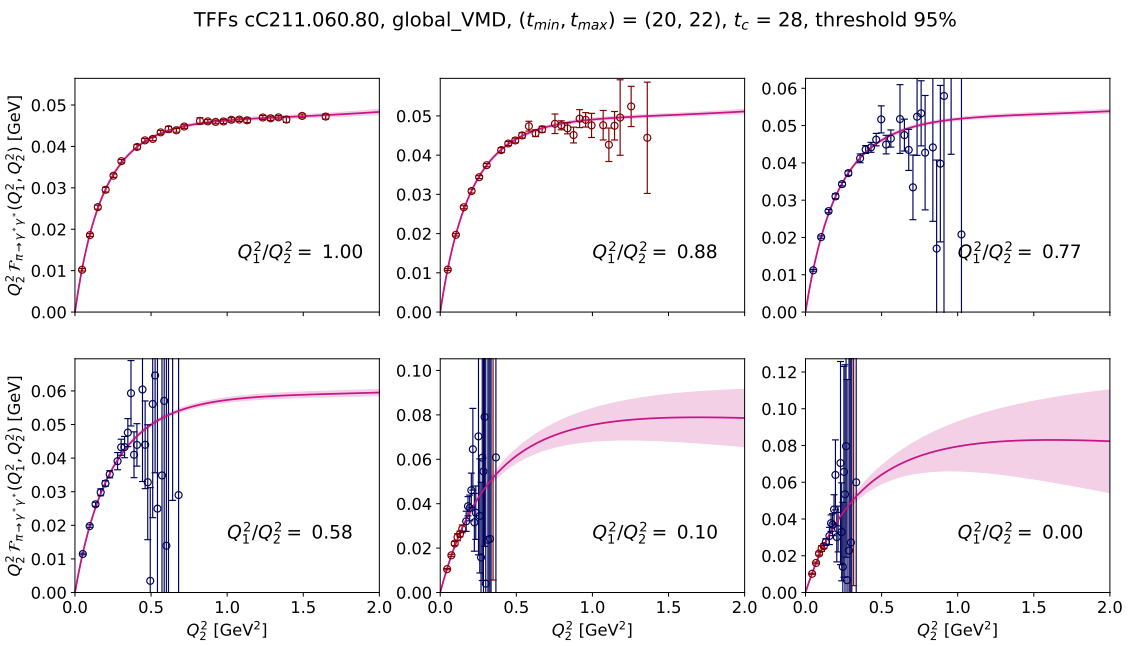

Figure D.27: $N = 2$ single analysis TFFs.

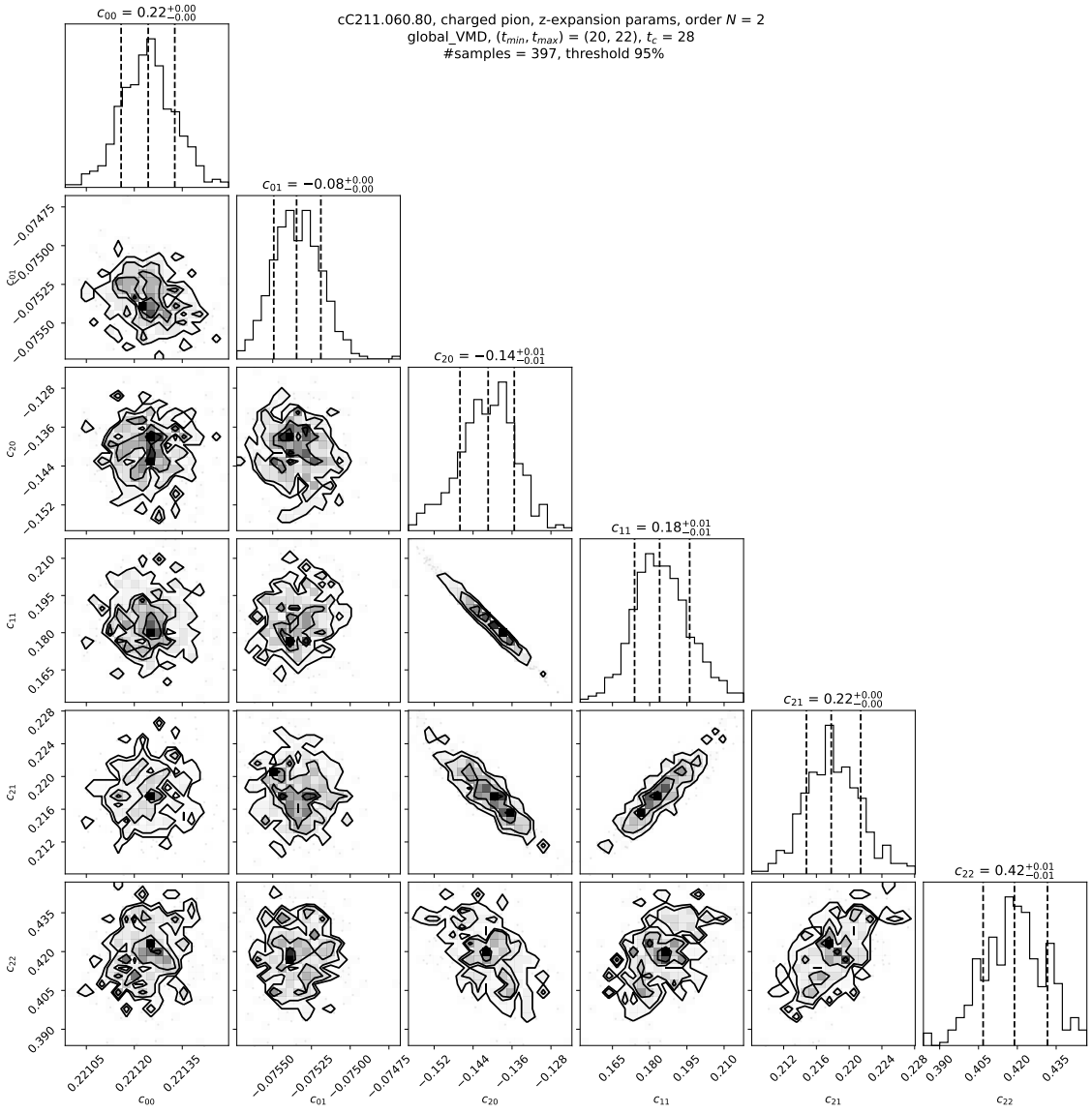

Figure D.28: $N = 2$ single analysis cornerplot.

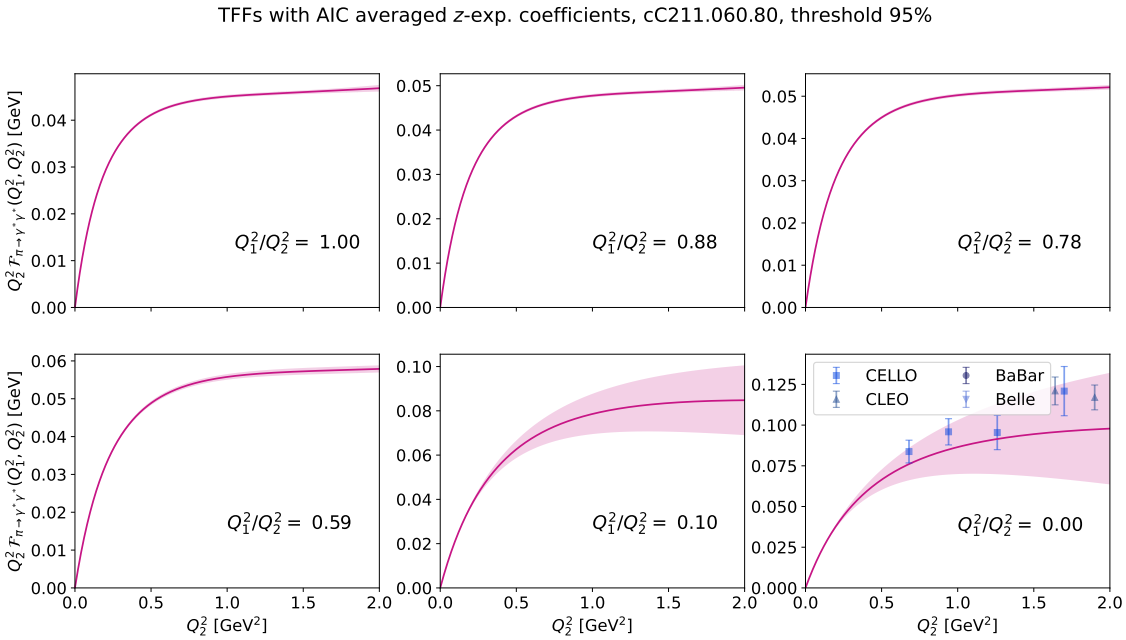

Figure D.29: $N = 2$ AIC averaged TFFs.

D.5.7 cD211.054.96 $N = 1$

c_{00}	c_{10}	c_{11}	$\chi^2_{\tilde{A}}$/d.o.f.	$\chi^2_{z-\text{exp.}}$/d.o.f.
0.2053(27)	-0.0742(36)	0.107(23)	0.98	1.05

Table D.14: z-expansion coefficients and χ^2/d.o.f. of the analysis shown in Figs. D.30 and D.31.

c_{00}	c_{10}	c_{11}	$\chi^2_{z-\text{exp.}}$/d.o.f.
0.2054(27)	-0.0742(36)	0.103(23)	1.11(6)

Table D.15: AIC averaged z-expansion coefficients and χ^2/d.o.f. of Fig. D.32.

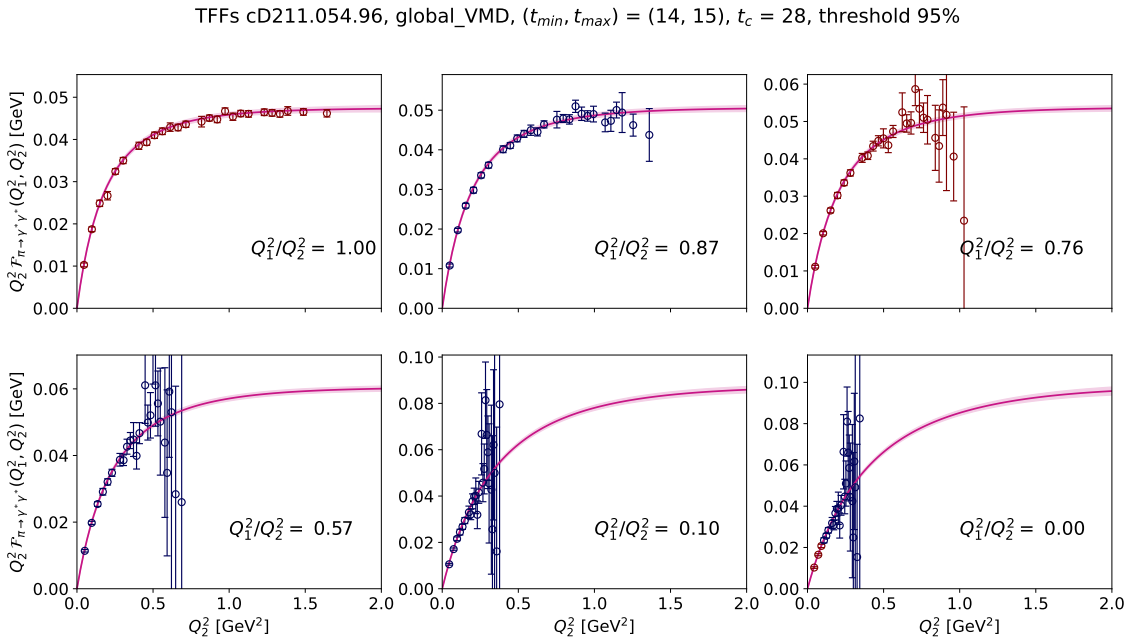

Figure D.30: $N = 1$ single analysis TFFs.

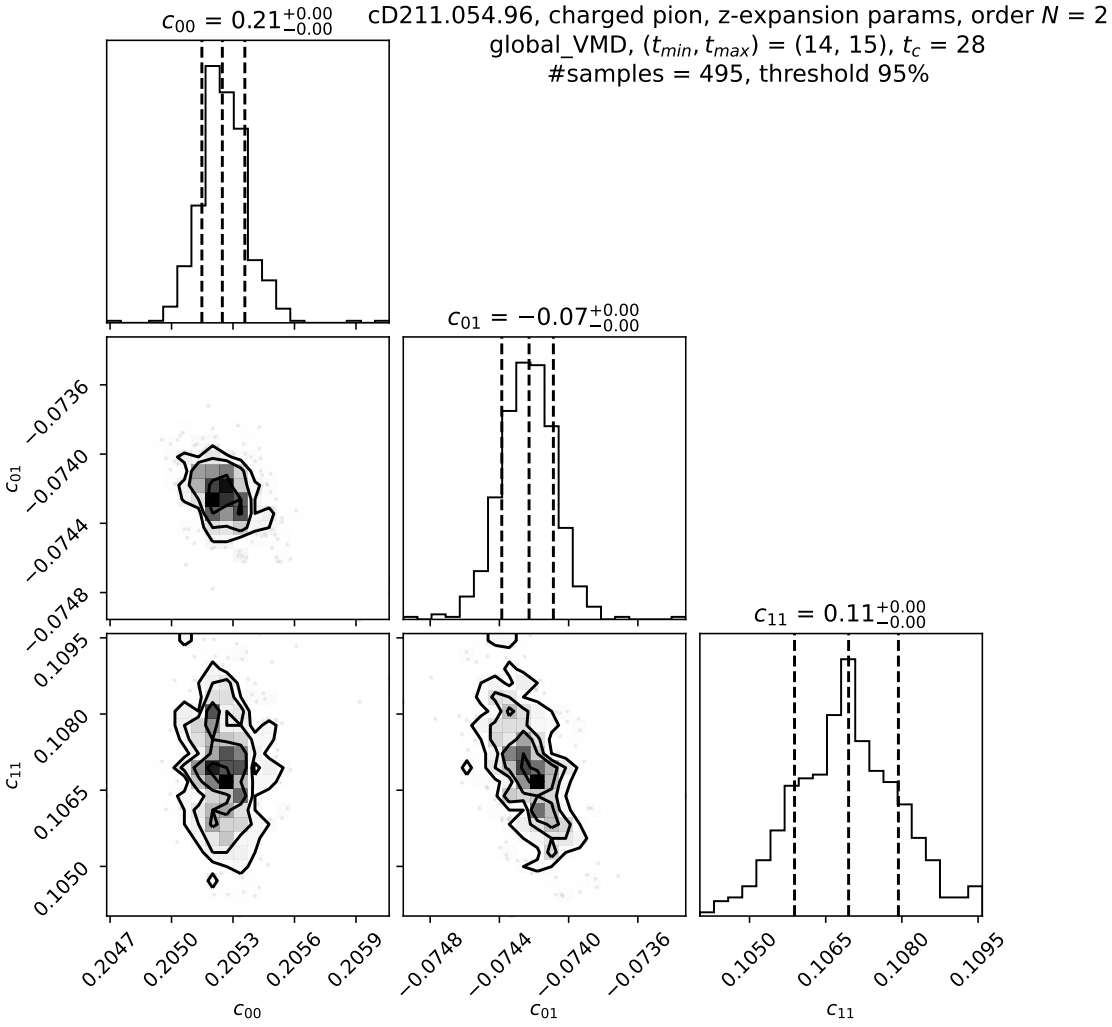

Figure D.31: $N = 1$ single analysis cornerplot.

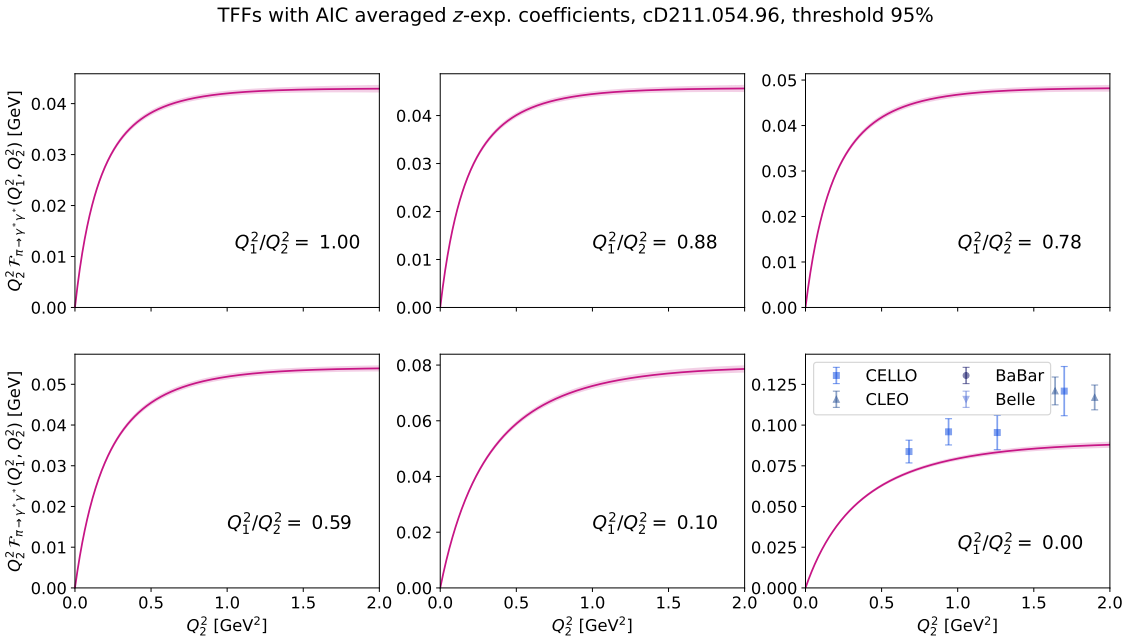

Figure D.32: $N = 1$ AIC averaged TFFs.

D.5.8 cD211.054.96 using c_{00}, c_{10}, c_{11} and c_{22}

c_{00}	c_{10}	c_{11}	c_{22}	$\chi^2_{\tilde{A}}$/d.o.f.	$\chi^2_{z-\text{exp.}}$/d.o.f.
0.2043(27)	-0.0713(34)	0.154(46)	-1.34(0.44)	0.98	0.92

Table D.16: z-expansion coefficients and χ^2/d.o.f. of the analysis shown in Figs. D.33 and D.34.

c_{00}	c_{10}	c_{11}	c_{22}	$\chi^2_{z-\text{exp.}}$/d.o.f.
0.2045(28)	-0.0714(34)	0.148(48)	-1.35(44)	0.96(5)

Table D.17: AIC averaged z-expansion coefficients and χ^2/d.o.f. of Fig. D.35.

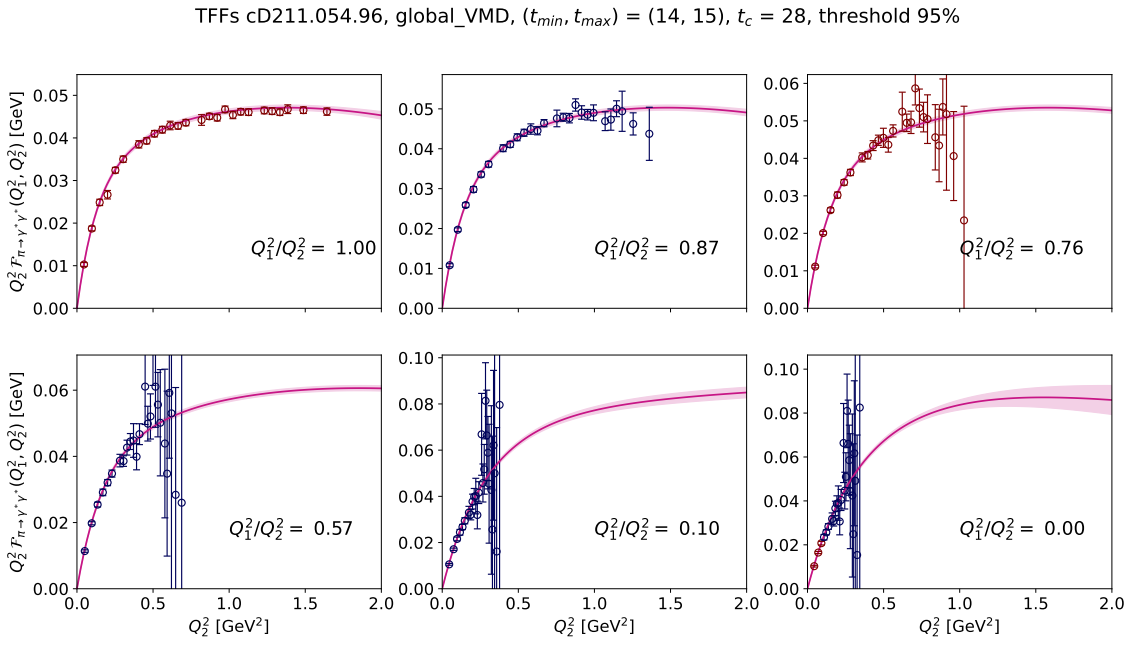

Figure D.33: c_{00}, c_{10}, c_{11} and c_{22} single analysis TFFs.

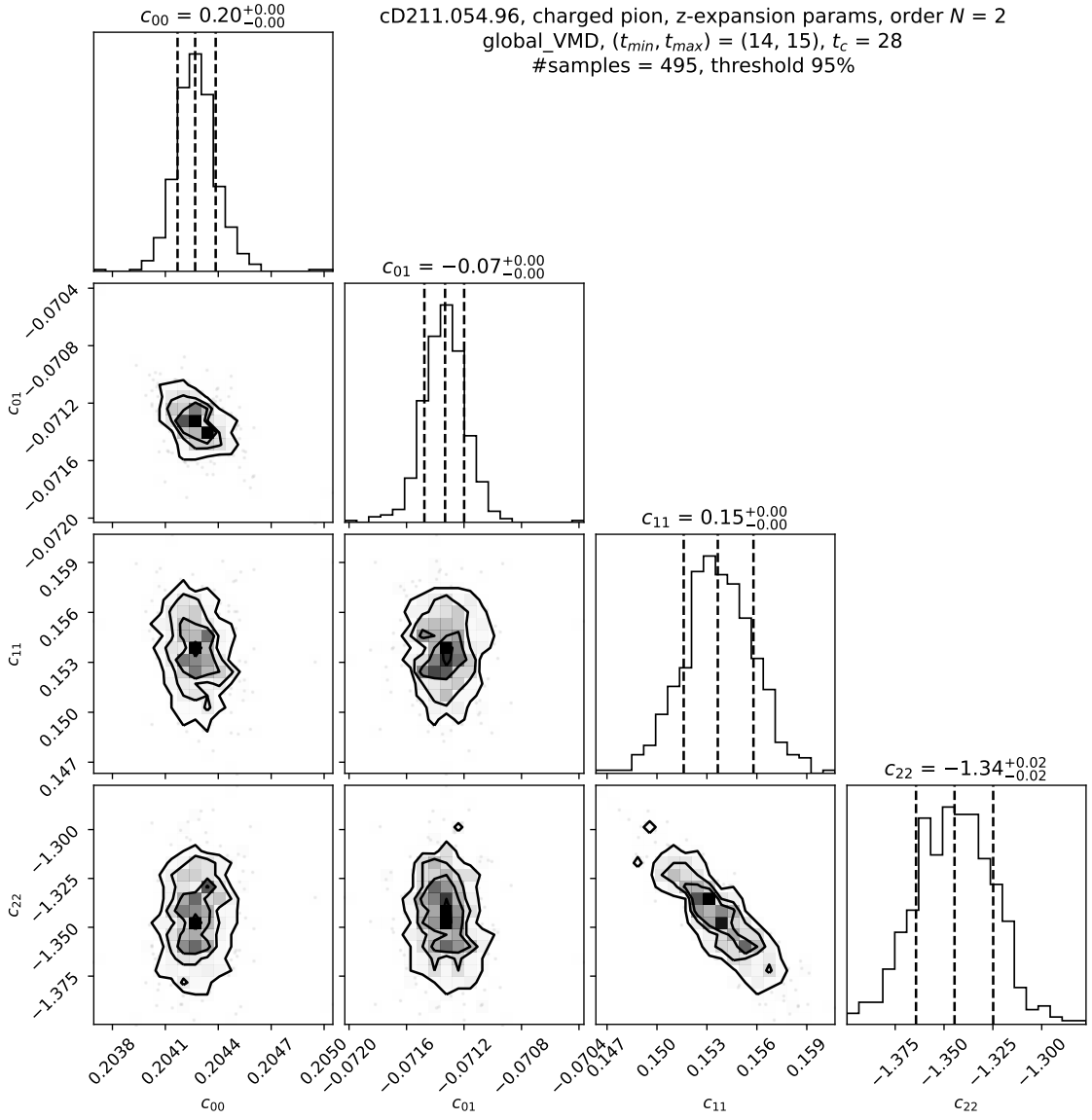

Figure D.34: c_{00}, c_{10}, c_{11} and c_{22} single analysis cornerplot.

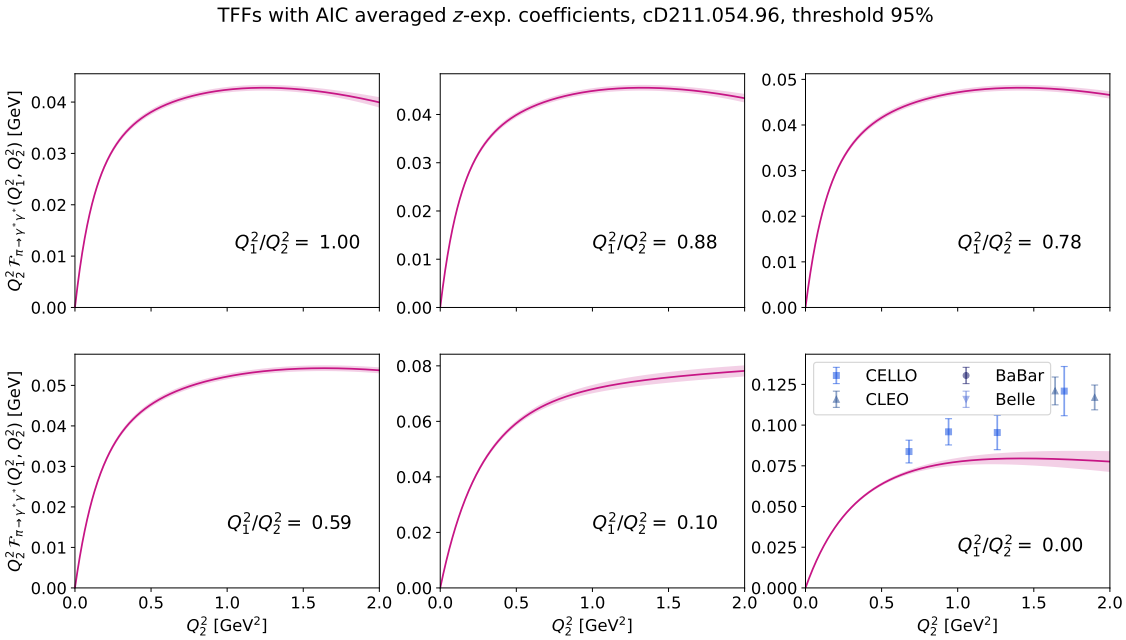

Figure D.35: c_{00}, c_{10}, c_{11} and c_{22} AIC averaged TFFs.

D.5.9 cD211.054.96 $N = 2$

c_{00}	c_{10}	c_{11}	c_{20}	c_{21}	c_{22}	$\chi^2_{\tilde{A}}$/d.o.f.	$\chi^2_{z-\text{exp.}}$/d.o.f.
0.2043(28)	-0.0738(46)	-0.35(86)	0.26(44)	-0.12(26)	-1.60(73)	0.98	0.94

Table D.18: z-expansion coefficients and χ^2/d.o.f. of the analysis shown in Figs. D.36 and D.37.

c_{00}	c_{10}	c_{11}	c_{20}	c_{21}	c_{22}	$\chi^2_{z-\text{exp.}}$/d.o.f.
0.2046(28)	-0.0738(47)	-0.27(87)	0.21(44)	-0.09(26)	-1.56(73)	0.99(4)

Table D.19: AIC averaged z-expansion coefficients and χ^2/d.o.f. of Fig. D.38.

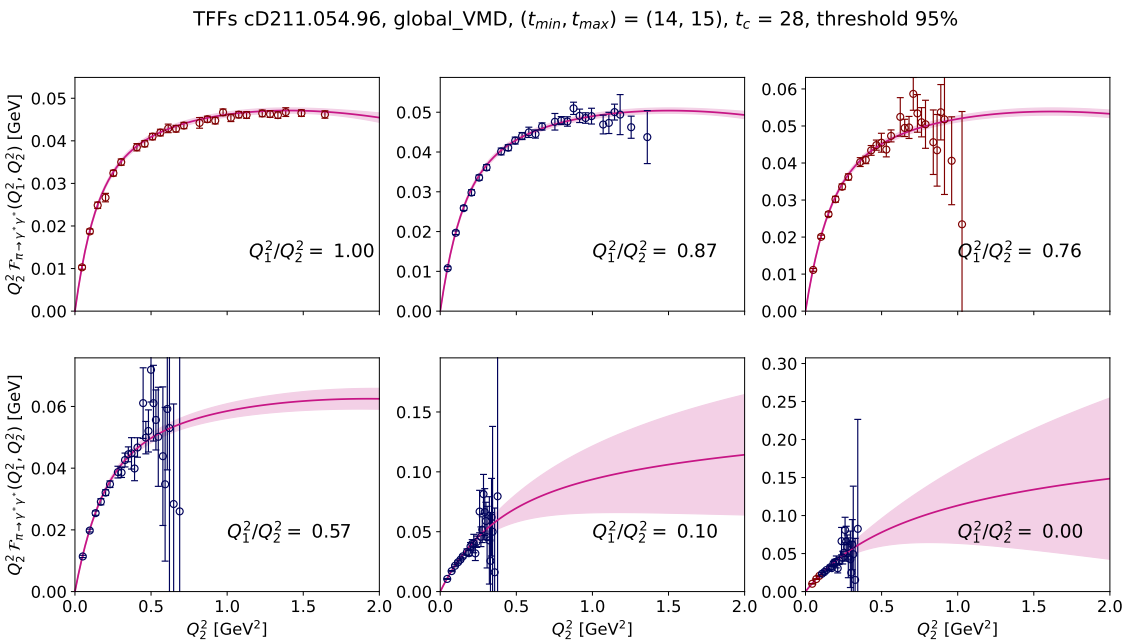

Figure D.36: $N = 2$ single analysis TFFs.

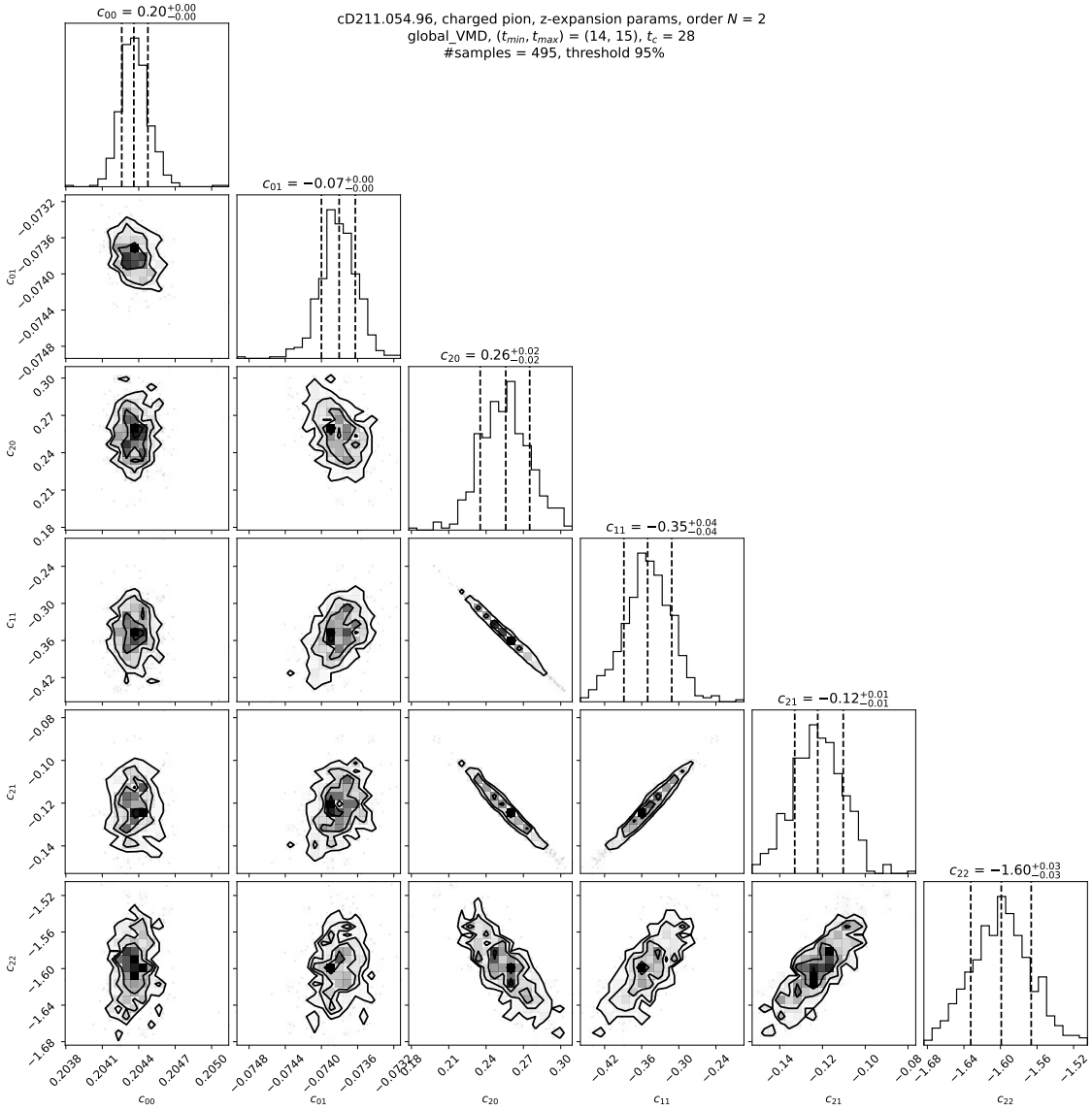

Figure D.37: $N = 2$ single analysis cornerplot.

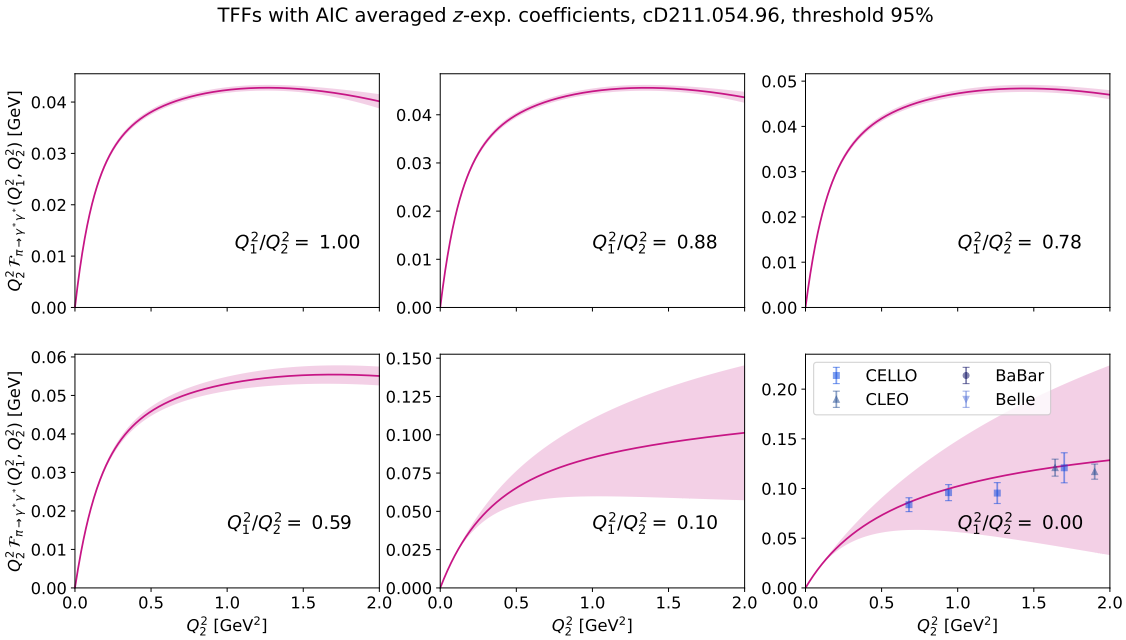

Figure D.38: $N = 2$ AIC averaged TFFs.

D.5.10 Combined fit $N = 1$ including correction coefficients

c_{00}	c_{10}	c_{11}	$\chi^2_{z-\text{exp.}}$/d.o.f.
0.2222(49)	-0.0581(68)	0.024(40)	1.38

Table D.20: AIC averaged z-expansion coefficients and χ^2/d.o.f. of Figs. D.39 and D.40.

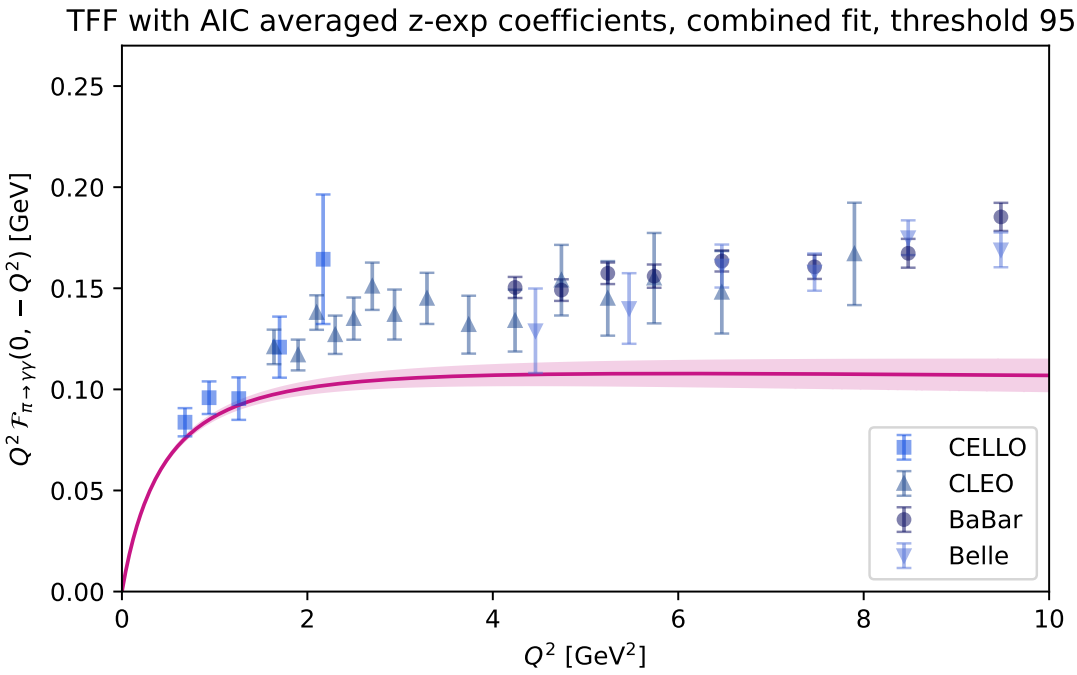

Figure D.39: $N = 1$ single-virtual AIC averaged TFF.

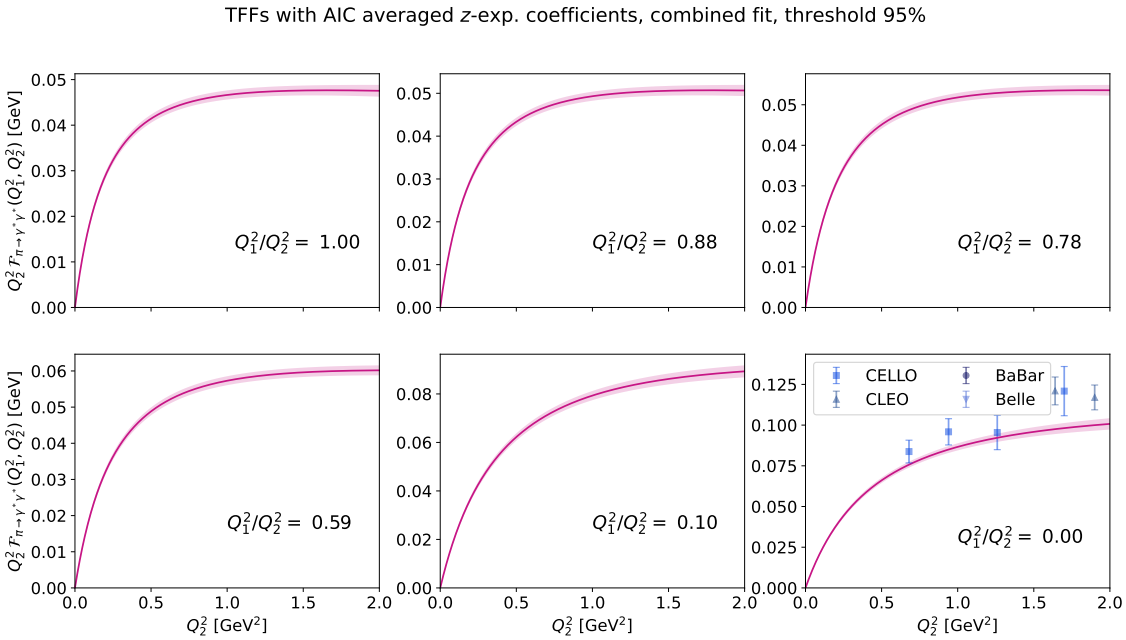

Figure D.40: $N = 1$ AIC averaged TFFs.

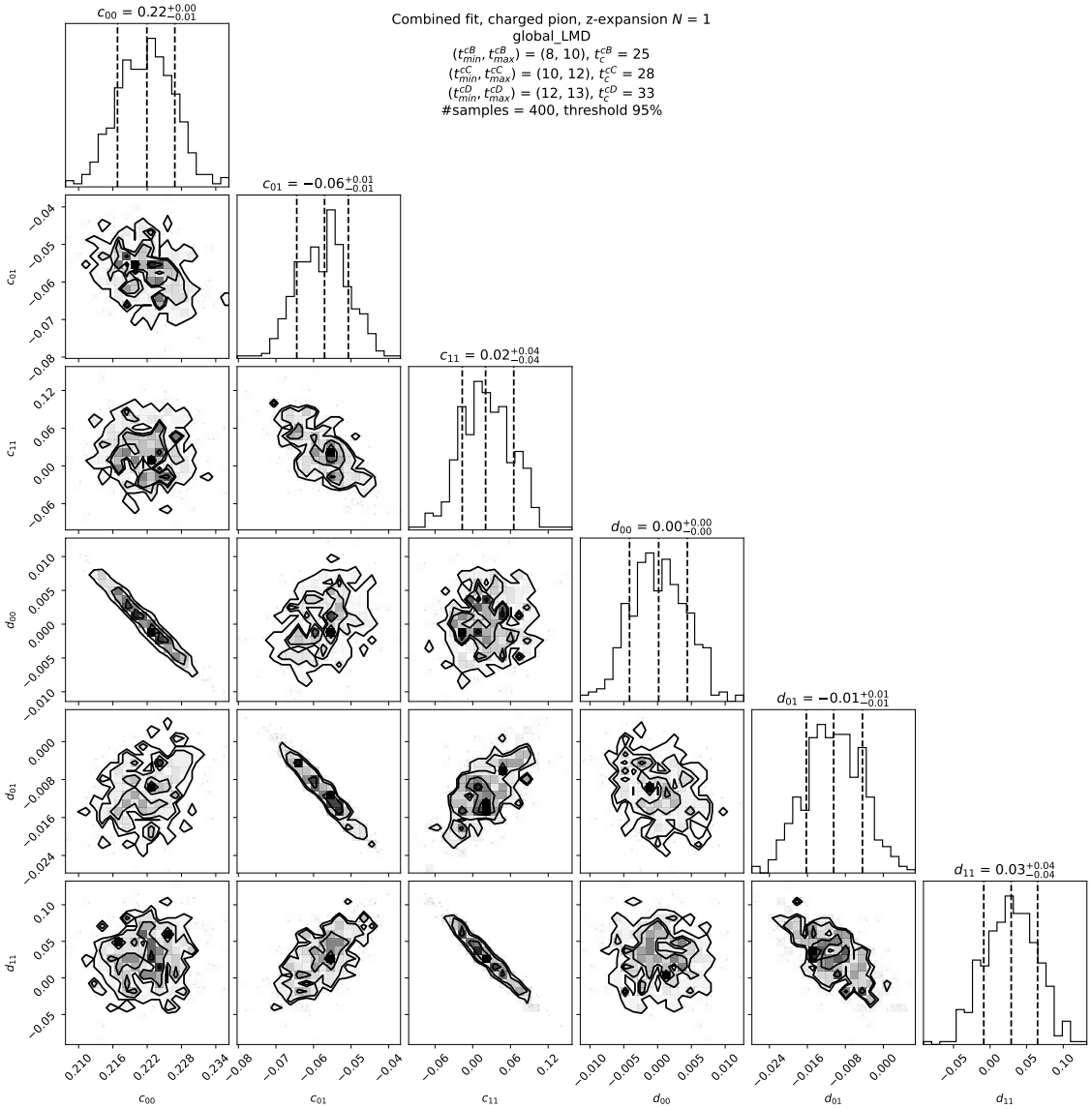

Figure D.41: $N = 1$ single analysis cornerplot, $\chi^2_{\tilde{A},\mathrm{cB}}/\mathrm{d.o.f.} = 1.51$, $\chi^2_{\tilde{A},\mathrm{cC}}/\mathrm{d.o.f.} = 1.39$, $\chi^2_{\tilde{A},\mathrm{cD}}/\mathrm{d.o.f.} = 1.60$, $\chi^2_{z-\mathrm{exp.}}/\mathrm{d.o.f.} = 1.36$.

D.5.11 Combined fit using c_{00}, c_{10}, c_{11} and c_{22} and d_{00}, d_{10}

c_{00}	c_{10}	c_{11}	c_{22}	$\chi^2_{z-\text{exp.}}$/d.o.f.
0.2220(48)	-0.0596(59)	-0.050(18)	0.27(14)	1.36

Table D.21: AIC averaged z-expansion coefficients and χ^2/d.o.f. of Figs. D.42 and D.43.

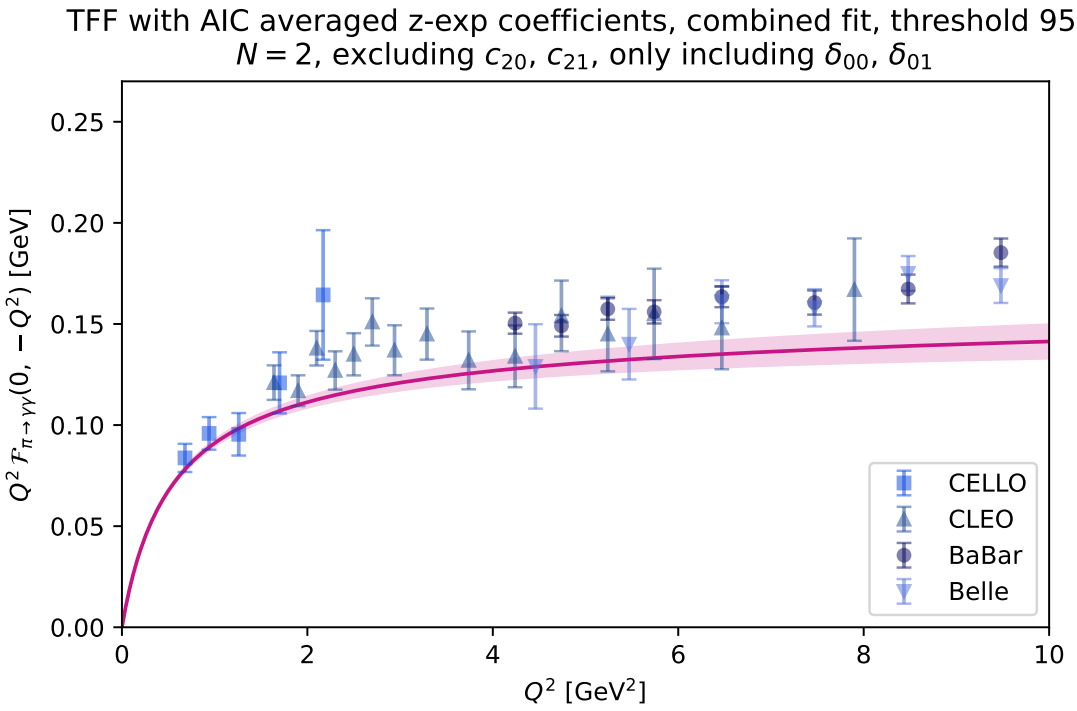

Figure D.42: c_{00}, c_{10}, c_{11} and c_{22} including correction coefficients d_{00} and d_{01} single-virtual AIC averaged TFF.

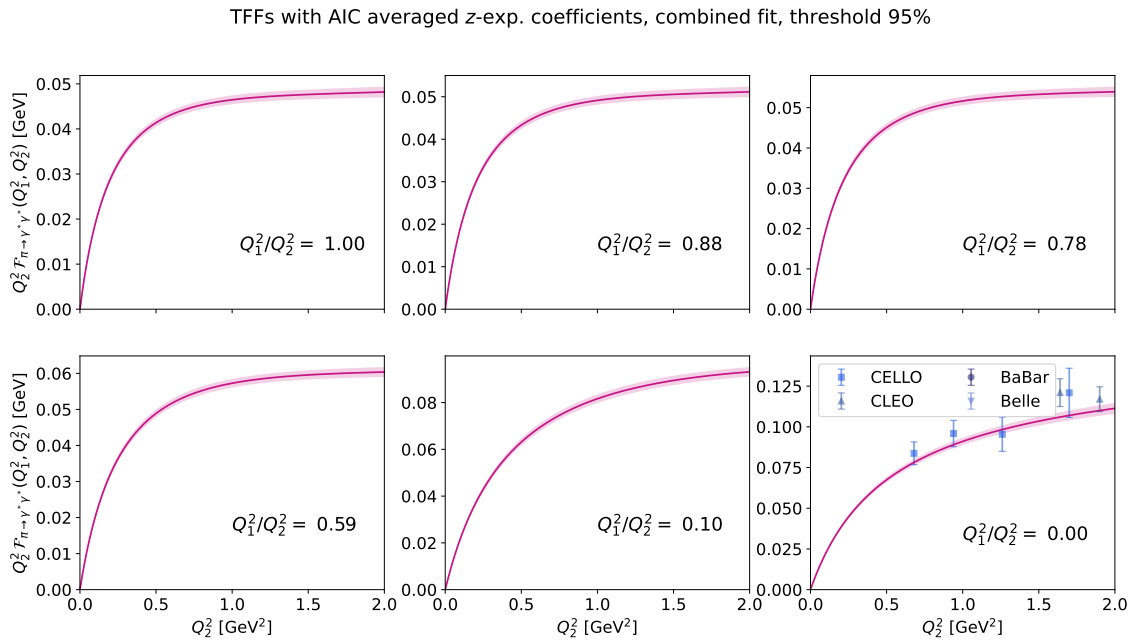

Figure D.43: c_{00}, c_{10}, c_{11} and c_{22} including correction coefficients d_{00} and d_{01} AIC averaged TFFs.

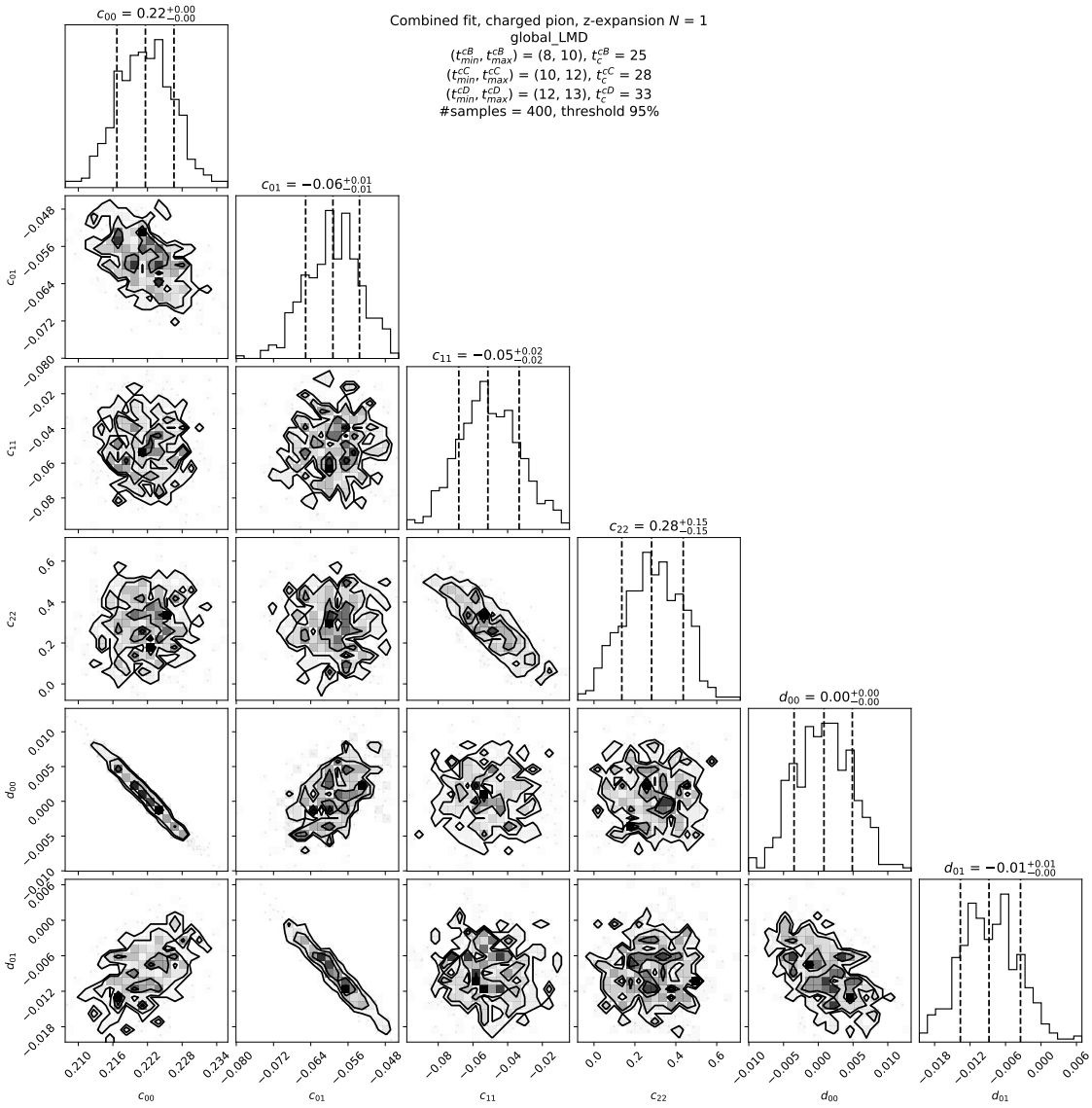

Figure D.44: c_{00}, c_{10}, c_{11} and c_{22} including correction coefficients d_{00} and d_{01} single analysis cornerplot, $\chi^2_{\tilde{A},\mathrm{cB}}/\mathrm{d.o.f.} = 1.51$, $\chi^2_{\tilde{A},\mathrm{cC}}/\mathrm{d.o.f.} = 1.39$, $\chi^2_{\tilde{A},\mathrm{cD}}/\mathrm{d.o.f.} = 1.60$, $\chi^2_{z-\mathrm{exp.}}/\mathrm{d.o.f.} = 1.34$.

D.5.12 Combined fit using c_{00}, c_{10}, c_{11} and c_{22} and no correction coefficients

c_{00}	c_{10}	c_{11}	c_{22}	$\chi^2_{z-\text{exp.}}$/d.o.f.
0.2226(98)	-0.0693(16)	-0.049(17)	0.25(14)	1.37

Table D.22: AIC averaged z-expansion coefficients and χ^2/d.o.f. of Figs. D.45 and D.46.

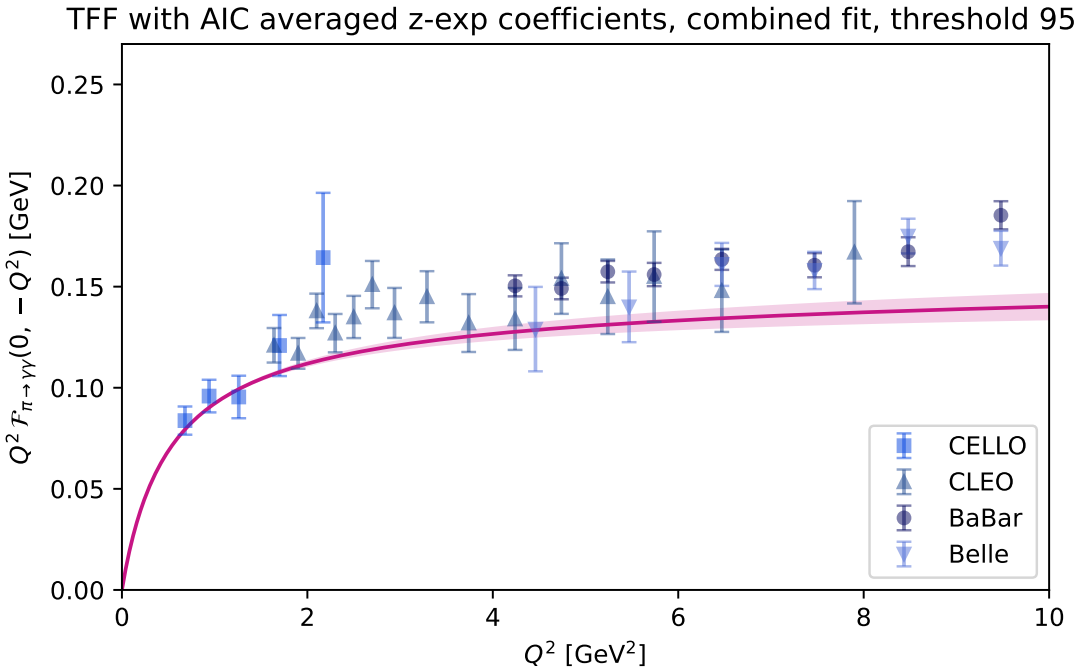

Figure D.45: c_{00}, c_{10}, c_{11} and c_{22} single-virtual AIC averaged TFF.

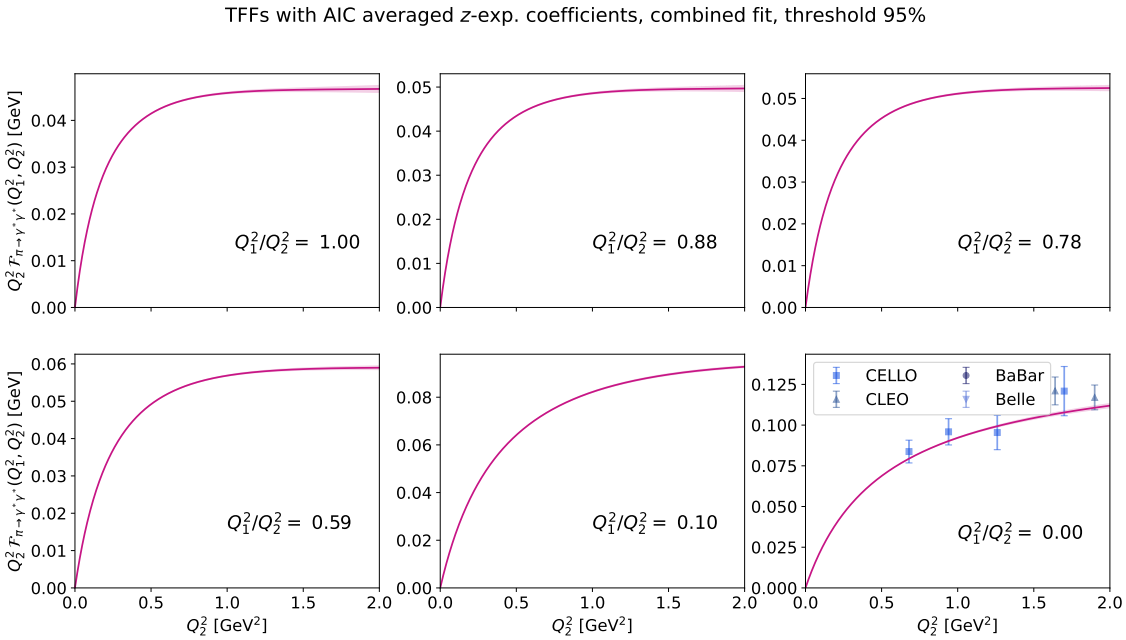

Figure D.46: c_{00}, c_{10}, c_{11} and c_{22} AIC averaged TFFs.

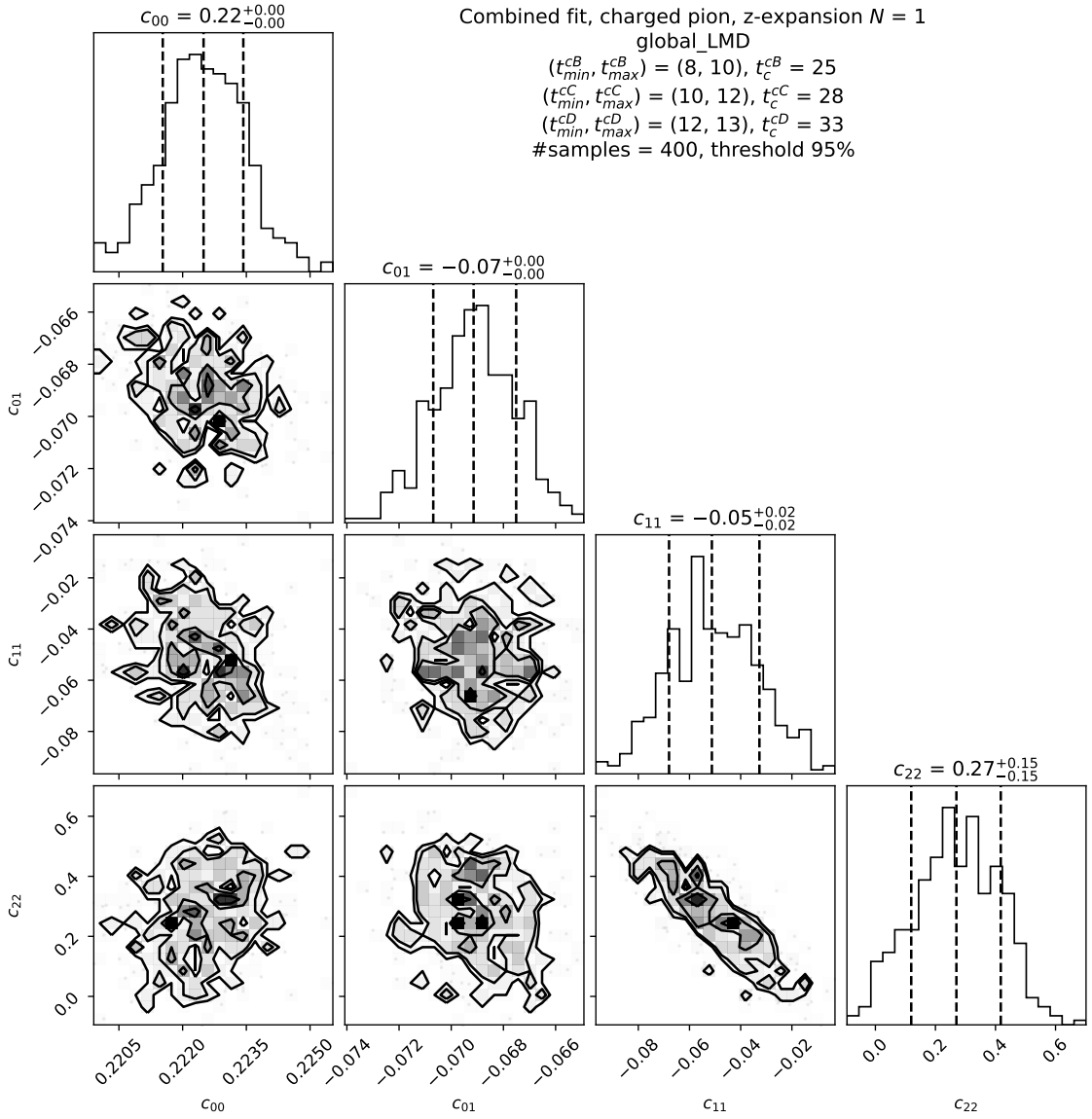

Figure D.47: c_{00}, c_{10}, c_{11} and c_{22} single analysis cornerplot, $\chi^2_{\tilde{A},\mathrm{cB}}/\mathrm{d.o.f.} = 1.51$, $\chi^2_{\tilde{A},\mathrm{cC}}/\mathrm{d.o.f.} = 1.39$, $\chi^2_{\tilde{A},\mathrm{cD}}/\mathrm{d.o.f.} = 1.60$, $\chi^2_{z-\mathrm{exp.}}/\mathrm{d.o.f.} = 1.35$.

D.5.13 Combined fit $N = 2$ including experimental TFF data

In this analysis, the single-virtual experimental data from [72–76] was included (without considering the correlation of the experimental data).

c_{00}	c_{10}	c_{11}	c_{20}	c_{21}	c_{22}	$\chi^2_{z-\text{exp.}}$/d.o.f.
0.2198(47)	-0.0494(71)	-0.117(26)	0.114(36)	-0.235(78)	-0.56(42)	1.09

Table D.23: AIC averaged z-expansion coefficients and χ^2/d.o.f. of Figs. D.48 and D.49.

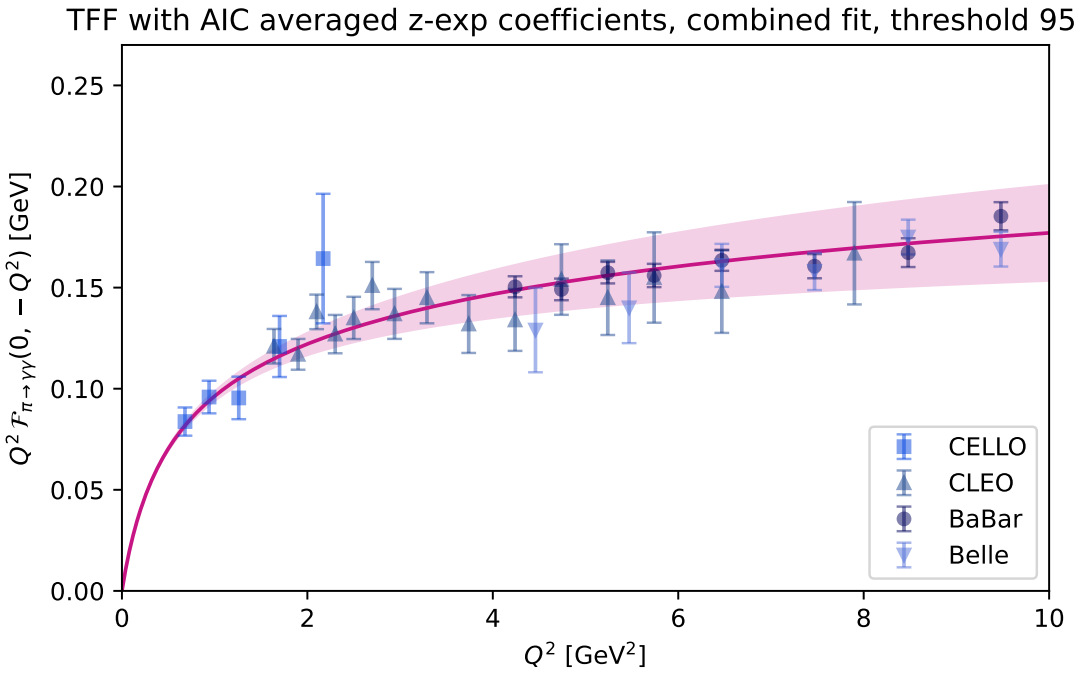

Figure D.48: $N = 2$ including experimental data single-virtual AIC averaged TFF.

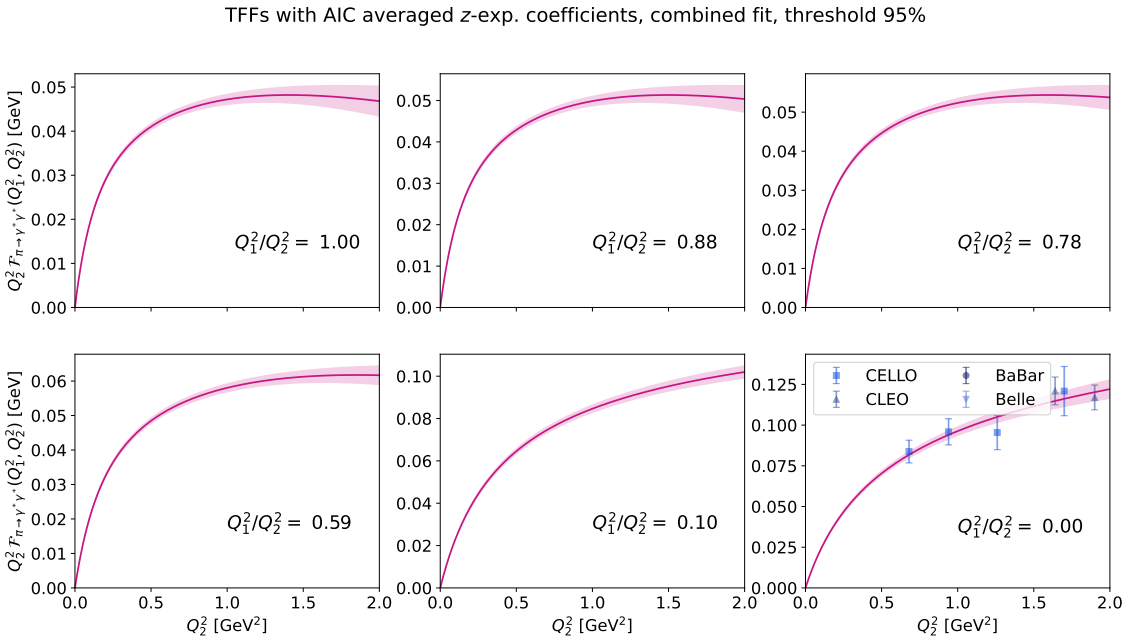

Figure D.49: $N = 2$ including experimental data AIC averaged TFFs.

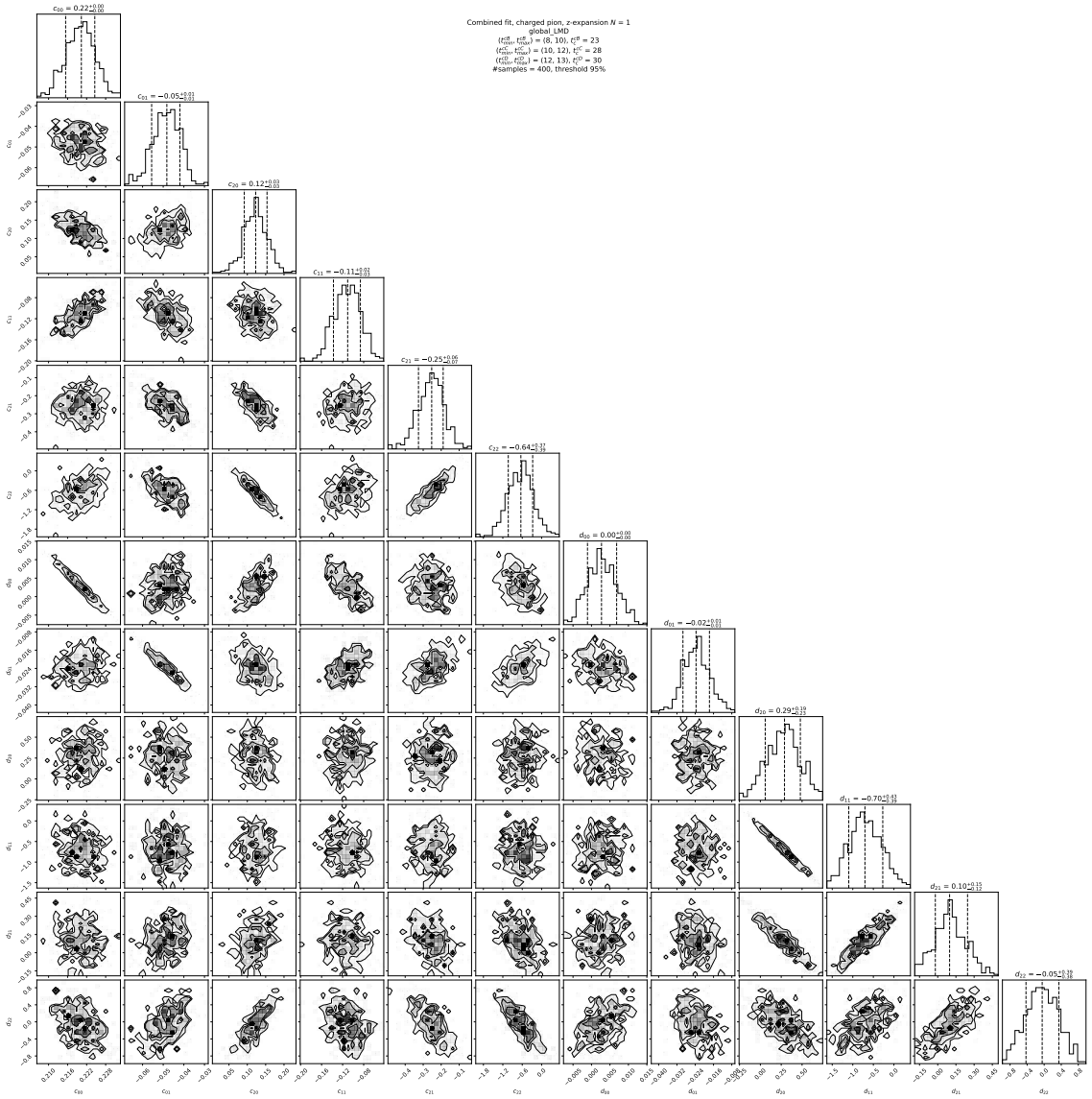

Figure D.50: $N = 2$ including experimental data single analysis cornerplot, $\chi^2_{\tilde{A},\mathrm{cB}}/\mathrm{d.o.f.} = 1.51$, $\chi^2_{\tilde{A},\mathrm{cC}}/\mathrm{d.o.f.} = 1.39$, $\chi^2_{\tilde{A},\mathrm{cD}}/\mathrm{d.o.f.} = 1.60$, $\chi^2_{z-\mathrm{exp.}}/\mathrm{d.o.f.} = 1.06$.

Bibliography

[1] T. Albahri, A. Anastasi, A. Anisenkov, K. Badgley, S. Baeßler, I. Bailey et al., *Measurement of the anomalous precession frequency of the muon in the Fermilab Muon $g-2$ Experiment*, *Phys. Rev. D* **103** (2021) 72002, [2104.03247].

[2] B. Abi, T. Albahri, S. Al-Kilani, D. Allspach, L. P. Alonzi, A. Anastasi et al., *Measurement of the Positive Muon Anomalous Magnetic Moment to 0.46 ppm*, *Phys. Rev. Lett.* **126** (2021) 141801, [2104.03281].

[3] T. Aoyama, N. Asmussen, M. Benayoun, J. Bijnens, T. Blum, M. Bruno et al., *The anomalous magnetic moment of the muon in the Standard Model*, *Phys. Rept.* **887** (2020) 1–166, [2006.04822].

[4] T. Blum, N. Christ, M. Hayakawa, T. Izubuchi, L. Jin, C. Jung et al., *Hadronic Light-by-Light Scattering Contribution to the Muon Anomalous Magnetic Moment from Lattice QCD*, *Phys. Rev. Lett.* **124** (2020) 132002, [1911.08123].

[5] Muon g-2 collaboration, K. R. Labe, *The Muon $g-2$ Experiment at Fermilab*, 2205.06336.

[6] P. A. M. Dirac, *The quantum theory of the electron. Part II*, *Proc. Roy. Soc. Lond. A* **118** (1928) 351.

[7] A. Keshavarzi, K. S. Khaw and T. Yoshioka, *Muon $g-2$: A review*, *Nucl. Phys. B* **975** (2022) 115675, [2106.06723].

[8] J. S. Schwinger, *On Quantum electrodynamics and the magnetic moment of the electron*, *Phys. Rev.* **73** (1948) 416–417.

[9] P. Kusch and H. M. Foley, *The Magnetic Moment of the Electron*, *Phys. Rev.* **74** (1948) 250.

[10] D. Hanneke, S. Fogwell and G. Gabrielse, *New Measurement of the Electron Magnetic Moment and the Fine Structure Constant*, *Phys. Rev. Lett.* **100** (2008) 120801, [0801.1134].

[11] F. Combley, F. J. Farley and E. Picasso, *The CERN muon $g-2$ experiments*, *Phys. Rept.* **68** (1981) 93–119.

[12] Particle Data Group collaboration, R. L. Workman and Others, *Review of Particle Physics*, *PTEP* **2022** (2022) 083C01.

[13] R. L. Garwin, L. M. Lederman and M. Weinrich, *Observations of the Failure of Conservation of Parity and Charge Conjugation in Meson Decays: The Magnetic Moment of the Free Muon*, *Phys. Rev.* **105** (1957) 1415–1417.

[14] J. M. Cassels, T. W. O'Keeffe, M. Rigby, A. M. Wetherell and J. R. Wormald, *Experiments with a polarized muon beam*, *Proceedings of the Physical Society. Section A* **70** (1957) 543.

[15] R. L. Garwin, D. P. Hutchinson, S. Penman and G. Shapiro, *Accurate determination of the μ^+ magnetic moment*, *Phys. Rev.* **118** (1960) 271–283.

[16] G. Charpak, F. J. M. Farley and R. L. Garwin, *A New Measurement of the Anomalous Magnetic Moment of the Muon*, *Phys. Lett.* **1** (1962) 16.

[17] G. Charpak, P. J. M. Farley, E. L. Garwin, T. Muller, J. C. Sens and A. Zichichi, *The anomalous magnetic moment of the muon*, *Nuovo Cim.* **37** (1965) 1241–1363.

[18] F. Combley and E. Picasso, *The Muon $g-2$ Precession Experiments: Past, Present and Future*, *Phys. Rept.* **14** (1974) 1.

[19] CERN-Mainz-Daresbury collaboration, J. Bailey et al., *Final Report on the CERN Muon Storage Ring Including the Anomalous Magnetic Moment and the Electric Dipole Moment of the Muon, and a Direct Test of Relativistic Time Dilation*, *Nucl. Phys. B* **150** (1979) 1–75.

[20] G. W. Bennett and Others, *Final Report of the Muon E821 Anomalous Magnetic Moment Measurement at BNL*, *Phys. Rev. D* **73** (2006) 72003, [0602035].

[21] *Fermilab muon $g-2$ experiment*, 2023. https://muon-$g-2$.fnal.gov/, accessed on 21.03.2023.

[22] J. Grange, V. Guarino, P. Winter, K. Wood, H. Zhao, R. M. Carey et al., *Muon $g-2$ technical design report*, 1501.06858.

[23] M. Abe et al., *A New Approach for Measuring the Muon Anomalous Magnetic Moment and Electric Dipole Moment*, *PTEP* **2019** (2019) 053C02, [1901.03047].

[24] K. Ishida, *Experiment J-PARC*, 2023. https://indico.ph.ed.ac.uk/event/112/contributions/1681/, talk at Fifth Plenary Workshop of the Muon $g-2$ Theory Initiative, accessed on 22.03.2023.

[25] *J-PARC muon $g-2$/EDM experiment*, 2023. https://$g-2$.kek.jp/overview/, accessed on 21.03.2023.

[26] S. Laporta, *High-precision calculation of the 4-loop contribution to the electron $g-2$ in QED*, *Phys. Lett. B* **772** (2017) 232–238, [1704.06996].

[27] M. Davier, A. Hoecker, B. Malaescu and Z. Zhang, *Reevaluation of the hadronic vacuum polarisation contributions to the Standard Model predictions of the muon $g-2$ and $\alpha(m_Z^2)$ using newest hadronic cross-section data*, *Eur. Phys. J. C* **77** (2017) 827, [1706.09436].

[28] M. Davier, A. Hoecker, B. Malaescu and Z. Zhang, *A new evaluation of the hadronic vacuum polarisation contributions to the muon anomalous magnetic moment and to $\alpha(m_Z^2)$*, *Eur. Phys. J. C* **80** (2020) 241, [1908.00921].

[29] A. Keshavarzi, D. Nomura and T. Teubner, *$g-2$ of charged leptons, $\alpha(M_Z^2)$, and the hyperfine splitting of muonium*, *Phys. Rev. D* **101** (2020) 014029, [1911.00367].

[30] A. Keshavarzi, D. Nomura and T. Teubner, *Muon $g-2$ and $\alpha(M_Z^2)$: a new data-based analysis*, *Phys. Rev. D* **97** (2018) 114025, [1802.02995].

[31] B.-L. Hoid, M. Hoferichter and B. Kubis, *Hadronic vacuum polarization and vector-meson resonance parameters from $e^+e^- \to \pi^0\gamma$*, *Eur. Phys. J. C* **80** (2020) 988, [2007.12696].

[32] G. Colangelo, M. Hoferichter and P. Stoffer, *Two-pion contribution to hadronic vacuum polarization*, *JHEP* **02** (2019) 006, [1810.00007].

[33] M. Hoferichter, B.-L. Hoid and B. Kubis, *Three-pion contribution to hadronic vacuum polarization*, *JHEP* **08** (2019) 137, [1907.01556].

[34] Y. Maeda, *$e^+e^- \to \pi^+\pi^-$ cross section measurement in Belle-II*, 2018. https://kds.kek.jp/event/26780/contributions/88954/, talk at 2018 workshop on hadronic vacuum polarization contributions to muon $g-2$, accessed on 22.03.2023.

[35] M. Davier, *Hadronic vacuum polarization contributions to muon $g-2$: Recent results and status of ongoing analyses in BaBar*, 2018. https://kds.kek.jp/event/26780/contributions/88957/, talk at 2018 workshop on hadronic vacuum polarization contributions to muon $g-2$, accessed on 22.03.2023.

[36] M. Ablikim, M. N. Achasov, P. Adlarson, S. Ahmed, M. Albrecht, M. Alekseev et al., *Future physics programme of BESIII*, *Chinese Physics C* **44** (2020) 040001.

[37] F. V. Ignatov, R. R. Akhmetshin, A. N. Amirkhanov, A. V. Anisenkov, V. M. Aulchenko, N. S. Bashtovoy et al., *Measurement of the $e^+e^- \to \pi^+\pi^-$ cross section from threshold to 1.2 GeV with the CMD-3 detector*, 2302.08834.

[38] S. Borsanyi, Z. Fodor, J. N. Guenther, C. Hoelbling, S. D. Katz, L. Lellouch et al., *Leading hadronic contribution to the muon magnetic moment from lattice QCD*, *Nature* **593** (2021) 51–55, [2002.12347].

[39] C. Lehner and A. S. Meyer, *Consistency of hadronic vacuum polarization between lattice qcd and the r ratio*, *Phys. Rev. D* **101** (2020) 074515.

[40] Extended Twisted Mass collaboration, C. Alexandrou, S. Bacchio, P. Dimopoulos, J. Finkenrath, R. Frezzotti, G. Gagliardi et al., *Lattice calculation of the short and intermediate time-distance hadronic vacuum*

polarization contributions to the muon magnetic moment using twisted-mass fermions, 2206.15084.

[41] M. Cè , A. Gérardin, G. von Hippel, R. Hudspith, S. Kuberski, H. Meyer et al., *Window observable for the hadronic vacuum polarization contribution to the muon $g-2$ from lattice QCD*, *Phys. Rev. D* **106** (2022) .

[42] T. Kinoshita, B. Nizic and Y. Okamoto, *Hadronic Contributions to the Anomalous Magnetic Moment of the Muon*, *Phys. Rev. D* **31** (1985) 2108.

[43] E. de Rafael, *Hadronic contributions to the muon $g-2$ and low-energy QCD*, *Phys. Lett. B* **322** (1994) 239–246, [hep-ph/9311316].

[44] J. Bijnens, E. Pallante and J. Prades, *Hadronic light by light contributions to the muon $g-2$ in the large $N(c)$ limit*, *Phys. Rev. Lett.* **75** (1995) 1447–1450, [hep-ph/9505251].

[45] J. Bijnens, E. Pallante and J. Prades, *Analysis of the hadronic light by light contributions to the muon $g-2$*, *Nucl. Phys. B* **474** (1996) 379–420, [hep-ph/9511388].

[46] J. Bijnens, E. Pallante and J. Prades, *Comment on the pion pole part of the light by light contribution to the muon $g-2$*, *Nucl. Phys. B* **626** (2002) 410–411, [hep-ph/0112255].

[47] M. Hayakawa, T. Kinoshita and A. I. Sanda, *Hadronic light by light scattering effect on muon $g-2$*, *Phys. Rev. Lett.* **75** (1995) 790–793, [hep-ph/9503463].

[48] M. Hayakawa, T. Kinoshita and A. I. Sanda, *Hadronic light by light scattering contribution to muon $g-2$*, *Phys. Rev. D* **54** (1996) 3137–3153, [hep-ph/9601310].

[49] M. Hayakawa and T. Kinoshita, *Pseudoscalar pole terms in the hadronic light by light scattering contribution to muon $g-2$*, *Phys. Rev. D* **57** (1998) 465–477, [hep-ph/9708227].

[50] M. Knecht and A. Nyffeler, *Hadronic light by light corrections to the muon $g-2$: The Pion pole contribution*, *Phys. Rev. D* **65** (2002) 73034, [0111058].

[51] K. Melnikov and A. Vainshtein, *Hadronic light-by-light scattering contribution to the muon anomalous magnetic moment revisited*, *Phys. Rev. D* **70** (2004) 113006, [hep-ph/0312226].

[52] G. Colangelo, M. Hoferichter, M. Procura and P. Stoffer, *Dispersive approach to hadronic light-by-light scattering*, *JHEP* **2014** (2014) 1–33, [1402.7081].

[53] G. Colangelo, M. Hoferichter, B. Kubis, M. Procura and P. Stoffer, *Towards a data-driven analysis of hadronic light-by-light scattering*, *Phys. Lett. B* **738** (2014) 6–12, [1408.2517].

[54] G. Colangelo, M. Hoferichter, M. Procura and P. Stoffer, *Dispersion relation for hadronic light-by-light scattering: theoretical foundations*, *JHEP* **09** (2015) 074, [1506.01386].

[55] V. Pauk and M. Vanderhaeghen, *Anomalous magnetic moment of the muon in a dispersive approach*, *Phys. Rev. D* **90** (2014) 113012, [1409.0819].

[56] T. Blum, S. Chowdhury, M. Hayakawa and T. Izubuchi, *Hadronic light-by-light scattering contribution to the muon anomalous magnetic moment from lattice QCD*, *Phys. Rev. Lett.* **114** (2015) 012001, [1407.2923].

[57] T. Blum, N. Christ, M. Hayakawa, T. Izubuchi, L. Jin and C. Lehner, *Lattice Calculation of Hadronic Light-by-Light Contribution to the Muon Anomalous Magnetic Moment*, *Phys. Rev. D* **93** (2016) 014503, [1510.07100].

[58] T. Blum, N. Christ, M. Hayakawa, T. Izubuchi, L. Jin, C. Jung et al., *Connected and Leading Disconnected Hadronic Light-by-Light Contribution to the Muon Anomalous Magnetic Moment with a Physical Pion Mass*, *Phys. Rev. Lett.* **118** (2017) 022005, [1610.04603].

[59] T. Blum, N. Christ, M. Hayakawa, T. Izubuchi, L. Jin, C. Jung et al., *Using infinite volume, continuum QED and lattice QCD for the hadronic light-by-light contribution to the muon anomalous magnetic moment*, *Phys. Rev. D* **96** (2017) 034515, [1705.01067].

[60] E. H. Chao, R. J. Hudspith, A. Gérardin, J. R. Green, H. B. Meyer and K. Ottnad, *Hadronic light-by-light contribution to* $(g-2)_\mu$ *from lattice QCD: a complete calculation*, *Eur. Phys. J. C* **81** (2021) 5–11, [2104.02632].

[61] E.-H. Chao, R. J. Hudspith, A. Gérardin, J. R. Green and H. B. Meyer, *The charm-quark contribution to light-by-light scattering in the muon $g-2$ from lattice QCD*, *Eur. Phys. J. C* **82** (2022) 664, [2204.08844].

[62] N. Asmussen, E.-H. Chao, A. Gérardin, J. R. Green, R. J. Hudspith, H. B. Meyer et al., *Hadronic light-by-light scattering contribution to the muon $g-2$ from lattice QCD: semi-analytical calculation of the QED kernel*, *JHEP* **04** (2023) 040, [2210.12263].

[63] M. Hoferichter, B.-L. Hoid, B. Kubis, S. Leupold and S. P. Schneider, *Pion-pole contribution to hadronic light-by-light scattering in the anomalous magnetic moment of the muon*, *Phys. Rev. Lett.* **121** (2018) 112002, [1805.01471].

[64] M. Hoferichter, B.-L. L. Hoid, B. Kubis, S. Leupold and S. P. Schneider, *Dispersion relation for hadronic light-by-light scattering: pion pole*, *JHEP* **10** (2018) 141, [1808.04823].

[65] P. Masjuan and P. Sanchez-Puertas, *Pseudoscalar-pole contribution to the $(g_\mu - 2)$: A rational approach*, *Phys. Rev. D* **95** (2017) 1–19, [1701.05829].

[66] A. Gérardin, H. B. Meyer and A. Nyffeler, *Lattice calculation of the pion transition form factor $\pi^0 \to \gamma^*\gamma^*$*, *Phys. Rev. D* **94** (2016) 74507, [1607.08174].

[67] A. Gérardin, H. B. Meyer and A. Nyffeler, *Lattice calculation of the pion transition form factor with $N_f = 2+1$ Wilson quarks*, *Phys. Rev. D* **100** (2019) 34520, [1903.09471].

[68] S. Burri, C. Alexandrou, S. Bacchio, G. Bergner, J. Finkenrath, A. Gasbarro et al., *Pion-pole contribution to HLbL from twisted mass lattice QCD at the physical point*, *PoS* **LATTICE2021** (2022) 519, [2112.03586].

[69] S. Burri, G. Kanwar, C. Alexandrou, S. Bacchio, G. Bergner, J. Finkenrath et al., *Pseudoscalar-pole contributions to the muon $g-2$ at the physical point*, *PoS* **LATTICE2022** (2023) 306, [2212.10300].

[70] A. Gérardin, J. N. Guenther, L. Varnhorst and W. E. A. Verplanke, *Pseudoscalar transition form factors and the hadronic light-by-light contribution to the muon $g-2$*, 2211.04159.

[71] C. Alexandrou, S. Bacchio, S. Burri, J. Finkenrath, A. Gasbarro, K. Hadjiyiannakou et al., *The $\eta \to \gamma^*\gamma^*$ transition form factor and the hadronic light-by-light η-pole contribution to the muon $g-2$ from lattice QCD*, 2212.06704.

[72] CLEO collaboration, J. Gronberg et al., *Measurements of the meson - photon transition form-factors of light pseudoscalar mesons at large momentum transfer*, *Phys. Rev. D* **57** (1998) 33–54, [hep-ex/9707031].

[73] CELLO collaboration, H. J. Behrend et al., *A Measurement of the π^0, η and η-prime electromagnetic form-factors*, *Z. Phys. C* **49** (1991) 401–410.

[74] BaBar collaboration, B. Aubert et al., *Measurement of the $\gamma\gamma^* \to \pi^0$ transition form factor*, *Phys. Rev. D* **80** (2009) 052002, [0905.4778].

[75] BaBar collaboration, P. del Amo Sanchez et al., *Measurement of the $\gamma\gamma^* \to \eta$ and $\gamma\gamma^* \to \eta'$ transition form factors*, *Phys. Rev. D* **84** (2011) 052001, [1101.1142].

[76] Belle Collaboration collaboration, S. Uehara, Y. Watanabe, H. Nakazawa, I. Adachi, H. Aihara, D. M. Asner et al., *Measurement of $\gamma\gamma^* \to \pi^0$ transition form factor at belle*, *Phys. Rev. D* **86** (2012-11) 092007.

[77] Alpha collaboration, R. Frezzotti, P. A. Grassi, S. Sint and P. Weisz, *Lattice QCD with a chirally twisted mass term*, *JHEP* **08** (2001) 058, [hep-lat/0101001].

[78] R. Frezzotti and G. C. Rossi, *Chirally improving Wilson fermions. 1. O(a) improvement*, *JHEP* **08** (2004) 007, [hep-lat/0306014].

[79] R. Frezzotti and G. C. Rossi, *Chirally improving Wilson fermions. II. Four-quark operators*, *JHEP* **10** (2004) 070, [hep-lat/0407002].

[80] S. Sint, *Lattice QCD with a chiral twist*, in *Perspectives in Lattice QCD*, World Scientific, 2007. 10.1142/9789812790927_0004.

[81] A. Shindler, *Twisted mass lattice QCD*, *Phys. Rept.* **461** (2008) 37–110, [0707.4093].

[82] A. Vladikas, *Three topics in renormalization and improvement*, in *Modern Perspectives in Lattice QCD: Quantum Field Theory and High Performance Computing: Lecture Notes of the Les Houches Summer School: Volume 93, August 2009*. Oxford University Press, 2011. 10.1093/acprof:oso/9780199691609.003.0003.

[83] H. Rothe, *Lattice Gauge Theories: An Introduction*, vol. 788. 2010, 10.1007/978-3-642-01850-3.

[84] C. Gattringer and C. B. Lang, *Quantum chromodynamics on the lattice*, vol. 788. Springer, Berlin, 2010, 10.1007/978-3-642-01850-3.

[85] F. Knechtli, M. Günther and M. Peardon, *Lattice Quantum Chromodynamics: Practical Essentials*. SpringerBriefs in Physics. Springer, 2017, 10.1007/978-94-024-0999-4.

[86] M. P. Hernández, *Lattice field theory fundamentals*, in *Modern Perspectives in Lattice QCD: Quantum Field Theory and High Performance Computing: Lecture Notes of the Les Houches Summer School: Volume 93, August 2009*. Oxford University Press, 2011. 10.1093/acprof:oso/9780199691609.003.0001.

[87] K. G. Wilson, *Confinement of quarks*, *Phys. Rev. D* **10** (1974) 2445–2459.

[88] K. G. Wilson, *Quarks and Strings on a Lattice*, *Zichichi A. (eds) New Phenomena in Subnuclear Physics. The Subnuclear Series* **13** (1977) 69–142.

[89] M. Lüscher, *Advanced lattice QCD*, in *Les Houches Summer School in Theoretical Physics, Session 68: Probing the Standard Model of Particle Interactions*, pp. 229–280, 1998. hep-lat/9802029.

[90] K. Symanzik, *Some topics in Quantum Field Theory*, in *6th International Conference on Mathematical Physics - Congress of Association for Mathematical Physics*, pp. 47–58, 1981.

[91] K. Symanzik, *Continuum Limit and Improved Action in Lattice Theories. 1. Principles and ϕ^4 Theory*, *Nucl. Phys. B* **226** (1983) 187–204.

[92] K. Symanzik, *Continuum Limit and Improved Action in Lattice Theories. 2. $O(N)$ Nonlinear Sigma Model in Perturbation Theory*, *Nucl. Phys. B* **226** (1983) 205–227.

[93] M. Lüscher and P. Weisz, *On-Shell Improved Lattice Gauge Theories*, *Commun. Math. Phys.* **97** (1985) 59.

[94] B. Sheikholeslami and R. Wohlert, *Improved Continuum Limit Lattice Action for QCD with Wilson Fermions*, *Nucl. Phys. B* **259** (1985) 572.

[95] T. Bhattacharya, R. Gupta, W. Lee, S. R. Sharpe and J. M. S. Wu, *Improved bilinears in lattice QCD with non-degenerate quarks*, *Phys. Rev. D* **73** (2006) 034504, [hep-lat/0511014].

[96] R. Frezzotti, P. A. Grassi, S. Sint and P. Weisz, *A Local formulation of lattice QCD without unphysical fermion zero modes*, *Nucl. Phys. B Proc. Suppl.* **83** (2000) 941–946, [hep-lat/9909003].

[97] T. Reisz, *Lattice Gauge Theory: Renormalization to All Orders in the Loop Expansion*, *Nucl. Phys. B* **318** (1989) 417–463.

[98] R. Frezzotti, G. Martinelli, M. Papinutto and G. Rossi, *Reducing cutoff effects in maximally twisted LQCD close to the chiral limit*, *JHEP* **2006** (2006) , [0503034].

[99] ETM collaboration, P. Boucaud et al., *Dynamical Twisted Mass Fermions with Light Quarks: Simulation and Analysis Details*, *Comput. Phys. Commun.* **179** (2008) 695–715, [0803.0224].

[100] C. Alexandrou et al., *Simulating twisted mass fermions at physical light, strange and charm quark masses*, *Phys. Rev. D* **98** (2018) 054518, [1807.00495].

[101] R. Frezzotti and G. C. Rossi, *Twisted mass lattice QCD with mass nondegenerate quarks*, *Nucl. Phys. B Proc. Suppl.* **128** (2004) 193–202, [hep-lat/0311008].

[102] C. Pena, S. Sint and A. Vladikas, *Twisted mass QCD and lattice approaches to the $\Delta I = 1/2$ rule*, *JHEP* **09** (2004) 069, [hep-lat/0405028].

[103] G. Bergner, P. Dimopoulos, J. Finkenrath, E. Fiorenza, R. Frezzotti, M. Garofalo et al., *Quark masses and decay constants in $N_f = 2 + 1 + 1$ isoQCD with Wilson clover twisted mass fermions*, *PoS* **LATTICE2019** (2020) 181, [2001.09116].

[104] Extended Twisted Mass collaboration, C. Alexandrou, S. Bacchio, G. Bergner, P. Dimopoulos, J. Finkenrath, R. Frezzotti et al., *Ratio of kaon and pion leptonic decay constants with $N_f = 2 + 1 + 1$ Wilson-clover twisted-mass fermions*, *Phys. Rev. D* **104** (2021) 74520, [2104.06747].

[105] J. Finkenrath, C. Alexandrou, S. Bacchio, M. Constantinou, P. Dimopoulos, R. Frezzotti et al., *Twisted mass gauge ensembles at physical values of the light, strange and charm quark masses*, *PoS* **LATTICE2021** (2022) 284, [2201.02551].

[106] K. Osterwalder and E. Seiler, *Gauge Field Theories on the Lattice*, *Annals Phys.* **110** (1978) 440.

[107] Y. Iwasaki, *Renormalization group analysis of lattice theories and improved lattice action: Two-dimensional non-linear O(N) sigma model*, *Nucl. Phys. B* **258** (1985) 141–156.

[108] Y. Iwasaki, *Renormalization Group Analysis of Lattice Theories and Improved Lattice Action. II. Four-dimensional non-Abelian SU(N) gauge model*, 1111.7054.

[109] K. Jansen, C. Liu, M. Luscher, H. Simma, S. Sint, R. Sommer et al., *Nonperturbative renormalization of lattice QCD at all scales*, *Phys. Lett. B* **372** (1996) 275–282, [hep-lat/9512009].

[110] M. Lüscher, S. Sint, R. Sommer and P. Weisz, *Chiral symmetry and O(a) improvement in lattice QCD*, *Nuclear Physics B* **478** (1996) 365–397, [hep-lat/9605038].

[111] S. Aoki, R. Frezzotti and P. Weisz, *Computation of the improvement coefficient c(SW) to one loop with improved gluon actions*, *Nucl. Phys. B* **540** (1999) 501–519, [hep-lat/9808007].

[112] R. Frezzotti, G. Martinelli, M. Papinutto and G. C. Rossi, *Reducing cutoff effects in maximally twisted lattice QCD close to the chiral limit*, *JHEP* **04** (2006) 38, [0503034].

[113] M. E. Peskin and D. V. Schroeder, *An Introduction to quantum field theory*. Addison-Wesley, Reading, USA, 1995.

[114] A. Maas, "Lattice quantum field theory - Lecture in SS 2020 at the KFU Graz."

[115] Extended Twisted Mass collaboration, C. Alexandrou, S. Bacchio, G. Bergner, M. Constantinou, M. D. Carlo, P. Dimopoulos et al., *Quark masses using twisted-mass fermion gauge ensembles*, *Phys. Rev. D* **104** (2021) 074515, [2104.13408].

[116] F. Jegerlehner and A. Nyffeler, *The muon $g-2$*, *Phys. Rept.* **477** (2009) 1–110, [0902.3360].

[117] J. Aldins, T. Kinoshita, S. J. Brodsky and A. J. Dufner, *Photon-Photon Scattering Contribution to the Sixth-Order Magnetic Moments of the Muon and Electron*, *Phys. Rev. D* **1** (1970) 2378.

[118] A. Nyffeler, *Precision of a data-driven estimate of hadronic light-by-light scattering in the muon $g-2$: Pseudoscalar-pole contribution*, *Phys. Rev. D* **94** (2016) 53006.

[119] X.-d. X. Ji and C.-w. C. Jung, *Studying hadronic structure of the photon in lattice QCD*, *Phys. Rev. Lett.* **86** (2001) 208, [0101014].

[120] X.-d. Ji and C.-w. Jung, *Photon structure functions from quenched lattice QCD*, *Phys. Rev. D* **64** (2001) 34506, [0103007].

[121] J. J. Dudek and R. G. Edwards, *Two Photon Decays of Charmonia from Lattice QCD*, *Phys. Rev. Lett.* **97** (2006) 172001, [0607140].

[122] X. Feng, S. Aoki, H. Fukaya, S. Hashimoto, T. Kaneko, J. I. Noaki et al., *Two-photon decay of the neutral pion in lattice QCD*, *Phys. Rev. Lett.* **109** (2012) 2–6, [1206.1375].

[123] F. Farchioni et al., *Dynamical twisted mass fermions*, *PoS* **LAT2005** (2006) 072, [hep-lat/0509131].

[124] B. Moussallam, *Chiral sum rules for $\mathcal{L}_{(6)}^{\mathrm{WZ}}$ parameters and its application to π^0,η,η' decays*, *Phys. Rev. D* **51** (1995) 4939–4949.

[125] M. Knecht, S. Peris, M. Perrottet and E. de Rafael, *Decay of Pseudoscalars into Lepton Pairs and Large-N_c QCD*, *Phys. Rev. Lett.* **83** (1999) 5230–5233.

[126] UKQCD collaboration, M. Foster and C. Michael, *Quark mass dependence of hadron masses from lattice QCD*, *Phys. Rev. D* **59** (1999) 074503, [hep-lat/9810021].

[127] UKQCD collaboration, C. McNeile and C. Michael, *Decay width of light quark hybrid meson from the lattice*, *Phys. Rev. D* **73** (2006) 074506, [hep-lat/0603007].

[128] ETMC collaboration, S. Simula, *Pseudo-scalar meson form-factors with maximally twisted Wilson fermions at $N_f = 2$*, *PoS* **LATTICE2007** (2007) 371, [0710.0097].

[129] A. S. Gambhir, A. Stathopoulos and K. Orginos, *Deflation as a Method of Variance Reduction for Estimating the Trace of a Matrix Inverse*, *SIAM J. Sci. Comput.* **39** (2017) A532–A558, [1603.05988].

[130] A. Stathopoulos, J. Laeuchli and K. Orginos, *Hierarchical probing for estimating the trace of the matrix inverse on toroidal lattices*, 1302.4018.

[131] G. Eichmann, C. S. Fischer, E. Weil and R. Williams, *Single pseudoscalar meson pole and pion box contributions to the anomalous magnetic moment of the muon*, *Phys. Lett. B* **797** (2019) 134855, [1903.10844].

[132] K. Raya, A. Bashir and P. Roig, *Contribution of neutral pseudoscalar mesons to a_μ^{HLbL} within a Schwinger-Dyson equations approach to QCD*, *Phys. Rev. D* **101** (2020) 074021, [1910.05960].

[133] D. Krause, *JUWELS: Modular Tier-0/1 Supercomputer at the Jülich Supercomputing Centre*, *JLSRF* **5** (2019) A135.

[134] K. Jansen and C. Urbach, *tmLQCD: A Program suite to simulate Wilson Twisted mass Lattice QCD*, *Comput. Phys. Commun.* **180** (2009) 2717–2738, [0905.3331].

[135] A. Deuzeman, K. Jansen, B. Kostrzewa and C. Urbach, *Experiences with OpenMP in tmLQCD*, *PoS* **LATTICE2013** (2014) 416, [1311.4521].

[136] A. Abdel-Rehim, F. Burger, A. Deuzeman, K. Jansen, B. Kostrzewa, L. Scorzato et al., *Recent developments in the tmLQCD software suite*, *PoS* **LATTICE2013** (2014) 414, [1311.5495].

[137] B. Kostrzewa, S. Bacchio, J. Finkenrath, M. Garofalo, F. Pittler, S. Romiti et al., *Twisted mass ensemble generation on GPU machines*, 2022-12. 2212.06635.

[138] C. Alexandrou, S. Bacchio, J. Finkenrath, A. Frommer, K. Kahl and M. Rottmann, *Adaptive Aggregation-based Domain Decomposition Multigrid for Twisted Mass Fermions*, *Phys. Rev. D* **94** (2016) 114509, [1610.02370].

[139] C. Alexandrou, S. Bacchio and J. Finkenrath, *Multigrid approach in shifted linear systems for the non-degenerated twisted mass operator*, *Comput. Phys. Commun.* **236** (2019) 51–64, [1805.09584].

[140] M. A. Clark, R. Babich, K. Barros, R. C. Brower and C. Rebbi, *Solving Lattice QCD systems of equations using mixed precision solvers on GPUs*, *Comput. Phys. Commun.* **181** (2010) 1517–1528, [0911.3191].

[141] R. Babich, M. A. Clark, B. Joo, G. Shi, R. C. Brower and S. Gottlieb, *Scaling Lattice QCD beyond 100 GPUs*, in *SC11 International Conference for High Performance Computing, Networking, Storage and Analysis*, 2011-09. 1109.2935. 10.1145/2063384.2063478.

[142] M. A. Clark, B. Joó, A. Strelchenko, M. Cheng, A. Gambhir and R. Brower, *Accelerating Lattice QCD Multigrid on GPUs Using Fine-Grained Parallelization*, 1612.07873.

[143] J. D. Hunter, *Matplotlib: A 2d graphics environment*, *Computing in Science & Engineering* **9** (2007) 90–95.

[144] L. Gan, B. Kubis, E. Passemar and S. Tulin, *Precision tests of fundamental physics with η and η' mesons*, *Phys. Rept.* **945** (2022) 1–105, [2007.00664].

[145] JADE collaboration, W. Bartel et al., *A measurement of the η radiative width $\Gamma(\eta \to \gamma\gamma)$*, *Phys. Lett. B* **158** (1985) 511.

[146] Crystal Ball collaboration, D. Williams et al., *Formation of the Pseudoscalars π^0, η and η' in the Reaction $\gamma\gamma \to \gamma\gamma$*, *Phys. Rev. D* **38** (1988) 1365.

[147] N. A. Roe et al., *A Measurement of the Radiative Width of the η and η' Mesons With the Asp Detector*, *Phys. Rev. D* **41** (1990) 17.

[148] S. E. Baru et al., *Measurement of two photon widths of the A2, eta-prime, eta*, *Z. Phys. C* **48** (1990) 581–586.

[149] KLOE-2 collaboration, D. Babusci et al., *Measurement of η meson production in $\gamma\gamma$ interactions and $\Gamma(\eta \to \gamma\gamma)$ with the KLOE detector*, *JHEP* **01** (2013) 119, [1211.1845].

[150] A. Browman, J. DeWire, B. Gittelman, K. M. Hanson, E. Loh and R. Lewis, *The Radiative Width of the eta Meson*, *Phys. Rev. Lett.* **32** (1974) 1067.

[151] T. Aoyama, M. Hayakawa, T. Kinoshita and M. Nio, *Complete Tenth-Order QED Contribution to the Muon $g-2$*, *Phys. Rev. Lett.* **109** (2012) 111808, [1205.5370].

[152] T. Aoyama, T. Kinoshita and M. Nio, *Theory of the Anomalous Magnetic Moment of the Electron*, *Atoms* **7** (2019) 28.

[153] A. Czarnecki, W. J. Marciano and A. Vainshtein, *Refinements in electroweak contributions to the muon anomalous magnetic moment*, *Phys. Rev. D* **67** (2003) 073006, [hep-ph/0212229].

[154] C. Gnendiger, D. Stöckinger and H. Stöckinger-Kim, *The electroweak contributions to $(g-2)_\mu$ after the Higgs boson mass measurement*, *Phys. Rev. D* **88** (2013) 053005, [1306.5546].

[155] A. Kurz, T. Liu, P. Marquard and M. Steinhauser, *Hadronic contribution to the muon anomalous magnetic moment to next-to-next-to-leading order*, *Phys. Lett. B* **734** (2014) 144–147, [1403.6400].

[156] G. Colangelo, M. Hoferichter, M. Procura and P. Stoffer, *Dispersion relation for hadronic light-by-light scattering: two-pion contributions*, *JHEP* **04** (2017) 161, [1702.07347].

[157] J. Bijnens, N. Hermansson-Truedsson and A. Rodríguez-Sánchez, *Short-distance constraints for the HLbL contribution to the muon anomalous magnetic moment*, *Phys. Lett. B* **798** (2019) 134994, [1908.03331].

[158] G. Colangelo, F. Hagelstein, M. Hoferichter, L. Laub and P. Stoffer, *Longitudinal short-distance constraints for the hadronic light-by-light contribution to $(g-2)_\mu$ with large-N_c Regge models*, *JHEP* **03** (2020) 101, [1910.13432].

[159] G. Colangelo, M. Hoferichter, A. Nyffeler, M. Passera and P. Stoffer, *Remarks on higher-order hadronic corrections to the muon $g-2$*, *Phys. Lett. B* **735** (2014) 90–91, [1403.7512].

[160] V. L. Chernyak and S. I. Eidelman, *Hard exclusive two photon processes in QCD*, *Prog. Part. Nucl. Phys.* **80** (2015) 1–42, [1409.3348].

[161] R. Escribano, P. Masjuan and P. Sanchez-Puertas, *The η transition form factor from space- and time-like experimental data*, *Eur. Phys. J. C* **75** (2015) 414, [1504.07742].

[162] B. Kubis and J. Plenter, *Anomalous decay and scattering processes of the η meson*, *Eur. Phys. J. C* **75** (2015) 283, [1504.02588].

[163] S. Borsanyi, S. Durr, Z. Fodor, C. Hoelbling, S. D. Katz, S. Krieg et al., *Ab initio calculation of the neutron-proton mass difference*, *Science* **347** (2015) 1452–1455.

[164] H. Akaike, *A Bayesian analysis of the minimum AIC procedure*, *Annals of the Institute of Statistical Mathematics* **30** (1978) 9–14.

[165] C. Alexandrou et al., *Pion Transition Form Factor from Twisted-Mass Lattice QCD and the Hadronic Light-by-Light π^0-pole Contribution to the Muon $g-2$*, 2308.12458.

[166] A. Gérardin, W. E. A. Verplanke, G. Wang, Z. Fodor, J. N. Guenther, L. Lellouch et al., *Lattice calculation of the π^0, η and η' transition form factors and the hadronic light-by-light contribution to the muon $g-2$*, 2305.04570.

[167] S. L. Adler, *Axial-Vector Vertex in Spinor Electrodynamics*, *Phys. Rev.* **177** (1969) 2426–2438.

[168] J. S. Bell and R. Jackiw, *A PCAC puzzle: $\pi^0 \to \gamma\gamma$ in the σ-model*, *Nuovo Cimento A* **60** (1969) 47–61.

[169] G. P. Lepage and S. J. Brodsky, *Exclusive Processes in Quantum Chromodynamics: Evolution Equations for Hadronic Wave Functions and the Form-Factors of Mesons*, *Phys. Lett. B* **87** (1979) 359–365.

[170] G. P. Lepage and S. J. Brodsky, *Exclusive Processes in Perturbative Quantum Chromodynamics*, *Phys. Rev. D* **22** (1980) 2157.

[171] S. J. Brodsky and G. P. Lepage, *Large Angle Two Photon Exclusive Channels in Quantum Chromodynamics*, *Phys. Rev. D* **24** (1981) 1808.

[172] V. A. Nesterenko and A. V. Radyushkin, *Comparison of the QCD Sum Rule Approach and Perturbative QCD Analysis for $\gamma^*\gamma^* \to \pi^0$ Process*, *Sov. J. Nucl. Phys.* **38** (1983) 284.

[173] V. A. Novikov, M. A. Shifman, A. I. Vainshtein, M. B. Voloshin and V. I. Zakharov, *Use and Misuse of QCD Sum Rules, Factorization and Related Topics*, *Nucl. Phys. B* **237** (1984) 525–552.

[174] C. G. Boyd, B. Grinstein and R. F. Lebed, *Model independent determinations of $\bar{B} \to Dl\bar{\nu}$, $D^* l\bar{\nu}$ form-factors*, *Nucl. Phys. B* **461** (1996) 493–511, [9508211].

[175] C. Bourrely, I. Caprini and L. Lellouch, *Model-independent description of $B \to \pi l\nu$ decays and a determination of $|V_{ub}|$*, *Phys. Rev. D* **79** (2009) 013008, [0807.2722].

[176] M. Crisafulli, V. Lubicz and A. Vladikas, *Improved renormalization of lattice operators: A Critical reappraisal*, *Eur. Phys. J. C* **4** (1998) 145–171, [hep-lat/9707025].

[177] L. H. Karsten and J. Smit, *Lattice Fermions: Species Doubling, Chiral Invariance, and the Triangle Anomaly*, *Nucl. Phys. B* **183** (1981) 103.

[178] M. Bochicchio, L. Maiani, G. Martinelli, G. C. Rossi and M. Testa, *Chiral Symmetry on the Lattice with Wilson Fermions*, *Nucl. Phys. B* **262** (1985) 331.

[179] PrimEx collaboration, I. Larin et al., *A New Measurement of the π^0 Radiative Decay Width*, *Phys. Rev. Lett.* **106** (2011) 162303, [1009.1681].

[180] I. Larin, Y. Zhang, A. Gasparian, L. Gan, R. Miskimen, M. Khandaker et al., *Precision measurement of the neutral pion lifetime*, *Science* **368** (2020) 506–509, [https://www.science.org/doi/pdf/10.1126/science.aay6641].

[181] W. I. Jay and E. T. Neil, *Bayesian model averaging for analysis of lattice field theory results*, *Phys. Rev. D* **103** (2021) , [2008.01069].

[182] P. Masjuan, *$\gamma^*\gamma \to \pi^0$ transition form factor at low-energies from a model-independent approach*, *Phys. Rev. D* **86** (2012) 094021, [1206.2549].

[183] K. Johnson, M. Baker and R. Willey, *Self-Energy of the Electron*, *Phys. Rev.* **136** (1964) B1111—-B1119.

[184] K. Johnson, R. Willey and M. Baker, *Vacuum Polarization in Quantum Electrodynamics*, *Phys. Rev.* **163** (1967) 1699–1715.

[185] J. L. Rosner, *Higher-order contributions to the divergent part of Z_3 in a model quantum electrodynamics*, *Annals of Physics* **44** (1967) 11–34.

[186] M. J. Levine and R. Roskies, *Hyperspherical approach to quantum electrodynamics: sixth-order magnetic moment*, *Phys. Rev. D* **9** (1974) 421–429.

[187] M. J. Levine, E. Remiddi and R. Roskies, *Analytic contributions to the g factor of the electron in sixth order*, *Phys. Rev. D* **20** (1979) 2068–2076.

[188] H. Bae, S. Monti, M. Montano, M. H. Steinberg, T. T. Perls and P. Sebastiani, *Learning Bayesian Networks from Correlated Data*, *Sci. Rep.* **6** (2016) .

[189] J. G. Ibrahim, H. Zhu, R. I. Garcia and R. Guo, *Fixed and Random Effects Selection in Mixed Effects Models*, *Biometrics* **67** (2011) 495–503.

[190] D. Lunn, C. Jackson, N. Best, A. Thomas and D. Spiegelhalter, *The BUGS Book: A Practical Introduction to Bayesian Analysis*. 2012.

[191] T. Leinster, *Effective Sample Size*, 2014. https://golem.ph.utexas.edu/category/2014/12/effective_sample_size.html, accessed on 13.07.2022.

[192] A. Sokal, *Monte Carlo Methods in Statistical Mechanics: Foundations and New Algorithms*. Springer US, Boston, MA, 1997, 10.1007/978-1-4899-0319-8_6.

[193] ALPHA collaboration, U. Wolff, *Monte Carlo errors with less errors*, *Comput. Phys. Commun.* **156** (2004) 143–153, [hep-lat/0306017].

[194] B. Efron, *Bootstrap methods: Another look at the jackknife*, *The Annals of Statistics* **7** (1979) 1–26.

[195] B. Efron and C. Stein, *The Jackknife Estimate of Variance*, *The Annals of Statistics* **9** (1981) 586–596.

[196] C. F. J. Wu, *Jackknife, Bootstrap and Other Resampling Methods in Regression Analysis*, *The Annals of Statistics* **14** (1986) 1261–1295.

[197] B. Efron and R. Tibshirani, *An Introduction to the Bootstrap*. Chapman and Hall/CRC, 1994, 10.1201/9780429246593.

[198] P. J. Bickel and D. A. Freedman, *Some asymptotic Theory for the Bootstrap*, *The Annals of Statistics* **9** (1981) 1196–1217.